Advances in High Energy Physics

Neutrino Physics in the Frontiers of Intensities and Very High Sensitivities

Guest Editors: Theocharis Kosmas, Hiro Ejiri, and Athanasios Hatzikoutelis

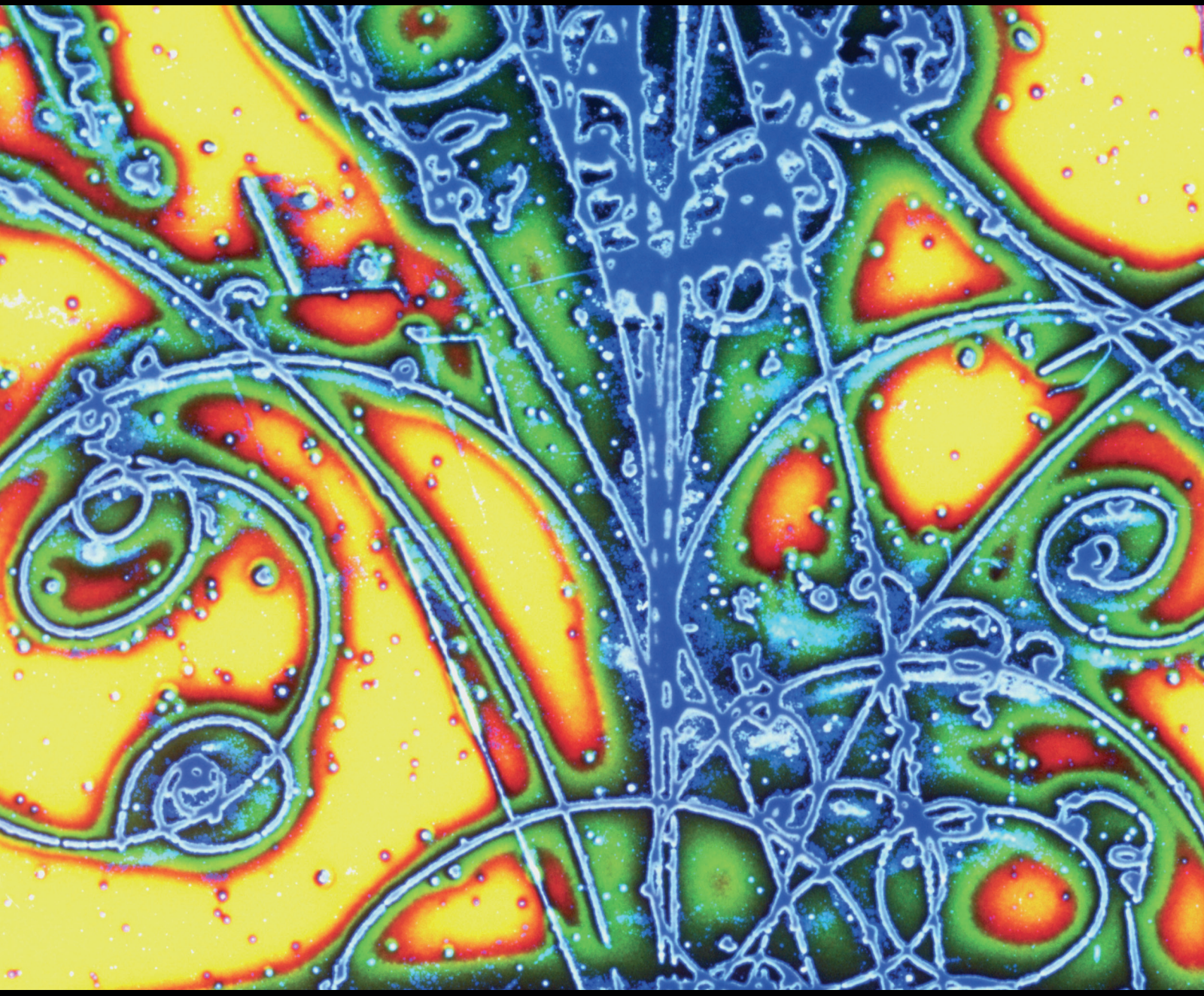

Neutrino Physics in the Frontiers of Intensities and Very High Sensitivities

Advances in High Energy Physics

Neutrino Physics in the Frontiers of Intensities and Very High Sensitivities

Guest Editors: Theocharis Kosmas, Hiro Ejiri, and Athanasios Hatzikoutelis

Editorial Board

Contents

Hindawi Publishing Corporation
Advances in High Energy Physics
Volume 2015, Article ID 806067, 3 pages
http://dx.doi.org/10.1155/2015/806067

Editorial

Neutrino Physics in the Frontiers of Intensities and Very High Sensitivities

Theocharis Kosmas,[1] Hiro Ejiri,[2] and Athanasios Hatzikoutelis[3]

[1] *Division of Theoretical Physics, University of Ioannina, 45110 Ioannina, Greece*
[2] *Research Center for Nuclear Physics, Osaka University, Osaka 567-0047, Japan*
[3] *Physics Department, University of Tennessee, Knoxville, TN 37996, USA*

Correspondence should be addressed to Theocharis Kosmas; hkosmas@uoi.gr

Received 29 March 2015; Accepted 29 March 2015

Historically, neutrino physics is a field of continuous advancement: from the neutrino discovery, proposed by Pauli in order to balance the missing energy of the beta decay in the early 20th century, to the proof of the neutrino mass through the measurement of the solar neutrino oscillations by the end of it. The beginning of the 21st century opened the intensity frontier with the development of near mega-watt accelerator machines. These machines, competing with the mega-watt reactors as sources of neutrinos, have been pushing the frontier back at a rate of 10^{12} events per second. So, such experiments are now comparing sensitivity reach in units of "MWatt-kton-years." Even from the first decade of this century, we have already the success of the neutrino oscillation mixing parameters going from unknown quantities to the best measured values in the field.

The sensitivity frontier is characterized by enormous detector systems that lead precision studies from laboratory or astrophysical neutrino sources. Relying on the detection sensitivity of these systems, there exist various works describing in high precision the fluxes, rates, distributions, and directions of reactor, beam, and supernova neutrinos. They review a wide range of subjects in accelerator neutrino oscillations at the GeV range, solar and astroneutrinos in sub-MeV to 10 MeV, neutrino nuclear interactions in the 10 MeV to GeV region, double beta decays, tritium beta decays, and interactions with complex nuclei. The phenomena are well known, but their absolute cross-sections need to be understood at a high precision in order to fix the strong part of the radiative corrections and be able to independently check the standard model, particularly in the light of the new boson discoveries. The frontiers have generated multinational collaborations tallying great numbers of scientists and engineers having built or designed multimillion projects.

Neutrino oscillation data come from a variety of solar (Super-K, SNO, BOREXINO, etc.), atmospheric (mainly Super-K), reactor (KamLAND, Double Chooz, RENO, and Daya Bay), and short- and long-baseline accelerator experiments (MINOS, MiniBooNE, MINERVA, OPERA, ICAROS, T2K, and NOvA) [1, 2]. They are fed by intense beams from advanced machines at JPARC, CERN, FERMILAB, and ORNL, along with several power plant nuclear reactors around the world. To describe them the simplest unitary form for the lepton mixing matrix is assumed and the state-of-the-art solar and atmospheric neutrino calculations are used. In this special issue, various papers are devoted to the latest research related to existing experiments as well as to the sensitivity estimations of future ones like Hyper-Kamiokande, MicroBOONE, DUNE (Deep Underground Neutrino Experiment, previously named LBNE), COHERENT, JUNO, LENA, and others [1, 3].

In the low-energy and intermediate-energy neutrino range, the charged-current (CC) and neutral-current (NC) neutrino-nucleus reactions provide crucial understanding of the underlying physics of fundamental electroweak interactions within and beyond the standard model. Coherent scattering of neutrinos on nuclei was proposed long ago as

an excellent probe of neutral-current ν-nucleus processes for a plethora of conventional neutrino physics applications and new-physics open issues, but it was not yet measured experimentally [4]. However, a great number of events are expected to be recorded in the going experiments (e.g., COHERENT, TEXONO, and GEMMA). On the theoretical side, the neutrino-nucleus cross-sections calculations (with nuclear methods like the shell model, quasiparticle random-phase approximation, QRPA, shell-model Monte Carlo, etc.) predict quite reliably the nuclear transitions for neutrino energies $E_\nu \leq 100$ MeV. Simulated signatures of neutrino interactions on various isotopes (^{48}Ti, ^{76}Ge, ^{114}Cd, ^{132}Xe, etc.) can, subsequently, be derived for several low- and intermediate-energy neutrino distributions of astrophysical neutrino sources, like the solar, supernova, and Earth neutrinos, as well as the laboratory neutrinos, the reactor neutrinos, the pion-muon stopped neutrinos, and the beta beam neutrinos [5–7]. In view of the operation of extremely intensive neutrino fluxes (at the SNS, PSI, JPARC, Fermilab, etc.), the sensitivity to search for new physics will be largely increased, and, therefore, through coherent neutrino-nucleus scattering cross-section measurements, several open questions involving nonstandard neutrino interactions, neutrino magnetic moment, sterile neutrino searches, and others may be answered.

Neutrinoless double beta decay ($0\nu\beta\beta$) is suitable for high-sensitivity studies for Majorana ν masses and possible new particles beyond the standard model. The ($0\nu\beta\beta$) transitions are extremely rare processes of the order of 10^{-34}–10^{-36} per sec. There are several existing ($0\nu\beta\beta$) experiments in progress as well as R&D on future ones such as MAJORANA, GERDA, MOON, Super-NEMO, CUORE, SNO+, EXO, KamLAND, COBRA, and NEXT [8]. The present volume includes two ($0\nu\beta\beta$) papers. One is an interesting description of cryogenic multiton scale detectors with scintillation light read-outs. The other is a ($0\nu\beta\beta$) study used to search for heavy ν and SUSY particles as a complementary probe to the energy frontier searches [8, 9].

During the last few years, there is growing interest in high-energy neutrino astronomy including high-energy γ-ray and neutrino astronomy with large neutrino telescopes under design or construction. New findings have been reported by ambitious projects in various stages of construction including ANTARES, NEMO, NESTOR, IceCube, AUGER, and AMANDA. Novel ideas for neutrino detection using acoustic and radio waves continue to receive serious attention. The relevant topics included in this volume refer to solar neutrinos, atmospheric neutrinos, results in high-energy neutrino astronomy, and plans in high-energy neutrino astronomy and dark matter research. Current experiments in the field of high-energy neutrino astronomy include AMANDA-II and IceCube at the South Pole. Astonishing developments in new telescopes and detector facilities are described for the CTA Cerenkov gamma-ray array, the Fermi orbital telescope, and the aforementioned IceCube neutrino detector. High-energy neutrinos are assumed to be produced in galactic XRB that include a stellar mass compact object with a companion (donor) star still in the main sequence that is away from the final stages of its evolution [10]. Such a binary system may emit in many different wavelengths, from radio and IR to high-energy gamma rays and neutrinos. In the present volume simulations of neutrino emissions from relativistic galactic astrophysical jets are modelled. These neutrinos have very high energies (in the order of 100 GeV) and specialized instruments are in operation in order to detect them, both on Earth and in space. Furthermore, some next generation instruments are in the process of design and construction.

Neutrino mass may be closely connected to the dark matter of the Universe. Thus, neutrino oscillations, along with neutrino mass generation schemes, suggest dark matter candidates with properties relevant to direct or indirect detection prospects. These issues may be closely interlinked and are several examples of neutrino-motivated dark matter candidates. Though all of them demonstrate cold dark matter properties, as far as the cosmic microwave background (CMB) is concerned, some of them may even behave as warm dark matter regarding its structure formation. When it comes to detection, some are ideal for direct detection, while others are ideal for indirect one through their decay products [11, 12]. These searches are presently negative, but they continue for other phenomena, such as weakly interacting massive particles or candidates of cold dark matter. Some of such developments are in this volume as well.

The knowledge about neutrinos continues to grow using atmospheric and solar neutrinos, though it is now concentrating on quantitative and not simply qualitative features of understanding the mixing parameters. It is expected that further understanding of the nature of neutrino will come from accelerator neutrinos, using off-axis beams, and reactor neutrinos, using multiple detectors underground. The sensitivity of the current and proposed detecting systems has spurred the detailed study of neutrino sources, be it man-made or astrophysical. Relying on the detection sensitivity of the intensity and sensitivity frontier systems there are various works of high precision estimation of fluxes, rates, and distributions of reactor, beam, and supernova neutrinos. The papers in this special issue are a sample of the world effort to push the frontiers even further back towards the neutrino mass hierarchy and the CP violation of the lepton sector. The road to the coveted new physics is now open, but perhaps this will be a subject for another special issue.

Theocharis Kosmas
Hiro Ejiri
Athanasios Hatzikoutelis

References

[1] S. Abe, T. Ebihara, S. Enomoto et al., "Precision measurement of neutrino oscillation parameters with KamLAND," *Physical Review Letters*, vol. 100, Article ID 221803, 2008.

[2] G. Bellini, J. Benziger, D. Bick et al., "Precision measurement of the Be7 solar neutrino interaction rate in borexino," *Physical Review Letters*, vol. 107, no. 14, Article ID 141302, 5 pages, 2011.

[3] M. Wurm, J. F. Beacom, L. B. Bezrukov et al., "The next-generation liquid-scintillator neutrino observatory LENA," *Astroparticle Physics*, vol. 35, pp. 685–766, 2012.

[4] J. D. Vergados, F. T. Avignone, and I. Giomataris, "Coherent neutral current neutrino-nucleus scattering at a spallation source: a valuable experimental probe," *Physical Review D*, vol. 79, no. 11, Article ID 113001, 2009.

[5] K. Langanke, *Stellar Evolution: From Hydrostatic Burning to Core Collapse*, vol. 178 of *Proceedings of the International School of Physics "Enrico Fermi"*, IOS Press, 2011.

[6] K. G. Balasi, K. Langanke, and G. Martinez-Pinedo, "Neutrino-nucleus reactions and their role for supernova dynamics and nucleosynthesis," http://arxiv.org/abs/1503.08095.

[7] V. Tsakstara and T. S. Kosmas, "Analyzing astrophysical neutrino signals using realistic nuclear structure calculations and the convolution procedure," *Physical Review C—Nuclear Physics*, vol. 84, no. 6, Article ID 064620, 2011.

[8] H. Ejiri, "Nuclear spin isospin responses for low-energy neutrinos," *Physics Report*, vol. 338, no. 3, pp. 265–351, 2000.

[9] N. Barros, J. Thurn, and K. Zuber, "Double beta decay searches of ^{134}Xe, ^{126}Xe and ^{124}Xe with large scale Xe detectors," *Journal of Physics G: Nuclear and Particle Physics*, vol. 41, no. 11, Article ID 115105, 2014.

[10] M. M. Reynoso and G. E. Romero, "Magnetic field effects on neutrino production in microquasars," *Astronomy & Astrophysics*, vol. 493, no. 1, pp. 1–11, 2009.

[11] T. S. Kosmas and J. D. Vergados, "Cold dark matter in SUSY theories: the role of nuclear form factors and the folding with the LSP velocity," *Physical Review D—Particles, Fields, Gravitation and Cosmology*, vol. 55, no. 4, pp. 1752–1764, 1997.

[12] J. D. Vergados, H. Ejiri, and K. G. Savvidy, "Theoretical direct WIMP detection rates for inelastic scattering to excited states," *Nuclear Physics B*, vol. 877, no. 1, pp. 36–50, 2013.

Hindawi Publishing Corporation
Advances in High Energy Physics
Volume 2015, Article ID 921757, 7 pages
http://dx.doi.org/10.1155/2015/921757

Research Article

High Energy Neutrino Emission from Astrophysical Jets in the Galaxy

T. Smponias[1] and O. T. Kosmas[2]

[1] *Division of Theoretical Physics, University of Ioannina, GR-45110 Ioannina, Greece*
[2] *Chair of Applied Dynamics, University of Erlangen-Nuremberg, Haberstrasse 1, D-91058 Erlangen, Germany*

Correspondence should be addressed to T. Smponias; t.smponias@hushmail.com

Received 11 July 2014; Revised 22 October 2014; Accepted 3 November 2014

Academic Editor: Athanasios Hatzikoutelis

We address simulated neutrino emission originated from astrophysical jets of compact objects within the Galaxy. These neutrinos are of high energies (E_ν of the order up to a few TeV) and for their observation specialized instruments are in operation, both on Earth and in orbit. Furthermore, some next generation telescopes and detector facilities are in the process of design and construction. The jet flow simulations are performed using the modern PLUTO hydrocode in its relativistic magnetohydrodynamic version. One of the main ingredients of the present work is the presence of a toroidal magnetic field that confines the jet flow and furthermore greatly affects the distribution of the high energy neutrinos.

1. Introduction

In recent years, a remarkable development of neutrino and gamma-ray astronomy took place. New telescopes and detector facilities were designed and implemented, such as the CTA Cerenkov gamma-ray array [1], Fermi orbital telescope [2], or the IceCube neutrino detector [3]. The IceCube neutrino observatory, located at the South Pole, detects neutrinos in a wide energy range, far exceeding the energies of man-made accelerator beams. IceCube features a large detector volume, increasing the possibility to detect neutrinos from individual astrophysical sources.

Potential sites for gamma-ray and neutrino production from jets include galactic sources of X-ray binaries (XRB) [4–6], as well as extragalactic sources [7] such as active galactic nuclei (AGN) ([8]). The above categories may be extended to include a wide range of different phenomena, such as supernova remnants [9, 10] and other possible sources of high energy particles. These systems may produce γ-rays and high energy neutrinos from interactions (collisions) of high energy protons with thermal ones. In general, a large detector volume is needed, since neutrinos are so weakly interacting with matter.

At the same time, γ-ray emission can also be observed, from such sources, by ground and satellite based gamma-ray telescopes (e.g., Fermi, CTA). When studying acceleration processes of those sources, it is often useful to compare the neutrino and γ-ray fluxes emanating from them.

XRB are binary stellar systems comprising a main sequence star and a compact object, emitting in the X-ray band, often also called microquasars [4, 11], in relation to the their cousins of galactic scale, quasars. They have relativistic jets that include acceleration sites allowing particles to reach energies up to TeV [12]. There, the cooling of TeV electrons is very strong due to the high density of the radiation, implying a hadronic mechanism for the gamma-ray emission. Simultaneous neutrino emission is then possible as well [5, 6].

In this work, we aim to simulate the neutrino flux generated from a model microquasar X-ray binary system, assuming a hadronic jet and hadron-related acceleration processes (nonthermal proton acceleration and interactions of high energy protons). Towards this purpose, a power law with an exponential cutoff spectrum is used [5, 13]. This is an extension of our previous calculations of γ-ray emission from a simulated relativistic hydrodynamical jet [14].

Table 1: Values of various physical and model parameters pertaining to the γ-ray emission from the jet, for the simulation run, obtained with the linear method and the Hancock integrator.

Parameter		Comments
Cell size ($\times 10^{10}$ cm)	0.25	PLUTO's computational cell
ρ_{jet} (cm^{-3})	1.0×10^{11}	Initial jet matter density
ρ_{sw} (cm^{-3})	1.0×10^{12}	Stellar wind density
ρ_{adw} (cm^{-3})	1.0×10^{12}	Accretion disk wind density
$t_{\text{run}}^{\max}$ (s)	1.5×10^{3}	Model execution time
Interpolation method	Linear	
Integrator	MUSCL-Hancock	
EOS	Ideal	Equation of state
BinSep (cm)	4.0×10^{12}	Binary star separation
$M_{\text{BH}}/M_{\text{sun}}$	3–10	Mass range of collapsed star
$M_{\text{star}}/M_{\text{sun}}$	10–30	Mass range of main Seq. star
$\beta = v_0/c$	0.26	Initial jet speed
L_k^p	2×10^{36}	Jet kinetic luminosity
q_{rel}	10^{-4}	Fast proton energy fraction
q_ν	0.1	Neutrino energy fraction (from fast protons)
α	-2	Fast proton power law index
$E_p^{\max}$ (GeV)	10^6	Cutoff energy of the fast proton distribution
Grid resolution	$120 \times 200 \times 120$	PLUTO grid resolution (xyz)

Neutrinos are mainly produced through pion and muon decay with the pions coming from inelastic pp-scatterings among nonthermal protons and thermal ones within the jet. Pion decay by-products include a muon and a muon neutrino as $\pi^{\pm} \rightarrow \mu^{\pm} + \nu_\mu(\tilde{\nu}_\mu)$. The muons can afterwards decay again into an electron or a positron and the associated neutrino. Another pion decay channel leads to two gamma-ray photons [6, 13, 15]:

$$\begin{aligned} pp &\longrightarrow pp\pi^0 + F \\ pp &\longrightarrow pn\pi^+ + F \end{aligned} \tag{1}$$

($m_p = 1.67 \times 10^{-24}$ g and $m_\pi = 2.38 \times 10^{-25}$ g). F comprises π^0 and $\pi^+\pi^-$ pairs. Subsequently, pion decay leads to muons, γ-rays, and neutrino production.

In the present work, we concentrate on simulations of neutrino emission from relativistic galactic astrophysical jets. These neutrinos have very high energy (of the order of TeV) and specialized instruments are in operation in order to detect them, both on Earth and in space. Furthermore, some next generation instruments are in the process of design and construction. The jet flow simulations are performed using the modern PLUTO hydrocode in its relativistic magnetohydrodynamic version [16]. We assume the existence of a toroidal magnetic field that confines the jet flow (in the region of the compact object) [17], affecting the production of the high energy neutrinos [6].

2. Description of the Method

The jet is modelled using the relativistic magnetohydrodynamic (RMHD) version of the PLUTO hydrocode [16]. The PLUTO RMHD module is employed in order to simulate the jet flow. The Generalized Lagrange Multiplier (GLM) correction method is used, enforcing magnetic divergence suppression through hyperbolic divergence cleaning, while the MUSCL-Hancock scheme is employed as the integrator. A toroidal magnetic field is used that helps constrain the jet, to an extent depending on the field strength. In this paper, we explore the existence of a strong magnetic field that keeps the emitted neutrino flux highly concentrated [17].

The toroidal magnetic field setup employed leads to a rather pronounced jet confinement, due to Lorentz forces acting on the jet matter towards the jet axis. The stellar wind is set to decrease away from the companion star as $1/r^2$, while a corona of $1/y^2$, y being the jet axis direction, is setup near the compact object, similar to [14]. The most important model parameters are shown in Table 1. The IDL suite and the VisIt visualization suite are then employed in order to present the results of the simulations in a graphical manner.

The boundary conditions are outflow at the top and at the sides of the computational domain ("box") and reflective at the bottom, where the jet base is located. The jet emanates from the middle of the bottom plane (x-z plane) moving upwards, that is, along the model's y-axis.

3. Radiative Transfer and Imaging

The line-of-sight (LOS) code of [18] is used to produce artificial neutrino "images" of the jet-corona system. The particle "emission" is calculated separately from each computational cell, under the twin assumptions that the particle distribution's dominant cooling time is smaller than the hydrocode's time step and also that the mean free path between collisions is smaller than the hydrocode computational cell dimensions. Then each cell can be treated individually from a radiative

point of view and its neutrino emission contribution, at a given energy level, is added to its corresponding LOS. Naturally, no absorption is relevant for neutrinos in such systems.

The emission calculation is performed in Mathematica, mainly following the analysis of [5, 6]. Furthermore, for converting the neutrino emission from the jet reference frame to our rest frame, the calculational procedure can be, for example, that of [19] or that of [20], and we have, respectively,

$$n(E,\Omega) = \frac{A}{4\pi}\frac{\Gamma^{-\alpha+1}E^{-\alpha}\left(1-\beta\cos(\theta)\sqrt{1-m^2c^4/E^2}\right)^{-\alpha}}{\left[\sin^2(\theta)+\Gamma^2\left(\cos(\theta)-\left(\beta/\sqrt{1-m^2c^4/E^2}\right)\right)^2\right]^{1/2}},$$
$$n(E,\Omega) = \frac{A}{4\pi}\frac{\Gamma^{-\alpha-1}E^{-\alpha}\left(1-\beta\cos(\theta)\sqrt{1-m^2c^4/E^2}\right)^{-\alpha-1}}{\left[\sin^2(\theta)+\Gamma^2\left(\cos(\theta)-\left(\beta/\sqrt{1-m^2c^4/E^2}\right)\right)^2\right]^{1/2}}, \quad (2)$$

where Ω is the line-of-sight solid angle, Γ denotes the jet beam Lorentz factor (for thermal, slow protons), and $\beta = u/c$, the known ratio.

The difference between the above expressions lies in the powers of the two factors of the denominators on their last fraction. In the present work, we have chosen to apply the expression of [19].

The nonthermal proton distribution suffers synchrotron and adiabatic losses, affecting the balance in the transport between protons and pions. Following the formalism of [5, 13], we may then obtain the neutrino emissivity:

$$F_\nu\left(x,E_p\right) = \frac{2}{\lambda}\int_0^\lambda F_\pi\left(\frac{E_\nu}{x},E_p\right)\frac{dx}{x}, \quad (3)$$

where $x = E_\pi/E_p$, $\lambda = 0.427$, and the F_π (for pion distribution) reads

$$F_\pi = \int_{E_\pi}^{E_p}\frac{F_\pi^{(\mathrm{inj})}\left(E'\right)t_{pp}^{-1}}{\left|b_\pi\left(E_\pi\right)\right|}\exp\left[\frac{1}{b_zE_\pi}+\frac{1}{b_zE'}+\frac{\alpha_z}{b_z^2}\log\left(\frac{E_\pi}{E'}\right)+\frac{a_z}{b_z^2}\log\left(\frac{b_z+\alpha_zE'}{b_z+\alpha_zE_\pi}\right)\right]dE'. \quad (4)$$

The function $F_\pi^{(\mathrm{inj})}$ is given in [13] and α_z, b_z are given in [5]. We note the dependency of b_z on the magnetic field B, among others.

On the other hand, adopting the approach of [6], also [15], we have the following line of calculations for the neutrino emission that was actually used in the current work. For the readers convenience we give here a brief presentation of the formalism of [6] (for more details see [6] and references therein).

Starting with the pion injection function, we have

$$Q_\pi^{(pp)}(E,z) = n(z)\,c\int_k^1\frac{dx}{x}N_p\left(\frac{E}{x},z\right)F_\pi^{(pp)}\left(x,\frac{E}{x}\right)\sigma_{pp}^{(\mathrm{inel})}\left(\frac{E}{x}\right), \quad (5)$$

where $k = E/E_p^{(\max)}$ and

$$F_\pi^{(pp)}\left(x,\frac{E}{x}\right) = 4\alpha B_\pi x^{\alpha-1}\left(\frac{1-x^\alpha}{1+rx^\alpha(1-x^\alpha)}\right)^4 \times\left(\frac{1}{1-x^\alpha}+\frac{r\left(1-2x^\alpha\right)}{1+rx^\alpha\left(1-x^\alpha\right)}\right)\left(1-\frac{m_\pi c^2}{xE_p}\right)^{1/2} \quad (6)$$

is the pion distribution per proton-proton interaction, $x = E/E_p$, $B_\pi = a'+0.25$, $a' = 3.67+0.83L+0.075L^2$, $r = 2.6/\sqrt{a'}$, and $\alpha = 0.98/\sqrt{a'}$ (see [6, 13]).

The pion energy distribution is provided as the solution of a transport equation

$$N_\pi(E,z) = \frac{1}{\left|b_\pi(E)\right|}\int_E^{E^{(\max)}}dE'Q\left(E',z\right)\exp\left[-\tau_\pi\right]\left(E,E'\right), \quad (7)$$

where

$$\tau_\pi\left(E',E\right) = \int_{E'}^{E}\frac{dE''t_\pi^{-1}(E,z)}{\left|b_\pi\left(E''\right)\right|}. \quad (8)$$

Finally, for the emissivity of neutrinos emanating from direct pion decays (prompt neutrinos), we have [6, 15]

$$Q_{\pi\to\nu}(E,z) = \int_E^{E_{\max}}dE_\pi t_{\pi,\mathrm{dec}}^{-1}\left(E_\pi\right)N_\pi\left(E_\pi,z\right)\frac{\Theta\left(1-r_\pi-x\right)}{E_\pi\left(1-r_\pi\right)}, \quad (9)$$

where $x = E/E_{pi}$ and $t_{\pi,\mathrm{dec}}$ is the pion decay time scale.

The neutrino emissivity can then be integrated over 3D cell volume (voxel volume) and divided by the surface of a sphere, whose radius is the distance to Earth. The result is a synthetic "neutrino emission observation" of the binary system. By repeating the process for many energies, we can then obtain a SED plot. In order to simplify the computations, the hydrodynamic quantities will first be obtained as an average over the whole of the jet and then used to calculate the point emission from the jet system, at a given energy (see below).

4. Results and Discussion

4.1. PLUTO Hydrodynamic Modeling. The jet is confined in a rather pronounced way by the toroidal magnetic field

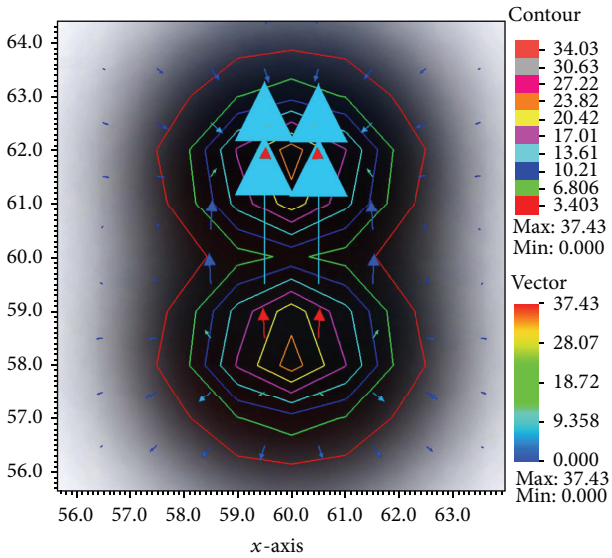

Figure 1: A 2-dimensional plot (jet cross-section, depicting a slice cut parallel to the xz-plane) of the strongest components of the jet magnetic field, in PLUTO simulation units. We can see that the toroidal component (ringwise) constitutes a significant part of the field, while other magnetic lines form part of the poloidal component, especially near the jet axis.

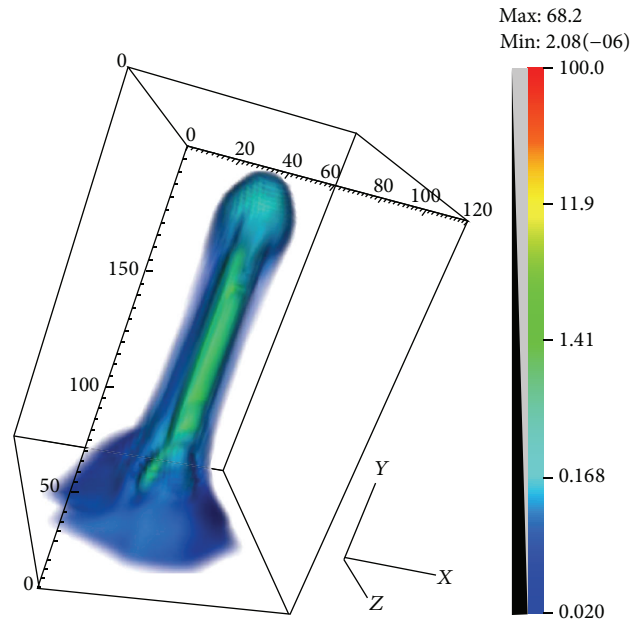

Figure 2: A plot of the magnetic field magnitude roughly half way into the simulation. We can see the jet self-confinement due to magnetic forces resulting in a narrow beam.

component (Figure 1), as opposed to the null RHD case in [14] (Figures 2 and 3). The various emission sites are then concentrated along the jet axis. This effect is even more pronounced because of local turbulence occurring naturally in the jet flow. The jet head advances through the surrounding stellar and corona winds, but its sideways expansion is limited. The magnetic field contributes to the emission mechanism so increased emission is expected from the inner flow funnel of the jet structure. The strong confinement is a result of adoption of a relatively intense field configuration, allowing the beam to remain focused late into the simulation; therefore emission is expected to be present at late stages of the numerical experiment.

The LOS code can create a synthetic image and we then add up all of its pixel's intensities for total neutrino intensity from the system, always at a given energy. By repeating the process for many different energies, we can obtain the spectral emission distribution of the model system. Using some kind of normalization in relation to an external factor, such as an energy estimate for the total energy emitted from the system in neutrinos, we could then adopt actual units and directly compare to past and planned observations.

Nevertheless, we omit the LOS step and simply add up the intensities of neutrino emission from all volume cells of the system. The reasons are twofold. On the one hand, no absorption occurs for neutrinos; therefore no need exists for a full solution of the equation of radiative transfer. On the other hand, current and near-future observations detect stellar neutrino sources as strictly point ones so no spatial resolution whatsoever exists for them. Combining the above two arguments we arrive at the conclusion that merely adding up emissions from all cells of the system provides an accurate model neutrino emission from a point source system, all the while the system is being modelled internally as a fully dynamical relativistic magnetohydrodynamical jet (RMHD jet). In Figure 1 a snapshot of the 3-dimensional jet magnetic field configuration can be seen, as the jet head advances through the middle of the computational domain. The two main components of the field can be determined and the presence of the toroidal component contributes to the jet confinement through the Lorentz force towards the jet axis. There is a strong dependence of the neutrino emission on the magnetic field, since the synchrotron energy loss mechanism's time scale strongly depends on the value of the field B.

In Figure 2 we can see the magnetic field magnitude, roughly halfway into the simulation run. The jet remains well confined, because of the magnetic force towards the jet axis acting due to the toroidal field component. This mechanism intensifies the possible neutrino emission, as it allows the magnetized matter to stay dense and also the field contributes to raise the emission levels (equation (4)).

Figure 3 shows the jet density at the middle of the simulation, where the jet is well confined and relatively little mixing has occurred between the jet matter and the surrounding winds. The sideways flow is still of secondary importance and therefore less emission is expected from the sides of the jet. This is opposed to the purely hydrodynamical jet case (e.g., [14]) where the jet expands much more and mixes with the ambient medium, allowing for more dynamical effects to occur over a larger volume at the jet sides. On the other hand, the magnetized jet here demonstrates a denser inner flow that stays focused and does not dissipate into the winds, maintaining stronger emission throughout the simulation.

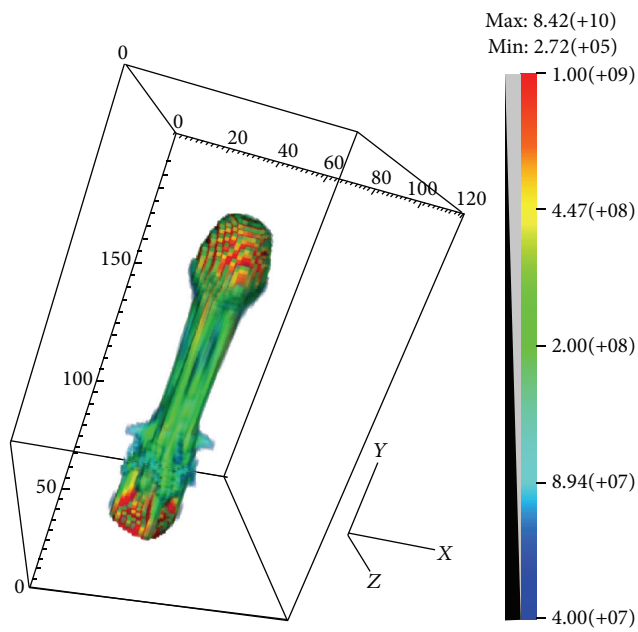

Figure 3: A plot of the jet density roughly halfway into the simulation. We can see the jet beam advancing along a narrow path through the ambient medium, kept together by the magnetic toroidal field component. This confined jet is then a suitable site for increased high energy γ-ray and neutrino emission/production, due to maintaining extreme conditions along the jet length.

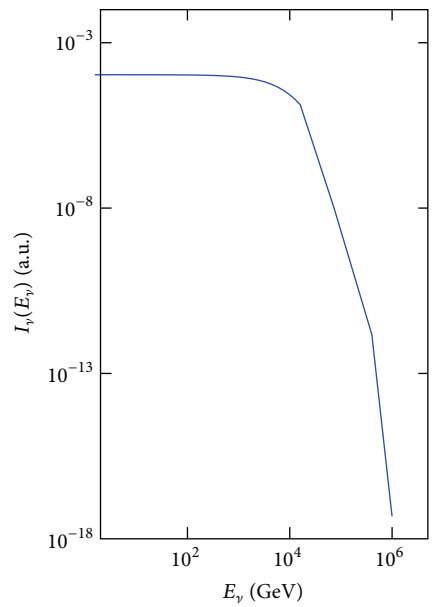

Figure 4: Unnormalized neutrino intensity, $I_\nu(E_\nu)$, on Earth as a function of the neutrino energy, E_ν, per energy interval. This neutrino intensity is coming out of the jet simulations in the presence of the strong toroidal magnetic field that appreciably affects the emission.

4.2. Neutrino Emission Simulations. In this work we simulate the neutrino emission from the SS433 microquasar system by extending the models of [5, 14] which refer to the emission of γ-rays from these jets. The differences between the two types of emission necessitate the employment of additional techniques. Towards this aim we have used the following:

(i) the formalism of [5, 6] which consider the cascade of particles in microquasar jets that lead to the production of neutrinos;

(ii) the computationally demanding numerical integration techniques used to reproduce the cascade of particles, at individual hydrocode grid cells, based on the works of [6, 13].

Due to the relatively limited availability of computing time the grid resolution of the hydrocode data was reduced to a more manageable size. Nevertheless, we still obtain a better resolution than that currently available from neutrino "observations" of microquasar systems, where only point sources are detected.

We should mention that, in studying the dependence of neutrino intensity originating from our model system, the PLUTO code produces jets whose dynamics directly affect the shape of the curve in the high energy tail (well above 100 GeV). More specifically, the fact that the inner jet has a higher proportion of faster protons and pions, relative to the outer jet, causes the neutrino emissivity there to begin dropping abruptly at higher energies compared to the behavior shown by the results of [6]. A more detailed analysis including muonic neutrino emissions and higher hydrodynamical grid resolution is currently performed and will appear in future work.

Figure 4 shows the unnormalized neutrino intensity on Earth, $I_\nu(E_\nu)$ per energy interval, coming out of the jet simulations. For simplicity, only promptly generated neutrinos from pion decay have been considered in this figure (delayed neutrinos [15] are to be included in future work). We concentrate on emissions produced not long after the beginning of the jet ejection event (consequently, our model emission here mainly comes from the inner part of the jet).

As a first approximation, the original hydrocode results of grid size $120 \times 200 \times 120$ have been regridded into a much smaller resolution of $3 \times 5 \times 3$. Then, following [6] the neutrino emission from pp interactions was obtained. We can see a general agreement with [6]. It should be stressed that the difference between the behaviour of $I_n u(E_n u)$ in the high energy tail illustrated in Figure 4 and that of [6] is mainly attributed to the strong magnetic confinement assumed in our present work, as compared to that used in [6].

In order to facilitate comparison with observations, the neutrino spectral intensity resulting from the jet is quantified using an energetic argument. At first, we assume that the energy fraction carried by the nonthermal (fast) proton distribution is of the order of 10^{-4} [5], while the neutrino energy fraction, of the fast protons, carried away from the system is roughly of the order of 10% [21]. In total, neutrinos are considered to carry away from the system around 10^{-5} of the total kinetic luminosity of the bulk flow proton

stream. The latter's kinetic luminosity is calculated, from the simulation initial conditions to be around 2×10^{36} erg/sec.

In order to constrain the luminosity $I_\nu(E_\nu)$, we then calculate the area under the curve in Figure 4 equal to 10^{-4} (arbitrary units) $\times 10^5$ GeV = 10 (arbitrary units) $\times$GeV. This may represent the power emitted; therefore we equate this area to 2×10^{31} erg/sec or 10^{34} GeV/sec, which is the neutrino fraction of the jet kinetic luminosity. This fixes the arbitrary unit to be equal to $10^{33}(\text{GeV s})^{-1}$. The intensity curve of Figure 4 flattens at around 10^{-4}, which is therefore found to be $10^{29}(\text{GeV s})^{-1}$. This value is lower than that of [5] by 1-2 orders of magnitude at lower energies but is higher by a similar amount at higher energies. The reason is that our jet is strongly confined by the toroidal magnetic field component which means that a higher energetic proton population is maintained later on. This is shown before the emission calculation binning and averaging process. Furthermore, this spectral emission distribution appears flatter at first and then drops rapidly. This favors emission at higher neutrino energies.

Detectability by current and upcoming arrays is consequently relatively worse than that in [5] (for the SS433 system's distance), which is taken to be marginal already. This implies that a more energetic jet is needed to provide higher neutrino flux, perhaps a jet of 100 times higher bulk mass flow rate. On the other hand, a more turbulent jet with more shock acceleration sites for nonthermal protons may lead to a q_{rel} of 10 times higher, that is, 0.001. This raises the expected flux by a corresponding factor of 10 as well. We conclude that the model jet may, under favorable conditions, fall within the detection limits of modern detectors discussed in Section 1.

5. Summary and Conclusions

The neutrino production from a relativistic magnetohydrodynamic model jet was studied, using a hadronic model for proton-proton interactions, leading to pion decay. High energy neutrinos are assumed to be produced in galactic XRB that include a stellar mass compact object. The companion (donor) star is a main sequence one, at an earlier stage of its evolution. The binary system in general emits in many different wavelengths, from radio and IR to high energy gamma-rays and neutrinos. The primary engine driving the jets and their emissions is the gravitational attraction of matter into the compact object. Adiabatic and synchrotron losses were assumed and a steady-state radiative condition was employed at a given hydrocode time step (the radiative process is presumed to occur faster than the cell contents change dynamically).

The toroidal magnetic field configuration of the system confines the jet and creates an environment that favors high energy emission of γ-rays and production of TeV neutrinos in the jet. A first attempt to model the energetic neutrino production in the system is expected to yield a direct connection between the jet dynamics and the energy spectra of the particles. Further work may accommodate additional effects, such as the full use of hydrocode data into the radiative transfer calculations and the consideration of the relativistic nature of the imaged jet system.

Finally, for the numerical solution of the partial differential equations (PDEs) arising from the problem, further, more accurate numerical schemes can be also considered, like the ones of [22].

Conflict of Interests

The authors declare that there is no conflict of interests regarding the publication of this paper.

Acknowledgments

One of the authors (T. Smponias) wishes to thank Professor T. S. Kosmas for stimulating and useful discussions and the grid node personnel of the University of Ioannina for technical assistance. T. Smponias also thanks D. Papoulias for technical assistance with Mathematica.

References

[1] M. Actis, G. Agnetta, F. Aharonian et al., "Design concepts for the Cherenkov Telescope Array CTA: an advanced facility for ground-based high-energy gamma-ray astronomy," *Experimental Astronomy*, vol. 32, pp. 193–316, 2011.

[2] A. A. Abdo, M. Ackermann, M. Axelsson et al., "Modulated high-energy gamma-ray emission from the microquasar cygnus X-3," *Science*, vol. 326, no. 5959, pp. 1512–1516, 2009.

[3] F. Halzen, G. M. Fuller, and X. Shi, "Observing the birth of supermassive black holes with the IceCube neutrino detector," *Physical Review Letters*, vol. 81, p. 5722, 1998.

[4] I. F. Mirabel and L. F. Rodrguez, "Sources of relativistic jets in the galaxy," *Annual Review of Astronomy and Astrophysics*, vol. 37, pp. 409–443, 1999.

[5] M. M. Reynoso, G. E. Romero, and H. R. Christiansen, "Production of gamma rays and neutrinos in the dark jets of the microquasar SS433," *Monthly Notices of the Royal Astronomical Society*, vol. 387, no. 4, pp. 1745–1754, 2008.

[6] M. M. Reynoso and G. E. Romero, "Magnetic field effects on neutrino production in microquasars," *Astronomy & Astrophysics*, vol. 493, no. 1, pp. 1–11, 2009.

[7] E. Waxman, "Viewpoint: the beginning of extra-galactic neutrino astronomy," *Physics*, vol. 7, p. 88, 2014.

[8] F. W. Stecker, "PeV neutrinos observed by IceCube from cores of active galactic nuclei," *Physical Review D*, vol. 88, Article ID 047301, 2013.

[9] R. Mou, "Ultra high energy neutrinos from supernova remnants," *Journal of Physics G: Nuclear and Particle Physics*, vol. 25, no. 1, pp. 129–134, 1999.

[10] F. Vissani and F. L. Villante, "Cosmic rays and neutrinos from supernova remnants. (or: the time when H.E.S.S. met Ginzburg and Syrovatskii)," *Nuclear Instruments and Methods in Physics Research, Section A: Accelerators, Spectrometers, Detectors and Associated Equipment*, vol. 588, no. 1-2, pp. 123–129, 2008.

[11] I. F. Mirabel, "Very energetic γ-rays from microquasars and binary pulsars," *Science*, vol. 312, no. 5781, pp. 1759–1760, 2006.

[12] F. Aharonian, A. G. Akhperjanian, K.-M. Aye et al., "Discovery of very high energy gamma rays associated with an X-ray binary," *Science*, vol. 309, no. 5735, pp. 746–749, 2005.

[13] S. R. Kelner, F. A. Aharonian, and V. V. Bugayov, "Energy spectra of gamma rays, electrons, and neutrinos produced at proton-proton interactions in the very high energy regime," *Physical Review D*, vol. 74, no. 3, Article ID 034018, 16 pages, 2006.

[14] T. Smponias and T. S. Kosmas, "Dynamical and radiative simulations of γ-ray jets in microquasars," *Monthly Notices of the Royal Astronomical Society*, vol. 438, no. 2, pp. 1014–1026, 2014.

[15] P. Lipari, M. Lusignoli, and D. Meloni, "Flavor composition and energy spectrum of astrophysical neutrinos," *Physical Review D*, vol. 75, Article ID 123005, 2007.

[16] A. Mignone, G. Bodo, S. Massaglia et al., "PLUTO: a numerical code for computational astrophysics," *The Astrophysical Journal, Supplement Series*, vol. 170, no. 1, pp. 228–242, 2007.

[17] D. A. Clarke, M. L. Norman, and J. O. Burns, "Numerical simulations of a magnetically confined jet," *The Astrophysical Journal Letters*, vol. 311, pp. L63–L67, 1986.

[18] T. Smponias and T. S. Kosmas, "Modelling the equatorial emission in a microquasar," *Monthly Notices of the Royal Astronomical Society*, vol. 412, no. 2, pp. 1320–1330, 2011.

[19] D. Purmohammad and J. Samimi, "On the hadronic beam model of TeV γ-ray flares from blazars," *Astronomy and Astrophysics*, vol. 371, no. 1, pp. 61–67, 2001.

[20] D. F. Torres and A. Reimer, "Hadronic beam models for quasars and microquasars," *Astronomy & Astrophysics*, vol. 528, p. L2, 2011.

[21] A. Levinson and E. Waxman, "Probing microquasars with TeV neutrinos," *Physical Review Letters*, vol. 87, Article ID 171101, 2001.

[22] O. T. Kosmas and D. Papadopoulos, "Multisymplectic structure of numerical methods derived using nonstandard finite difference schemes," *Journal of Physics: Conference Series*, vol. 490, Article ID 012123, 2013.

Hindawi Publishing Corporation
Advances in High Energy Physics
Volume 2015, Article ID 398796, 11 pages
http://dx.doi.org/10.1155/2015/398796

Research Article

Electron Capture Cross Sections for Stellar Nucleosynthesis

P. G. Giannaka and T. S. Kosmas

Division of Theoretical Physics, University of Ioannina, 45100 Ioannina, Greece

Correspondence should be addressed to P. G. Giannaka; pgiannak@cc.uoi.gr

Received 11 July 2014; Accepted 8 October 2014

Academic Editor: Athanasios Hatzikoutelis

In the first stage of this work, we perform detailed calculations for the cross sections of the electron capture on nuclei under laboratory conditions. Towards this aim we exploit the advantages of a refined version of the proton-neutron quasiparticle random-phase approximation (pn-QRPA) and carry out state-by-state evaluations of the rates of exclusive processes that lead to any of the accessible transitions within the chosen model space. In the second stage of our present study, we translate the abovementioned e^--capture cross sections to the stellar environment ones by inserting the temperature dependence through a Maxwell-Boltzmann distribution describing the stellar electron gas. As a concrete nuclear target we use the ^{66}Zn isotope, which belongs to the iron group nuclei and plays prominent role in stellar nucleosynthesis at core collapse supernovae environment.

1. Introduction

Weak interaction processes occurring in the presence of nuclei under stellar conditions play crucial role in the late stages of the evolution of massive stars and in the presupernova stellar collapse [1–6]. As it is known, the core of a massive star, at the end of its hydrostatic burning, is stabilized by electron degeneracy pressure as long as its mass does not exceed an appropriate mass (the Chandrasekhar mass limit, M_{Ch}) [6–10]. When the core mass exceeds M_{Ch}, electron degeneracy pressure cannot longer stabilize the center of the star and the collapse starts. In the early stage of collapse electrons are captured by nuclei in the iron group region [6, 10].

During the presupernova evolution of core collapse supernova, the Fermi energy (or equivalently the chemical potential) of the degenerate electron gas is sufficiently large to overcome the threshold energy E_{thr} (E_{thr} is given by negative Q values of the reactions involved in the interior of the stars) [11] and the nuclear matter in the stellar core is neutronized. This high Fermi energy of the degenerate electron gas leads to enormous e^--capture on nuclei and reduces the electron to baryon ratio Y_e [12, 13]. In this way, the electron pressure is reduced and the energy as well as the entropy drop. One of the important characteristics of the early pre-explosion evolution is the fact that electron capture on nuclei (specifically on nuclei of the pf shell) plays a key role [14, 15].

In the early stage of collapse (for densities lower than a few 10^{10} g cm^{-3}), the electron chemical potential is of the same order of magnitude as the nuclear Q value, and the e^--capture cross sections are sensitive to the details of GT strength distributions in daughter nuclei. For this reason, some authors restrict the calculations only to the GT strength and evaluate e^--capture rates on the basis of the GT transitions (at these densities, electrons are captured mostly on nuclei with mass number $A \leq 60$) [9–12, 15, 16]. Various methods, used for calculating e^--capture on nuclei during the collapse phase, have shown that this process produces neutrinos with rather low energies in contrast to the inelastic neutrino-nucleus reactions occurring in supernova [17–20]. These neutrinos escape the star carrying away energy and entropy from the core which is an effective cooling mechanism of the exploding massive star [21]. For higher densities and temperatures, e^- capture occurs on heavier nuclei $A \geq 65$ [8, 10, 13–15]. As a consequence, the nuclear composition is shifted to more neutron-rich and heavier nuclei (including those with $N > 40$) which dominate the matter composition for densities larger than about 10^{10} g cm^{-3} [1, 15, 21, 22].

The first calculations of stellar electron capture rates for iron group nuclei have been performed by employing the

independent particle model (IPM) [2–4]. Recently, similar studies have been addressed by using continuum RPA (CRPA) [25], large scale shell model [26, 27], RPA [11], and so forth [28]. In the present work e^--capture cross sections are obtained within a refined version of the quasiparticle random phase approximation (QRPA) which is reliable for constructing all the accessible final (excited) states of the daughter nuclei in the iron group region of the periodic table [29–38]. For the description of the required correlated nuclear ground states we determine single-particle occupation numbers calculated within the BCS theory [29, 31, 32]. Our nuclear method is tested through the reproducibility of experimental muon capture rates relying on detailed calculations of exclusive, partial, and total muon capture rates [23, 24, 39–42]. The agreement with experimental data provided us with high confidence level of our method and we continued with the calculations of electron capture cross sections in supernova conditions (where the densities and temperatures are high) using the pn-QRPA method. In this paper, we performed calculations for ^{66}Zn isotope (it belongs to the iron group nuclei) that plays prominent role in core collapse supernovae stellar nucleosynthesis [18, 19, 43].

Our strategy in this work is, at first, to perform extensive calculations of the transition rates for all the abovementioned nuclear processes, assuming laboratory conditions, and then to translate these rates to the corresponding quantities within stellar environment through the use of an appropriate convolution procedure [9, 14, 15, 21, 26]. To this purpose, we assume that leptons under such conditions follow Maxwell-Boltzmann energy distribution [9, 26].

2. Construction of Nuclear Ground and Excited States

Electrons of energy E_e are captured by nuclei interacting weakly with them via W^- boson exchange as follows:

$$(A, Z) + e^- \longrightarrow (A, Z-1)^* + \nu_e. \tag{1}$$

The outgoing ν_e neutrino carries energy E_ν while the daughter nucleus $(A, Z-1)$ absorbs a part of the incident electron energy given by the difference between the initial E_i and the final E_f nuclear energies as $E_\nu = E_f - E_i$.

The nuclear calculations for the cross sections of reaction (1) start by writing down the weak interaction Hamiltonian $\widehat{\mathscr{H}}_w$ which is given as a product of the leptonic, j_μ^{lept}, and the hadronic, $\widehat{\mathscr{J}}^\mu$, currents (current-current interaction Hamiltonian) as follows:

$$\widehat{\mathscr{H}}_w = \frac{G}{\sqrt{2}} j_\mu^{\text{lept}} \widehat{\mathscr{J}}^\mu, \tag{2}$$

where $G = G_F \cos\theta_c$ with G_F and θ_c being the well-known weak interaction coupling constant and the Cabibbo angle, respectively [31, 32, 44].

From the nuclear theory point of view, the main task is to calculate the cross sections of reaction (1) which are based on the evaluation of the nuclear transition matrix elements between the initial $|i\rangle$ and a final $|f\rangle$ nuclear states of the form

$$\left\langle f \left| \widehat{H_w} \right| i \right\rangle = \frac{G}{\sqrt{2}} \ell^\mu \int d^3x e^{-i\mathbf{q}\cdot\mathbf{x}} \left\langle f \left| \widehat{\mathscr{J}_\mu} \right| i \right\rangle. \tag{3}$$

The quantity $\ell^\mu e^{-i\mathbf{q}\cdot\mathbf{x}}$ stands for the leptonic matrix element written in coordinate space with $\mathbf{q}$ being the 3-momentum transfer. For the calculation of these transition matrix elements one may take advantage of the Donnelly-Walecka multipole decomposition which leads to a set of eight independent irreducible tensor multipole operators containing polar-vector and axial-vector components [44] (see Appendix A).

In the present work, in (3) the ground state of the parent nucleus $|i\rangle$ is computed by solving the relevant BCS equations which give us the quasiparticle energies and the amplitudes V and U that determine the probability for each single particle level to be occupied or unoccupied, respectively [31]. Towards this aim, at first, we consider a Coulomb corrected Woods-Saxon potential with a spin orbit part as a mean field for the description of the strong nuclear field [45, 46]. For the latter potential we adopt the parameterization of IOWA group [47]. Then, we use as pairing interaction the monopole part of the Bonn C-D one meson exchange potential. The renormalization of this interaction, to fit in the ^{66}Zn isotope, is achieved through the two pairing parameters $g_{\text{pair}}^{p,n}$, $p(n)$ for proton (neutron) pairs, and the values of which are tabulated in Table 1.

As it is well known, the pairing parameters, $g_{\text{pair}}^{p,n}$, are determined through the reproduction of the energy gaps, $\Delta_{p,n}^{\text{exp}}$, from neighboring nuclei as follows (3-point formula):

$$\begin{aligned} \Delta_n^{\text{exp}} &= -\frac{1}{4}\left[S_n(A-1,Z) - 2S_n(A,Z) + S_n(A+1,Z)\right], \\ \Delta_p^{\text{exp}} &= -\frac{1}{4}\left[S_p(A-1,Z-1)\right. \\ &\qquad \left. -2S_p(A,Z) + S_p(A+1,Z+1)\right], \end{aligned} \tag{4}$$

where S_p and S_n are the experimental separation energies for protons and neutrons, respectively, of the target nucleus (A, Z) and the neighboring nuclei $(A\pm1, Z\pm1)$ and $(A\pm1, Z)$. For the readers convenience in Table 2 we show the values of experimental separation energies for the target $^{66}_{30}$Zn and the neighboring nuclei $^{65}_{29}$Cu, $^{67}_{31}$Ga, $^{65}_{30}$Zn, and $^{67}_{30}$Zn.

Subsequently, the excited states $|f\rangle$ of the studied daughter nucleus ^{66}Cu are constructed by solving the pn-QRPA equations [29–38], which are written as follows in matrix form [29]:

$$\begin{pmatrix} \mathscr{A} & \mathscr{B} \\ -\mathscr{B} & -\mathscr{A} \end{pmatrix} \begin{pmatrix} X^\nu \\ Y^\nu \end{pmatrix} = \Omega_{J^\pi}^\nu \begin{pmatrix} X^\nu \\ Y^\nu \end{pmatrix}, \tag{5}$$

$\Omega_{J^\pi}^\nu$ denotes the excitation energy of the QRPA state $|J_\nu^\pi\rangle$ with spin J and parity π.

The solution of (5) is an eigenvalue problem which provides the amplitudes for forward and backward scattering X and Y, respectively, and the QRPA excitation energies $\Omega_{J^\pi}^\nu$

Table 1: Parameters for the renormalization of the interaction of proton pairs, g^p_{pair}, and neutron pairs, g^n_{pair}. They have been fixed in such a way that the corresponding experimental gaps, Δ^{exp}_p and Δ^{exp}_n of ^{66}Zn isotope, are quite accurately reproduced.

Nucleus	g^n_{pair}	g^p_{pair}	Δ^{exp}_n (MeV)	Δ^{theor}_n (MeV)	Δ^{exp}_p (MeV)	Δ^{theor}_p (MeV)
^{66}Zn	1.0059	0.9271	1.7715	1.7716	1.2815	1.2814

Table 2: The experimental separation energies in MeV for protons and neutrons of the target (A, Z) and neighboring $(A \pm 1, Z \pm 1)$ and $(A \pm 1, Z)$ nuclei.

Nucleus	$S_n(A-1, Z)$	$S_n(A, Z)$	$S_n(A+1, Z)$	$S_p(A-1, Z-1)$	$S_p(A, Z)$	$S_p(A+1, Z+1)$
^{66}Zn	7.979	11.059	7.052	7.454	8.924	5.269

[31–34]. In our method the solution of the QRPA equations is carried out separately for each multipole set of states $|J^\pi\rangle$.

For the renormalization of the residual 2-body interaction (Bonn C-D potential), the strength parameters, for the particle-particle (g_{pp}) and particle-hole (g_{ph}) interaction entering the QRPA matrices $\mathscr{A}$ and $\mathscr{B}$, are determined (separately for each multipolarity) from the reproducibility of the low-lying experimental energy spectrum of the final nucleus. The values of these parameters in the case of the spectrum of ^{66}Cu are listed in Table 3.

At this point, it is worth mentioning that, for measuring the excitation energies of the daughter nucleus ^{66}Cu from the ground state of the initial one ^{66}Zn, a shifting of the entire set of QRPA eigenvalues is necessary. Such a shifting is required whenever in the pn-QRPA a BCS ground state is used, a treatment adopted by other groups previously [9, 40, 48, 49]. The shifting, for the spectrum of the daughter nucleus ^{66}Cu, is done in such a way that the first calculated value of each multipole state of ^{66}Cu (i.e. $1^+_1, 2^+_1, \ldots$, etc.) approaches as close as possible the corresponding lowest experimental multipole excitation. Table 4 shows the shifting applied to our QRPA spectrum for each multipolarity of the parent nucleus ^{66}Zn. We note that a similar treatment is required in pn-QRPA calculations performed for double-beta decay studies where the excitations derived for the intermediate odd-odd nucleus (intermediate states) through p-n and n-p reactions from the neighboring nuclei, left or right nuclear isotope, do not match to each other [48, 49]. The resulting low-energy spectrum, after using the parameters of Tables 1 and 3 and the shifting shown in Table 4, agrees well with the experimental one (see Figure 1).

We must also mention that, usually, in nuclear structure calculations we test a nuclear method in two phases: first through the construction of the excitation spectrum as discussed before and second through the calculations of electron scattering cross sections or muon capture rates. Following the above steps, we test the reproducibility of the relevant experimental data for many nuclear models employed in nuclear applications (nuclear structure and nuclear reactions) and in nuclear astrophysics [1, 9].

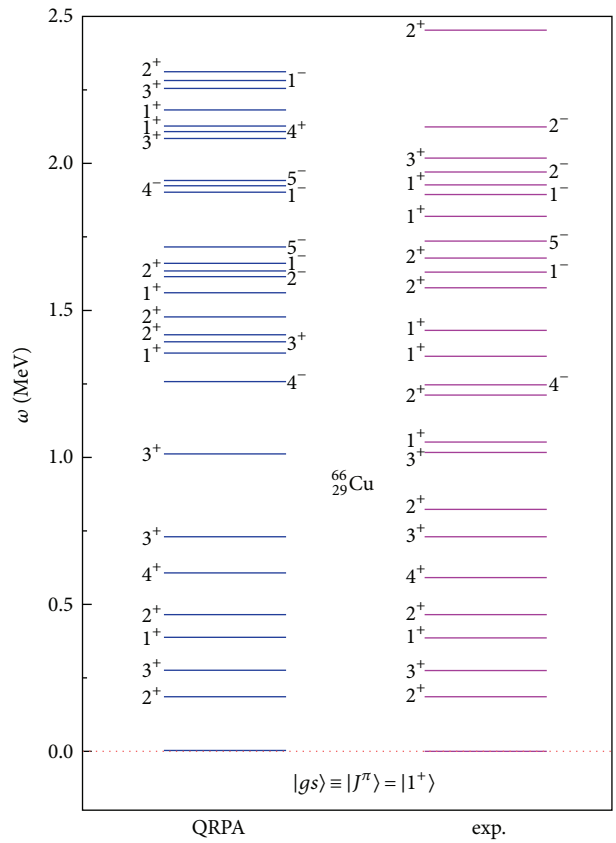

Figure 1: Comparison of the theoretical excitation spectrum (resulting from the solution of the QRPA eigenvalue problem) with the low-lying (up to about 3 MeV) experimental one for ^{66}Cu nucleus. As it can be seen, the agreement is very good below 1 MeV but for higher excitation energies it becomes moderate.

3. Results and Discussion

In this work we perform detailed cross section calculations for the electron capture on ^{66}Zn isotope on the basis of the pn-QRPA method. The required nuclear matrix elements between the initial $|J_i\rangle$ and the final $|J_f\rangle$ states are determined by solving the BCS equations for the ground state [29, 31, 32] and the pn-QRPA equations for the excited states [31–34] (see Section 2). For the calculations of the original cross sections, a quenched value of g_A (see Appendix B) is considered which subsequently modifies all relevant multipole matrix elements [23, 24, 50, 51].

At this point of the present work and in order to increase the confidence level of our method, we perform total muon capture rates calculations [23, 24, 39–42]. The comparison

Table 3: Strength parameters for the particle-particle (g_{pp}) and particle-hole (g_{ph}) interaction for various multipolarities (for the rest of multipolarities, $J^\pi \leq 5^\pm$, the bare 2-body interaction has been used), in the case of the spectrum of ^{66}Cu nucleus.

	Positive parity states					Negative parity states			
J^π	0^+	1^+	2^+	3^+	4^+	1^-	2^-	3^-	4^-
g_{pp}	0.827	0.547	0.686	0.854	1.300	0.994	0.200	0.486	0.622
g_{ph}	0.336	0.200	1.079	0.235	0.200	1.200	0.200	1.200	1.200

Table 4: The shift (in MeV) applied on the spectrum (seperately of each multipole set of states) of ^{66}Cu isotope, daughter nucleus of the electron capture on ^{66}Zn.

Positive parity states		Negative parity states	
0^+	0.90	0^-	5.00
1^+	2.50	1^-	6.80
2^+	2.55	2^-	3.85
3^+	2.50	3^-	2.60
4^+	1.75	4^-	3.55
5^+	0.55	5^-	3.00

with experimental and other theoretical results is shown in Section 3.1. Afterwards, we study in detail the electron capture process as follows. (i) Initially we consider laboratory conditions; that is, the initial (parent) nucleus is considered in the ground state and no temperature dependence is assumed (see Section 3.2.1). (ii) Second, we consider stellar conditions; that is, the parent nucleus is assumed to be in any initial excited state and due to the e^--capture process it goes to any final excited state of the daughter nucleus. At these conditions it is necessary to take into account the temperature dependence of the cross sections (see Section 3.2.2) [10].

3.1. Calculations of Muon Capture Rates for ^{66}Zn. Despite the fact that the muon capture on nuclei does not play a crucial role in stellar-nucleosynthesis, it is, however, important to start our study from this process since the nuclear matrix elements required for an accurate description of the μ-capture are the same for all semileptonic charge-changing weak interaction processes. In addition, the excitation spectrum of the daughter $(A, Z-1)$ nucleus, as we saw before, is in good agreement with the experimental data.

The calculations of the muon capture rates are performed in three steps. In the first step we carry out realistic state-by-state calculations of exclusive ordinary muon capture (OMC) rates in ^{66}Zn isotope for all multipolarities with $J^\pi \leq 5^\pm$ (higher multipolarities contribute negligibly). The appropriate expression for the exclusive muon capture rates is written as follows:

$$\begin{aligned}\Lambda_{gs\to J_f^\pi} &\equiv \Lambda_{J_f^\pi} \\ &= 2G^2\langle\Phi_{1s}\rangle^2 R_f q_f^2 \\ &\quad\times\left[\left|\left\langle J_f^\pi \left\| \left(\widehat{\mathscr{M}}_J - \widehat{\mathscr{L}}_J\right)\right\| 0_{gs}^+\right\rangle\right|^2\right. \\ &\quad\left.+\left|\left\langle J_f^\pi \left\| \left(\widehat{\mathscr{T}}_J^{\mathrm{el}} - \widehat{\mathscr{T}}_J^{\mathrm{magn}}\right)\right\| 0_{gs}^+\right\rangle\right|^2\right],\end{aligned} \tag{6}$$

where Φ_{1s} represents the muon wave function in the $1s$ muonic orbit. The operators in (6) are refered to as Coulomb $\widehat{\mathscr{M}}_J$, longitudinal $\widehat{\mathscr{L}}_J$, transverse electric $\widehat{\mathscr{T}}_J^{\mathrm{el}}$, and transverse magnetic $\widehat{\mathscr{T}}_J^{\mathrm{mag}}$ multipole operators (see Appendix A). The factor R_f in (6) takes into consideration the nuclear recoil which is written as $R_f = (1 + q_f/M_{\mathrm{targ}})^{-1}$, with M_{targ} being the mass of the target (parent) nucleus.

Due to the fact that there are no available data in the literature for exclusive muon capture rates, the test of our method is realized by comparing partial and total muon capture rates with experimental data and other theoretical results [23, 24]. Towards this purpose, our second step includes calculations of the partial μ^--capture rates for various low-spin multipolarities, Λ_{J^π} (for $J^\pi \leq 4^\pm$), in the studied nucleus. These partial rates are found by summing over the contributions of all the individual multipole states of the studied multipolarity as follows:

$$\begin{aligned}\Lambda_{J^\pi} &= \sum_f \Lambda_{gs\to J_f^\pi} \\ &= 2G^2\langle\Phi_{1s}\rangle^2\left[\sum_f q_f^2 R_f\left|\left\langle J_f^\pi \left\| \left(\widehat{\mathscr{M}}_J - \widehat{\mathscr{L}}_J\right)\right\| 0_{gs}^+\right\rangle\right|^2\right. \\ &\quad\left.+\sum_f q_f^2 R_f\left|\left\langle J_f^\pi \left\| \left(\widehat{\mathscr{T}}_J^{\mathrm{el}} - \widehat{\mathscr{T}}_J^{\mathrm{magn}}\right)\right\| 0_{gs}^+\right\rangle\right|^2\right]\end{aligned} \tag{7}$$

(f runs over all states of the multipolarity $|J^\pi\rangle$). We also estimate the percentage (portion) of their contribution into the total μ-capture rate for the most important multipolarities. In Table 5 we tabulate the individual portions of the low-spin multipole transitions ($J^\pi = 4^\pm$) into the total muon capture rate. As it can be seen, the contribution of the 1^- multipole transitions is the most important multipolarity exhausting about 44% of the total muon capture rate. Such an important contribution was found in ^{16}O and ^{48}Ca isotopes studied in [41].

In the last step of testing our method, we evaluate total muon capture rates for the ^{66}Zn isotope. These rates are obtained by summing over all partial multipole transition rates (up to $J^\pi = 4^\pm$) as follows:

$$\Lambda_{\mathrm{tot}} = \sum_{J^\pi}\Lambda_{J^\pi} = \sum_{J^\pi}\sum_f \Lambda_{J_f^\pi}. \tag{8}$$

For the sake of comparison, the abovementioned μ-capture calculations have been carried out using the

Table 5: The percentage of each multipolarity into the total muon capture rate evaluated with our pn-QRPA method.

Positive parity transitions		Negative parity transitions	
J^π	Portions (%)	J^π	Portions (%)
0^+	8.22	0^-	7.94
1^+	21.29	1^-	44.21
2^+	2.85	2^-	13.32
3^+	1.58	3^-	0.34
4^+	0.01	4^-	0.23

quenched value $g_A = 1.135$ [23, 24]. The results are listed in Table 6, where we also include the experimental total rates and the theoretical ones of [23, 24]. Moreover, in Table 6 we show the individual contribution into the total muon capture rate of the polar-vector (Λ^V_{tot}), the axial-vector (Λ^A_{tot}), and the overlap ($\Lambda^{VA}_{\text{tot}}$) parts. As it can be seen, our results obtained with the quenched g_A coupling constant are in very good agreement with the experimental total muon capture rates (the deviations from the corresponding experimental rates are smaller than 7%). This agreement provides us with high confidence level for our method.

3.2. Electron Capture Cross Section. After acquiring a high confidence level for our nuclear method, we proceed with the main goal of the present study which concerns the calculations of the electron capture cross sections. As mentioned before, this includes original (see Section 3.2.1) and stellar electron capture investigations (Section 3.2.2).

3.2.1. Original Electron Capture Cross Section on ^{66}Zn Isotope. The original cross sections for the electron capture process in the ^{66}Zn isotope are obtained by using the pn-QRPA method considering all the accessible transitions of the final nucleus ^{66}Cu. In the Donnelly-Walecka formalism the expression for the differential cross section in electron capture by nuclei reads [10]

$$\begin{aligned}\frac{d\sigma_{ec}}{d\Omega} = {} & \frac{G_F^2\cos^2\theta_c}{2\pi}\frac{F(Z,E_e)}{(2J_i+1)} \\ & \times\Bigg\{\sum_{J\geq 1}\mathscr{W}(E_e,E_\nu) \\ & \times\Bigg\{\left[1-\alpha\cos\Phi+b\sin^2\Phi\right] \\ & \times\left[\left|\left\langle J_f\left\|\widehat{\mathscr{T}}^{\text{mag}}_J\right\|J_i\right\rangle\right|^2+\left|\left\langle J_f\left\|\widehat{\mathscr{T}}^{\text{el}}_J\right\|J_i\right\rangle\right|^2\right] \\ & -\left[\frac{(\varepsilon_i+\varepsilon_f)}{q}(1-\alpha\cos\Phi)-d\right] \\ & \times 2\,\text{Re}\left\langle J_f\left\|\widehat{\mathscr{T}}^{\text{mag}}_J\right\|J_i\right\rangle\left\langle J_f\left\|\widehat{\mathscr{T}}^{\text{el}}_J\right\|J_i\right\rangle^*\Bigg\} \\ & +\sum_{J\geq 0}\mathscr{W}(E_e,E_\nu) \\ & \times\Bigg\{(1+\alpha\cos\Phi)\left|\left\langle J_f\left\|\widehat{\mathscr{M}}_J\right\|J_i\right\rangle\right|^2 \\ & +\left(1+\alpha\cos\Phi-2b\sin^2\Phi\right)\left|\left\langle J_f\left\|\widehat{\mathscr{L}}_J\right\|J_i\right\rangle\right|^2 \\ & -\left[\frac{\omega}{q}(1+\alpha\cos\Phi)+d\right]2\,\text{Re}\left\langle J_f\left\|\widehat{\mathscr{L}}_J\right\|J_i\right\rangle \\ & \times\left\langle J_f\left\|\widehat{\mathscr{M}}_J\right\|J_i\right\rangle^*\Bigg\}\Bigg\},\end{aligned} \tag{9}$$

where $F(Z,E_e)$ is the well-known Fermi function [18]. The factor $W(E_e,E_\nu) = E_\nu^2/(1+E_\nu/M_T)$ accounts for the nuclear recoil [8], M_T is the mass of the target nucleus, and parameters α, b, and d are given, for example, in [31]. The nuclear transition matrix elements between the initial state $|J_i\rangle$ and the final state $|J_f\rangle$ correspond to the Coulomb $\widehat{\mathscr{M}}_{JM}$, longitudinal $\widehat{\mathscr{L}}_{JM}$, transverse electric $\widehat{\mathscr{T}}^{\text{el}}_{JM}$, and transverse magnetic $\widehat{\mathscr{T}}^{\text{mag}}_{JM}$ multipole operators (discussed in Appendix A).

From the energy conservation in the reaction (1), the energy of the outgoing neutrino E_ν is written as follows:

$$E_\nu = E_e - Q + E_i - E_f, \tag{10}$$

which includes the difference between the initial E_i and the final E_f nuclear states. The Q value of the process is determined from the experimental masses of the parent (M_i) and the daughter (M_f) nuclei as $Q = M_f - M_i$ [9].

It is worth mentioning that for low momentum transfer, various authors use the approximation $q \to 0$ for all multipole operators of (9). Then, the transitions of the Gamow-Teller operator ($\text{GT}^+ = \sum_i \tau_i^+\sigma_i$) provide the dominant contribution to the total cross section [9].

While performing detailed calculations for the original electron capture cross sections on ^{66}Zn isotope we assumed that (i) the initial state of the parent nucleus ^{66}Zn is the ground state $|0^+\rangle$ and (ii) the nuclear system is under laboratory conditions (no temperature dependence of the cross sections is needed). The cross sections as a function of the incident electron energy E_e are calculated with the use of realistic two-body interactions as mentioned before. The obtained total original electron capture cross sections for ^{66}Zn target nucleus are illustrated in Figure 2 where the individual contributions of various multipole channels ($J^\pi \leq 5^\pm$) are also shown. The electron capture cross sections in Figure 2 exhibit a sharp increase by several orders of magnitude within the first few MeV above energy-threshold, and this reflects the GT^+ strength distribution. For electron energy $E_e \geq 10$ MeV the calculated cross sections show a moderate increase. From experimental and astrophysical point of view, the important range of the incident electron energy E_e is up to 30 MeV. At these energies the 1^+ multipolarity has the largest contribution to the total electron capture cross sections [9, 10]. In the present work we have extended the

Table 6: Individual contribution of polar-vector, axial-vector, and overlap parts into the total muon-capture rate. The total muon capture rates, obtained by using the pn-QRPA with the quenched value of $g_A = 1.135$ for the medium-weight nucleus ^{66}Zn, are compared with the available experimental data and with the theoretical rates of [23, 24].

	Total muon capture rates $\Lambda_{\text{tot}}(\times 10^6\, s^{-1})$						
	Present pn-QRPA calculations				Experiment	Other theoretical methods	
Nucleus	Λ^V_{tot}	Λ^A_{tot}	$\Lambda^{VA}_{\text{tot}}$	Λ_{tot}	$\Lambda^{\text{exp}}_{\text{tot}}$	$\Lambda^{\text{theor}}_{\text{tot}}$ [23]	$\Lambda^{\text{theor}}_{\text{tot}}$ [24]
^{66}Zn	1.651	4.487	−0.204	5.934	5.809	4.976	5.809

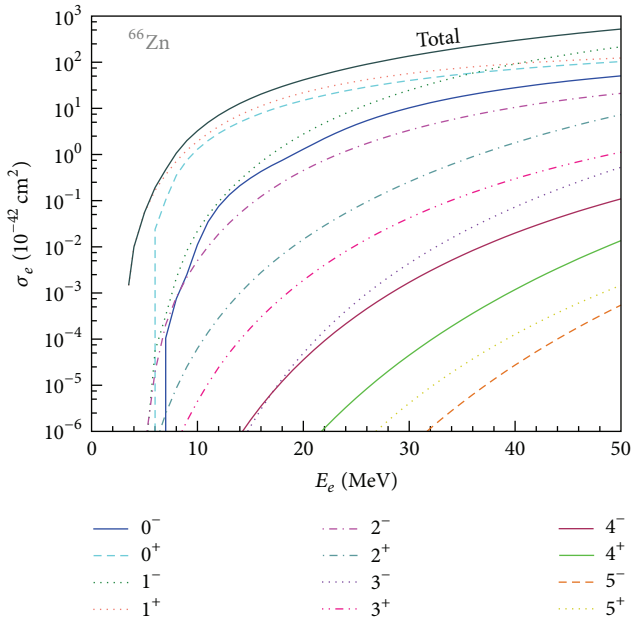

Figure 2: Original total cross sections of electron capture on the ^{66}Zn (parent) nucleus calculated with pn-QRPA method as a function of the incident electron energy E_e. The individual contributions of various multipole channels (for $J^\pi \leq 5^\pm$) are also demonstrated.

range of E_e up to 50 MeV since at higher energies (around 40 MeV) the contribution of other multipolarities like 1^-, 0^+, and 0^- becomes noticeable and cannot be omitted (see Figure 2).

From the study of the original electron capture cross sections we conclude that the total cross sections can be well approximated with the Gamow-Teller transitions only in the region of low energies [9–12, 15, 16]. For higher incident electron energies the inclusion of the contributions originating from other multipolarities leads to better agreement [10].

3.2.2. Stellar Electron Capture on ^{66}Zn Isotope. As it is well known, electron capture process plays a crucial role in late stages of evolution of a massive star, in presupernova and in supernova phases [1–6]. In presupernova collapse, that is, at densities $\rho \leq 10^{10}\,\text{g cm}^{-3}$ and temperatures $300\,\text{keV} \leq T \leq 800\,\text{keV}$, electrons are captured by nuclei with $A \leq 60$ [9–12, 15, 16]. During the collapse phase, at higher densities $\rho \geq 10^{10}\,\text{g cm}^{-3}$ and temperatures $T \simeq 1.0$ MeV, electron capture process is carried out on heavier and more neutron rich nuclei with $Z < 40$ and $N \geq 40$ [8, 10, 13–15].

In an independent particle picture, the Gamow-Teller transitions (which is the most important in the electron capture cross section calculations) are forbidden for these nuclei [2–4]. However, as it has been demonstrated in several studies, GT transitions in these nuclei are unblocked by finite temperature excitations [21, 22]. At high temperatures, $T \simeq 1.5$ MeV, GT transitions are thermally unblocked as a result of the excitation of neutrons from the pf-shell into the $g_{9/2}$ orbital.

For astrophysical environment, where the finite temperature and the matter density effects cannot be ignored (the initial nucleus is at finite temperature), in general, the initial nuclear state needs to be a weighted sum over an appropriate energy distribution. Then, assuming Maxwell-Boltzmann distribution of the initial state $|i\rangle$ in (9) [9, 26], the total e^--capture cross section is given by the expression [10]

$$\sigma(E_e, T) = \frac{G_F^2 \cos^2\theta_c}{2\pi} \sum_i F(Z, E_e) \frac{(2J_i + 1)\, e^{-E_i/(kT)}}{G(Z, A, T)} \times \sum_{f,J} \left(E_e - Q + E_i - E_f\right)^2 \frac{\left|\left\langle i \left| \widehat{O}_J \right| f \right\rangle\right|^2}{(2J_i + 1)}. \tag{11}$$

The sum over initial states in the latter equation denotes a thermal average of levels, with the corresponding partition function $G(Z, A, T)$ [10]. The finite temperature induces the thermal population of excited states in the parent nucleus. In the present work we assume that these excited states in the parent nucleus are all the possible states up to about 2.5 MeV. Calculations involving in addition other states lying at higher energies show that they have no sizeable contribution to the total electron capture cross sections. As mentioned before, for the evaluation of the total electron capture cross sections, the use of a quenched value of g_A is necessary [23, 24, 50, 51]. Since the form factor $F_A(q^2)$ multiplies the four components of the axial-vector operator (see (A.2)–(A.5)), a quenched value of g_A must enter the multipole operators generating the pronounced excitations $0^-, 1^\pm, \ldots$, and so forth. For this reason, in our QRPA calculations we multiplied the free nucleon coupling constant $g_A = 1.262$ by the factor 0.8 [23, 24, 50, 51].

The results coming out of the study of electron capture cross sections under stellar conditions are shown in Figure 3, where the same picture as in the original cross section calculations, but now with larger contribution, is observed.

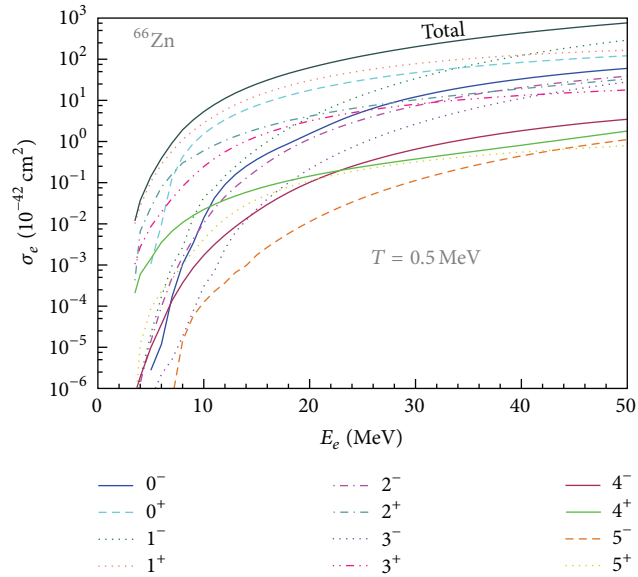

FIGURE 3: Electron capture cross sections for the ^{66}Zn parent nucleus at high temperature (T = 0.5 MeV) in stellar environment obtained assuming Maxwell-Boltzmann statistics for the incident electrons. The total cross section and the dominant individual multipole channels ($J^\pi \leq 5^\pm$) are demonstrated as functions of the incident electron energy E_e.

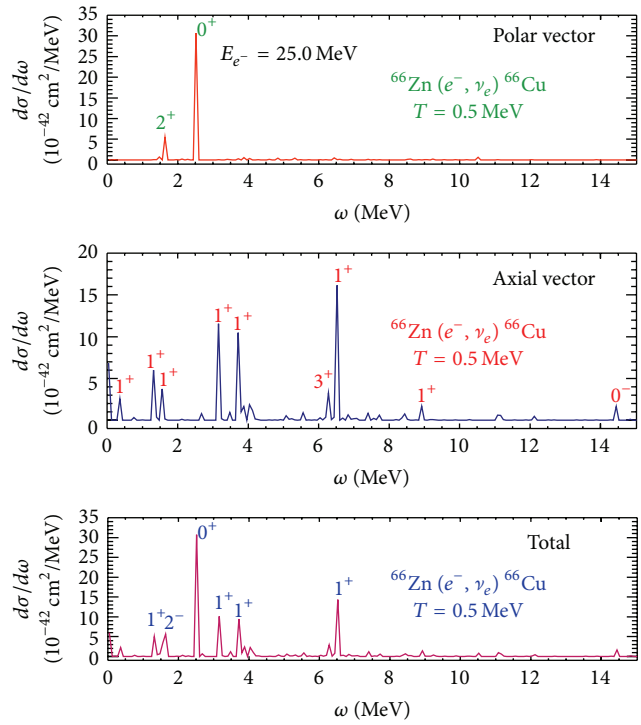

FIGURE 4: Individual contributions of the polar-vector, (Λ_V), and axial-vector, (Λ_A), components and total electron capture rate as functions of the excitation energy ω (^{66}Zn is the parent nucleus).

As discussed before, the dominant multipolarity is the 1^+, which contributes by more than 40% to the total cross section. In the region of low energies (up to 30 MeV), the total e^--capture cross section can be described by taking into account only the GT transitions, but at higher incident energies the contributions of other multipolarities become significant and cannot be omitted.

The percentage contributions of various multipolarities (with $J^\pi \leq 5^\pm$) into the total e^--capture cross section at T = 0.5 MeV and for incident electron energy E_e = 25 MeV are tabulated in Table 7. In addition, in this table we list the values of the individual e^--capture cross sections of each multipolarity with $J^\pi \leq 5^\pm$. More specifically, for E_e = 25 MeV the 1^+ multipolarity contributes to about 44%, the 0^+ contributes to about 26%, and the 1^- contributes to about 11%. The contributions coming from other multipolarities are less important (smaller than 5%).

In performing state-by-state calculations for the electron capture cross sections, our code has the possibility to provide separately the contribution of the polar-vector, the axial-vector, and the overlap parts induced by the corresponding components of the electron capture operators. In Figure 4 we illustrate the stellar differential cross sections of each individual transition of the polar-vector and axial-vector components.

As mentioned before, our code gives separately the partial e^--capture cross sections of each multipolarity. In order to study the dependence of the differential cross sections on the excitation energy ω throughout the entire pn-QRPA spectrum of the daughter nucleus, a rearrangement of all possible excitations ω in ascending order, with the corresponding cross sections, is required. This was performed by using a special code appropriate for matrices [33]. In the model space chosen for ^{66}Zn isotope, for all multipolarities up to $J^\pi = 5^\pm$, we have a number of 447 final states. The differential electron capture cross sections illustrated in Figure 4 present some characteristic clearly pronounced peaks at various excitation energies ω. These peaks correspond mainly to 0^+, 1^+, and 2^+ transitions. More specifically, in the ^{66}Cu daughter nucleus the maximum peak corresponds to the 0_1^+ QRPA transition at ω = 2.538 MeV and other characteristic peaks correspond to 1_7^+, 1_8^+, and 1_{10}^+ transitions, located at energies ω = 3.194 MeV, ω = 3.686 MeV, and ω = 6.555 MeV, respectively (see Figure 4). The other less important peaks are also shown in Figure 4.

Before closing, it should be mentioned that the e-capture cross sections presented in this work may be useful in estimating neutrino-spectra arising from e-capture on nuclei during supernova phase. The knowledge of ν-spectra at every point and time in the core is quite relevant for simulations of the final collapse and explosion phase of a massive star. As it is known [21], in the collapse phase, neutrinos are mainly produced by e-capture on nuclei and on free protons. The energy spectra of the emerging neutrinos from both reactions are important ingredients in stellar modelling and stellar simulations [21, 27].

Furthermore, in core collapse simulations one defines the reaction rate of electron capture on nuclei given by

$$R_h = \sum_i Y_i \lambda_i, \tag{12}$$

Table 7: Total e^--capture cross sections (in 10^{-42} MeV^{-1} cm^2) for $E_e = 25$ MeV. The percentage of each multipolarity into the total e^--capture cross section evaluated with our pn-QRPA code is also tabulated here.

	Positive parity transitions			Negative parity transitions	
J^π	$\sigma_e(\times 10^{-42}$ cm^2 MeV^{-1})	Portions (%)	J^π	σ_e ($\times 10^{-42}$ cm^2 MeV^{-1})	Portions (%)
0^+	31.164	25.96	0^-	5.288	4.41
1^+	52.779	43.98	1^-	13.409	11.14
2^+	6.921	5.77	2^-	3.262	2.72
3^+	5.499	4.58	3^-	0.905	0.75
4^+	0.244	0.20	4^-	0.299	0.25
5^+	0.208	0.17	5^-	0.042	0.04

where the sum runs over all nuclear isotopes present in the astrophysical environment (Y_i denotes the abundance of a given nuclear isotope and λ_i is the calculated electron capture rate for this isotope). The rates of (12) must be known for a wide range of the parameters: T (temperature) and ρ (nuclear density) of the studied star. Thus, for the calculation of the quantity $Y \cdot \lambda$ of a specific nuclear isotope one needs to know in addition to the nuclear composition Y the electron capture rates λ calculated as we have shown in our present work. The rates of electron capture on various nuclear isotopes and the corresponding emitted neutrino spectra in the range of the parameters (T, ρ, Y_e) describing the star until reaching equilibrium during the core collapse are comprehensively studied in [21, 26, 27] for a great number of nuclear isotopes by using the large scale shell model. We are currently performing similar calculations for a set of isotopes by employing the present pn-QRPA method [52].

Furthermore, the average neutrino energy, $\langle E_\nu \rangle$, of the neutrinos emitted by e-capture on nuclei can be obtained by dividing the neutrino-energy loss rate (defined by an expression similar to (12) by replacing the rate λ_i with the energy loss rate E_j) with the reaction rate for e-capture on nuclei R_h. Assuming, for example, power-law energy distribution for the neutrino spectrum produced by the e-capture in supernova phase, the average neutrino-energy $\langle E_\nu \rangle$ determines a specific supernova-neutrino scenario. In addition, the neutrino emissivity is obtained by multiplying the electron capture rate at nuclear statistical equilibrium with the neutrino-spectra [21, 26, 27]. Finally we note that the rates for the inverse neutrino absorption process are also determined from the electron capture rates obtained as discussed in this section [21].

4. Summary and Conclusions

The electron capture on nuclei plays crucial role during the presupernova and collapse phase (in the late stage e^--capture on free protons is also significant). It becomes increasingly possible as the density in the star's center is enhanced and it is accompanied by an increase of the chemical potential (Fermi energy) of the degenerate electron gas. This process reduces the electron-to-baryon ratio Y_e of the matter composition.

In this work, by using our numerical approach based on a refinement of the pn-QRPA that describes reliably all the semileptonic weak interaction processes in nuclei, we studied in detail the electron capture process on ^{66}Zn isotope and calculated original and stellar e^--capture cross sections. We tested our nuclear model (the pn-QRPA) through the reproducibility of orbital muon capture rates for this isotope. The agreement with experimental data and other reliable theoretical results of partial and total μ-capture rates and of the percentage contributions of various low-lying excitations is quite good which provides us with high confidence level for the obtained cross sections.

Our future plans are to extend the application of this method and make similar calculations for other interesting nuclei [52]. Also this method could be applied to other semileptonic nuclear processes like beta-decay and charged-current neutrino-nucleus processes important in nuclear astrophysics and neutrino nucleosynthesis.

Appendices

A. Nuclear Matrix Elements

The eight different tensor multipole operators entering the above equations (see Section 3), refered to as Coulomb $\widehat{\mathscr{M}}_{JM}$, longitudinal $\widehat{\mathscr{L}}_{JM}$, transverse electric $\widehat{\mathscr{T}}^{\text{el}}_{JM}$, and transverse magnetic $\widehat{\mathscr{T}}^{\text{magn}}_{JM}$, are defined as follows:

$$\widehat{\mathscr{M}}_{JM}(qr) = \widehat{M}^{\text{coul}}_{JM} + \widehat{M}^{\text{coul5}}_{JM}, \qquad \widehat{\mathscr{L}}_{JM}(qr) = \widehat{L}_{JM} + \widehat{L}^{5}_{JM},$$
$$\widehat{\mathscr{T}}^{\text{el}}_{JM}(qr) = \widehat{T}^{\text{el}}_{JM} + \widehat{T}^{\text{el5}}_{JM}, \qquad \widehat{\mathscr{T}}^{\text{magn}}_{JM}(qr) = \widehat{T}^{\text{magn}}_{JM} + \widehat{T}^{\text{magn5}}_{JM}. \tag{A.1}$$

These multipole operators contain polar-vector and axial-vector parts and are written in terms of seven independent basic multipole operators as follows:

$$\widehat{M}^{\text{coul}}_{JM}(q\mathbf{r}) = F_1^V\left(q_\mu^2\right) M^J_M(q\mathbf{r}), \tag{A.2}$$

$$\widehat{L}_{JM}(q\mathbf{r}) = \frac{q_0}{q}\widehat{M}^{\text{coul}}_{JM}(q\mathbf{r}), \tag{A.3}$$

$$\widehat{T}^{\text{el}}_{JM}(q\mathbf{r}) = \frac{q}{M_N}\left[F_1^V\left(q_\mu^2\right)\Delta'^J_M(q\mathbf{r}) + \frac{1}{2}\mu^V\left(q_\mu^2\right)\Sigma^J_M(q\mathbf{r})\right], \tag{A.4}$$

$$i\widehat{T}^{\mathrm{mag}}_{JM}(q\mathbf{r}) = \frac{q}{M_N}\left[F_1^V\left(q_\mu^2\right)\Delta^J_M(q\mathbf{r}) - \frac{1}{2}\mu^V\left(q_\mu^2\right)\Sigma'^J_M(q\mathbf{r})\right], \tag{A.5}$$

$$i\widehat{M}^5_{JM}(q\mathbf{r}) = \frac{q}{M_N}\left[F_A\left(q_\mu^2\right)\Omega^J_M(q\mathbf{r}) + \frac{1}{2}\left(F_A\left(q_\mu^2\right) + q_0F_P\left(q_\mu^2\right)\right)\Sigma''^J_M(q\mathbf{r})\right], \tag{A.6}$$

$$-i\widehat{L}^5_{JM}(q\mathbf{r}) = \left[F_A\left(q_\mu^2\right) - \frac{q^2}{2M_N}F_P\left(q_\mu^2\right)\right]\Sigma''^J_M(q\mathbf{r}), \tag{A.7}$$

$$-i\widehat{T}^{\mathrm{el5}}_{JM}(q\mathbf{r}) = F_A\left(q_\mu^2\right)\Sigma'^J_M(q\mathbf{r}), \tag{A.8}$$

$$\widehat{T}^{\mathrm{mag5}}_{JM}(q\mathbf{r}) = F_A\left(q_\mu^2\right)\Sigma^J_M(q\mathbf{r}), \tag{A.9}$$

where the form factors F_X, $X = 1, A, P$, and μ^V are functions of the 4-momentum transfer q_μ^2 and M_N is the nucleon mass.

These multipole operators, due to the Conserved Vector Current (CVC) theory, are reduced to seven new basic operators expressed in terms of spherical Bessel functions, spherical harmonics, and vector spherical harmonics (see [24, 31, 44]). The single particle reduced matrix elements of the form $\langle j_1\|T_i^J\|j_2\rangle$, where T_i^J represents any of the seven basic multipole operators (M^J_M, Ω^J_M, Σ^J_M, Σ'^J_M, Σ''^J_M, Δ^J_M, Δ'^J_M) of (A.2)–(A.9), have been written in closed compact expressions as follows [31]:

$$\left\langle (n_1l_1)\, j_1 \left\| T^J \right\| (n_2l_2)\, j_2 \right\rangle = e^{-y}y^{\beta/2}\sum_{\mu=0}^{n_{\max}} P^J_\mu y^\mu, \tag{A.10}$$

where the coefficients P^J_μ are given in [31]. In the latter summation the upper index $n_{\max}$ represents the maximum harmonic oscillator quanta included in the active model space chosen as $n_{\max} = (N_1 + N_2 - \beta)/2$, where $N_i = 2n_i + l_i$, $i = 1, 2$, and β is related to the rank of the above operators [31].

In the context of the pn-QRPA, the required reduced nuclear matrix elements between the initial $|0^+_{gs}\rangle$ and the final $|f\rangle$ state entering the rates of (6) are given by

$$\left\langle f \left\| \widehat{T}^J \right\| 0^+_{gs} \right\rangle = \sum_{j_2\geq j_1} \frac{\left\langle j_2 \left\| \widehat{T}^J \right\| j_1 \right\rangle}{[J]}\left[X_{j_2j_1}u^p_{j_2}v^n_{j_1} + Y_{j_2j_1}v^p_{j_2}u^n_{j_1}\right], \tag{A.11}$$

where u_j and v_j are the probability amplitudes for the j-level to be unoccupied or occupied, respectively (see the text) [31, 32].

These matrix elements enter the description of various semileptonic weak interaction processes in the presence of nuclei [31–38, 44, 53, 54].

B. Nuclear Form Factors

In (A.2)–(A.9) the standard set of free nucleon form factors $F_X(q_\mu^2)$, $X = 1, A, P$ and $\mu^V(q_\mu^2)$ reads

$$\begin{aligned} F_1^V\left(q_\mu^2\right) &= 1.000\left[1 + \left(\frac{q}{840\,\mathrm{MeV}}\right)^2\right]^{-2}, \\ \mu^V\left(q_\mu^2\right) &= 4.706\left[1 + \left(\frac{q}{840\,\mathrm{MeV}}\right)^2\right]^{-2}, \\ F_A\left(q_\mu^2\right) &= g_A\left[1 + \left(\frac{q}{1032\,\mathrm{MeV}}\right)^2\right]^{-2}, \\ F_P\left(q_\mu^2\right) &= \frac{2M_NF_A\left(q_\mu^2\right)}{q^2 + m_\pi^2}, \end{aligned} \tag{B.1}$$

where M_N is the nucleon mass and g_A is the axial vector free nucleon coupling constant (see the text).

Conflict of Interests

The authors declare that there is no conflict of interests regarding the publication of this paper.

Acknowledgments

This research has been cofinanced by the European Union (European Social Fund-ESF) and Greek national funds through the Operational Program "Education and Lifelong Learning" of the National Strategic Reference Framework (NSRF)—Research Funding Program: Heracleitus II, investing in knowledge society through the European Social Fund.

References

[1] K. Langanke and G. Martinez-Pinedo, "Nuclear weak-interaction processes in stars," *Reviews of Modern Physics*, vol. 75, p. 819, 2003.

[2] G. M. Fuller, W. A. Fowler, and M. J. Newman, "Stellar weak-interaction rates for sd-shell nuclei. I. Nuclear matrix element systematics with application to Al-26 and selected nuclei of importance to the supernova problem," *Astrophysical Journal Supplement Series*, vol. 42, pp. 447–473, 1980.

[3] G. M. Fuller, W. A. Fowler, and M. J. Newman, "Stellar weak interaction rates for intermediate-mass nuclei. II—A = 21 to A = 60," *The Astrophysical Journal*, vol. 252, pp. 715–740, 1982.

[4] G. M. Fuller, W. A. Fowler, and M. J. Newman, "Stellar weak interaction rates for intermediate mass nuclei. III—rate tables for the free nucleons and nuclei with A = 21 to A = 60," *Astrophysical Journal Supplement*, vol. 48, pp. 279–319, 1982.

[5] M. B. Aufderheide, I. Fushiki, S. E. Woosley, and D. H. Hartmann, "Search for important weak interaction nuclei in presupernova evolution," *Astrophysical Journal, Supplement Series*, vol. 91, no. 1, pp. 389–417, 1994.

[6] H. A. Bethe, "Supernova mechanisms," *Reviews of Modern Physics*, vol. 62, p. 801, 1990.

[7] K. Langanke and G. Martinez-Pinedo, "Supernova electron capture rates for ^{55}Co and ^{56}Ni," *Physics Letters B: Nuclear,*

Elementary Particle and High-Energy Physics, vol. 436, no. 1-2, pp. 19–24, 1998.

[8] Y. F. Niu, N. Paar, D. Vretenar, and J. Meng, "Stellar electron-capture rates calculated with the finite-temperature relativistic random-phase approximation," *Physical Review C*, vol. 83, no. 4, Article ID 045807, pp. 045850–10, 2011.

[9] D. J. Dean, K. Langanke, L. Chatterjee, P. B. Radha, and M. R. Strayer, "Electron capture on iron group nuclei," *Physical Review C*, vol. 58, no. 1, pp. 536–544, 1998.

[10] N. Paar, G. Colo, E. Khan, and D. Vretenar, "Calculation of stellar electron-capture cross sections on nuclei based on microscopic Skyrme functionals," *Physical Review C*, vol. 80, Article ID 055801, 2009.

[11] J. U. Nabi, M. U. Rahman, and M. Sajjad, "Electron and positron capture rates on ^{55}Co in stellar matter," *Brazilian Journal of Physics*, vol. 37, no. 4, 2007.

[12] J. U. Nabi, "Ground and excited states Gamow-Teller strength distributions of iron isotopes and associated capture rates for core-collapse simulations," *Astrophysics and Space Science*, vol. 331, no. 2, pp. 537–554, 2011.

[13] J. U. Nabi, M. Sajjad, and M. U. Rahman, "Electron capture rates on titanium isotopes in stellar matter," *Acta Physica Polonica B*, vol. 38, no. 10, pp. 3203–3224, 2007.

[14] A. L. Cole, T. S. Anderson, R. G. T. Zegers et al., "Gamow-Teller strengths and electron-capture rates for *pf*-shell nuclei of relevance for late stellar evolution," *Physical Review C*, vol. 86, Article ID 015809, 2012.

[15] Q. Zhi, K. Langanke, G. Martínez-Pinedo, F. Nowacki, and K. Sieja, "The ^{76}Se Gamow-Teller strength distribution and its importance for stellar electron capture rates," *Nuclear Physics A*, vol. 859, no. 1, pp. 172–184, 2011.

[16] P. Sarriguren, E. M. de Guerra, and R. Álvarez-Rodríguez, "Gamow-Teller strength distributions in Fe and Ni stable isotopes," *Nuclear Physics A*, vol. 716, pp. 230–244, 2003.

[17] J. Toivanen, E. Kolbe, K. Langanke, G. Martínez-Pinedo, and P. Vogel, "Supernova neutrino induced reactions on iron isotopes," *Nuclear Physics A*, vol. 694, no. 1-2, pp. 395–408, 2001.

[18] E. Kolbe, K. Langanke, G. Martínez-Pinedo, and P. Vogel, "Neutrino-nucleus reactions and nuclear structure," *Journal of Physics G: Nuclear and Particle Physics*, vol. 29, no. 11, pp. 2569–2596, 2003.

[19] C. Frohlich, G. Martinez-Pinedo, M. Liebendorfer et al., "Neutrino-induced nucleosynthesis of $A > 64$ nuclei: the νp process," *Physical Review Letters*, vol. 96, no. 14, Article ID 142502, 4 pages, 2006.

[20] A. Juodagalvis, K. Langanke, G. Martínez-Pinedo, W. R. Hix, D. J. Dean, and J. M. Sampaio, "Neutral-current neutrino-nucleus cross sections for A~50–65 nuclei," *Nuclear Physics A*, vol. 747, no. 1, pp. 87–108, 2005.

[21] K. Langanke, G. Martinez-Pinedo, J. M. Sampaio et al., "Electron capture rates on nuclei and implications for stellar core collapse," *Physical Review Letters*, vol. 90, no. 24, Article ID 241102, 4 pages, 2003.

[22] K. Langanke, E. Kolbe, and D. J. Dean, "Unblocking of the Gamow-Teller strength in stellar electron capture on neutron-rich germanium isotopes," *Physical Review C*, vol. 63, no. 3, Article ID 032801, 5 pages, 2001.

[23] N. T. Zinner, K. Langanke, and P. Vogel, "Muon capture on nuclei: pandom phase approximation evaluation versus data for $6 \leq Z \leq 94$ nuclei," *Physical Review C*, vol. 74, Article ID 024326, 2006.

[24] T. Marketin and N. Paar, "Relativistic quasiparticle random-phase approximation calculation of total muon capture rates," *Physical Review C*, vol. 79, no. 5, Article ID 054323, 8 pages, 2009.

[25] E. Kolbe, K. Langanke, and P. Vogel, "Comparison of continuum random phase approximation and the elementary particle model for the inclusive muon neutrino reaction on 12_C," *Nuclear Physics A*, vol. 613, no. 4, pp. 382–396, 1997.

[26] K. Langanke and G. Martinez-Pinedo, "Shell-model calculations of stellar weak interaction rates: II. Weak rates for nuclei in the mass range A=45–65 in supernovae environments," *Nuclear Physics A*, vol. 673, no. 1–4, pp. 481–508, 2000.

[27] K. Langanke, G. Martinez-Pinedo, and J. M. Sampaio, "Neutrino spectra from stellar electron capture," *Physical Review C*, vol. 64, no. 5, Article ID 055801, 7 pages, 2001.

[28] R. W. Hix, O. E. B. Messer, A. Mezzacappa et al., "Consequences of nuclear electron capture in core collapse supernovae," *Physical Review Letters*, vol. 91, Article ID 201102, 2003.

[29] P. Ring and P. Schuck, *The Nuclear Many-Body Problem*, Springer, New York, NY, USA, 1969.

[30] T. S. Kosmas and E. Oset, "Charged current neutrino-nucleus reaction cross sections at intermediate energies," *Physical Review C: Nuclear Physics*, vol. 53, no. 3, pp. 1409–1415, 1996.

[31] V. C. Chasioti and T. S. Kosmas, "A unified formalism for the basic nuclear matrix elements in semi-leptonic processes," *Nuclear Physics A*, vol. 829, no. 3-4, pp. 234–252, 2009.

[32] P. G. Giannaka and T. S. Kosmas, "Electron-capture and its role to explosive neutrino-nucleosynthesis," *Journal of Physics: Conference Series*, vol. 410, no. 1, Article ID 012124, 2013.

[33] V. Tsakstara and T. S. Kosmas, "Low-energy neutral-current neutrino scattering on ^{128,130}Te isotopes," *Physical Review C*, vol. 83, no. 5, Article ID 054612, 13 pages, 2011.

[34] K. G. Balasi, E. Ydrefors, and T. S. Kosmas, "Theoretical study of neutrino scattering off the stable even Mo isotopes at low and intermediate energies," *Nuclear Physics A*, vol. 868–869, pp. 82–98, 2011.

[35] K. G. Balasi, E. Ydrefors, T. S. Kosmas, and J. Suhonena, "The response of ^{95,97}Mo to supernova neutrinos," *Nuclear Physics A*, vol. 866, pp. 67–78, 2011.

[36] V. Tsakstara and T. S. Kosmas, "Analyzing astrophysical neutrino signals using realistic nuclear structure calculations and the convolution procedure," *Physical Review C*, vol. 84, no. 6, Article ID 064620, 14 pages, 2011.

[37] E. Ydrefors, K. G. Balasi, T. S. Kosmas, and J. Suhonen, "Detailed study of the neutral-current neutrino–nucleus scattering off the stable Mo isotopes," *Nuclear Physics A*, vol. 896, pp. 1–23, 2012.

[38] V. Tsakstara and T. S. Kosmas, "Nuclear responses of ^{64,66}Zn isotopes to supernova neutrinos," *Physical Review C*, vol. 86, no. 4, Article ID 044618, 10 pages, 2012.

[39] T. S. Kosmas, A. Faessler, and J. D. Vergados, "The new limits of the neutrinoless (μ^-, e^-) conversion branching ratio," *Journal of Physics G: Nuclear and Particle Physics*, vol. 23, no. 6, pp. 693–703, 1997.

[40] R. A. Eramzhyan, V. A. Kuz'min, and T. V. Tetereva, "Calculations of ordinary and radiative muon capture on ^{58,60,62}Ni," *Nuclear Physics A*, vol. 642, no. 3-4, pp. 428–448, 1998.

[41] E. Kolbe, K. Langanke, and P. Vogel, "Muon capture on nuclei with $N > Z$, random phase approximation, and in-medium value of the axial-vector coupling constant," *Physical Review C*, vol. 62, no. 5, Article ID 055502, 4 pages, 2000.

[42] T. S. Kosmas, "Exotic $\mu^- \rightarrow e^-$ conversion in nuclei: energy moments of the transition strength and average energy of the outgoing," *Nuclear Physics A*, vol. 683, no. 1, pp. 443–462, 2001.

[43] B. S. Meyer, "The r-, s-, and p-processes in nucleosynthesis," *Annual Review of Astronomy and Astrophysics*, vol. 32, pp. 153–190, 1994.

[44] T. W. Donnelly and R. D. Peccei, "Neutral current effects in nuclei," *Physics Reports*, vol. 50, no. 1, pp. 1–85, 1979.

[45] Y. Tanaka, Y. Oda, F. Petrovich, and R. K. Sheline, "Effect of the spin-orbit potential on the single particle levels in the superheavy region," *Physics Letters B*, vol. 83, no. 3-4, pp. 279–283, 1979.

[46] E. V. Bugaev, G. S. Bisnovatyi-Kogan, M. A. Rudzsky, and Z. F. Seidov, "The interaction of intermediate energy neutrinos with nuclei," *Nuclear Physics A*, vol. 324, no. 2-3, pp. 350–364, 1979.

[47] J. Vary, Private communication, http://nuclear.physics.iastate.edu/npc.php.

[48] M. S. Yousef, V. Rodin, A. Faessler, and F. Simkovic, "Two-neutrino double β decay of deformed nuclei within the quasi-particle random-phase approximation with a realistic interaction," *Physical Review C*, vol. 79, Article ID 014314, 2009.

[49] V. Rodin and A. Faessler, "First application of the continuum-QRPA to the description of the double beta decay," *Progress in Particle and Nuclear Physics*, vol. 57, pp. 226–234, 2006.

[50] O. Hausser, M. C. Vetterli, R. W. Fergerson et al., "Nuclear response in the ^{54}Fe($p \rightarrow$, $p \rightarrow'$) reaction at 290 MeV," *Physical Review C*, vol. 43, no. 1, pp. 230–249, 1991.

[51] B. H. Wildenthal, "Empirical strengths of spin operators in nuclei," *Progress in Particle and Nuclear Physics*, vol. 11, pp. 5–51, 1984.

[52] P. G. Giannaka and T. S. Kosmas, In preparation.

[53] D. K. Papoulias and T. S. Kosmas, "Nuclear aspects of neutral current non-standard ν-nucleus reactions and the role of the exotic $\mu^- \rightarrow e^-$ transitions experimental limits," *Physics Letters B*, vol. 728, p. 482, 2014.

[54] D. K. Papoulias and T. S. Kosmas, "Exotic lepton flavour violating processes in the presence of nuclei," *Journal of Physics: Conference Series*, vol. 410, Article ID 012123, 2013.

Hindawi Publishing Corporation
Advances in High Energy Physics
Volume 2015, Article ID 374061, 11 pages
http://dx.doi.org/10.1155/2015/374061

Research Article

Asymmetric Velocity Distributions from Halo Density Profiles in the Eddington Approach

J. D. Vergados[1,2]

[1] *TEI of Western Macedonia, 50100 Kozani, Greece*
[2] *University of Ioannina, 45110 Ioannina, Greece*

Correspondence should be addressed to J. D. Vergados; vergados@uoi.gr

Received 9 July 2014; Accepted 11 September 2014

Academic Editor: Theocharis Kosmas

We show how to obtain the energy distribution *f(E)* in our vicinity starting from WIMP density profiles in a self-consistent way by employing the Eddington approach and adding reasonable angular momentum dependent terms in the expression of the energy. We then show how we can obtain the velocity dispersions and the asymmetry parameter β in terms of the parameters describing the angular momentum dependence. From this expression, for *f(E)*, we proceed to construct an axially symmetric WIMP a velocity distribution, which, for a gravitationally bound system, automatically has a velocity upper bound and is characterized by the same asymmetriy β. This approach is tested and clarified by constructing analytic expressions in a simple model, with adequate structure. We then show how such velocity distributions can be used in determining the event rates, including modulation, in both the standard and the directional WIMP searches.

1. Introduction

The combined MAXIMA-1 [1–3], BOOMERANG [4, 5], DASI [6], and COBE/DMR cosmic microwave background (CMB) observations [7] imply that the Universe is flat [8] and that most of the matter in the Universe is Dark [9], that is, exotic. These results have been confirmed and improved by the recent WMAP [10] and Planck [11] data. Combining the data of these quite precise measurements one finds the following:

$$\Omega_b = 0.0456 \pm 0.0015, \qquad \Omega_{\mathrm{CDM}} = 0.228 \pm 0.013, \qquad \Omega_\Lambda = 0.726 \pm 0.015 \tag{1}$$

(the more recent Planck data yield a slightly different combination $\Omega_{\mathrm{CDM}} = 0.274 \pm 0.020$, $\Omega_\Lambda = 0.686 \pm 0.020$). It is worth mentioning that both the WMAP and the Plank observations yield essentially the same value of $\Omega_m h^2$, but they differ in the value of h; namely, $h = 0.704 \pm 0.013$ (WMAP) and $h = 0.673 \pm 0.012$ (Planck). Since any "invisible" nonexotic component cannot possibly exceed 40% of the above Ω_{CDM} [12], exotic (nonbaryonic) matter is required and there is room for cold dark matter candidates or WIMPs (weakly interacting massive particles).

Even though there exists firm indirect evidence for a halo of dark matter in galaxies from the observed rotational curves, see for example, the review [13], it is essential to directly detect such matter in order to unravel the nature of the constituents of dark matter. The possibility of direct dark matter detection, however, depends on the nature of the dark matter constituents (WIMPs). At present, there exists a plethora of such candidates: the LSP (lightest supersymmetric particle) [14–23], technibaryon [24, 25], mirror matter [26, 27], Kaluza-Klein models with universal extra dimensions [28, 29], and so forth.

Since the WIMP is expected to be very massive, $m_\chi \geq 30\,\mathrm{GeV}$, and extremely nonrelativistic with average kinetic energy $T \approx 50\,\mathrm{KeV}(m_\chi/100\,\mathrm{GeV})$, it cannot excite the nucleus, except in some very exceptional cases. It can, thus, be directly detected mainly via the recoiling of a nucleus

(A, Z) following WIMP-nucleus elastic scattering. The event rate for such a process can be computed following a number of steps [30]. In the present work, we will focus on one of the ingredients entering the computation of the event rates, namely, the WIMP density in our vicinity and its velocity distribution.

In the past, various velocity distributions have been considered. The one most commonly used is the isothermal Maxwell-Boltzmann (M-B) velocity distribution. Extensions of the M-B distribution were also considered; in particular, those that were axially symmetric with enhanced dispersion in the galactocentric direction [31–34]. In all such distributions, an upper cutoff $v_{esc} = 2.84v_0$ was introduced by hand, in the range obtained by Cochanek [35]. In a different approach, Tsallis type functions, derived from simulations of dark matter densities, were employed; see for example recent calculations [36] and references there in.

Nonisothermal models have also been considered, like the late infall of dark matter into the galaxy, that is, caustic rings [37–41], dark matter orbiting the Sun [42], and Sagittarius dark matter [43].

The more correct approach in our view is to consider the Eddington approach [44], which allows one to relate the dark matter density and the corresponding velocity distribution in a self-consistent way. Furthermore, this approach has the advantage that the upper velocity cut off is not imposed by hand, but it comes in naturally. It has, thus, been used by Merritt [45] and applied to dark matter by Ullio and Kamionkowski [13] and by us [46, 47].

It is the purpose of the present paper to extend the previous work and obtain a dark matter velocity distribution, which need not be spherically symmetric, even though it may originate from density profiles that are spherically symmetric. To this end, we have considered a one-parameter family of self-consistent star clusters that are spherically symmetric but anisotropic in velocity space. These were computed modifying the distribution (DF) by including suitable angular momentum factors along the lines suggested by Wojtak et al. [48] and more recently by Fornasa and Green [49]. Also a one-parameter family of self-consistent star clusters that are spherically symmetric was shown to be anisotropic in velocity space [50] (see also [51]). The last model was constructed first in the Newtonian limit and then, after the first, post-Newtonian corrections were computed. Anisotropic velocity distributions obtained by adopting an ansatz for the dark matter phase space distribution. This allows one to construct self-consistent halo models, which feature a degree of anisotropy as a function of the radius such as suggested by the simulations [52]. Furthermore this has been applied [53] in the case of the NFW halo profile to obtain the asymmetry parameter.

To clarify some of the issues involved in these approaches, we will concentrate on some cases amenable to analytic solutions like the celebrated Plummer solution [54]. We will show how this method can be used to obtain, in a self-consistent fashion, asymmetric velocity distributions with asymmetry parameter β. For detailed applications to dark matter searches realistic velocity distributions are necessary, but we leave this case to be discussed in a future publication.

We believe that even the prelude of such searches, as discussed here, falls within the novel subject of The Frontiers of Intensities and Very High Sensitivities.

2. The Dark Matter Distribution in the Context of the Eddington Approach

One assumes that the system is in steady state. This may not be exactly true, since simulated halos contain substructures corresponding to streams [55] and, more recently, to non-completely phase-mixed DM, dubbed "debris flow" [56]. This, however, may be a reasonable assumption at the solar radius. Thus, in this approach, one starts with a phase space dark matter distribution function $f_{ps}(E, L)$, which is a function of the energy E and the angular momentum L with the goal of obtaining the dark matter velocity distribution $f_{r_s}(\boldsymbol{v})$. The function $f_{ps}(E, L)$ is factorized into a function $f(E)$, which depends on the energy only, and a function of the angular momentum $F_L(L)$. This factorization has been tested qualitatively by Wojtak et al. [48] and it has subsequently been discussed and used by [49]. Furthermore, these authors used the ansatz,

$$F_L(L) = \left(1 + \frac{L^2}{2L_0^2}\right)^{-\beta_\infty+\beta_0} L^{-2\beta_0}, \tag{2}$$

in terms of three new parameters. L_0 is an angular momentum parameter. This ansatz showed that the thus obtained self-consistent solutions match the radial dependence of the anisotropy parameter $\beta(r)$ (see below). The parameter β_0 affects the anisotropy in the cental region of the halo density, while β_∞ has an effect at large distances [48]. To see this, we consider the limits previously considered; that is,

$$F_L(L) = \begin{cases} \left(\dfrac{L}{L_0}\right)^{-2\beta_0} & L \ll L_0 \\ \left(\dfrac{L}{L_0}\right)^{-2\beta_\infty} & L \gg L_0, \end{cases} \tag{3}$$

where β_0 is the the central anisotropy of the system. This means that, if this parameter is zero, there is no asymmetry in this region. In fact, it can be shown that $\beta_0 \leq \gamma/2$, where $\propto r^{-\gamma}$, is the halo density at the center. In the popular halo density profile [57], $\beta_0 \leq 1/2$. In our analytically soluble model, we can better see the effect of these parameters on the asymmetry parameter.

2.1. The Distribution Is a Function of the Total Energy Only. The introduction of the matter distribution can be given [47] as follows:

$$dM = 2\pi f\left(\Phi(\mathbf{r}), v_r, v_t\right) dxdydz v_t dv_t dv_r, \tag{4}$$

where the function f depends on $\mathbf{r}$ through the potential $\Phi(\mathbf{r})$ and the tangential and radial velocities v_t and v_r. We will limit ourselves in spherically symmetric systems. Then, the density of matter $\rho(|r|)$ satisfies the following equation:

$$d\rho = 2\pi f\left(\Phi(|\mathbf{r}|), v_r, v_t\right) v_t dv_t dv_r. \tag{5}$$

The energy is given by $E = \Phi(r) + v^2/2$. Then,

$$\rho(r) = 4\pi \int f\left(\Phi(r) + \frac{v^2}{2}\right) v^2 dv = 4\pi \int_{\Phi}^{0} f(E)\sqrt{2(E-\Phi)}dE. \quad (6)$$

This is an integral equation of the Abel type. It can be inverted to yield

$$f(E) = \frac{\sqrt{2}}{4\pi^2}\frac{d}{dE}\int_{E}^{0}\frac{d\Phi}{\sqrt{\Phi - E}}\frac{d\rho}{d\Phi}. \quad (7)$$

The above equation can be rewritten as

$$f(E) = \frac{1}{2\sqrt{2}\pi^2}\left[\int_{E}^{0}\frac{d\Phi}{\sqrt{\Phi-E}}\frac{d^2\rho}{d\Phi^2} - \frac{1}{\sqrt{-E}}\frac{d\rho}{d\Phi}\bigg|_{\Phi=0}\right]. \quad (8)$$

The potential $\Phi(r)$ for a given density $\rho(r)$ is obtained by solving Poisson's equation. In order to proceed further, it is necessary to know the density as a function of the potential, treating, for example, r as a parameter. Only in few cases, this can be done analytically.

Once the function $f(E)$ is known, we can obtain the needed velocity distribution $f_{r_s}(v)$ in our vicinity ($r = r_s$) by writing

$$f_{r_s}(v') = \mathcal{N} f\left(\Phi(r)|_{r=r_s} + \frac{v'^2}{2}\right), \quad (9)$$

where $\mathcal{N}$ is a normalization factor.

2.2. Angular Momentum Dependent Terms. As we have already mentioned in the phase distribution function, one introduces additional angular dependent terms. The presence of such terms can introduce asymmetries in the velocity dispersions.

In such an approach [48], we get

$$\rho(\mathbf{r}) = \iiint f(E)\left(1 + \frac{L^2}{2L_0^2}\right)^{-\beta_\infty+\beta_0} L^{-2\beta_0}\, d^3\boldsymbol{v}. \quad (10)$$

Introducing the new parameters L and E in terms of v_t and v_r via

$$v_t = \frac{L}{r}, \qquad v_r = \sqrt{2(E-\Phi) - \frac{L^2}{r^2}}$$
$$\text{or} \quad v_t = \frac{L_0}{r}\sqrt{2\lambda}, \qquad v_r = \sqrt{2}\frac{L_0}{r}\sqrt{x-\lambda}, \qquad \lambda = \frac{L^2}{2L_0^2}, \quad (11)$$

we can perform the integration in cylindrical coordinates and get

$$\rho(\mathbf{r}) = 2^{1/2-\beta_0} L_0^{1-2\beta_0}\frac{\pi}{r}\int_{\Phi}^{0} f(E)\,dE\int_0^x \frac{\lambda^{-\beta_0}(\lambda+1)^{-\beta_\infty+\beta_0}}{\sqrt{x-\lambda}}d\lambda. \quad (12)$$

In the above expressions, $x = (r^2/L_0^2)(\Phi - E)$.

Before proceeding further, we prefer to write the above formula in terms of dimensionless variables $\Phi = \Phi_0\xi$, $\rho = \rho_0\eta$, $E = \Phi_0\epsilon$, and $f(E) = \rho_0\Phi_0^{-3/2}\tilde{f}(\epsilon)$. Thus, the last equation becomes

$$\eta = 2^{1/2-\beta_0} L_0^{-2\beta_0}\frac{1}{\sqrt{a}}\pi\int_{\xi}^{0}\tilde{f}(\epsilon)\,d\epsilon\int_0^x \frac{\lambda^{-\beta_0}(\lambda+1)^{-\beta_\infty+\beta_0}}{\sqrt{x-\lambda}}d\lambda \quad (13)$$

with $a = r^2\Phi_0^2/L_0^2$ and $x = a(\xi - \epsilon)$.

The second integral can be done analytically to yield

$$\frac{\sqrt{\pi}x^{1/2-\beta_0}\Gamma(1-\beta_0)}{\Gamma(3/2-\beta_0)}\,{}_2F_1(1-\beta_0, -\beta_0+\beta_\infty, 3/2-\beta_0, -x), \quad (14)$$

with ${}_2F_1$ the usual hypergeometric function. Then, (12) becomes

$$\eta = 2^{1/2-\beta_0} L_0^{-2\beta_0}\frac{1}{\sqrt{a}}\pi\frac{\sqrt{\pi}\Gamma(1-\beta_0)}{\Gamma(3/2-\beta_0)}\int_{\xi}^{0}\tilde{f}(\epsilon)\,d\epsilon x^{1/2-\beta_0} \times {}_2F_1(1-\beta_0, -\beta_0+\beta_\infty, 3/2-\beta_0, -x). \quad (15)$$

In the limit in which $\beta_0 -> 0, L_0 -> \infty$, the last expression is reduced to (6).

Equation (10) allows the calculation of moments of the velocity. In particular, following the procedure of [48], one finds

$$\begin{aligned} &\prec v_t^2 \succ \\ &= 2\left(\frac{L_0}{r}\right)^2(2-\beta_0) \\ &\quad\times \frac{\int_{\xi}^{0}\tilde{f}(\epsilon)\,d\epsilon x^{3/2-\beta_0}\,{}_2F_1(2-\beta_0, -\beta_0+\beta_\infty, 5/2-\beta_0, -x)}{\int_{\xi}^{0}\tilde{f}(\epsilon)\,d\epsilon x^{1/2-\beta_0}\,{}_2F_1(1-\beta_0, -\beta_0+\beta_\infty, 3/2-\beta_0, -x)} \\ &\prec v_r^2 \succ \\ &= \left(\frac{L_0}{r}\right)^2(1-\beta_0) \\ &\quad\times \frac{\int_{\xi}^{0}\tilde{f}(\epsilon)\,d\epsilon x^{3/2-\beta_0}\,{}_2F_1(1-\beta_0, -\beta_0+\beta_\infty, 5/2-\beta_0, -x)}{\int_{\xi}^{0}\tilde{f}(\epsilon)\,d\epsilon x^{1/2-\beta_0}\,{}_2F_1(1-\beta_0, -\beta_0+\beta_\infty, 3/2-\beta_0, -x)}. \end{aligned} \quad (16)$$

The extra factor of 2 in the case of the tangential velocity can be understood, since there exist two such components. The moments of the velocity are, of course, functions of the three parameters of the model. The model clearly can accommodate asymmetries in the velocity dispersion, even if the density is spherically symmetric.

Equation (12) can be inverted to yield the distribution function $\tilde{f}(\epsilon)$, even though this is technically more complicated than in the standard Eddington approach without

the angular momentum factors. Given the function $\tilde{f}(\epsilon)$, we define the quantities

$$\begin{aligned}\Lambda_t &= (2-\beta_0)\\ &\quad\times\int_\xi^0 \tilde{f}(\epsilon)\,d\epsilon\,{}_2F_1\left(2-\beta_0,-\beta_0+\beta_\infty,5/2-\beta_0,-x\right),\\ \Lambda_r &= (1-\beta_0)\\ &\quad\times\int_\xi^0 \tilde{f}(\epsilon)\,d\epsilon\,{}_2F_1\left(1-\beta_0,-\beta_0+\beta_\infty,5/2-\beta_0,-x\right).\end{aligned} \tag{17}$$

Then, the asymmetry parameter β defined by

$$\beta = 1-\frac{\prec v_t^2 \succ}{2\prec v_r^2 \succ},\qquad \beta = 1-\frac{\Lambda_t}{\Lambda_r}. \tag{18}$$

The axially symmetric velocity distribution, with respect to the center of the galaxy, is, thus, obtained from $f(E)$ as described in the Appendix, for a number of cases, some of which, to the best of our knowledge, have not been obtained before in analytic form.

Clearly, for a given matter density profile, both the distribution function $\tilde{f}(\epsilon)$ and the integrals Λ_t and Λ_r are functions of r_s β_0 β_∞ and L_0. So is the asymmetry parameter β. The above equations get simplified in the following cases.

(1) In the limit in which $\beta_0 = 0$ and $\beta_\infty = -1$,

$$\begin{aligned}\eta &= 4\pi\int_\xi^0 \tilde{f}(\epsilon)\,d\epsilon\sqrt{2(\epsilon-\xi)}\left(1+\frac{2}{3}a(\epsilon-\xi)\right),\\ a &= \frac{r^2\Phi_0}{L_0^2}\end{aligned} \tag{19}$$

$$\prec v_t^2 \succ = \frac{2}{15}\frac{L_0^2}{r^2}\frac{\int_\xi^0 \tilde{f}(\epsilon)\,d\epsilon(\epsilon-\xi)^{3/2}(5+4a(\epsilon-\xi))}{\int_\xi^0 \tilde{f}(\epsilon)\,d\epsilon\sqrt{\epsilon-\xi}\,(1+(2/3)a(\epsilon-\xi))} \tag{20}$$

$$\prec v_r^2 \succ = \frac{1}{15}\frac{L_0^2}{r^2}\frac{\int_\xi^0 \tilde{f}(\epsilon)\,d\epsilon(\epsilon-\xi)^{3/2}(5+2a(\epsilon-\xi))}{\int_\xi^0 \tilde{f}(\epsilon)\,d\epsilon\sqrt{\epsilon-\xi}\,(1+(2/3)a(\epsilon-\xi))} \tag{21}$$

$$\beta = 1-\frac{\int_\xi^0 \tilde{f}(\epsilon)\,d\epsilon\,(\epsilon-\xi)^{3/2}(5+4a(\epsilon-\xi))}{\int_\xi^0 \tilde{f}(\epsilon)\,d\epsilon\,(\epsilon-\xi)^{3/2}(5+2a(\epsilon-\xi))}. \tag{22}$$

(2) $\beta_\infty = 1$, $\beta_0 = 0$.

In this case,

$$\begin{aligned}&\frac{1}{\sqrt{a}}x^{1/2-\beta_0}\,{}_2F_1\left(1-\beta_0,-\beta_0+\beta_\infty,3/2-\beta_0,-x\right)\\ &\quad\longrightarrow \frac{1}{\sqrt{a}}\frac{\sinh^{-1}\left(\sqrt{x}\right)}{\sqrt{1+x}}.\end{aligned} \tag{23}$$

This function is very complicated to handle. Note, however, that, for sufficiently small values of a, one finds that the above expression for $x = a(\epsilon-\xi)$ is reduced to

$$2\sqrt{\epsilon-\xi}\left(1-\frac{2}{3}a(\epsilon-\xi)\right). \tag{24}$$

We, thus, recover the previous formula with just a change of sign in a. The corresponding expressions for the velocity dispersions become

$$\begin{aligned}\Lambda_t &\Longleftrightarrow 2\left(\sqrt{x}-\frac{\sinh^{-1}\left(\sqrt{x}\right)}{\sqrt{1+x}}\right),\\ \Lambda_r &\Longleftrightarrow 4\left(-\sqrt{x}+\sqrt{1+x}\sinh^{-1}\left(\sqrt{x}\right)\right).\end{aligned} \tag{25}$$

In the limit of small a, we again recover the previous expressions with $a \to -a$.

(3) The case of $L \gg L_0$ is as follows.

In this case, the integral equation

$$\eta = \pi\sqrt{2\pi}a^{-\beta_\infty}\frac{\Gamma(1-\beta_\infty)}{\Gamma(3/2-\beta_\infty)}\int_\xi^0 (\epsilon-\xi)^{1/2-\beta_\infty}\tilde{f}(\epsilon)\,d\epsilon \tag{26}$$

can be solved exactly (see Appendix) to yield

$$\begin{aligned}\tilde{f}(\epsilon) &= \frac{a^{\beta_\infty}}{\pi^2\sqrt{2\pi}}\frac{\Gamma(3/2-\beta_\infty)}{\Gamma(1-\beta_\infty)}\frac{\sin(\pi(1/2-\beta_\infty))}{(1/2-\beta_\infty)}\\ &\quad\times\frac{d}{d\epsilon}\int_\epsilon^0 (\xi-\epsilon)^{-1/2+\beta_\infty}\frac{d\eta(\xi)}{d\xi}d\xi,\end{aligned} \tag{27}$$

provided that $\eta(0) = 0$. In this case, however, we find that

$$\beta = 1-\frac{\Lambda_t}{\Lambda_r} = 1-\frac{\Gamma(2-\beta_\infty)}{\Gamma(1-\beta_\infty)} = 1-\beta_\infty,\quad \beta_\infty < 1, \tag{28}$$

regardless of the velocity distribution.

3. Asymmetries in the Velocity Distribution

Proceeding as above, we get the function $f_{(\beta_\infty,\beta_0,L_0)}(E)$. We, then, proceed to construct a velocity distribution, which is characterized by the same asymmetry in velocity dispersion along lines similar to those previously adopted [58], that is, by considering models of the Osipkov-Merritt type [45, 59, 60]. Thus, the velocity distribution in our vicinity ($r = r_s$) is written as

$$f_{r_s}(\boldsymbol{v}) = \mathcal{N}(1+\alpha_s)\,f_{0,0,\infty}\left(\Phi(r_r s)+\frac{v_r'^2}{2}+(1+\alpha_s)\frac{v_t'^2}{2}\right), \tag{29}$$

where v_r' and v_t' are the radial, that is, outwards from the center of the galaxy, and the tangential components of the velocity, with respect to the center of the galaxy. The parameter $\alpha_s = \beta/(1-\beta)$ can be determined by calculating the moments of the velocity as above; that is, it is a function of the parameters L_0, β_0, and β_∞. Since these parameters

are usually treated as phenomenological parameters, we will treat β phenomenologically. We note that this function is only axially symmetric and the normalization constant $\mathcal{N}$ is a normalization constant, the same as in the case of $\alpha_s = 0$. The isotropic case follows as a special case in the limit $\alpha_s \to 0$.

The characteristic feature of this approach is that the velocity distribution automatically vanishes outside a given region specified by a cut-off velocity v_m, given by $v_m = \sqrt{2|\Phi(r_s)|}$.

4. A Simple Test Density Profile

Before proceeding further, we will examine a simple model, amenable to analytic solution, that is, the famous Plummer solution [54], and leave the case of realistic density profiles, like, for example, those often employed [13, 47, 57], for a future publication. It is well known that a spherical density distribution [54] of the type

$$\eta = \frac{\rho(x)}{\rho_0} = \frac{1}{(1+x^2/3)^{5/2}}, \qquad x = \frac{r}{a_0}, \tag{30}$$

which is sometimes used as an ordinary matter profile, leads to a potential of the form

$$\xi = \frac{\Phi(x)}{\Phi_0} = -\frac{1}{(1+x^2/3)^{1/2}}, \qquad \Phi_0 = 4\pi G_N a_0^2 \rho_0. \tag{31}$$

In the above expressions, a_0 is a scale length. More precisely, $a_0 = 3^{-1/6}R$ with R being the radius of a sphere, containing the same mass, uniformly distributed. It is interesting to remark that the Plummer solution naturally arises in a model involving self-consistent star clusters studied in the Newtonian limit as well as after the first post-Newtonian corrections were computed [50].

From these, we obtain the desired relation:

$$\begin{gathered}\eta(\xi) = -\xi^5, \quad \text{with } \eta''(\xi) = -20\xi^3, \\ \eta(\xi)\big|_{\xi=0} = 0, \quad \frac{d\eta}{d\xi}\bigg|_{\xi=0} = 0.\end{gathered} \tag{32}$$

Then, the solution to (19) is given by

$$\begin{aligned}\tilde{f}(x) = {} & \frac{16e^{-ax}}{a^{9/2}\pi x} \\ & \times e^{ax}\left(\sqrt{a}\sqrt{x}\left(2ax\left(2ax\left(2ax-5\right)+15\right)-15\right)\right. \\ & \left. + 15\sqrt{ax}\right) \\ & - 15a\sqrt{\pi}x\operatorname{erfi}\left(\sqrt{ax}\right), \quad x = -\epsilon.\end{aligned} \tag{33}$$

This leads to a velocity distribution:

$$f_{\xi(xs)}(y) = \tilde{f}\left(\xi(xs) - \frac{y^2}{2}\right), \tag{34}$$

where $\xi(xs)$ is the value of the potential in our vicinity. In our simple model $\xi(xs) \approx \sqrt{3}/2$. We also used a larger value $\xi(xs) = 10$.

(1) The choice $a > 0$ is as follows.

The obtained velocity distribution which is properly normalized is exhibited in Figure 1. We notice that the dependence on a is very mild.

We next compute the asymmetry parameter $\beta = 1 - \Lambda_t/\Lambda_r$ as a function of the potential ξ for various values of a. This is exhibited in Figure 2. The asymmetry is negative, opposite to what is commonly believed; see, for example, [31–34, 36, 61]; that is, it does not lead to enhanced dispersion in the galactocentric direction, regardless of the values of ξ. Thus, the positive values of a are not acceptable; that is, the choice $\beta_\infty = -1$, $\beta_0 = 0$ is not physically acceptable.

(2) The choice $\beta_\infty = 1$, $\beta_0 = 0$ is as follows.

In this case, we will explore the regime of negative absolutely small values of a, which is the physically interesting case. The velocity distribution obtained is exhibited in Figure 3, while the asymmetry parameter as a function of ξ, for the same values of a, is exhibited in Figure 4. Finally, the asymmetry parameter as a function of a, $a < 0$, is presented in Figure 5 for various values of ξ.

5. The Velocity Distribution in WIMP Searches

The asymmetric velocity distribution in the galactic frame can be written as

$$g(\beta, y') = \frac{1}{1-\beta} f_{0,0,\infty}\left(\Phi(r_s) + \frac{1}{2}\left(\frac{1}{1-\beta}\left(y'^2 - \beta y_r'^2\right)\right)\right). \tag{35}$$

This function depends, of course, on the assumed density profile and is expressed in terms of two variables, the solar coordinate r_s and the asymmetry parameter β. The latter depends on the parameters describing the angular momentum function $F_L(L)$. In order to get a feeling of what to expect in realistic calculations, we exhibit in Figure 6 the dependence on the asymmetry β of the angular average of the distribution function obtained in our simple model. The values of β employed were related to a as above. The results shown here exhibit the same trends as those obtained by using, for example, Tsallis functions (see [36]).

Our next task is to transform the velocity distribution from the galactic to the local frame. The needed equation, see, for example, [62], is

$$\begin{gathered}\mathbf{y} \longrightarrow \mathbf{y} + \hat{v}_s + \delta\left(\sin\alpha\hat{x} - \cos\alpha\cos\gamma\hat{y} + \cos\alpha\sin\gamma\hat{v}_s\right), \\ y = \frac{v}{v_0},\end{gathered} \tag{36}$$

with $\gamma \approx \pi/6$, $\hat{v}_s$ being a unit vector in the Sun's direction of motion, $\hat{x}$ a unit vector radially out of the galaxy in our position, and $\hat{y} = \hat{v}_s \times \hat{x}$. The last term in the first expression of (36) corresponds to the motion of the Earth around the Sun with δ being the ratio of the modulus of the Earth's velocity around the Sun divided by the Sun's velocity around the center of the Galaxy; that is, $v_0 \approx 220$ km/s and $\delta \approx 0.135$.

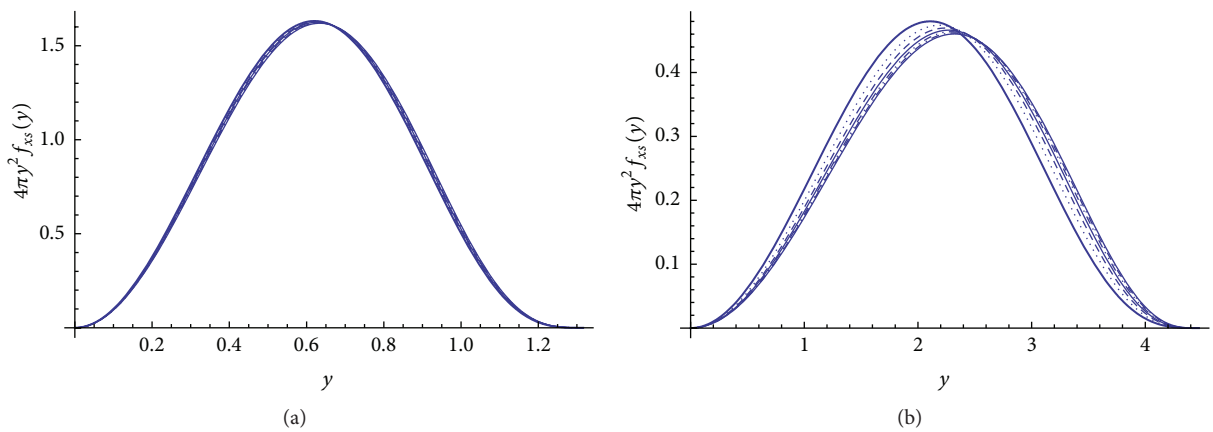

Figure 1: We show the properly normalized velocity distribution obtained in our simple model for various values of a for the value $\xi(xs) = \sqrt{3}/2$ (a) and a larger, perhaps more realistic, value $\xi(xs) = 10$ (b). The obtained velocity distribution depends mildly on a.

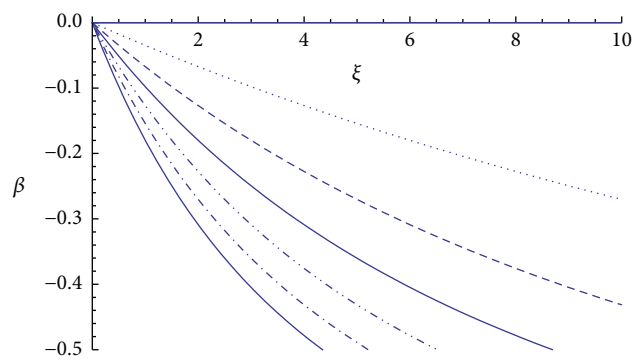

Figure 2: The asymmetry parameter $\beta = \Lambda_t/\Lambda_r$ as a function of ξ for values of $a = 0, 0.25, 0.50, 0.75, 1.0, 1.25, 1.50$ increasing downwards.

The above formula assumes that the motion of both the Sun around the Galaxy and the Earth around the Sun is uniformly circular. The exact orbits are, of course, more complicated [63, 64], but such deviations are not expected to significantly modify our results. In (36), α is the phase of the Earth ($\alpha = 0$ around June 3rd). (One could, of course, make the time dependence of the rates, due to the motion of the Earth, more explicit by writing $\alpha \approx (6/5)\pi\,(2(t/T) - 1)$, where t/T is the fraction of the year).

5.1. Standard Nondirectional Experiments. We have seen that, in the galactic frame, in the presence of asymmetry β, the relevant quantity is

$$y_x'^2 + \frac{1}{1-\beta}\left(y_y'^2 + y_z'^2\right) = \frac{1}{1-\beta}\left(y'^2 - \beta y_x'^2\right). \tag{37}$$

In the local frame, the components y_x, y_y, y_z of the velocity vector $\mathbf{y}$ are, thus, given by

$$\begin{aligned} y_r = y_x &= \frac{1}{sc}\left(y\cos\phi\sin\theta + \delta\sin\alpha\right), \\ y_t &= \sqrt{y_y^2 + y_z^2} \\ y_y &= \frac{1}{sc}\left(y\sin\theta\sin\phi - \delta\cos\alpha\cos\gamma\right), \\ y_z &= \frac{1}{sc}\left(y\cos\theta + \delta\cos\alpha\sin\gamma + 1\right), \\ y &= \frac{v}{v_0}, \end{aligned} \tag{38}$$

where s_c is a suitable scale factor to bring the WIMP velocity into units of the Sun's velocity, $y = v/v_0$; that is, $sc = \sqrt{|\Phi_0|}/v_0$. One finds

$$\begin{aligned} &\frac{1}{1-\beta}\left(y'^2 - \beta y_x'^2\right) \\ &\quad\longrightarrow Y^2 \\ &\quad= \frac{1}{sc^2}\frac{1}{1-\beta}\left(-\beta(\delta\sin(\alpha) + y\cos(\phi)\sin(\theta))^2\right. \\ &\qquad + (y\cos(\theta) + \delta\cos(\alpha)\sin(\gamma) + 1)^2 \\ &\qquad \left. +(\delta\cos(\alpha)\cos(\gamma) - y\sin(\theta)\sin(\phi))^2\right). \end{aligned} \tag{39}$$

Thus, the velocity distribution for the standard (nondirectional) case becomes

$$g_{\text{nodir}}(Y) = \frac{1}{1-\beta} f_{0,0,\infty}\left(\Phi(r_s) + \frac{1}{2}Y^2\right). \tag{40}$$

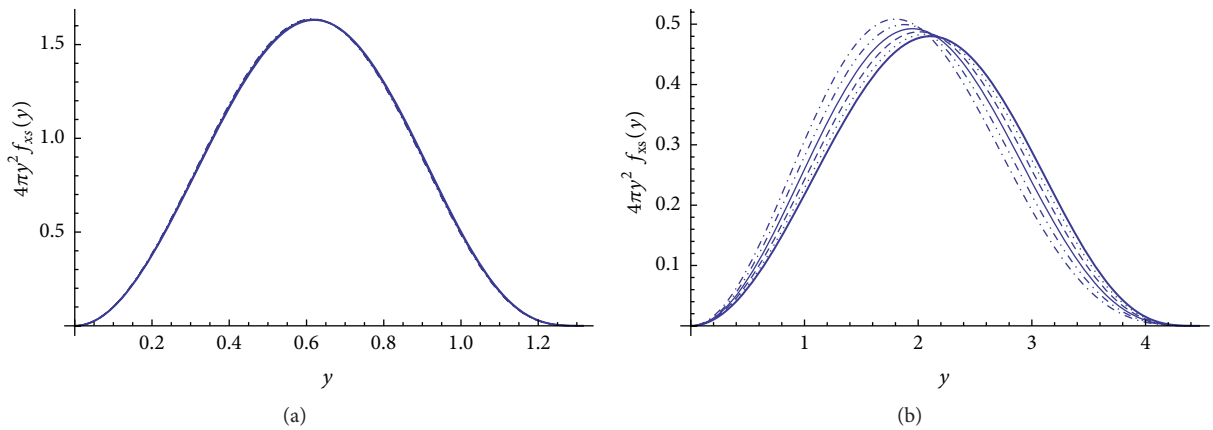

Figure 3: We show the properly normalized velocity distribution obtained in our simple model for negative values of a; that is, $a = 0, -0.1, -0.2, -0.3, -0.4, -0.5$ for the value $\xi(xs) = \sqrt{3}/2$ (a) and a larger, perhaps more realistic, value $\xi(xs) = 10$ (b). The obtained velocity distribution depends mildly on a in (a) and it is noticeable in (b). In the plots, a is increasing from left to right.

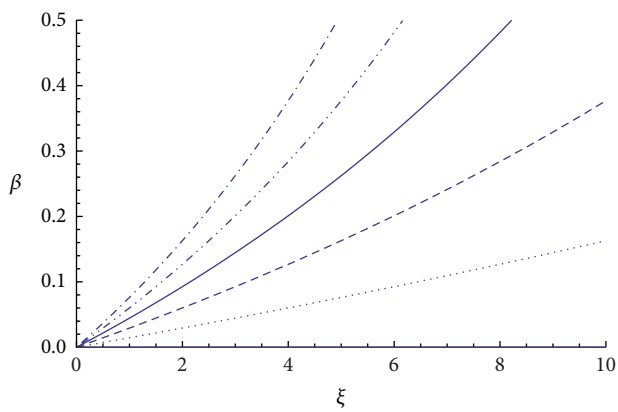

Figure 4: The asymmetry parameter $\beta = \Lambda_t/\Lambda_r$ as a function of ξ for values of a is the same as in Figure 3. In the plots, a is increasing upwards.

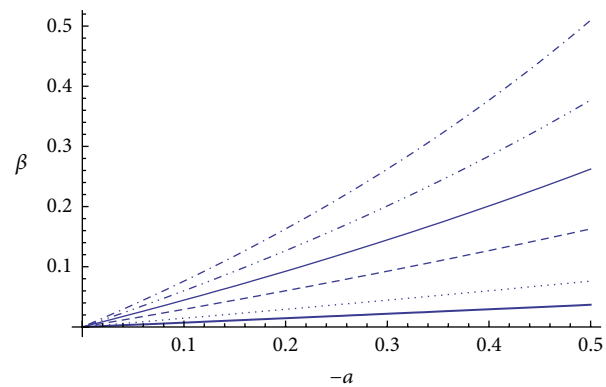

Figure 5: The asymmetry parameter $\beta = \Lambda_t/\Lambda_r$ as a function of a for values of $\xi(r_s) = (1, 2, 4, 6, 8, 10)/2$. In the plots $\xi(r_s)$ is increasing upwards. Note that, on the x-axes, the opposite of a is indicated.

5.2. Directional Experiments. In the Eddington theory the asymmetric velocity distribution is given by

$$g_{\text{dir}}(X) = \frac{1}{1-\beta} f_{0,0,\infty}\left(\Phi(r_s) + \frac{1}{2}X^2\right), \tag{41}$$

where f is the symmetric normalized velocity distribution with respect to the center of the galaxy, β is the asymmetry parameter, and X is given, [65], by

$$\begin{aligned} X^2 &= \frac{1}{(1-\beta)\, s_c^2} \\ &\quad \times \left(\sqrt{3}\delta\cos\alpha\cos\Phi - 2\sqrt{1-\xi^2}\sin\phi + 2\delta\sin\alpha\sin\Phi\right)^2 \\ &\quad - \beta\Big(2\sqrt{1-\xi^2}\cos\phi - (\delta\cos\alpha + 2)\sin\Theta \\ &\qquad + \delta\cos\Theta\left(2\cos\Phi\sin\alpha - \sqrt{3}\cos\alpha\sin\Phi\right)\Big)^2 \\ &\quad + \Big(2\xi y + (\delta\cos\alpha + 2)\cos\Theta \\ &\qquad + \delta\sin\Theta\left(2\cos\Phi\sin\alpha - \sqrt{3}\cos\alpha\sin\Phi\right)\Big)^2 \\ &\quad + \Big(-2\sqrt{1-\xi^2}\cos\phi + (\delta\cos\alpha + 2)\sin\Theta \\ &\qquad + \delta\cos\Theta\left(\sqrt{3}\cos\alpha\sin\Phi - 2\cos\Phi\sin\alpha\right)\Big)^2. \end{aligned} \tag{42}$$

The direction of the WIMP velocity is specified by $\xi = \cos\theta$ and ϕ. The direction of observation is specified by the angles Θ and Φ.

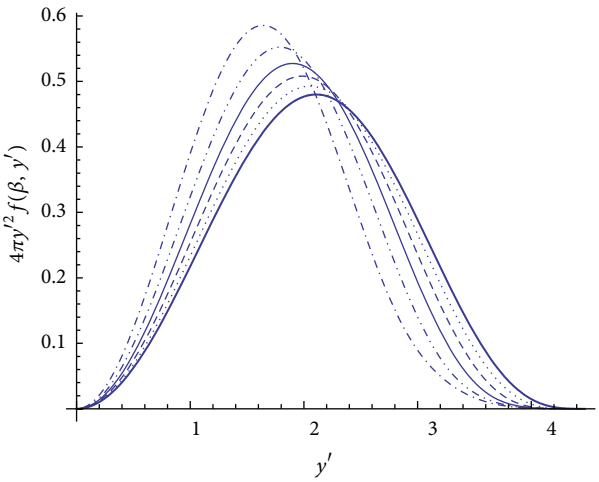

Figure 6: We show the angular average of the properly normalized velocity distribution for values of the asymmetry parameter $\beta = (0.0.1, 0.2, 0.3, 0.4, 0.5)$. In the plots, β is increasing from right to left. The results depend on the value of the potential in our vicinity. Here, the value of $\xi(xs) = 10$ was adopted.

6. Discussion and Conclusions

In the present work, we studied how one can construct the velocity distribution in the Eddington approach starting from dark matter density profiles. This is very important in the case of using this distribution for calculating the event rates expected in direct dark matter searches. First, because it allows a consistency between the velocity distribution employed and the WIMP density in our vicinity. Second, because the upper cut-off in the velocity distribution comes out of the model and is not put in by hand as is common practice. It is, therefore, interesting to generalize the Eddington approach in order to obtain asymmetric velocity distributions.

With this in mind, we have seen that, by modifying the phase space distribution function by suitable angular momentum functions $F_L(L)$, one can obtain asymmetric velocity distributions as well, with αv asymmetry parameter β, which is described in terms of the parameters specifying $F_L(L)$. We clarified some of the issues involved in this approach by considering a simple model, which can yield analytic solutions.

Results of realistic calculations for dark matter searches, employing the present technique and using realistic density profiles [13, 47, 57], will appear elsewhere [66]. We do not expect the effects of the asymmetry on the standard nondirectional rates to be very different from those obtained in a more phenomenological treatment [36], that is, negligible in the case of time averaged events and small in the case of time dependent rates (modulation effect due to the motion of the Earth). We expect, however, the effects of asymmetry to be very important in the case of directional experiments, that is, experiments measuring not only the energy but also the direction of the recoiling nucleus. Even though velocity distributions without asymmetry [65] were employed, it has been found that there is a strong dependence of the event rates on the angle of observation relative to the direction of the velocity of the Sun, for both the time averaged and the modulated events.

Appendix

Analytic Solutions of Some Integral Equations

Consider an integral equation of the following form:

$$\int_0^x f(y) K(x-y)\, dy = g(x). \tag{A.1}$$

Applying the Laplace transform on both sides, this is reduced to

$$L(f) L(K(t)) = L(g) \Longrightarrow L(f) = \frac{L(g)}{L(K(t))}. \tag{A.2}$$

The solution can be obtained if we can find a function $\widetilde{K}(t)$ such that $L(\widetilde{K}) = 1/L(K)$. This, however, cannot be done analytically except in very few cases. Some cases of interest are as follows:

(1) $K(t) = (\Gamma(1-\nu)/\Gamma(3/2-\nu))\, t^{1/2-\nu}$.

Then, one can show that

$$L\left(\frac{x^{\nu-5/2}}{\Gamma(1-\nu)\Gamma(\nu-3/2)}\right) = \left(\frac{\Gamma(1-\nu)}{\Gamma(3/2-\nu)} t^{1/2-\nu}\right)^{-1} \tag{A.3}$$

or

$$L\left(\frac{t^{-2-\nu}}{\Gamma(-1-\nu)\Gamma(1+\nu)}\right) = \frac{1}{L(t^{\nu})}. \tag{A.4}$$

Thus,

$$\begin{aligned} g(x) &= \int_0^x f(y)(x-y)^{\nu} dy \Longrightarrow \\ f(x) &= \frac{1}{\Gamma(-1-\nu)\Gamma(1+\nu)} \int_0^x (x-y)^{-2-\nu} g(y) \end{aligned} \tag{A.5}$$

or better still

$$\frac{1}{\Gamma(1+\nu)\Gamma(1-\nu)} sL(t^{-\nu})\, s = \frac{1}{L(t^{\nu})}, \quad -1 < \Re(\nu) < 1, \tag{A.6}$$

where

$$s \Longleftrightarrow \frac{d}{dt} \Longleftrightarrow L\left(\frac{du}{dt}\right) = sL(u), \quad u(0) = 0. \tag{A.7}$$

Thus,

$$\begin{aligned} g(x) &= \int_0^x f(y)(x-y)^{\nu} dy \Longrightarrow \\ f(x) &= \frac{1}{\pi} \frac{\sin \pi\nu}{\nu} \frac{d}{dx} \int_0^x (x-y)^{-\nu} \frac{dg(y)}{dy}, \quad -1 < \Re(\nu) < 1. \end{aligned} \tag{A.8}$$

(2)

$$K(t) = \sqrt{t}\left(1 + \frac{2}{3}at\right) \Longrightarrow L(K) = \sqrt{\pi}\frac{1}{2s^{5/2}}(a+s), \quad \text{(A.9)}$$

which is a special case of (19).

Then, we notice that

$$\frac{L(g)}{L(K(t))} = sL\left(\frac{2e^{-at}\operatorname{erfi}\left(\sqrt{a}\sqrt{t}\right)}{\sqrt{a}\sqrt{\pi}}\right)L\left(g''\right), \quad \text{(A.10)}$$

$$\text{if } g(0) = 0, \quad g'(0) = 0,$$

where erfi is the error function with imaginary part; that is,

$$\operatorname{erfi}(x) = -i\operatorname{erf}(ix). \quad \text{(A.11)}$$

Thus, the solution becomes

$$f(x) = \frac{d}{dx}\int_0^x \left(\frac{2e^{-a(x-y)}\operatorname{erfi}\left(\sqrt{a}\sqrt{(x-y)}\right)}{\sqrt{a}\sqrt{\pi}}\right)g''(y). \quad \text{(A.12)}$$

Thus, the solution of (19) takes the following form:

$$\tilde{f}(\epsilon) = \frac{1}{2\pi\sqrt{2\pi}}\frac{d}{d\epsilon}\int_\epsilon^0 \left(\frac{e^{-a(\xi-\epsilon)}\operatorname{erfi}\left(\sqrt{a}\sqrt{(\xi-\epsilon)}\right)}{\sqrt{a}}\right)\eta''(\xi). \quad \text{(A.13)}$$

This reduces to (8) in the limit of $a \to 0$.

Conflict of Interests

The author declares that there is no conflict of interests regarding the publication of this paper.

Acknowledgments

This research has been partially supported by the European Union Social Fund (ESF) and the Greek national funds through the program THALIS of the Hellenic Open University: Development and Applications of Novel Instrumentation and Experimental Methods in Astroparticle Physics.

References

[1] S. Hanary, "MAXIMA-1: a measurement of the cosmic microwave background anisotropy on angular scales of $10'$-5°," *The Astrophysical Journal*, vol. 545, no. 1, pp. L5–L10, 2000.

[2] J. H. P. Wu, A. Balbi, J. Borrill et al., "Tests for gaussianity of the MAXIMA-1 cosmic microwave background map," *Physical Review Letters*, vol. 87, Article ID 251303, 2001.

[3] M. G. Santos, A. Balbi, J. Borrill et al., "Estimate of the cosmological bispectrum from the MAXIMA-1 cosmic microwave background map," *Physical Review Letters*, vol. 88, Article ID 241302, 2002.

[4] P. D. Mauskopf, P. A. Ade, P. de Bernardis et al., "Measurement of a peak in the cosmic microwave background power spectrum from the North American test flight of boomerang," *The Astrophysical Journal*, vol. 536, no. 2, pp. L59–L62, 2002.

[5] S. Mosi, P. de Bernardis, G. de Troia et al., "The BOOMERanG experiment and the curvature of the universe," *Progress in Particle and Nuclear Physics*, vol. 48, no. 1, pp. 243–261, 2002.

[6] N. W. Halverson, E. M. Leitch, C. Pryke et al., "Degree angular scale interferometer first results: a measurement of the cosmic microwave background angular power spectrum," *The Astrophysical Journal*, vol. 568, no. 1, pp. 38–45, 2002.

[7] G. F. Smoot, C. L. Bennett, A. Kogut et al., "Structure in the COBE differential microwave radiometer first-year maps," *The Astrophysical Journal*, vol. 396, pp. L1–L5, 1992.

[8] A. H. Jaffe, P. A. R. Ade, A. Balbi et al., "Cosmology from MAXIMA-1, BOOMERANG, and COBE DMR cosmic microwave background observations," *Physical Review Letters*, vol. 86, no. 16, pp. 3475–3479, 2001.

[9] D. N. Spergel, L. Verde, H. V. Peiris et al., "First-year wilkinson microwave anisotropy probe (WMAP) observations: determination of cosmological parameters," *The Astrophysical Journal Supplement Series*, vol. 148, no. 1, pp. 175–194, 2003.

[10] D. Spergel, R. Bean, and O. Dore, "Three-Year Wilkinson microwave anisotropy probe (WMAP) Observations: implications for cosmology," *The Astrophysical Journal Supplement Series*, vol. 170, p. 377, 2007.

[11] P. A. R. Ade, N. Aghanim, C. Armitage-Caplan et al., "Planck 2013 results. XVI. Cosmological parameters," In press, http://arxiv.org/abs/1303.5076.

[12] D. P. Bennett, "Experimental limits on the dark matter halo of the galaxy from gravitational microlensing," *Physical Review Letters*, vol. 74, pp. 2867–2871, 1995.

[13] P. Ullio and M. Kamioknowski, "Velocity distributions and annual-modulation signatures of weakly-interacting massive particles," *Journal of High Energy Physics*, vol. 2001, no. 03, p. 049, 2001.

[14] R. Arnowitt and P. Nath, "Event rates in dark matter detectors for neutralinos including constraints from $b \to s\gamma$ decay," *Physical Review Letters*, vol. 74, no. 23, pp. 4592–4595, 1995.

[15] R. Arnowitt and P. Nath, "Predictions of neutralino dark matter event rates in minimal supergravity unification," *Physical Review D*, vol. 54, pp. 2374–2384, 1996.

[16] R. Arnowitt and P. Nath, "Annual modulation signature for the direct detection of milky way WIMP's and supergravity models," *Physical Review D*, vol. 60, no. 4, Article ID 044002, 1999.

[17] A. Bottino, V. de Alfaro, N. Fornengo, A. Morales, J. Puimedon, and S. Scopel, "Exploring the supersymmetric parameter space by direct search for WIMPs," *Physics Letters B*, vol. 402, no. 1-2, pp. 113–121, 1997.

[18] J. Ellis and R. A. Flores, "Elastic supersymmetric relic-nucleus scattering revisited," *Physics Letters B*, vol. 263, pp. 259–266, 1991.

[19] J. Ellis and R. A. Flores, "Prospects for neutralino detection with a ^{73}Ge + ^{76}Ge detector," *Physics Letters B*, vol. 300, no. 1-2, pp. 175–182, 1993.

[20] J. Ellis and R. A. Flores, "Implications of LEP on laboratory searches for dark matter neutralinos," *Nuclear Physics B*, vol. 400, pp. 25–36, 1993.

[21] J. Ellis and L. Roszkowski, "Supergravity dark matter," *Physics Letters B*, vol. 283, pp. 252–260, 1992.

[22] M. E. Gómez, G. Lazarides, and C. Pallis, "Supersymmetric cold dark matter with Yukawa unification," *Physical Review D*, vol. 61, no. 12, Article ID 123512, 2000.

[23] M. E. Gómez and J. D. Vergados, "Cold dark matter detection in SUSY models at large tanβ," *Physics Letters B*, vol. 512, no. 3-4, pp. 252–260, 2001.

[24] S. B. Gudnason, C. Kouvaris, and F. Sannino, "Dark matter from new technicolor theories," *Physical Review D*, vol. 74, Article ID 095008, 2006.

[25] S. Nussinov, "Some estimates of interaction in matter of neutral technibaryons made of colored constituents," *Physics Letters B*, vol. 279, no. 1-2, pp. 111–116, 1992.

[26] R. Foot, "Mirror & hidden sector dark matter in the light of new CoGeNT data," *Physics Letters B*, vol. 703, no. 1, pp. 7–13, 2011.

[27] R. Foot, H. Lew, and R. R. Volkas, "A model with fundamental improper spacetime symmetries," *Physics Letters B*, vol. 272, no. 1-2, pp. 67–70, 1991.

[28] V. K. Oikonomou, J. D. Vergados, and C. C. Moustakidis, "Direct detection of dark matter rates for various wimps," *Nuclear Physics B*, vol. 773, no. 1-2, pp. 19–42, 2007.

[29] G. Servant and T. M. P. Tait, "Is the lightest Kaluza-Klein particle a viable dark matter candidate?" *Nuclear Physics B*, vol. 650, no. 1-2, pp. 391–419, 2003.

[30] J. D. Vergados, "On the direct detection of dark matter," in *The Invisible Universe: Dark Matter and Dark Energy*, vol. 720 of *Lecture Notes in Physics*, pp. 69–100, Springer, Berlin, Germany, 2007.

[31] J. Collar and F. T. Avignone III, "Diurnal modulation effects in cold dark matter experiments," *Physics Letters B*, vol. 275, no. 1-2, pp. 181–185, 1992.

[32] A. K. Drukier, K. Freese, and D. N. Spergel, "Detecting cold dark-matter candidates," *Physical Review D*, vol. 33, no. 12, pp. 3495–3508, 1986.

[33] N. W. Evans, C. M. Carollo, and P. T. de Zeeuw, "Triaxial haloes and particle dark matter detection," *Monthly Notices of the Royal Astronomical Society*, vol. 318, no. 4, pp. 1131–1143, 2000.

[34] J. D. Vergados, "Modulation effect for supersymmetric dark matter detection with asymmetric velocity dispersion," *Physical Review D*, vol. 62, no. 2, Article ID 023519, 2000.

[35] C. S. Cochanek, "The mass of the milky way," *The Astrophysical Journal*, vol. 457, p. 228, 1996.

[36] J. Vergados, S. N. Hansen, and O. Host, "Impact of going beyond the Maxwell distribution in direct dark matter detection rates," *Physical Review D*, vol. 77, Article ID 023509, 2008.

[37] G. Gelmini and P. Gondolo, "Adiabatic and isocurvature perturbations from inflation: power spectra and consistency relations," *Physical Review D*, vol. 64, no. 12, Article ID 123504, 2001.

[38] A. M. Green, "Potential weakly interacting massive particle signature for the caustic ring halo model," *Physical Review D*, vol. 63, no. 10, Article ID 103003, 2001.

[39] P. Sikivie, "Caustic rings of dark matter," *Physics Letters B*, vol. 432, no. 1-2, pp. 139–144, 1998.

[40] P. Sikivie, "Caustic ring singularity," *Physical Review D*, vol. 60, no. 6, Article ID 063501, 1999.

[41] J. D. Vergados, "Searching for supersymmetric dark matter: the directional rate and the modulation effect due to caustic rings," *Physical Review D*, vol. 63, no. 6, Article ID 063511.

[42] C. Copi, J. Heo, and L. Krauss, "Directional sensitivity, WIMP detection, and the galactic halo," *Physics Letters B*, vol. 461, no. 1-2, pp. 43–48, 1999.

[43] A. M. Green, "Effect of halo modeling on weakly interacting massive particle exclusion limits," *Physical Review D*, vol. 66, no. 8, Article ID 083003, 2002.

[44] A. S. Eddington, "The distribution of stars in globular clusters," *Monthly Notices of the Royal Astronomical Society*, vol. 76, pp. 572–585, 1916.

[45] D. Merritt, "Spherical stellar systems with spheroidal velocity distributions," *The Astronomical Journal*, vol. 90, pp. 1027–1037, 1985.

[46] D. Owen and J. D. Vergados, "New velocity distribution for cold dark matter in the context of the Eddington theory," *The Astrophysical Journal*, vol. 589, no. 1, pp. 17–28, 2003.

[47] J. Vergados and D. Owen, "Direct dark matter event rates with a velocity distribution in the Eddington approach," *Physical Review D*, vol. 75, no. 4, Article ID 043503, 2007.

[48] R. Wojtak, E. L. Łokas, G. A. Mamon, S. Gottlöber, A. Klypin, and Y. Hoffman, "The distribution function of dark matter in massive haloes," *Monthly Notices of the Royal Astronomical Society*, vol. 388, no. 2, pp. 815–828, 2008.

[49] M. Fornasa and A. Green, "A self-consistent phase-space distribution function for the anisotropic dark matter halo of the milky way," *Physical Review D*, vol. 89, no. 6, Article ID 063531, 2013.

[50] P. H. Nguyen and J. F. Pedraza, "Anisotropic models for globular clusters, galactic bulges, and dark halos," *Physical Review D*, vol. 88, no. 6, Article ID 064020, 2013.

[51] C. A. Agón, J. F. Pedraza, and J. Ramos-Caro, "Kinetic theory of collisionless self-gravitating gases: post-newtonian polytropes," *Physical Review D*, vol. 83, no. 12, Article ID 123007, 2011.

[52] N. Bozorgnia, R. Catena, and T. Schwetz, "Anisotropic dark matter distribution functions and impact on WIMP direct detection," *Journal of Cosmology and Astroparticle Physics*, vol. 2013, no. 12, article 050, 2013.

[53] D. Hunter, "Derivation of the anisotropy profile, constraints on the local velocity dispersion, and implications for direct detection," *Journal of Cosmology and Astroparticle Physics*, vol. 2014, no. 02, article 023, 2014.

[54] H. C. Plummer, "On the problem of distribution in globular star clusters," *Monthly Notices of the Royal Astronomical Society*, vol. 71, pp. 460–470, 1911.

[55] A. Natarajan, C. Savage, and K. Freese, "Probing dark matter streams with CoGeNT," *Physical Review D*, vol. 84, no. 10, Article ID 103005, 2011.

[56] M. Kuhlen, M. Lisanti, and D. Speregel, "Direct detection of dark matter debris flows," *Physical Review D*, vol. 86, no. 6, Article ID 063505, 2002.

[57] J. F. Navarro, C. S. Frenk, and S. D. M. White, "The structure of cold dark matter halos," *Astrophysical Journal Letters*, vol. 462, no. 2, pp. 563–575, 1996.

[58] J. Binney and S. Tremain, *Galactic Dynamics*, Princeton University Press, Princeton, NJ, USA, 2008.

[59] D. Merritt, "Distribution functions for spherical galaxies," *Monthly Notices of the Royal Astronomical Society*, vol. 214, no. 1, pp. 25P–28P, 1985.

[60] L. Osipkov, " Spherical systems of gravitating bodies with an ellipsoidal velocity distribution," *Soviet Astronomy Letters*, vol. 5, pp. 42–44, 1979.

[61] S. H. Hansen, B. Moore, M. Zemp, and J. Stadel, "A universal velocity distribution of relaxed collisionless structures," *Journal of Cosmology and Astroparticle Physics*, vol. 2006, no. 01, article 014, 2006.

[62] J. D. Vergados, "Debris flows in direct dark matter searches: the modulation effect," *Physical Review D*, vol. 85, no. 12, Article ID 123502, 2012.

[63] A. Green, "Effect of realistic astrophysical inputs on the phase and shape of the weakly interacting massive particles annual modulation signal," *Physical Review D*, vol. 68, Article ID 023004, 2003.

[64] A. Green, "Erratum in: effect of realistic astrophysical inputs on the phase and shape of the weakly interacting massive particles annual modulation signal, *Physical Review D*, vol. 68, Article ID 023004, 2003," *Physical Review D*, vol. 69, Article ID 109902, 2004.

[65] J. D. Vergados and C. C. Moustakidis, "WIMP event rates in directional experiments: the diurnal variation signature," *Central European Journal of Physics*, vol. 9, no. 3, pp. 628–643, 2011.

[66] C. C. Moustakidis, D. Owen, and J. Vergados, "Realistic asymmetric velocity distributions obtained in Eddington approach and their application to to dark matter searches.," to be published, 2014.

Hindawi Publishing Corporation
Advances in High Energy Physics
Volume 2015, Article ID 763648, 17 pages
http://dx.doi.org/10.1155/2015/763648

Research Article

Standard and Nonstandard Neutrino-Nucleus Reactions Cross Sections and Event Rates to Neutrino Detection Experiments

D. K. Papoulias and T. S. Kosmas

Division of Theoretical Physics, University of Ioannina, 45100 Ioannina, Greece

Correspondence should be addressed to D. K. Papoulias; dimpap@cc.uoi.gr

Received 11 July 2014; Accepted 3 November 2014

Academic Editor: Athanasios Hatzikoutelis

In this work, we explore ν-nucleus processes from a nuclear theory point of view and obtain results with high confidence level based on accurate nuclear structure cross sections calculations. Besides cross sections, the present study includes simulated signals expected to be recorded by nuclear detectors and differential event rates as well as total number of events predicted to be measured. Our original cross sections calculations are focused on measurable rates for the standard model process, but we also perform calculations for various channels of the nonstandard neutrino-nucleus reactions and come out with promising results within the current upper limits of the corresponding exotic parameters. We concentrate on the possibility of detecting (i) supernova neutrinos by using massive detectors like those of the GERDA and SuperCDMS dark matter experiments and (ii) laboratory neutrinos produced near the spallation neutron source facilities (at Oak Ridge National Lab) by the COHERENT experiment. Our nuclear calculations take advantage of the relevant experimental sensitivity and employ the severe bounds extracted for the exotic parameters entering the Lagrangians of various particle physics models and specifically those resulting from the charged lepton flavour violating $\mu^- \to e^-$ experiments (Mu2e and COMET experiments).

1. Introduction

Coherent scattering of neutrinos on complex nuclei was proposed long ago [1, 2] as a prominent probe to study neutral-current (NC) ν-nucleus processes, but up to now no events have been experimentally measured. Neutrino detection constitutes an excellent probe to search for a plethora of conventional neutrino physics applications and new-physics open issues [3–5]. In principle, low-energy astrophysical and laboratory neutrino searches provide crucial information towards understanding the underling physics of the fundamental electroweak interactions within and beyond the SM [6, 7]. Well-known neutrino sources include (i) supernova neutrinos (with energies up to 60–100 MeV) and (ii) laboratory neutrinos (with energies up to 52.8 MeV) emerging from stopped-pion and muon decays at muon factories (Fermilab, PSI, JPARC, etc.) and at the spallation neutron source (SNS) at Oak Ridge National Lab [8]. Recently, it became feasible [9] to detect neutrinos by exploiting the neutral current interactions and measuring the nuclear recoil signals through the use of very low threshold-energy detectors [10, 11]. To this purpose, great experimental effort has been put and new experiments have been proposed to be performed at facilities with stopped-pion neutrino beams, based on promising nuclear detectors like those of the COHERENT experiment [12, 13] and others [14] at the SNS, or alternative setups at the Booster Neutrino Beam (BNB) at Fermilab [15, 16]. The nuclear ν-detectors adopted by the relevant experiments include liquid noble gases, such as ^{20}Ne, ^{40}Ar, and ^{132}Xe, as well as ^{76}Ge and CsI[Na] detection materials [17].

On the theoretical side, the ν-signals of low-energy neutrinos, expected to be recorded in sensitive nuclear detectors [18–20], could be simulated through nuclear calculations of ν-nucleus scattering cross sections. Such results may provide useful information relevant for the evolution of distant stars, the core collapse supernovae, explosive nucleosynthesis, and other phenomena [21, 22]. In fact, coherent neutral current ν-nucleus scattering events are expected to be observed by using the high intensity stopped-pion neutrino beams

[23, 24] and nuclear targets for which recoil energies are of the order of a few to tens of keV and therefore appropriate for detection of WIMPs [25, 26], candidates of cold dark matter [27–29]. Such detectors are, for example, the SuperCDMS [30], GERDA [31], and other multipurpose detectors [32–34]. For low energies, the dominant vector components of NC interactions lead to a coherent contribution of all nucleons (actually all neutrons) in the target nucleus [35–37].

It is worth mentioning that, after the discovery [38–42] of neutrino oscillations in propagation, the challenge of neutral and charged lepton flavour violation (LFV) is further investigated by extremely sensitive experiments [43–49] searching for physics beyond the current standard model (SM) [50]. To this end, neutrino-nucleus coherent scattering experiments may probe new physics beyond the SM involved in exotic neutrino-nucleus interactions [9, 51–53], an undoubtable signature of nonstandard physics. Therefore, new data and insights will be provided to the physics of flavour changing neutral-current (FCNC) processes, in the leptonic sector, in nonstandard neutrino oscillation effects [54–56], in neutrino transition magnetic moments [57], in sterile neutrino search [58], and others [59]. Furthermore, such experimental sensitivity may also inspire advantageous probes to shed light on various open issues in nuclear astrophysics [60, 61].

In recent works [53], neutral-current (NC) nonstandard interactions (NSI) involving (anti)neutrino scattering processes on leptons, nucleons, and nuclei have been investigated. The reactions of this type that take place in nuclei are represented by

$$\nu_\alpha\left(\tilde{\nu}_\alpha\right) + (A, Z) \longrightarrow \nu_\beta\left(\tilde{\nu}_\beta\right) + (A, Z) \tag{1}$$

($\alpha, \beta = e, \mu, \tau$ with $\alpha \neq \beta$). It has been suggested [62] that, theoretically, the latter processes can be studied with the same nuclear methods as the exotic cLFV process of $\mu^- \rightarrow e^-$ conversion in nuclei [63–66]. The corresponding Lagrangians may be derived within the context of various extensions of the SM [6, 7, 67], like the four-fermion contact interaction, seesaw model [68, 69], left-right symmetric models [70], gluonic operator model [71], and so forth.

It is well known that neutrino NSI may have rather significant impact in many areas of modern physics research and thus motivate a great number of similar studies [72]. Particularly in astrophysical applications, constraints coming out of some supernova explosion scenarios [73–75] may be affected and eventually lead to the necessity of further investigation of NSI in both LFV and cLFV processes that may occur in solar and supernova environment [76–80]. Such open issues motivated our present work too.

One of our main purposes in this paper, which is an extension of our previous study [53], is to comprehensively study the above issues by performing nuclear structure calculations for a set of experimentally interesting nuclei. We estimate reliably the nuclear matrix elements describing both interaction channels, the exotic and the standard model ones, but we mainly focus on the SM component of the neutrino-nucleus processes; that is, we consider $\alpha = \beta$ in the reactions of (1). Exotic neutrino-nucleus events are also computed. By exploiting our accurate original cross sections, we obtain simulated ν-signals and flux averaged cross sections which are experimentally interesting quantities for both supernova and SNS neutrinos. The total number of events expected to be recorded over the energy threshold for the studied nuclear targets is also presented for both cases.

We stress the fact that we have devoted special effort to obtain results of high accuracy by constructing the nuclear ground state within the context of the quasiparticle random phase approximation (QRPA), that is, by solving iteratively the BCS equations for realistic pairing interactions (the Bonn C-D potential) [81–83], and achieving high reproducibility of the available experimental data [84]. In addition, we made comparisons with the results of other methods evaluating the nuclear form factors that enter the coherent rate [85, 86] as the one which employs fractional occupation probabilities (FOP) of the states (on the basis of analytic expressions) [87] and other well-known methods [88].

2. Description of the Formalism

In this section, we present briefly the necessary formalism for describing all channels of the NSI processes of the reactions (1), derived by starting from the corresponding nuclear-level Feynman diagrams.

In Figure 1, the exchange of a Z-boson between a lepton and a nucleon is represented, for the SM ν-nucleus scattering, Figure 1(a), and for the exotic ν-nucleus scattering, Figure 1(b). As already mentioned in the Introduction, the nonstandard ν-nucleus processes [53] and the exotic cLFV $\mu^- \rightarrow e^-$ conversion in nuclei [50, 63, 76, 77, 79, 80] can be predicted within the context of the same new-physics models [62, 68]. For this reason, in Figure 1(c), we also show the exchange of a Z-boson or a virtual γ-photon leading to the nuclear $\mu^- \rightarrow e^-$ conversion [64, 68]. Thus, the leptonic vertex in the cases of Figures 1(b) and 1(c) is a complicated one. A general effective Lagrangian that involves SM interactions ($\mathscr{L}_{\mathrm{SM}}$) and NSI ($\mathscr{L}_{\mathrm{NSI}}$) with a nonstandard flavour preserving (FP) term, a nonuniversal (NU) term, and a flavour changing (FC) term reads

$$\mathscr{L}_{\mathrm{tot}} = \mathscr{L}_{\mathrm{SM}} + \mathscr{L}_{\mathrm{NSI}} = \mathscr{L}_{\mathrm{SM}} + \mathscr{L}_{\mathrm{NU}} + \mathscr{L}_{\mathrm{FC}}. \tag{2}$$

Each of the components $\mathscr{L}_{\mathrm{SM}}$ and $\mathscr{L}_{\mathrm{NSI}}$, the individual terms $\mathscr{L}_{\mathrm{NU}}$ and $\mathscr{L}_{\mathrm{FC}}$, and the nuclear matrix elements that arise from each part are discussed below.

2.1. Coherent Cross Sections of Nonstandard ν-Nucleus Reactions. The quark-level Lagrangian for neutral current nonstandard neutrino interactions $\mathscr{L}_{\mathrm{NSI}}$, at the four-fermion approximation (energies $\ll M_Z$), is parametrized as [9, 52, 73]

$$\mathscr{L}_{\mathrm{NSI}} = -2\sqrt{2}G_F \sum_{\substack{f=u,d \\ \alpha,\beta=e,\mu,\tau}} \epsilon_{\alpha\beta}^{fP}\left[\overline{\nu}_\alpha \gamma_\rho L \nu_\beta\right]\left[\overline{f}\gamma^\rho P f\right], \tag{3}$$

where f denotes a first generation SM quark, ν_α are three light neutrinos with Majorana masses, and $P = \{L, R\}$ are the chiral projectors. In the latter Lagrangian (3), two classes of

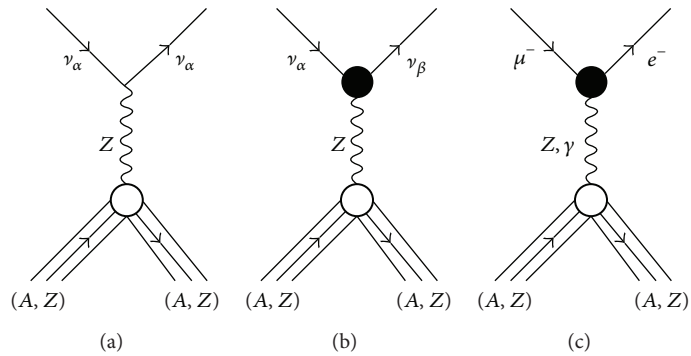

Figure 1: Nuclear level Feynman diagrams for (a) SM Z-exchange neutral-current ν-nucleus reactions, (b) nonstandard Z-exchange ν-nucleus reactions, and (c) Z-exchange and photon-exchange $\mu^- \to e^-$ in the presence of a nucleus (muon-to-electron conversion). The nonstandard (cLFV or LFV) physics enters in the complicated vertex denoted by the bullet • [53].

nonstandard terms are considered (i) flavour preserving non-SM terms that are proportional to $\epsilon_{\alpha\alpha}^{fP}$ (known as nonuniversal, NU interactions) and (ii) flavour changing (FC) terms proportional to $\epsilon_{\alpha\beta}^{fP}$, $\alpha \neq \beta$. These couplings are defined with respect to the strength of the Fermi coupling constant G_F [52, 73]. In the present work, we examine spin-zero nuclei; thus, the polar-vector couplings defined as $\epsilon_{\alpha\beta}^{fV} = \epsilon_{\alpha\beta}^{fL} + \epsilon_{\alpha\beta}^{fR}$ are mainly of interest. For the axial-vector couplings it holds $\epsilon_{\alpha\beta}^{fA} = \epsilon_{\alpha\beta}^{fL} - \epsilon_{\alpha\beta}^{fR}$.

Following [79, 80], the nuclear physics aspects of the neutrino-matter NSI can be explored by transforming the quark-level Lagrangian (3) eventually to the nuclear level where the hadronic current is written in terms of NC nucleon form factors that are functions of the four-momentum transfer. Generally, for inelastic ν-nucleus scattering, the magnitude of the three-momentum transfer, $q = |\vec{q}|$, is a function of the scattering angle of the outgoing neutrino θ (in laboratory frame) and the initial, E_i, and final, E_f, nuclear energies, as well as the excitation energy of the target nucleus, ω, and takes the form $q^2 = \omega^2 + 2E_iE_f(1-\cos\theta)$ [81, 85]. Our analysis in the present paper concentrates on the dominant coherent (elastic) channel where only $gs \to gs$ transitions occur ($\omega = 0$, $E_i = E_f$) and the momentum transfer in terms of the incoming neutrino energy, E_ν, becomes $q^2 = 2E_\nu^2(1-\cos\theta)$ or equivalently $q = 2E_\nu \sin(\theta/2)$.

The NSI coherent differential cross section of neutrinos scattering off a spin-zero nucleus, with respect to the scattering angle θ, reads [53]

$$\frac{d\sigma_{\mathrm{NSI},\nu_\alpha}}{d\cos\theta} = \frac{G_F^2}{2\pi} E_\nu^2 (1+\cos\theta) \left|\langle gs| \left|G_{V,\nu_\alpha}^{\mathrm{NSI}}(q)\right| |gs\rangle\right|^2, \quad (4)$$

where $\alpha = e, \mu, \tau$ denotes the flavour of incident neutrinos and $|gs\rangle$ represents the nuclear ground state (for even-even nuclei assumed here, $|gs\rangle = |J^\pi\rangle \equiv |0^+\rangle$). The nuclear matrix element, which enters the cross section of (4), is written as [53]

$$\begin{aligned}
&\left|\mathscr{M}_{V,\nu_\alpha}^{\mathrm{NSI}}\right|^2 \\
&\quad \equiv \left|\langle gs| \left|G_{V,\nu_\alpha}^{\mathrm{NSI}}(q)\right| |gs\rangle\right|^2 \\
&\quad = \left[\left(2\epsilon_{\alpha\alpha}^{uV} + \epsilon_{\alpha\alpha}^{dV}\right) ZF_Z\left(q^2\right) + \left(\epsilon_{\alpha\alpha}^{uV} + 2\epsilon_{\alpha\alpha}^{dV}\right) NF_N\left(q^2\right)\right]^2 \\
&\qquad + \sum_{\beta\neq\alpha} \left[\left(2\epsilon_{\alpha\beta}^{uV} + \epsilon_{\alpha\beta}^{dV}\right) ZF_Z\left(q^2\right) + \left(\epsilon_{\alpha\beta}^{uV} + 2\epsilon_{\alpha\beta}^{dV}\right) NF_N\left(q^2\right)\right]^2
\end{aligned} \quad (5)$$

($\beta = e, \mu, \tau$) where $F_{Z(N)}$ denote the nuclear (electromagnetic) form factors for protons (neutrons). We stress the fact that, in the adopted NSI model, the coherent NC ν-nucleus cross section is not flavour blind as in the SM case. Obviously, by incorporating the nuclear structure details, in (4) and (5), the cross sections become more realistic and accurate [9]. The structure of the Lagrangian (2) implies that in the right-hand side of (5) the first term is the NU matrix element, $\mathscr{M}_{V,\nu_\alpha}^{\mathrm{NU}}$, and the summation is the FC matrix element, $\mathscr{M}_{V,\nu_\alpha}^{\mathrm{NU}}$; hence we write

$$\left|\mathscr{M}_{V,\nu_\alpha}^{\mathrm{NSI}}\right|^2 = \left|\mathscr{M}_{V,\nu_\alpha}^{\mathrm{NU}}\right|^2 + \left|\mathscr{M}_{V,\nu_\alpha}^{\mathrm{FC}}\right|^2. \quad (6)$$

From experimental physics perspectives, it is rather crucial to express the differential cross section with respect to the recoil energy of the nuclear target, T_N. In recent years, it became feasible for terrestrial neutrino detectors to detect neutrino events by measuring nuclear recoil [16, 17]. Therefore, it is important to compute also the differential cross sections $d\sigma/dT_N$. In the coherent process, the nucleus recoils (intrinsically it remains unchanged) with energy which, in the approximation $T_N \ll E_\nu$, takes the maximum value $T_N^{\max} = 2E_\nu^2/(M + 2E_\nu)$, with M denoting the nuclear mass [36, 37]. Then, to a good approximation, the square of the three-momentum transfer is equal to $q^2 = 2MT_N$, and the coherent NSI differential cross section with respect to T_N can be cast in the form

$$\frac{d\sigma_{\mathrm{NSI},\nu_\alpha}}{dT_N} = \frac{G_F^2 M}{\pi}\left(1 - \frac{MT_N}{2E_\nu^2}\right) \left|\langle gs| \left|G_{V,\nu_\alpha}^{\mathrm{NSI}}(q)\right| |gs\rangle\right|^2. \quad (7)$$

We note that, compared to previous studies [60, 72], we have also taken into consideration the interaction ν-u quark (see (5)), in addition to the momentum dependence of the nuclear

form factors [53]. Both (4) and (7) are useful for studying the nuclear physics of NSI of neutrinos with matter.

Furthermore, by performing numerical integrations to (4) over the scattering angle θ or to (7) over the recoil energy T_N, one can obtain integrated (total) coherent NSI cross sections, $\sigma_{\mathrm{NSI},\nu_\alpha}$. Following (6), the individual cross sections $\sigma_{\mathrm{NU},\nu_\alpha}$ and $\sigma_{\mathrm{FC},\nu_\alpha}$ may be evaluated accordingly.

2.2. Standard Model Coherent ν-Nucleus Cross Sections. The effective (quark-level) SM ν-nucleus interaction Lagrangian, $\mathscr{L}_{\mathrm{SM}}$, at low and intermediate neutrino energies, is written as

$$\mathscr{L}_{\mathrm{SM}} = -2\sqrt{2}G_F \sum_{\substack{f=u,d\\ \alpha=e,\mu,\tau}} g_P^f \left[\overline{\nu}_\alpha \gamma_\rho L \nu_\alpha\right]\left[\overline{f}\gamma^\rho P f\right], \tag{8}$$

where $g_L^u = 1/2 - (2/3)\sin^2\theta_W$ and $g_R^u = -(2/3)\sin^2\theta_W$ are the left- and right-handed couplings of the u-quark to the Z-boson and $g_L^d = -1/2 + (1/3)\sin^2\theta_W$ and $g_R^d = (1/3)\sin^2\theta_W$ are the corresponding couplings of the d-quark (θ_W is the Weinberg mixing angle) [85].

For coherent ν-nucleus scattering, the SM angle-differential cross section reads

$$\frac{d\sigma_{\mathrm{SM},\nu_\alpha}}{d\cos\theta} = \frac{G_F^2}{2\pi} E_\nu^2 (1+\cos\theta) \left|\langle gs| \left|\widehat{\mathscr{M}}_0(q)\right| |gs\rangle\right|^2. \tag{9}$$

The operator $\widehat{\mathscr{M}}_0$ in the nuclear matrix element of the latter equation is the Coulomb operator which is equal to the product of the zero-order spherical Bessel function times the zero-order spherical harmonic [81, 85]. This matrix element can be cast in the form [78]

$$\begin{aligned}\left|\mathscr{M}_{V,\nu_\alpha}^{\mathrm{SM}}\right|^2 &\equiv \left|\langle gs| \left|\widehat{\mathscr{M}}_0(q)\right| |gs\rangle\right|^2 \\ &= \left[g_V^p Z F_Z\left(q^2\right) + g_V^n N F_N\left(q^2\right)\right]^2,\end{aligned} \tag{10}$$

where the polar-vector couplings of protons g_V^p and neutrons g_V^n with the Z-boson (see Figure 1(a)) are written as $g_V^p = 2(g_L^u + g_R^u) + (g_L^d + g_R^d) = 1/2 - 2\sin^2\theta_W$ and $g_V^n = (g_L^u + g_R^u) + 2(g_L^d + g_R^d) = -1/2$, respectively. As can be easily seen, the vector contribution of all protons is very small ($g_V^p \sim 0.04$); hence, the coherence in (10) essentially refers to all neutrons only of the studied nucleus. After some straightforward elaboration, the differential cross section with respect to the nuclear recoil energy, T_N, takes the form

$$\frac{d\sigma_{\mathrm{SM},\nu_\alpha}}{dT_N} = \frac{G_F^2 M}{\pi}\left(1 - \frac{MT_N}{2E_\nu^2}\right)\left|\langle gs| \left|\widehat{\mathscr{M}}_0(q)\right| |gs\rangle\right|^2. \tag{11}$$

The Lagrangian $\mathscr{L}_{\mathrm{tot}}$ of (2) contains the flavour preserving (FP) part, equal to $\mathscr{L}_{\mathrm{FP}} \equiv \mathscr{L}_{\mathrm{NU}} + \mathscr{L}_{\mathrm{SM}}$, which can be evaluated through the Coulomb matrix element

$$\left|\mathscr{M}_{V,\nu_\alpha}^{\mathrm{FP}}\right|^2 = \left|\mathscr{M}_{V,\nu_\alpha}^{\mathrm{SM}} + \mathscr{M}_{V,\nu_\alpha}^{\mathrm{NU}}\right|^2. \tag{12}$$

Subsequently, the total coherent cross section may be computed on the basis of the matrix element

$$\left|\mathscr{M}_{V,\nu_\alpha}^{\mathrm{tot}}\right|^2 = \left|\mathscr{M}_V^{\mathrm{FP}}\right|^2 + \left|\mathscr{M}_{V,\nu_\alpha}^{\mathrm{FC}}\right|^2. \tag{13}$$

In a previous work [53], we evaluated original differential cross sections $d\sigma_{\lambda,\nu_\alpha}/d\cos\theta$ and $d\sigma_{\lambda,\nu_\alpha}/dT_N$, as well as individual angle-integrated cross sections of the form $\sigma_{\lambda,\nu_\alpha}(E_\nu)$, with $\alpha = e,\mu,\tau$ and $\lambda = \mathrm{SM}, \mathrm{NU}, \mathrm{FP}, \mathrm{FC}$ (FC stands for the six flavour changing processes $\nu_e \leftrightarrow \nu_\mu, \nu_e \leftrightarrow \nu_\tau, \nu_\mu \leftrightarrow \nu_\tau$).

In this work, we perform standard model cross sections calculations (for convenience, from now on, we drop the index $\lambda = \mathrm{SM}$ and always consider $\nu_\alpha = \nu_\beta$) for a set of nuclei throughout the periodic table up to ^{208}Pb. We adopt various nuclear models (see Section 3) to compute the nuclear form factors. Then, for a great part of the cross section results (except differential cross sections), we evaluate folded cross sections and event rates.

3. Evaluation of the Nuclear Form Factors

3.1. Nuclear Structure Calculations. At first, we study the nuclear structure details of the matrix elements entering (10); such results reflect the dependence of the coherent cross section on the incident-neutrino energy E_ν and the scattering angle θ (or the recoil energy T_N). We mention that for the even-even nuclei this study involves realistic QRPA calculations for the differential cross sections $d\sigma_{\nu_\alpha}/d\cos\theta$ and $d\sigma_{\nu_\alpha}/dT_N$, performed after constructing the nuclear ground state $|gs\rangle$ by solving iteratively the Bardeen Cooper Schrieffer (BCS) equations. The solution of these equations provides the probability amplitudes $v_{N_n}^j$ and $v_{N_n}^j$ of the jth single nucleon level to be occupied or unoccupied, respectively. Moreover, the latter equations provide the single quasiparticle energies, based on the single particle energies of the nuclear field (a Coulomb corrected Woods-Saxon potential in our case) as well as the pairing part of the residual two-body interaction (Bonn C-D potential in our case). Then, the nuclear form factors for protons (neutrons) are obtained as [78]

$$F_{N_n}\left(q^2\right) = \frac{1}{N_n}\sum_j [j] \langle j|j_0(qr)|j\rangle \left(v_{N_n}^j\right)^2, \tag{14}$$

with $[j] = \sqrt{2j+1}$, $N_n = Z$ (or N). For each nuclear system studied, the chosen active model space, the harmonic oscillator (h.o.) parameter b, and the values of the two parameters $g_{\mathrm{pair}}^{p(n)}$ for proton (neutron) pairs that renormalise the monopole (pairing) residual interaction (obtained from the Bonn C-D two-body potential describing the strong two-nucleon forces) are presented in Table 1. The adjustment of $g_{\mathrm{pair}}^{p(n)}$ is achieved through the reproducibility of the pairing gaps $\Delta_{p(n)}$ (see, e.g., [22]).

3.2. Other Methods for Obtaining the Nuclear Form Factors. The nuclear form factor, which is the Fourier transform of the nuclear charge density distribution $\rho_p(r)$, is defined as

$$F_Z\left(q^2\right) = \frac{4\pi}{Z}\int \rho_p(r)\, j_0(qr)\, r^2 dr, \tag{15}$$

with j_0 being the zero-order spherical Bessel function. Due to the significance of the nuclear form factors in our calculations

Table 1: The values of proton g^p_{pair} and neutron g^n_{pair} pairs that renormalise the residual interaction and reproduce the respective empirical pairing gaps Δ_p and Δ_n. The active model space and the harmonic oscillator parameter, for each isotope, are also presented.

Nucleus	Model-space	b	Δ_p	Δ_n	g^p_{pair}	g^n_{pair}
^{12}C	8 (no core)	1.522	4.68536	4.84431	1.12890	1.19648
^{16}O	8 (no core)	1.675	3.36181	3.49040	1.06981	1.13636
^{20}Ne	10 (no core)	1.727	3.81516	3.83313	1.15397	1.27600
^{28}Si	10 (no core)	1.809	3.03777	3.14277	1.15568	1.23135
^{40}Ar	15 (no core)	1.902	1.75518	1.76002	0.94388	1.01348
^{48}Ti	15 (no core)	1.952	1.91109	1.55733	1.05640	0.99890
^{76}Ge	15 (no core)	2.086	1.52130	1.56935	0.95166	1.17774
^{132}Xe	15 (core ^{40}Ca)	2.262	1.19766	1.20823	0.98207	1.13370

and for the benefit of the reader, we devote a separate discussion to summarise some useful possibilities of obtaining these observables.

3.2.1. Use of Available Experimental Data. For many nuclei and especially for odd-A isotopes, the proton nuclear form factors $F_Z(q^2)$ are computed by means of a model independent analysis (using a Fourier-Bessel expansion model or others) of the electron scattering data for the proton charge density $\rho_p(r)$ [84] wherever possible. The absence of similar data for neutron densities restricts us from assuming that $F_N(q^2) = F_Z(q^2)$. In this work, we consider this method only for the case of the very heavy doubly closed ^{208}Pb nucleus.

3.2.2. Fractional Occupation Probabilities in a Simple Shell-Model. In [87], the form factor $F_Z(q^2)$, for h.o. wavefunctions, has been written as [76, 77]

$$F_Z\left(q^2\right) = \frac{1}{Z} e^{-(qb)^2/4} \Phi\left(qb, Z\right),$$
$$\Phi\left(qb, Z\right) = \sum_{\lambda=0}^{N_{\max}} \theta_\lambda \left(qb\right)^{2\lambda}. \tag{16}$$

The radial nuclear charge density distribution $\rho_p(r)$, entering the definition of (15), is written in the following compact form [76, 77]:

$$\rho_p\left(r\right) = \frac{1}{\pi^{3/2} b^3} e^{-(r/b)^2} \Pi\left(\frac{r}{b}, Z\right), \qquad \Pi\left(\chi, Z\right) = \sum_{\lambda=0}^{N_{\max}} f_\lambda \chi^{2\lambda}, \tag{17}$$

where $\chi = r/b$, with b denoting the h.o. size parameter. $N_{\max} = (2n + \ell)_{\max}$ stands for the number of quanta of the highest occupied proton (neutron) level. The coefficients f_λ are expressed as

$$f_\lambda = \sum_{(n,\ell)j} \frac{\pi^{1/2} \left(2j+1\right) n! C^{\lambda-\ell}_{n\ell}}{2\Gamma\left(n + \ell + 3/2\right)}, \tag{18}$$

where $\Gamma(x)$ is the Gamma function. For the coefficients θ_λ, $C^{\lambda-\ell}_{n\ell}$ and further information, see [76, 77].

Up to this point, the proton occupation probabilities entering (15) and (16) have been considered equal to unity for the states below the Fermi surface and zero for those above the Fermi surface. In [87], the authors introduced depletion and occupation numbers, to parametrise the partially occupied levels of the states. These parameters satisfy the relation

$$\sum_{\substack{(n\ell)j \\ \text{all}}} \alpha_{n\ell j} \left(2j+1\right) = N_n. \tag{19}$$

Within this context, the "active" surface nucleons (above or below the Fermi level) have nonzero occupation probability $\alpha_{n\ell j} \neq 0$, smaller than unity, while the "core" levels have occupation probability $\alpha_{n\ell j} = 1$. In this paper, we extend the work of [87] where three parameters α_1, α_2, and α_3 are used to describe the partial occupation probabilities of the surface orbits. We improve the formalism by introducing more parameters, increasing this way the number of "active" nucleons in the studied nuclear system, and come out with higher reproducibility of the experimental data [84]. To this aim, we introduce four parameters α_i, $i = 1, 2, 3, 4$, in (19). Then, the assumed "active" single-particle levels are five and (16) of [87] becomes

$$\begin{aligned}
&\Pi\left(\chi, Z, \alpha_i\right) \\
&\quad = \Pi\left(\chi, Z_2\right) \frac{\alpha_1}{Z_1 - Z_2} + \Pi\left(\chi, Z_1\right) \left[\frac{\alpha_2}{Z_c - Z_1} - \frac{\alpha_1}{Z_1 - Z_2}\right] \\
&\qquad + \Pi\left(\chi, Z_c\right) \left[\frac{Z' - Z}{Z' - Z_c} - \frac{\alpha_2}{Z_c - Z_1} - \frac{\alpha_3}{Z' - Z_c}\right] \\
&\qquad + \Pi\left(\chi, Z'\right) \left[\frac{Z - Z_c}{Z' - Z_c} + \frac{\alpha_3}{Z' - Z_c} - \frac{\alpha_4}{Z'' - Z'}\right] \\
&\qquad + \Pi\left(\chi, Z''\right) \left[\frac{\alpha_4}{Z'' - Z'} - \frac{\lambda}{Z''' - Z''}\right] \\
&\qquad + \Pi\left(\chi, Z'''\right) \frac{\lambda}{Z''' - Z''},
\end{aligned} \tag{20}$$

with $\lambda = \alpha_1 + \alpha_2 - \alpha_3 - \alpha_4$. By substituting the polynomial $\Pi(\chi, Z)$ of (17) with that of the latter expression and using the experimental data [84], we fit the parameters α_i (and similarly for the form factor of (16)). As an example, for the ^{40}Ar isotope we have, $Z_2 = 10$, $Z_1 = 12$, $Z = Z_c = 18$,

$Z' = 20$, $Z'' = 22$, and $Z''' = 30$. The resulting fractional occupation probabilities that fit the experimental charge density distribution are $\alpha_1 = 0.85$, $\alpha_2 = 1.25$, $\alpha_3 = 0.85$, and $\alpha_4 = 0.75$. Similarly for the ^{48}Ti nucleus, we have $Z_2 = 18$, $Z_1 = 20$, $Z = Z_c = 22$, $Z' = 30$, $Z'' = 34$, and $Z''' = 40$ and the fitting parameters are $\alpha_1 = 1.0$, $\alpha_2 = 1.5$, $\alpha_3 = 0.35$, and $\alpha_4 = 0.1$. In Figure 2, the prediction of the method is compared with that of the simple shell-model and the experimental data. We note that in the momentum transfer range of our interest (i.e., $q < 2\,\mathrm{fm}^{-1}$), the form factor has excellent behaviour. We however mention that even though the FOP method presents very high reproducibility of the experimental data, it is not always applicable, for example, for deformed nuclei (where BCS appears to be still successful).

3.2.3. Use of Effective Expressions for the Nuclear Form Factors. We finally discuss one of the most accurate effective methods for calculating the nuclear form factor by [88]

$$F\left(q^2\right) = \frac{3j_1\left(qR_0\right)}{qR_0}\exp\left[-\frac{1}{2}\left(qs\right)^2\right], \tag{21}$$

where $j_1(x)$ is the known first-order spherical Bessel function and $R_0^2 = R^2 - 5s^2$, with R and s being the radius and surface thickness parameters of the nucleus, respectively. The radius parameter is usually given from the semiempirical form $R = 1.2A^{1/3}$ fm while s is of the order of 0.5 fm (see [84]).

It is worth noting that, by inserting the form factors $F_{Z(N)}$ obtained as described above in (10), the resulting cross sections have a rather high confidence level. In the next part of the paper, the results show that the momentum dependence of the nuclear form factors becomes crucial, especially for intermediate and high energies. In some cases, differences of even an order of magnitude may occur as compared to the calculations neglecting the momentum dependence of the nuclear form factors.

4. Results and Discussion

4.1. Integrated Coherent ν-Nucleus Cross Sections. The next phase of our calculational procedure is related to the total coherent ν-nucleus cross sections, obtained through numerical integration of (9) over angles (or (11) over T_N) as

$$\sigma_{\nu_\alpha}\left(E_\nu\right) = \int \frac{d\sigma_{\nu_\alpha}}{d\cos\theta}\left(\theta, E_\nu\right) d\cos\theta. \tag{22}$$

The results for the standard model cross sections, for a set of different promising targets throughout the periodic table, are presented in Figure 3. As can be seen, the present nuclear structure calculations indicate that, between light and heavy nuclear systems, the cross sections may differ by even two orders of magnitude (or more) as a consequence of the dependence on the nuclear parameters (i.e., mass, form factors, etc.). We also see that for heavier nuclei the cross sections flatten more quickly (at lower neutrino energies) compared to that of lighter nuclear isotopes. The latter conclusion originates mainly from the fact that, for heavy nuclei, the suppression of the cross sections due to the nuclear form factors becomes more significant. Thus, for heavy material, the nuclear effects become important even at low energies. Such original cross section results are helpful for the simulations of the standard and nonstandard model signals of ν-detection experiments (see below).

4.2. Supernova Neutrino Simulations. As discussed previously, our present calculations may also be useful for ongoing and future neutrino experiments related to supernova (SN) neutrino detection, since, as it is known, the neutrinos emitted in SN explosions transfer the maximum part of the total energy released. Then, the total neutrino flux, $\Phi(E_\nu)$, arriving at a terrestrial detector as a function of the SN neutrino energy E_ν, the number of emitted (anti)neutrinos N_{ν_α} at a distance d from the source (here we consider $d = 10$ kpc), reads [25, 35]

$$\Phi\left(E_\nu\right) = \sum_{\nu_\alpha}\Phi_{\nu_\alpha}\eta_{\nu_\alpha}^{\mathrm{SN}}\left(E_\nu\right) = \sum_{\nu_\alpha}\frac{N_{\nu_\alpha}}{4\pi d^2}\eta_{\nu_\alpha}^{\mathrm{SN}}\left(E_\nu\right) \tag{23}$$

($\alpha = e, \mu, \tau$) where $\eta_{\nu_\alpha}^{\mathrm{SN}}$ denotes the energy distribution of the (anti)neutrino flavour α.

The emitted SN neutrino energy spectra $\eta_{\nu_\alpha}^{\mathrm{SN}}(E_\nu)$ may be parametrised by Maxwell-Boltzmann distributions that depend only on the temperature T_{ν_α} of the (anti)neutrino flavour ν_α or $\tilde{\nu}_\alpha$ (the chemical potential is ignored); we have

$$\eta_{\nu_\alpha}^{\mathrm{SN}}\left(E_\nu\right) = \frac{E_\nu^2}{2T_{\nu_\alpha}^3}e^{-E_\nu/T_{\nu_\alpha}} \tag{24}$$

($T_{\nu_e} = 3.5$ MeV, $T_{\tilde{\nu}_e} = 5.0$ MeV, and $T_{\nu_x,\tilde{\nu}_x} = 8.0$ MeV, $x = \mu, \tau$ [36]). For each flavour, the total number of emitted neutrinos N_{ν_α} is obtained from the mean neutrino energy [53]

$$\left\langle E_{\nu_\alpha}\right\rangle = 3T_{\nu_\alpha} \tag{25}$$

and the total energy released from a SN explosion, $U = 3 \times 10^{53}$ erg [18, 19].

4.3. Laboratory Neutrino Simulations. The spallation neutron source (SNS) at Oak Ridge National Lab [8] produces neutrons by firing a pulsed proton beam at a liquid mercury target [59]. The main aim of the COHERENT proposal [12, 13] (or of other similar concepts [14, 15]) concerns possible detection of neutrino-nucleus coherent scattering events at the SNS. Our simulations here are mainly motivated by previous studies [9, 16, 17, 58] and the hope to provide our accurate nuclear structure calculations.

In stopped-pion muon sources, neutrinos are produced by the pion decay chain. Pion decay at rest $\pi^+ \to \mu^+\nu_\mu$ ($\tau = 26$ ns) produces monochromatic muon neutrinos ν_μ at 29.9 MeV, followed by electron neutrinos ν_e and muon antineutrinos $\tilde{\nu}_\mu$ that are produced by the muon decay $\mu^+ \to \nu_e e^+\tilde{\nu}_\mu$ ($\tau = 2.2\,\mu$s) [23, 24]. For pulsed beams in time-scales narrower than μs, ν_e's and $\tilde{\nu}_\mu$'s will be delayed with the beam while ν_μ's will be prompt with the beam [9]. The emitted ν_e

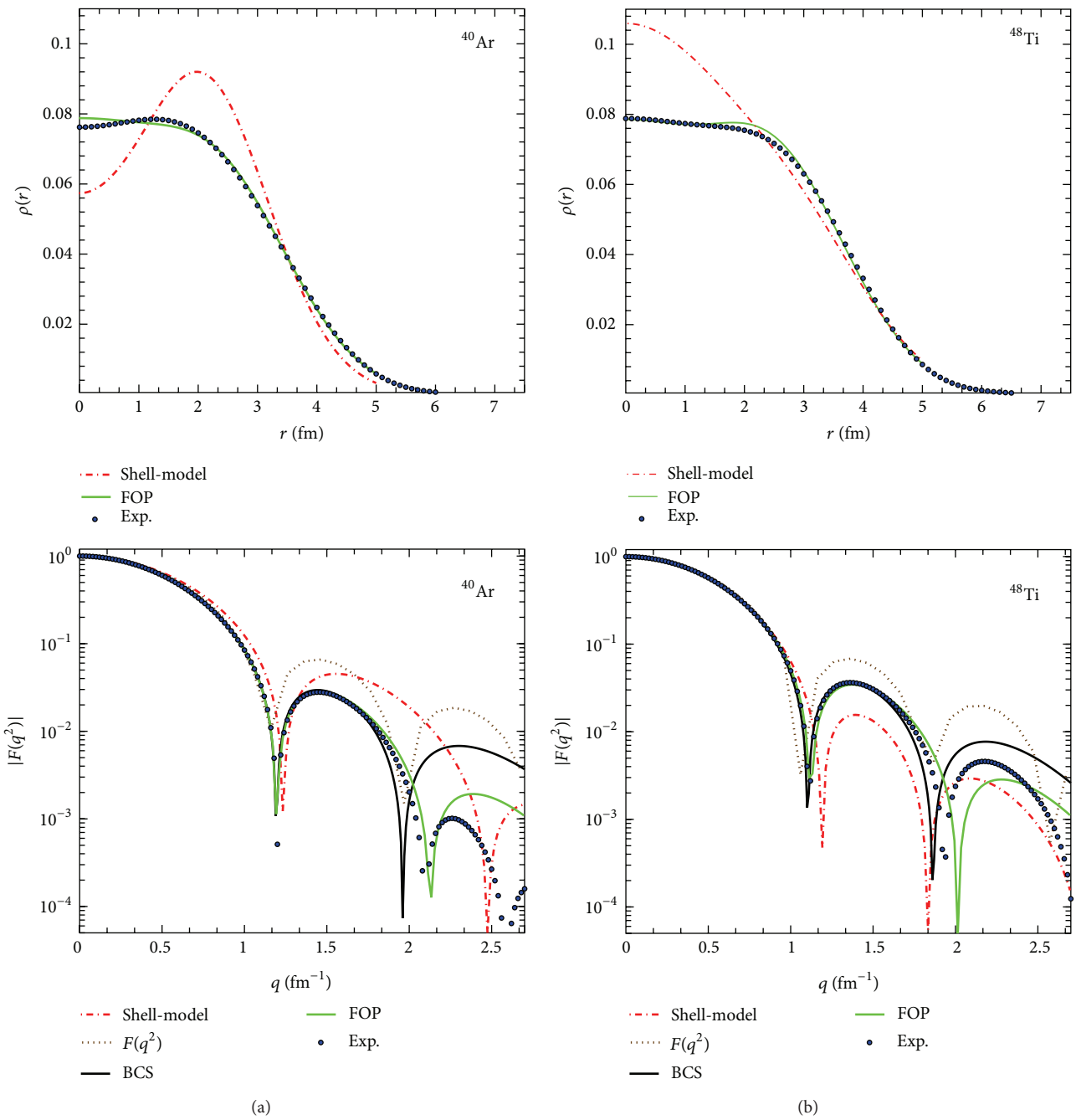

FIGURE 2: The charge density distribution (a) and the form factor as a function of the momentum transfer (b), for the cases of ^{40}Ar and ^{48}Ti nuclei. The introduction of fractional occupation probabilities (FOP) of the states provides higher reproducibility of the experimental data, compared to the simple shell-model and that of (21). The BCS nuclear neutron form factor $F_N(q^2)$ is also presented and compared.

and $\tilde{\nu}_\mu$ neutrino spectra are described by the high precision normalized distributions, known as the Michel spectrum [11]

$$\eta_{\nu_e}^{\text{lab.}} = 96E_\nu^2 M_\mu^{-4}\left(M_\mu - 2E_\nu\right),$$
$$\eta_{\tilde{\nu}_\mu}^{\text{lab.}} = 16E_\nu^2 M_\mu^{-4}\left(3M_\mu - 4E_\nu\right) \tag{26}$$

($M_\mu = 105.6$ MeV is the muon rest mass). The maximum neutrino energy in the latter distributions is $E_\nu^{\max} = M_\mu/2 = 52.8$ MeV (see, e.g., [10]).

The spallation neutron source (SNS) at Oak Ridge National Lab is currently the most powerful facility to detect for a first time neutrino-nucleus coherent scattering events, since it provides exceptionally intense fluxes $\Phi_{\nu_\alpha} = 2.5 \times 10^7\ \nu\text{s}^{-1}\ \text{cm}^{-2}$ at 20 m and $\Phi_{\nu_\alpha} = 6.3 \times 10^6\ \nu\text{s}^{-1}\ \text{cm}^{-2}$ at 40 m from the source [23, 24]. The simulated laboratory neutrino

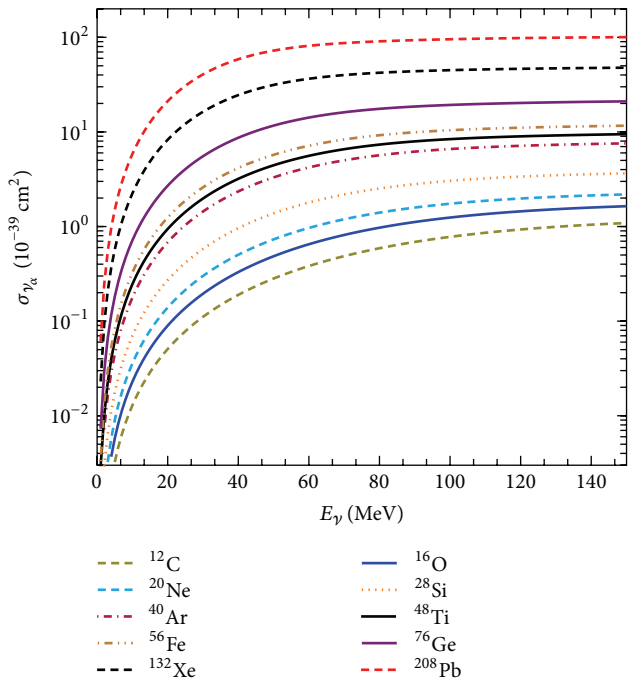

FIGURE 3: Total coherent cross sections $\sigma_{\nu_\alpha(\bar{\nu}_\alpha)}(E_\nu)$ in units 10^{-39} cm^2 for a set of nuclei as a function of the incoming neutrino energy E_ν, for the SM neutrino processes $\nu_\alpha(\bar{\nu}_\alpha) + (A, Z) \rightarrow \nu_\alpha(\bar{\nu}_\alpha) + (A, Z)$.

signals $\sigma^{\text{sign}}_{\nu,\text{lab.}}$ coming out of our calculations for the adopted nuclear targets are discussed below.

4.4. Simulated Neutrino Signals. By weighting the integrated cross section $\sigma_{\nu_\alpha}(E_\nu)$ with the neutrino distributions of (24), for SN neutrinos, or (26), for laboratory neutrinos, the total signal produced on a terrestrial detector is described by [82, 83]

$$\sigma^{\text{sign}}_{\nu,\xi}(E_\nu) = \sum_{\nu_\alpha} \sigma_{\nu_\alpha}(E_\nu)\, \eta^{\xi}_{\nu_\alpha}(E_\nu), \quad \xi = \text{SN, lab.} \tag{27}$$

The resulting signals, $\sigma^{\text{sign}}_{\nu,\xi}(E_\nu)$, obtained by inserting in (27) the cross sections σ_{ν_α} of Figure 3 are plotted in Figure 4.

In our previous work [53], it was shown that the simulated cross sections reflect the characteristics of the incident neutrino spectrum of the specific neutrino flavour α and, therefore, such a simulated signal is characterised by its own position of the maximum peak and width of the distribution $\eta^{\text{SN}}_{\nu_\alpha}$. We, however, recall that, within the framework of the SM, coherent neutrino scattering is a flavour blind and a particle-antiparticle blind process. For this particular case, our results are shown in Figure 4 for supernova and laboratory (SNS) neutrinos.

In neutrino simulations, another useful quantity is the flux averaged cross section [5] which in our notation is written as

$$\langle \sigma_\nu \rangle_\xi = \sum_{\nu_\alpha} \int \sigma_{\nu_\alpha}(E_\nu)\, \eta^{\xi}_{\nu_\alpha}(E_\nu)\, dE_\nu. \tag{28}$$

The results for $\langle \sigma_\nu \rangle_\xi$, obtained by using the angle-integrated cross sections of Figure 3, are listed in Table 2 for both neutrino sources.

4.5. Differential and Total Event Rates. From experimental physics perspectives, predictions for the differential event rate, Y_{ν_α}, of a ν-detector are crucial [25]. The usual expression for computing the yield in events is based on the neutrino flux and is defined as [35]

$$\begin{aligned} Y_{\nu_\alpha}(T_N) &= \frac{dN}{T_N} \\ &= K \sum_{\nu_\alpha} \Phi_{\nu_\alpha} \int \eta^{\xi}_{\nu_\alpha} dE_\nu \int \frac{d\sigma_{\nu_\alpha}}{d\cos\theta}\, \delta\left(T_N - \frac{q^2}{2M}\right) d\cos\theta, \end{aligned} \tag{29}$$

where $K = N_{\text{targ.}} t_{\text{tot.}}$ accounts for the total number of nuclei (atoms) in the detector material $N_{\text{targ.}}$ times the total time of exposure t_{tot}. Using the latter equation, one concludes that the lower the energy recoil, the larger the potentially detected number of events (see Figures 5 and 6). In principle, in order to maximize the potential detection of a rare event process like the ν-nucleus scattering, detector materials with very-low-energy recoil threshold and low-background are required.

In the last stage of our study, we make predictions for the total number of coherent scattering events, the most important quantity, both from theoretical and from experimental perspectives. To this purpose, we evaluate the number

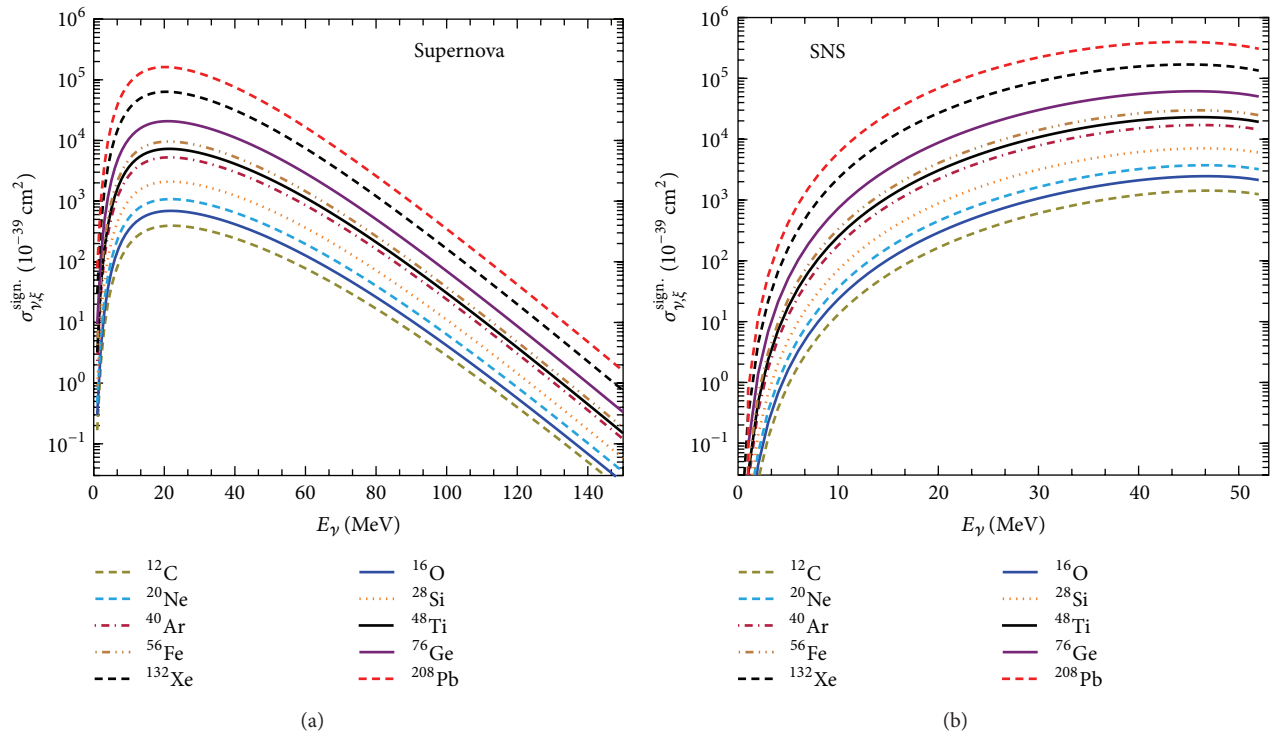

Figure 4: The signal cross sections that represent the expected signal to be recorded on a terrestrial nuclear ν-detector, (a) for supernova neutrinos (ξ = SN), evaluated with Maxwell-Boltzmann distributions at d = 10 kpc, and (b) for SNS neutrinos (ξ = lab.), at 20 m from the source. For the case of SNS neutrinos, the figure takes into account only the delayed beam, evaluated with the generic flux of $\Phi_{\nu_\alpha} \sim 10^7\ \nu\text{s}^{-1}\ \text{cm}^{-2}$. Different nuclear detectors have been studied.

Table 2: Flux averaged cross sections $\langle\sigma_\nu\rangle_\xi$ in units 10^{-40} cm^2 for the adopted supernova (d = 10 kpc) and laboratory (delayed flux only) neutrino spectra. For the case of SNS neutrinos, we adopt the generic flux, that is, $\Phi_{\nu_\alpha} \sim 10^7\ \nu\text{s}^{-1}\ \text{cm}^{-2}$ at 20 m for all nuclear targets.

Nucleus	^{12}C	^{16}O	^{20}Ne	^{28}Si	^{40}Ar	^{48}Ti	^{56}Fe	^{76}Ge	^{132}Xe	^{208}Pb
$\langle\sigma_\nu\rangle_{\text{SN}}$	1.46	2.51	3.91	7.52	18.59	25.43	33.29	70.63	207.56	514.93
$\langle\sigma_\nu\rangle_{\text{lab.}}$	3.07	5.33	8.13	15.52	37.91	51.50	67.02	139.83	395.59	949.50

Table 3: Total number of events per ton of the target materials for a supernova at a distance of 10 kpc. We assume various energy thresholds 5, 10, 25, or 50 keV. Our present results are in excellent agreement with those of [25, 35].

Nucleus	T_N	$T_N > 5$ keV	$T_N > 10$ keV	$T_N > 25$ keV	$T_N > 50$ keV
^{12}C	2.52	2.25	2.05	1.60	1.14
^{16}O	3.29	2.84	2.51	1.83	1.19
^{20}Ne	4.03	3.35	2.87	1.96	1.16
^{40}Ar	9.46	6.63	5.01	2.53	1.00
^{48}Ti	10.73	7.04	5.06	2.27	0.76
^{56}Fe	12.00	7.36	5.04	2.01	0.57
^{76}Ge	18.58	9.61	5.82	1.70	0.30
^{132}Xe	30.68	9.84	4.16	0.46	0.01
^{208}Pb	46.93	7.86	1.95	0.03	$<10^{-3}$

of expected counts, for the studied detector materials, by performing numerical integration of (29) over the nuclear recoil threshold $T_N^{\text{thres.}}$ (see Table 3).

As has been discussed previously [25, 26], SN neutrino detection might become possible by the massive dark matter detectors [32] which have very good energy resolution and low threshold capabilities [35]. These experiments are designed (or planned) to search for WIMPs [27–29] and/or other rare events such as the neutrinoless double beta decay. The latter use heavy nuclei as nuclear detectors, for example, Ge (GERDA [31] and SuperCDMS [30] experiments). In addition, we report that SN neutrino events can be potentially

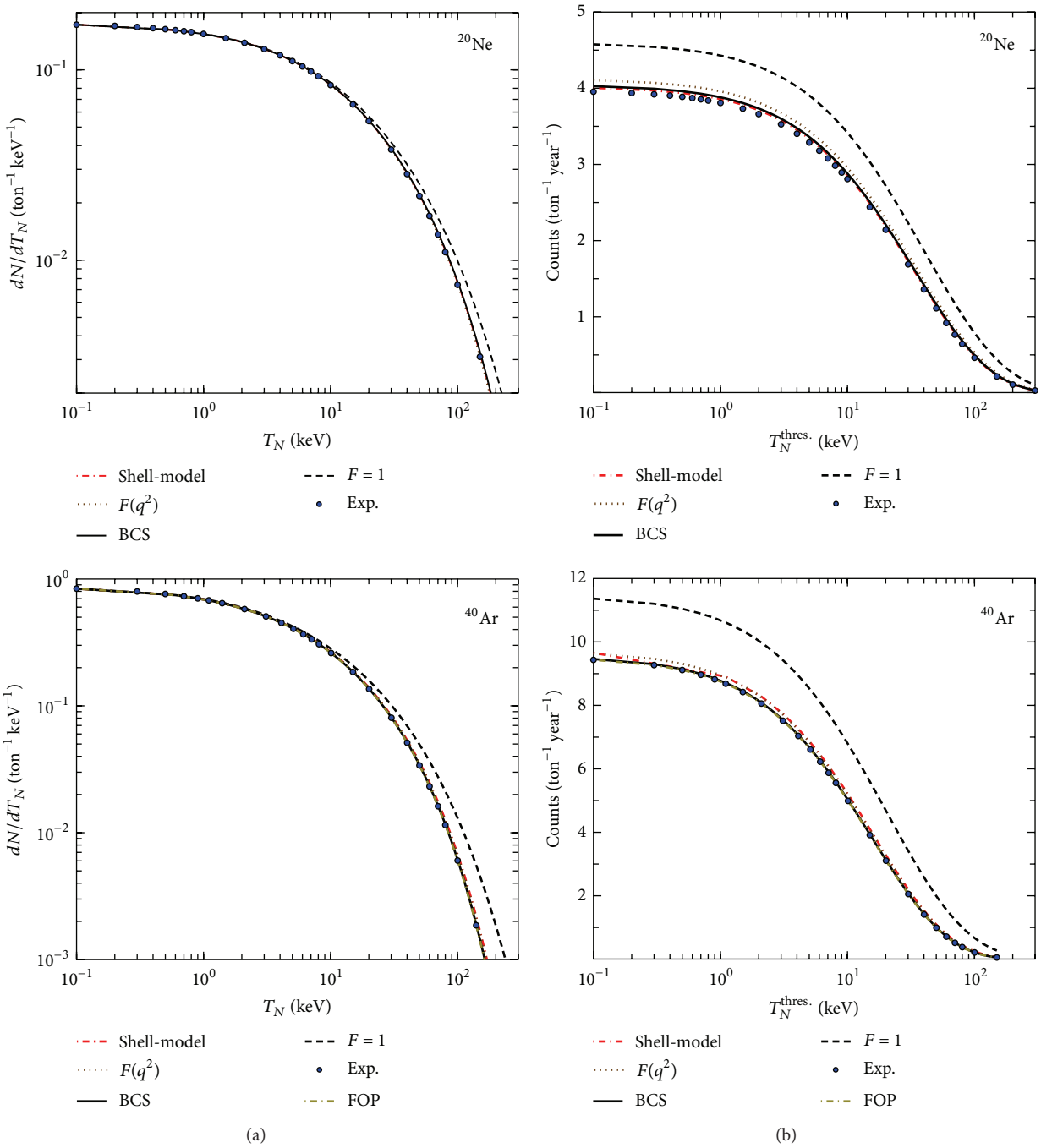

Figure 5: Yield in events (a) and total number of events over nuclear recoil threshold $T_N^{\text{thres.}}$ (b), for supernova neutrinos at $d = 10$ kpc. Here, 1 ton of perfectly efficient ^{20}Ne and ^{40}Ar detectors has been considered and also possible effects of neutrino oscillation in propagation are neglected. For heavier nuclear targets the differences become rather significant. In this figure, $F(q^2)$ stands for (21) and FOP for the method of fractional occupation probabilities of the states. For more details, see the text.

detected by experiments using noble gases like Ne (CLEAN detector [32]), Ar (WARP programme [33]), and Xe (XENON 100 Collaboration [34]).

As mentioned in Section 3, in order to test our nuclear calculations, we have also employed other nuclear methods. To this purpose, we have compared our original results evaluated with the BCS method with those obtained as discussed in Section 3.2 and concluded that for the case of the coherent channel all available nuclear methods are in good agreement, but their results differ significantly from those obtained assuming $F_Z(q^2) = F_N(q^2) = 1$ (see Figures 5 and 6). We stress, however, the fact that since the cross section is mostly sensitive to the neutron distribution of the target nucleus, the most accurate method (at low and

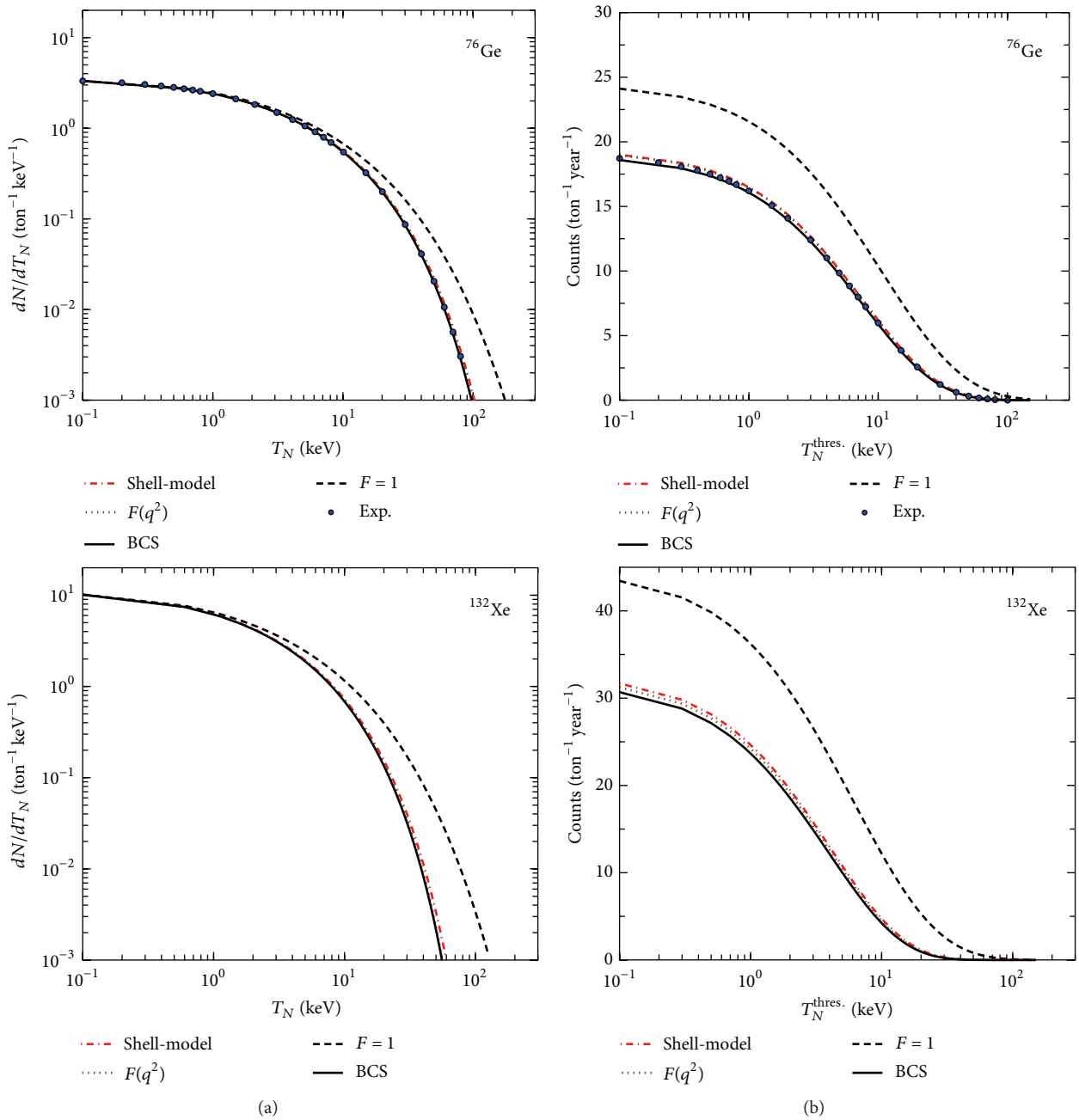

FIGURE 6: Same as Figure 5 but for ^{76}Ge and ^{132}Xe.

intermediate energies) is the BCS method which provides realistic proton as well as neutron form factors. All other methods employed here consider only the proton distribution and assume $F_Z(q^2) = F_N(q^2)$, which, especially for heavy nuclei, is a rather crude approximation. We remark, however, that the aforementioned nuclear methods offer reliable results on the differential and total event rates for low energies (see Figures 5 and 6), but in order to correctly estimate the neutron form factor, methods like the BSC are probably more appropriate.

Our present nuclear structure calculations for laboratory (SNS) neutrinos [8] (see Figure 7) are in good agreement with previous results [9]. They imply that a comparably large number of coherent neutrino scattering events are expected to be measured by using LNe, LAr, LXe, Ge, and CsI[Na] materials adopted by the COHERENT Collaboration [12, 13]. The predictions of the BCS method for these nuclei are illustrated in Figure 7 and compared with those of other promising nuclear targets. Because the neutrino flux produced at the SNS is very high (of the order of $\Phi_{\nu_\alpha} \sim 10^7\ \nu s^{-1}\ cm^{-2}$ per flavour at 20 m from the source [23]), even kg-scale experiments expect to measure neutrino-nucleus coherent scattering events at significantly higher rates than those of supernova neutrinos.

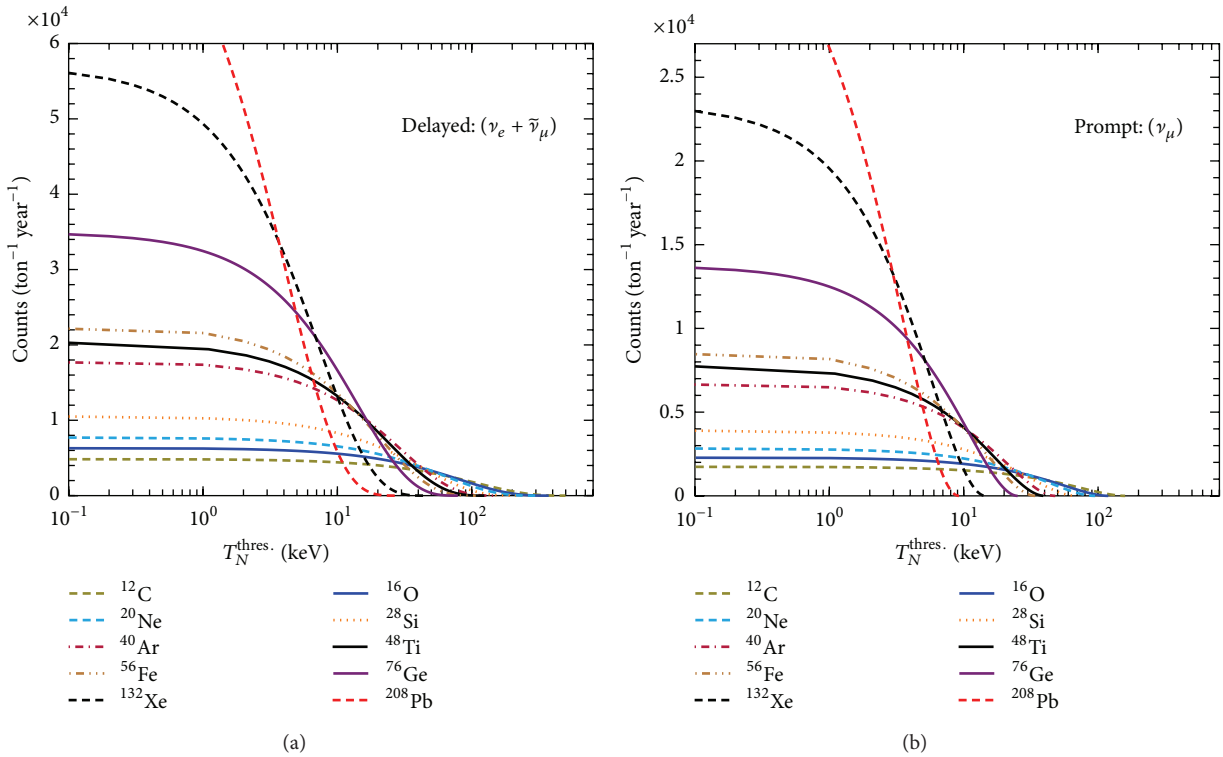

Figure 7: Total number of expected events over nuclear recoil threshold for 1 ton of various nuclear targets at 20 m from the source ($\Phi_{\nu_\alpha} \sim 10^7\ \nu\text{s}^{-1}\ \text{cm}^{-2}$). The left (right) panel assumes the delayed (prompt) flux of laboratory stopped-pion neutrino sources. This figure assumes a perfectly efficient detector and negligible neutrino oscillation effects.

It is worth noting that the choice of the target nucleus plays also a crucial role, since a light nuclear target may yield almost constant number of events throughout the energy range, but small number of counts. On the other hand, a heavy nuclear target provides more counts but yields low-energy recoil, making the detection more difficult. This leads to the conclusion that the most appropriate choice for a nuclear detector might be a combination of light and heavy nuclear isotopes, like the scintillation detectors discussed in [35].

4.6. Nonstandard Neutrino Interactions at the COHERENT Detector. The multitarget approach of the COHERENT experiment [12, 13] aiming at neutrino detection can also explore nonstandard physics issues such as NSI [52, 53], neutrino magnetic moment [57], and sterile neutrino [58]. In this subsection, we find it interesting to evaluate the nonstandard neutrino-nucleus events that could be potentially detected by this experiment in each of the proposed nuclear targets. The high intensity SNS neutrino beams [8] and the two promising ν-detectors, liquid ^{20}Ne (391 kg) and liquid ^{40}Ar (456 kg) [58], firstly proposed by the CLEAR [14] and CLEAN [32] designs (located at distance 20 m from the source), constitute excellent probes to search for the exotic ν-reactions. Other possibilities [12, 13] include medium and heavy weight targets like ^{76}Ge (100 kg) inspired by the dark matter SuperCDMS [30] detector (located at 20 m) and ^{132}Xe (100 kg located at 40 m).

In Figures 8 and 9, the resulting number of exotic events is illustrated and compared with the SM predictions. We note, however, that, especially for the case of the flavour changing (FC) channel $\nu_\mu \to \nu_e$, by using the extremely high sensitivity of the ongoing $\mu^- \to e^-$ conversion experiments (COMET [43, 44] and Mu2e [47]), very robust bounds have been set on the vector parameters $\epsilon_{\mu e}^{fV}$ [53]. To this end, we conclude that if the Mu2e and COMET experiments will not detect muon-to-electron conversion events, then the new $\epsilon_{\mu e}^{fV}$ parameters extracted in [53] will lead to undetectable coherent rates at the SNS facility for this channel.

For our present calculations we used the current bounds [53] set by the sensitivity of the PSI experiment [89] and found countable number of events for the near detectors in the case of the corresponding $\nu_\mu \to \nu_e$ reaction. The other exotic parameters, that is, $\epsilon_{\alpha\alpha}^{fV}$ with $\alpha = e, \mu$ and $\epsilon_{e\tau}^{fV}$, have been taken from [51]. As discussed in [53], we do not take into account the $\epsilon_{\tau\tau}^{fV}$ contribution, since the corresponding limits are poorly constrained and eventually predict unacceptably high rates.

Before closing, it is worth noting that the present calculations indicate significant possibility of detecting exotic neutrino-nucleus events through coherent scattering in the aforementioned experiments. Since neutrino-physics enters a precision era [9], a difference from the standard model

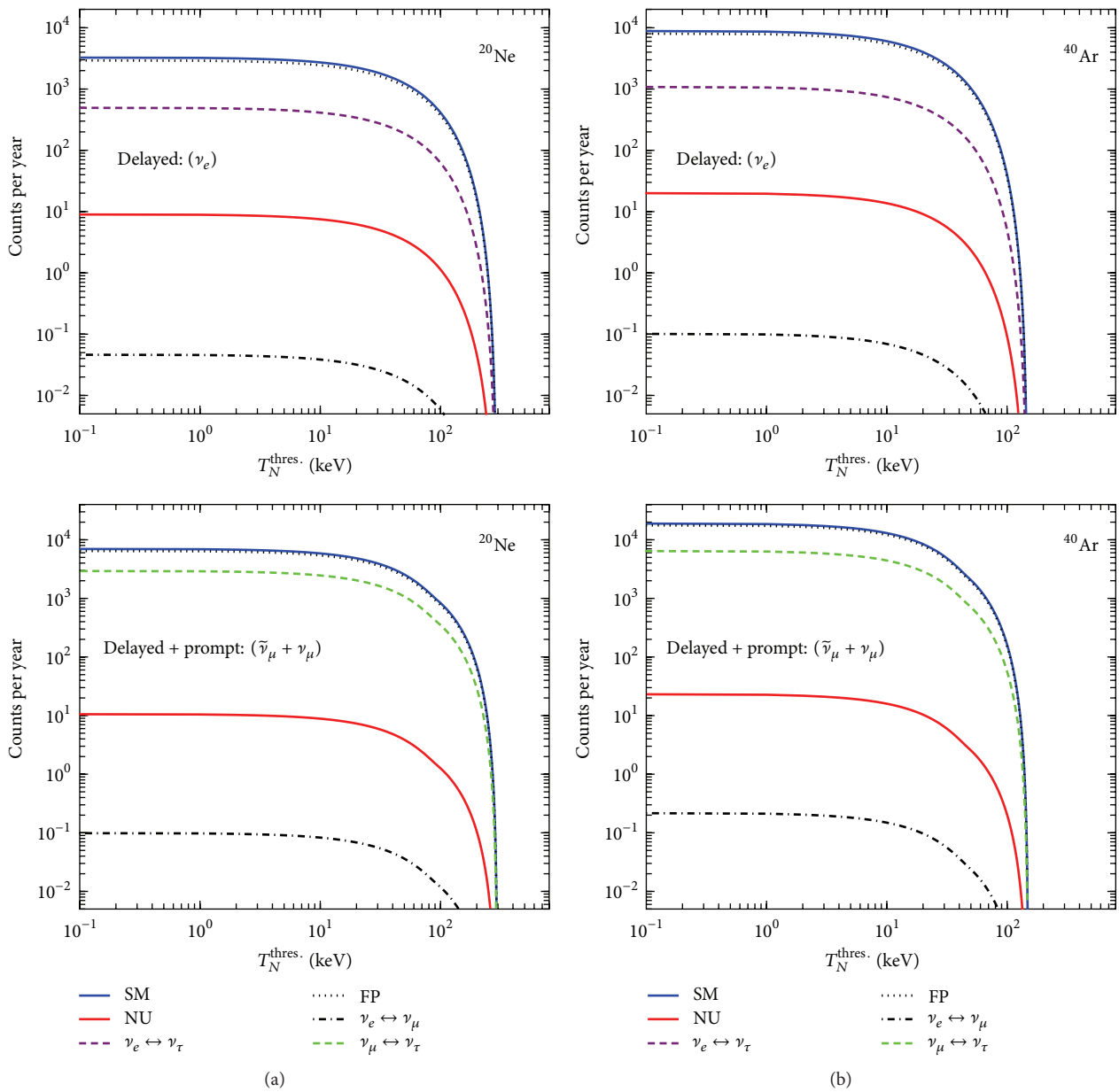

Figure 8: The expected nonstandard neutrino scattering events over the recoil energy threshold at the COHERENT detector, filled with (a) 391 kg of liquid ^{20}Ne and (b) 456 kg of liquid ^{40}Ar, both located at a distance of 20 m ($\Phi_{\nu_\alpha} = 2.5 \times 10^7\ \nu s^{-1}\ cm^{-2}$) from the source. A perfectly efficient detector and negligible neutrino oscillation effects are assumed.

predictions leads to undoubtable evidence of nonstandard neutrino-nucleus interactions (NSI). We recall that, in order to experimentally constrain simultaneously all the exotic parameters at high precision, the detector material should consist of maximally different ratio $k = (A + N)/(A + Z)$ [9, 52].

Our future plans include estimation of the incoherent channel which may provide a significant part of the total cross section, especially for energies higher than $E_\nu \approx 20$–40 MeV (depending on the nuclear target [81] and the particle model predicting the exotic process).

5. Summary and Conclusions

Initially, in this paper, the evaluation of all required nuclear matrix elements, related to standard model and exotic neutral-current ν-nucleus processes, is formulated, and realistic nuclear structure calculations of ν-nucleus cross sections for a set of interesting nuclear targets are performed. The first stage involves cross sections calculations for the dominant coherent channel in the range of incoming neutrino-energies $0 \leq E_\nu \leq 150$ MeV (it includes ν-energies of stopped-pion muon neutrino decay sources, supernova neutrinos, etc.).

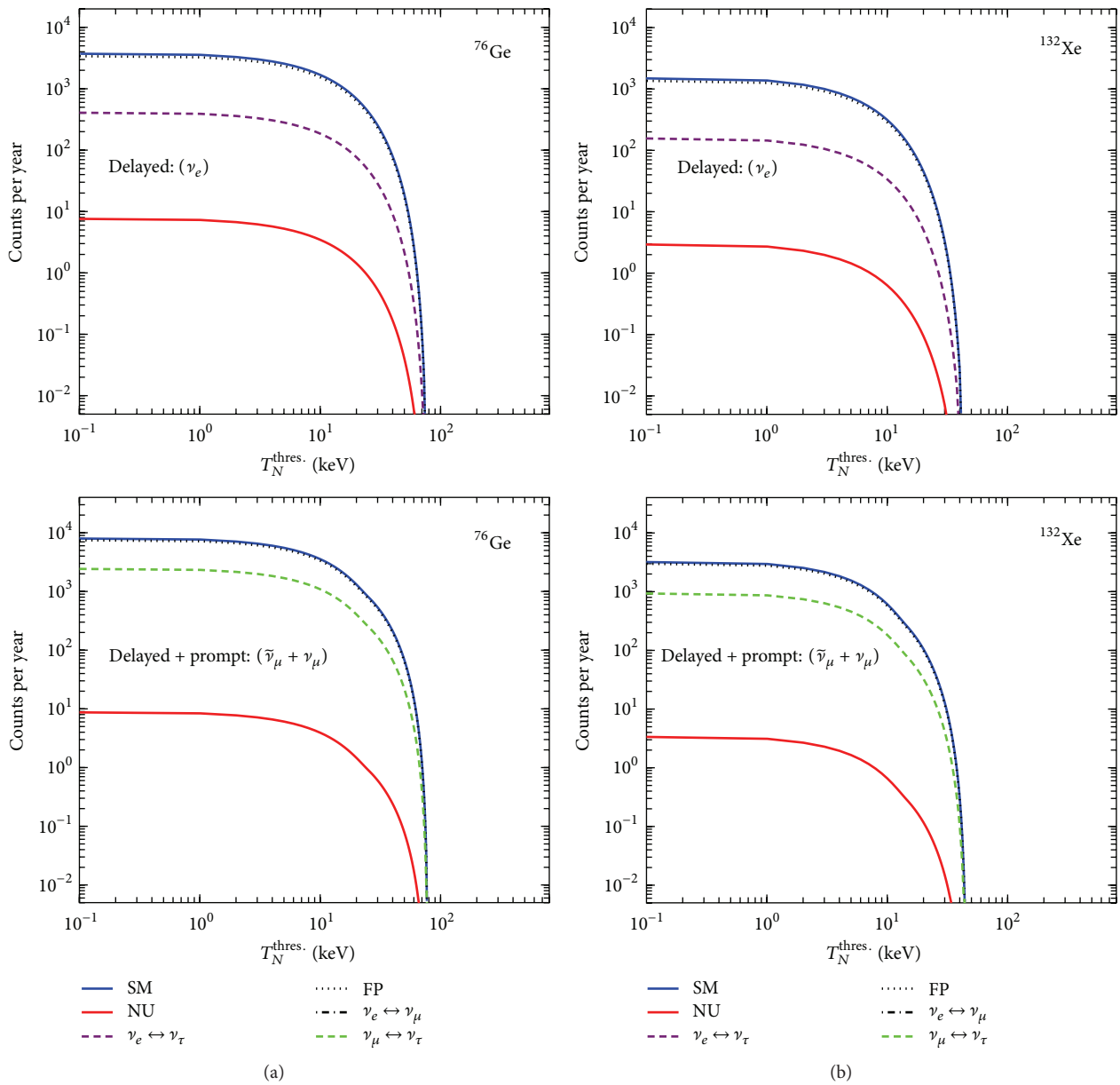

FIGURE 9: Same as Figure 8, but for 100 kg of ^{76}Ge at 20 m ($\Phi_{\nu_\alpha} = 2.5 \times 10^7\ \nu s^{-1}\ cm^{-2}$) and 100 kg of liquid ^{132}Xe at 40 m ($\Phi_{\nu_\alpha} = 6.3 \times 10^6\ \nu s^{-1}\ cm^{-2}$) from the source.

Additionally, new results for the total number of events expected to be observed in one ton of various ν-detector materials are provided and the potentiality of detecting supernova as well as laboratory neutrino-nucleus events is in detail explored. The calculations are concentrated on interesting nuclei, like ^{20}Ne, ^{40}Ar, ^{76}Ge, and ^{132}Xe, which are important detector materials for several rare event experiments, like the COHERENT at Oak Ridge National Laboratory, and also experiments searching for dark matter events as the GERDA, SuperCDMS, XENON 100, CLEAN, and so forth. By comparing our results with those of other methods, we see that the nuclear physics aspects (reflecting the accuracy of the required ν-nucleus cross sections) appreciably affect the coherent $gs \rightarrow gs$ transition rate, a result especially useful for supernova ν-detection probes.

In the present work, the QRPA method that considers realistic nuclear forces has been adopted in evaluating the nuclear form factors, for both categories of ν-nucleus processes, the conventional and the exotic ones. Also, a comparison with other simpler methods as (i) effective methods and (ii) the method of fractional occupation probabilities, which improves over the simple shell-model and gives higher reproducibility of the available experimental data, is presented and discussed. We conclude that among all the adopted methods the agreement is quite good, especially for light and medium nuclear isotopes. However, since coherent

neutrino-nucleus scattering can probe the neutron nuclear form factors, methods like the BCS provide more reliable results.

In view of the operation of extremely intensive neutrino fluxes (at the SNS, PSI, J-PARC, Fermilab, etc.), the sensitivity to search for new physics will be largely increased, and therefore, through coherent neutrino-nucleus scattering cross section measurements, several open questions (involving nonstandard neutrino interactions, neutrino magnetic moment, sterile neutrino searches, and others) may be answered. Towards this purpose, we have comprehensively studied the nonstandard neutrino-nucleus processes and provided results for interesting nuclear detectors. Our predictions for the total number of events indicate that, within the current limits of the respective flavour violating parameters, the COHERENT experiment may come out with promising results on NSI. Moreover, this experiment in conjunction with the designed sensitive muon-to-electron conversion experiments (Mu2e, COMET) may offer significant contribution for understanding the fundamental nature of electroweak interactions in the leptonic sector and for constraining the parameters of beyond the SM Lagrangians.

Conflict of Interests

The authors declare that there is no conflict of interests regarding the publication of this paper.

Acknowledgment

One of the authors, D. K. Papoulias, wishes to thank Dr. O. T. Kosmas for technical assistance.

References

[1] D. Z. Freedman, "Coherent effects of a weak neutral current," *Physical Review D*, vol. 9, no. 5, pp. 1389–1392, 1974.

[2] A. Drukier and L. Stodolsky, "Principles and applications of a neutral-current detector for neutrino physics and astronomy," *Physical Review D*, vol. 30, no. 11, pp. 2295–2309, 1984.

[3] K. Langanke, "Weak interaction, nuclear physics and supernovae," *Acta Physica Polonica B*, vol. 39, no. 2, p. 265, 2008.

[4] H. Ejiri, "Nuclear spin isospin responses for low-energy neutrinos," *Physics Reports*, vol. 338, no. 3, pp. 265–351, 2000.

[5] T. S. Kosmas and E. Oset, "Charged current neutrino-nucleus reaction cross sections at intermediate energies," *Physical Review C: Nuclear Physics*, vol. 53, no. 3, pp. 1409–1415, 1996.

[6] J. Schechter and J. W. F. Valle, "Neutrino Masses in SU(2) x U(1) Theories," *Physical Review D*, vol. 22, no. 9, pp. 2227–2235, 1980.

[7] J. Schechter and J. W. F. Valle, "Neutrino decay and spontaneous violation of lepton number," *Physical Review D*, vol. 25, p. 774, 1982.

[8] http://www.phy.ornl.gov/nusns.

[9] K. Scholberg, "Prospects for measuring coherent neutrino-nucleus elastic scattering at a stopped-pion neutrino source," *Physical Review D*, vol. 73, Article ID 033005, 2006.

[10] A. A. Aguilar-Arevalo, C. E. Anderson, A. O. Bazarko et al., "Neutrino flux prediction at MiniBooNE," *Physical Review D*, vol. 79, no. 7, Article ID 072002, 38 pages, 2009.

[11] W. C. Louis, "Searches for muon-to-electron (anti) neutrino flavor change," *Progress in Particle and Nuclear Physics*, vol. 63, no. 1, pp. 51–73, 2009.

[12] A. Bolozdynya, F. Cavanna, Y. Efremenko et al., "Opportunities for neutrino physics at the spallation neutron source: a white paper," http://arxiv.org/abs/1211.5199.

[13] D. Akimov, A. Bernstein, P. Barbeau et al., "Coherent scattering investigations at the spallation neutron source: a snowmass white paper," http://arxiv.org/abs/1310.0125.

[14] K. Scholberg, T. Wongjirad, E. Hungerford et al., "The CLEAR experiment," http://arxiv.org/abs/0910.1989.

[15] J. Yoo, Measuring coherent-NCν as at Fermilab, 2011, http://if-neutrino.fnal.gov/neutrino1-pagers.pdf.

[16] S. J. Brice, "A method for measuring coherent elastic neutrino-nucleus scattering at a far off-axis high-energy neutrino beam target," *Physical Review D*, vol. 89, no. 7, Article ID 072004, 20 pages, 2014.

[17] J. I. Collar, N. E. Fields, E. Fuller et al., "Coherent neutrino-nucleus scattering detection with a CsI[Na] scintillator at the SNS spallation source," http://arxiv.org/abs/1407.7524.

[18] K. Hirata, T. Kajita, M. Koshiba et al., "Observation of a neutrino burst from the supernova SN1987A," *Physical Review Letters*, vol. 58, p. 1490, 1987.

[19] R. M. Bionta, G. Blewitt, C. B. Bratton et al., "Observation of a neutrino burst in coincidence with supernova 1987a in the large magellanic cloud," *Physical Review Letters*, vol. 58, no. 14, pp. 1494–1496, 1987.

[20] M. T. Keil, G. G. Raffelt, and H.-T. Janka, "Monte Carlo study of supernova neutrino spectra formation," *Astrophysical Journal Letters*, vol. 590, no. 2 I, pp. 971–991, 2003.

[21] W. C. Haxton, "Radiochemical neutrino detection via $^{127}|\,(\nu_e, e^-)^{127} \times e$," *Physical Review Letters*, vol. 60, no. 9, pp. 768–771, 1988.

[22] P. G. Giannaka and T. S. Kosmas, "Electron-capture and its role to explosive neutrino-nucleosynthesis," *Journal of Physics: Conference Series*, vol. 410, Article ID 012124, 2013.

[23] F. T. Avignone III and Y. V. Efremenko, "Neutrino-nucleus cross-section measurements at intense, pulsed spallation sources," *Journal of Physics G: Nuclear and Particle Physics*, vol. 29, no. 11, pp. 2615–2628, 2003.

[24] Y. Efremenko and W. Hix, "Opportunities for neutrino physics at the Spallation Neutron Source (SNS)," *Journal of Physics: Conference Series*, vol. 173, no. 1, Article ID 012006, 2009.

[25] C. J. Horowitz, K. J. Coakley, and D. N. McKinsey, "Supernova observation via neutrino-nucleus elastic scattering in the CLEAN detector," *Physical Review D*, vol. 68, no. 2, Article ID 023005, 7 pages, 2003.

[26] A. J. Anderson, J. M. Conrad, E. Figueroa-Feliciano, K. Scholberg, and J. Spitz, "Coherent neutrino scattering in dark matter detectors," *Physical Review D: Particles, Fields, Gravitation and Cosmology*, vol. 84, no. 1, Article ID 013008, 2011.

[27] T. S. Kosmas and J. D. Vergados, "Cold dark matter in SUSY theories: the role of nuclear form factors and the folding with the LSP velocity," *Physical Review D: Particles, Fields, Gravitation and Cosmology*, vol. 55, no. 4, pp. 1752–1764, 1997.

[28] J. D. Vergados and T. S. Kosmas, "Muon-number-violating processes in nuclei," *Physics of Atomic Nuclei*, vol. 61, p. 1066, 1998.

[29] J. D. Vergados and T. S. Kosmas, "Searches for cold dark-matter—a case of the coexistence of supersymmetry and nuclear-physics," *Physics of Atomic Nuclei*, vol. 61, no. 7, pp. 1066–1080, 1998.

[30] P. Brink, B. Cabrera, and C. L. Chang, "Beyond the CDMS-II dark matter search: superCDMS," in *Proceedings of the 22nd Texas Symposium on Rela Conference*, Stanford, Calif, USA, December 2004.

[31] GERDA Collaboration, "The GERDA experiment at Gran Sasso," *Acta Physica Polonica B*, vol. 41, pp. 1469–1476, 2010.

[32] D. N. McKinsey and K. J. Coakley, "Neutrino detection with CLEAN," *Astroparticle Physics*, vol. 22, no. 5-6, pp. 355–368, 2005.

[33] R. Brunetti, E. Calligarich, M. Cambiaghi et al., "WARP liquid argon detector for dark matter survey," *New Astronomy Reviews*, vol. 49, no. 2–6, pp. 265–269, 2005.

[34] XENON100 Collaboration, "The XENON100 dark matter experiment," http://arxiv.org/abs/1107.2155v1.

[35] M. Biassoni and C. Martinez, "Study of supernova ν-nucleus coherent scattering interactions," *Astroparticle Physics*, vol. 36, pp. 151–155, 2012.

[36] Y. Giomataris and J. D. Vergados, "A network of neutral current spherical TPCs for dedicated supernova detection," *Physics Letters B: Nuclear, Elementary Particle and High-Energy Physics*, vol. 634, no. 1, pp. 23–29, 2006.

[37] J. Monroe and P. Fisher, "Neutrino backgrounds to dark matter searches," *Physical Review D*, vol. 76, Article ID 033007, 2007.

[38] S. Fukuda, Y. Fukuda, M. Ishitsuka et al., "Solar ^8B and hep Neutrino Measurements from 1258 Days of Super-Kamiokande Data," *Physical Review Letters*, vol. 86, no. 25, pp. 5651–5655, 2001.

[39] Q. R. Ahmad, R. C. Allen, T. C. Andersen et al., "Measurement of day and night neutrino energy spectra at SNO and constraints on neutrino mixing parameters," *Physical Review Letters*, vol. 89, Article ID 011302, 2002.

[40] K. Eguchi, S. Enomoto, K. Furuno et al., "First results from KamLAND: evidence for reactor antineutrino disappearance," *Physical Review Letters*, vol. 90, no. 2, 6 pages, 2003.

[41] D. V. Forero, M. Tortola, and J. W. F. Valle, "Global status of neutrino oscillation parameters after Neutrino-2012," *Physical Review D*, vol. 86, Article ID 073012, 2012.

[42] J. W. F. Valle, "Understanding and probing neutrinos," *Nuclear Physics B—Proceedings Supplements*, vol. 229–232, pp. 23–29, 2012.

[43] Y. G. Cui, R. Palmer, Y. Arimoto et al., "KEK Report 2009-10".

[44] COMET Collaboration, The COMET Proposal to JPARC, JPARC Proposal, 2007.

[45] R. J. Abrams, D. Alezander, G. Ambrosio et al., "Mu2e conceptual design report," http://arxiv.org/abs/1211.7019.

[46] Mu2e Collaboration and F. Cervelli, "The Mu2e experiment at Fermilab," *Journal of Physics: Conference Series*, vol. 335, no. 1, Article ID 012073, 2011.

[47] R. H. Bernstein and P. S. Cooper, "Charged lepton flavor violation: an experimenter's guide," *Physics Reports*, vol. 532, no. 2, pp. 27–64, 2013.

[48] R. J. Barlow, "The PRISM/PRIME project," *Nuclear Physics B—Proceedings Supplements*, vol. 218, no. 1, pp. 44–49, 2011.

[49] Y. Kuno, "COMET and PRISM—search for charged Lepton flavor violation with muons," *Nuclear Physics B—Proceedings Supplements*, vol. 225-227, pp. 228–231, 2012.

[50] Y. Kuno and Y. Okada, "Muon decay and physics beyond the standard model," *Reviews of Modern Physics*, vol. 73, p. 151, 2001.

[51] S. Davidson, C. Pena-Garay, N. Rius, and A. Santamaria, "Present and future bounds on non-standard neutrino interactions," *Journal of High Energy Physics*, vol. 2003, no. 03, article 011, 2003.

[52] J. Barranco, O. G. Miranda, and T. I. Rashba, "Probing new physics with coherent neutrino scattering off nuclei," *Journal of High Energy Physics*, vol. 2005, article 021, 2005.

[53] D. K. Papoulias and T. S. Kosmas, "Nuclear aspects of neutral current non-standard ν-nucleus reactions and the role of the exotic $\mu^- \to e^-$ transitions experimental limits," *Physics Letters B*, vol. 728, pp. 482–488, 2014.

[54] A. Friedland, C. Lunardini, and C. Peña-Garay, "Solar neutrinos as probes of neutrino–matter interactions," *Physics Letters B*, vol. 594, no. 3-4, pp. 347–354, 2004.

[55] A. Friedland, C. Lunardini, and M. Maltoni, "Atmospheric neutrinos as probes of neutrino-matter interactions," *Physical Review D: Particles, Fields, Gravitation and Cosmology*, vol. 70, no. 11, Article ID 111301, pp. 1–111301, 2004.

[56] A. Friedland, C. Lunardini, and D. Phys. Rev, "Test of tau neutrino interactions with atmospheric neutrinos and K2K data," *Physical Review D*, vol. 72, no. 5, Article ID 053009, 16 pages, 2005.

[57] K. J. Healey, A. A. Petrov, and D. Zhuridov, "Nonstandard neutrino interactions and transition magnetic moments," *Physical Review D*, vol. 87, Article ID 117301, 11 pages, 2013.

[58] A. J. Anderson, J. M. Conrad, E. Figueroa-Feliciano et al., "Measuring active-to-sterile neutrino oscillations with neutral current coherent neutrino-nucleus scattering," *Physical Review D: Particles, Fields, Gravitation and Cosmology*, vol. 86, no. 1, Article ID 013004, 2012.

[59] P. S. Amanik and G. C. McLaughlin, "Nuclear neutron form factor from neutrino-nucleus coherent elastic scattering," *Journal of Physics G: Nuclear and Particle Physics*, vol. 36, no. 1, Article ID 015105, 2009.

[60] P. S. Amanik, G. M. Fuller, and B. Grinstein, "Flavor changing supersymmetry interactions in a supernova," *Astroparticle Physics*, vol. 24, no. 1-2, pp. 160–182, 2005.

[61] A. Esteban-Pretel, R. Tomas, and J. W. F. Valle, "Interplay between collective effects and nonstandard interactions of supernova neutrinos," *Physical Review D*, vol. 81, no. 6, Article ID 063003, 16 pages, 2010.

[62] D. K. Papoulias and T. S. Kosmas, "Exotic lepton flavour violating processes in the presence of nuclei," *Journal of Physics: Conference Series*, vol. 410, Article ID 012123, 2013.

[63] H. C. Chiang, E. Oset, T. S. Kosmas, A. Faessler, and J. D. Vergados, "Coherent and incoherent (μ^-, e^-) conversion in nuclei," *Nuclear Physics A*, vol. 559, no. 4, pp. 526–542, 1993.

[64] T. S. Kosmas and J. D. Vergados, "(μ^-, e^-) conversion: a symbiosis of particle and nuclear physics," *Physics Report*, vol. 264, no. 1–5, pp. 251–266, 1996.

[65] T. S. Kosmas, "Exotic $\mu^- \to e^-$ conversion in nuclei: energy moments of the transition strength and average energy of the outgoing e^-," *Nuclear Physics A*, vol. 683, no. 1–4, pp. 443–462, 2001.

[66] T. S. Kosmas, "Current nuclear physics issues in studying the neutrinoless (μ^-, e^-) conversion in nuclei," *Progress in Particle and Nuclear Physics*, vol. 48, pp. 307–316, 2002.

[67] T. S. Kosmas, G. K. Leontaris, and J. D. Vergados, "Lepton flavor non-conservation," *Progress in Particle and Nuclear Physics*, vol. 33, pp. 397–447, 1994.

[68] F. Deppisch, T. S. Kosmas, and J. W. F. Valle, "Enhanced μ^--e^- conversion in nuclei in the inverse seesaw model," *Nuclear Physics B*, vol. 752, no. 1-2, pp. 80–92, 2006.

[69] D. V. Forero, S. Morisi, M. Tortola, and J. W. F. Valle, "Lepton flavor violation and non-unitary lepton mixing in low-scale

type-I seesaw," *Journal of High Energy Physics*, vol. 2011, article 142, 2011.

[70] S. P. Das, F. F. Deppisch, O. Kittel, and J. W. F. Valle, "Heavy neutrinos and lepton flavor violation in left-right symmetric models at the LHC," *Physical Review D*, vol. 86, no. 5, Article ID 055006, 20 pages, 2012.

[71] A. A. Petrov and D. V. Zhuridov, "Lepton flavor-violating transitions in effective field theory and gluonic operators," *Physical Review D*, vol. 89, Article ID 033005, 2014.

[72] P. S. Amanik and G. M. Fuller, "Stellar collapse dynamics with neutrino flavor changing neutral currents," *Physical Review D*, vol. 75, Article ID 083008, 2007.

[73] J. Barranco, O. G. Miranda, C. A. Moura, and J. W. F. Valle, "Constraining nonstandard interactions in νee or $\nu\bar{e}$e scattering," *Physical Review D: Particles, Fields, Gravitation and Cosmology*, vol. 73, no. 11, Article ID 113001, 2006.

[74] O. G. Miranda, M. A. Tortola, and J. W. F. Valle, "Are solar neutrino oscillations robust?" *Journal of High Energy Physics*, vol. 2006, no. 10, article 8, 2006.

[75] J. Barranco, O. G. Miranda, and T. I. Rashba, "Sensitivity of low energy neutrino experiments to physics beyond the standard model," *Physical Review D*, vol. 76, Article ID 073008, 2007.

[76] T. S. Kosmas and J. D. Vergados, "Nuclear matrix elements for the coherent μ-e conversion process," *Physics Letters B*, vol. 215, no. 3, pp. 460–464, 1988.

[77] T. S. Kosmas and J. D. Vergados, "Study of the flavour violating (μ^-, e^-) conversion in nuclei," *Nuclear Physics A*, vol. 510, no. 4, pp. 641–670, 1990.

[78] T. S. Kosmas, J. D. Vergados, O. Civitarese, and A. Faessler, "Study of the muon number violating (μ^-, e$^-$ conversion in a nucleus by using quasi-particle RPA," *Nuclear Physics Section A*, vol. 570, no. 3-4, pp. 637–656, 1994.

[79] T. S. Kosmas, S. Kovalenko, and I. Schmidt, "Nuclear $\mu^- - e^-$ conversion in strange quark sea," *Physics Letters B*, vol. 511, no. 2–4, pp. 203–208, 2001.

[80] T. S. Kosmas, S. Kovalenko, and I. Schmidt, "b-quark mediated neutrinoless μ^-–e$^-$ conversion in presence of R-parity violation," *Physics Letters B*, vol. 519, no. 1-2, pp. 78–82, 2001.

[81] V. C. Chasioti and T. S. Kosmas, "A unified formalism for the basic nuclear matrix elements in semi-leptonic processes," *Nuclear Physics A*, vol. 829, no. 3-4, pp. 234–252, 2009.

[82] V. Tsakstara and T. S. Kosmas, "Low-energy neutral-current neutrino scattering on ^{128,130}Te isotopes," *Physical Review C*, vol. 83, Article ID 054612, 2011.

[83] V. Tsakstara and T. S. Kosmas, "Analyzing astrophysical neutrino signals using realistic nuclear structure calculations and the convolution procedure," *Physical Review C*, vol. 84, no. 6, Article ID 064620, 14 pages, 2011.

[84] H. de Vries, C. W. de Jager, and C. de Vries, "Nuclear charge-density-distribution parameters from elastic electron scattering," *Atomic Data and Nuclear Data Tables*, vol. 36, no. 3, pp. 495–536, 1987.

[85] T. W. Donnelly and J. D. Walecka, "Semi-leptonic weak and electromagnetic interactions with nuclei: isoelastic processes," *Nuclear Physics, Section A*, vol. 274, no. 3-4, pp. 368–412, 1976.

[86] W. M. Alberico, S. M. Bilenky, C. Giunti, and K. M. Graczyk, "Electromagnetic form factors of the nucleon: new fit and analysis of uncertainties," *Physical Review C*, vol. 79, no. 6, Article ID 065204, 12 pages, 2009.

[87] T. S. Kosmas and J. D. Vergados, "Nuclear densities with fractional occupation probabilities of the states," *Nuclear Physics A*, vol. 536, no. 1, pp. 72–86, 1992.

[88] J. Engel, "Nuclear form factors for the scattering of weakly interacting massive particles," *Physics Letters B*, vol. 264, pp. 114–119, 1991.

[89] P. Wintz, in *Proceedings of the First International Symposium on Lepton and Baryon Number Violation*, H. V. Klapdor-Kleingrothaus and I. V. Krivosheina, Eds., p. 534, Institute of Physics Publishing, Philadelphia, Pa, USA, 1998.

Hindawi Publishing Corporation
Advances in High Energy Physics
Volume 2015, Article ID 817530, 7 pages
http://dx.doi.org/10.1155/2015/817530

Research Article

A $CaMoO_4$ Crystal Low Temperature Detector for the AMoRE Neutrinoless Double Beta Decay Search

G. B. Kim,[1,2,3] S. Choi,[2] F. A. Danevich,[4] A. Fleischmann,[5] C. S. Kang,[1,3] H. J. Kim,[6] S. R. Kim,[1,3] Y. D. Kim,[1,7] Y. H. Kim,[1,3,8] V. A. Kornoukhov,[9] H. J. Lee,[1,3] J. H. Lee,[3] M. K. Lee,[3] S. J. Lee,[3,10] J. H. So,[1,3] and W. S. Yoon[1,3,8]

[1] *Institute for Basic Science, Daejeon 305-811, Republic of Korea*
[2] *Department of Physics and Astronomy, Seoul National University, Seoul 151-747, Republic of Korea*
[3] *Korea Research Institute of Standards and Science, Daejeon 305-340, Republic of Korea*
[4] *Institute for Nuclear Research, 03680 Kyiv, Ukraine*
[5] *Kirchhoff-Institut für Physik, Universität Heidelberg, 69120 Heidelberg, Germany*
[6] *Physics Department, Kyungpook National University, Daegu 702-701, Republic of Korea*
[7] *Department of Physics, Sejong University, Seoul 143-747, Republic of Korea*
[8] *Korea University of Science and Technology, Daejeon 305-350, Republic of Korea*
[9] *Institute for Theoretical and Experimental Physics, 117218 Moscow, Russia*
[10] *NASA Goddard Space Flight Center, Greenbelt, MD 20771, USA*

Correspondence should be addressed to Y. H. Kim; yhk@ibs.re.kr

Received 4 July 2014; Accepted 30 August 2014

Academic Editor: Hiro Ejiri

We report the development of a $CaMoO_4$ crystal low temperature detector for the AMoRE neutrinoless double beta decay ($0\nu\beta\beta$) search experiment. The prototype detector cell was composed of a 216 g $CaMoO_4$ crystal and a metallic magnetic calorimeter. An overground measurement demonstrated FWHM resolution of 6–11 keV for full absorption gamma peaks. Pulse shape discrimination was clearly demonstrated in the phonon signals, and 7.6 σ of discrimination power was found for the α and β/γ separation. The phonon signals showed rise-times of about 1 ms. It is expected that the relatively fast rise-time will increase the rejection efficiency of two-neutrino double beta decay pile-up events which can be one of the major background sources in $0\nu\beta\beta$ searches.

1. Introduction

Recent neutrino oscillation experiments have been unveiling the properties of neutrinos [1, 2]. Their experimental evidences strongly suggest that neutrinos are massive and encounter flavor mixing of mass eigenvalues. The mixing angles and the differences between the square masses have been estimated. However, those observations do not provide a direct measurement of the absolute mass and do not answer the question of whether neutrino is its own antiparticle (Majorana-type) or not (Dirac-type).

Search for neutrinoless double beta decay ($0\nu\beta\beta$) is a key experiment to reveal unanswered nature of neutrinos [3–7]. The double beta decay ($2\nu\beta\beta$) that accompanies the simultaneous emission of two electrons and two antineutrinos is a rare process that is an allowed transition in the standard model. Another type of double beta decay that does not emit any neutrinos, $0\nu\beta\beta$, can occur if neutrino is massive Majorana particles (i.e., it is its own antiparticle). In the $0\nu\beta\beta$ process, the full available energy of the decay is carried by the two electrons and the recoiled daughter which has a very small amount of energy compared with that of the electrons.

Therefore, while the electron sum energy spectrum in the $2\nu\beta\beta$ is continuous up to the available energy release ($Q_{\beta\beta}$), in the $0\nu\beta\beta$, the spectrum should have a sharp peak at $Q_{\beta\beta}$ [2].

The observation of $0\nu\beta\beta$ would clearly demonstrate that neutrino is not Dirac-type but rather is Majorana-type particle. In that case, physical processes that do not conserve lepton number would be allowed. Moreover, the absolute mass scale, so-called "effective Majorana neutrino mass", $\langle m_\nu \rangle$ can be estimated using the $0\nu\beta\beta$ half life ($T_{1/2}^{0\nu}$),

$$\left(T_{1/2}^{0\nu}\right)^{-1} = G^{0\nu}\left|M^{0\nu}\right|^2 \frac{\langle m_\nu \rangle^2}{m_e^2}, \tag{1}$$

where m_e is the electron mass, $G^{0\nu}$ is the kinematic phase-space factor calculable with reasonable precision, and $M^{0\nu}$ is the model dependent nuclear matrix element. Here, the Majorana mass is defined as

$$\langle m_\nu \rangle = \left|\sum U_{ej}^2 m_j\right|, \tag{2}$$

where the m_j's are the mass eigenstates of the neutrino and U_{ej}'s are the elements of the mixing matrix between the flavor states and mass eigenstates.

Experimentally, the measurement limit of half life is often used as the sensitivity to probe the rare event [7]. In a measurement with nonnegligible backgrounds, the sensitivity becomes

$$T_{1/2}^{0\nu} \propto \delta\varepsilon\sqrt{\frac{Mt}{b\Delta E}}, \tag{3}$$

where δ is the concentration of $\beta\beta$ isotope in the detector, ε is the detection efficiency, M is the detector mass, t is the measurement time, b is the background rate per unit mass and energy, and ΔE is the energy resolution of the detector, in other words, the region of interest (ROI) of the energy window at the $Q_{\beta\beta}$ value. However, in a case of a zero-background experiment that observes no event in ROI during the measurement time, the sensitivity becomes proportional to the detector mass and the measurement time,

$$T_{1/2}^{0\nu} \propto \delta\varepsilon M t. \tag{4}$$

To increase the detection sensitivity, it is essential to have a detector with high concentration of the isotope of interest, detection efficiency, energy resolution, and efficient background rejection capability as well as to minimize backgrounds from internal and external sources in the region of interest. High energy resolution and detection efficiency experiment can be realized with crystal detectors containing the isotope of interest. The detector performance of recently developed low temperature detectors (LTDs) that operate at sub-Kelvin temperatures can perfectly meet the requirements by utilizing state-of-the-art detector technologies with extreme energy sensitivity, such as neutron transmutation doped (NTD) Ge thermistors, superconducting transition edge sensors (TESs), or metallic magnetic calorimeters (MMCs) [8].

The AMoRE (Advanced Mo-based Rare process Experiment) project is an experiment to search for $0\nu\beta\beta$ of ^{100}Mo [9]. AMoRE uses $CaMoO_4$ crystals as the absorber and MMCs as the sensor [10, 11]. $CaMoO_4$ is a scintillating crystal that has the highest light output at room and low temperatures among Mo-containing crystals (molybdates) [12, 13].

Choosing of ^{100}Mo as the source of $0\nu\beta\beta$ is advantageous. The nucleus has a high Q value of 3034.40(17) keV [14] that is above the intensive 2615 keV gamma quanta from ^{208}Tl decay (^{232}Th family). The natural abundance of ^{100}Mo is 9.8% [15], which is comparatively high. Furthermore, enriched ^{100}Mo can be produced by centrifugation method in amount of tens of kilograms per year with a reasonable price. Also, the theoretically estimated half life of ^{100}Mo is relatively shorter than that of other $0\nu\beta\beta$ candidates [16, 17]. However, $2\nu\beta\beta$ of ^{48}Ca with $Q_{\beta\beta} = 4272$ keV (despite rather low concentration of the isotope $\approx$ 0.2%) can be an irremovable background source in the ROI of ^{100}Mo. The AMoRE collaboration has successfully grown $^{40}Ca^{100}MoO_4$ crystals using ^{100}Mo enriched and ^{48}Ca depleted materials. Three of the doubly-enriched crystals with masses in the range of 0.2–0.4 kg were tested in a low background 4π veto system to determine their internal backgrounds [18].

The present experimental work aims to test the low temperature detection concept with a $CaMoO_4$ crystal and an MMC that is suitable for a high resolution experiment to search for $0\nu\beta\beta$ of ^{100}Mo. A 216 g natural $CaMoO_4$ crystal with an MMC phonon sensor was employed in this experiment, which was performed in an overground measurement facility. The energy resolution and linearity of the detector setup, particle, and randomly coinciding events discrimination by pulse shape analysis for background rejection in a $0\nu\beta\beta$ experiment are discussed in this report.

2. Experimental Details

The detector setup was structured in a cylindrical shape with copper support details as shown in Figure 1. A $CaMoO_4$ crystal, 4 cm in diameter and 4 cm height, was mounted inside the copper structure using metal springs. The mass of the crystal was 216 g. It was grown with natural Ca and Mo elements at the Bogoroditsk plant in Russia. A patterned gold film was evaporated on one side of the crystal to serve as a phonon collector. An MMC device, the primary sensor for detecting the phonon signals absorbed in the gold film, was placed on a semicircular copper plate over the crystal. The thermal connection between the gold film and the MMC was made using annealed gold wires. Details regarding the measurement principle and the detector structure of the MMC device were presented in previous reports [19, 20].

When a particle hits a dielectric material, most of the energy deposited into the absorber is converted into the form of phonons. High energy phonons with frequencies that are close to the Debye frequency are generated initially. However, they quickly decay to lower frequency phonons via anharmonic processes. When their energy becomes 20–50 K, they can travel ballistically in the crystal [21].

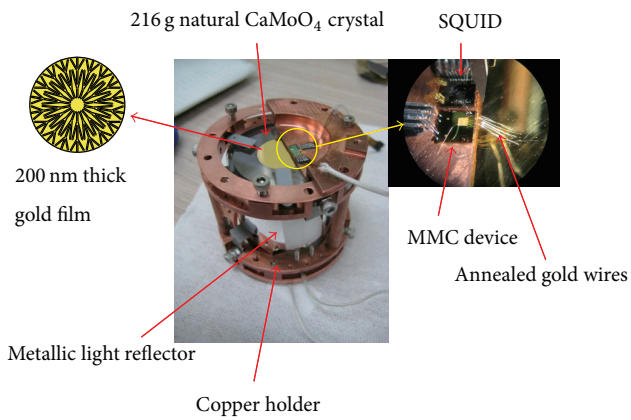

Figure 1: (Color online) low temperature detector setup with a 216 g $CaMoO_4$ crystal and an MMC sensor.

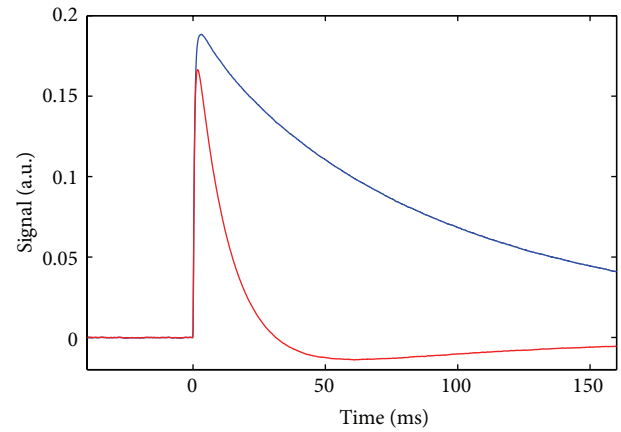

Figure 2: (Color online) a typical signal of 2.6 MeV gamma-ray full absorption events at 40 mK in DC (blue, bigger) and AC (red, smaller) coupling.

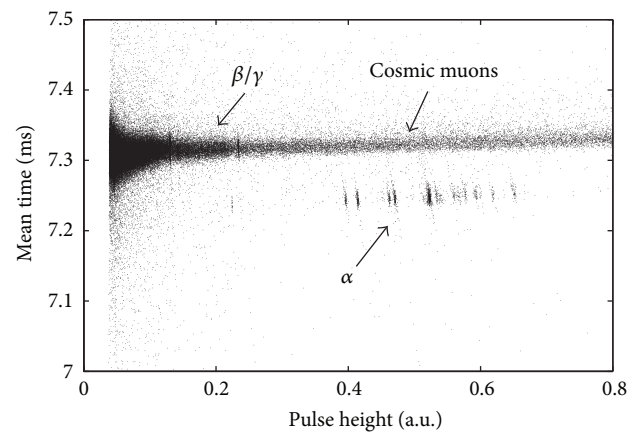

Figure 3: A scatter plot of the mean-time and pulse height obtained from the background measurement of 95 h in an overground laboratory. α and β/γ (including cosmic muons) events are clearly separated in terms of their mean-time values.

The major down-conversion processes of these athermal phonons are isotope scattering, inelastic scatterings by impurities and lattice dislocations, and inelastic scatterings at crystal surfaces [22]. These excess phonons eventually change the equilibrium thermal phonon distribution, thereby causing temperature increase.

In the detector setup with the $CaMoO_4$ crystal and the gold phonon collector film, the ballistic athermal phonons can hit the crystal and gold interface, transmit into the gold film, and transfer their energy to the electrons in the film [23]. The electron temperature of the gold film increases quickly via electron-electron scatterings. This temperature change is measured by the MMC sensor that is thermally connected with the gold wires. The size of the gold film and number of gold wires were chosen based on a thermal model study that considered the efficient athermal heat flow process [11]. Consequently the gold film had a diameter of 2 cm, a thickness of 200 nm, and an additional gold pattern of 200 nm thickness on top of the gold film to increase the lateral thermal conductivity of the gold film.

The detector assembly was installed in a dilution refrigerator in an overground laboratory at KRISS (Korea Research Institute of Standards and Science). The refrigerator was surrounded by a 10 cm thick lead shield (except the top surface) to reduce environmental gamma-ray background. The detector with an MMC operates well in the temperature range of 10–50 mK. The signal size increases at lower temperatures since the MMC sensitivity enhanced and the heat capacities decreased. However, the signals have slower rise and decay times at lower temperatures as thermal conductances become poorer. Larger signal size improves the energy threshold and baseline energy resolution of the detector. The energy resolution of the detector measured for particle absorption events can be worse than the baseline resolution because of any uncorrelated mechanism that affects the signal size and shape. Examples of such mechanisms include temperature fluctuations due to instrumental instability or frequent event rates, position dependence of signal shapes, or scintillation processes that are associates with phonon generations in an inhomogeneous way. Therefore, larger signal size does not guarantee a better energy resolution at certain temperatures. At the present experimental condition including the background rate from cosmic muons and external gamma-rays, 40 mK was selected as the main measurement temperature. At this temperature, about 1 ms rise-time was obtained for the 2.6 MeV gamma line without degrading the energy resolution. A typical signal of 2.6 MeV gamma-ray full absorption events is shown in Figure 2. The rise-time of the DC coupled signal is 1.1 ms, which is somewhat slower than that of earlier measurements for which shorter gold wires were used [11].

3. Pulse Shape Analysis

A two dimensional scatter plot of the pulse heights and mean-times of signals obtained in a 95 h background measurement is shown in Figure 3. The pulse height is the difference between the maximum value and baseline level of a signal. The maximum value is found using a quadratic polynomial

fit to the region of the signal near the pulse maximum. The baseline level is the average voltage value in the time region before the signal rises. The mean-time parameter is defined as

$$t_{\text{mean}} = \frac{\sum_{t_{10}-l}^{t_{10}+r} \left(v_t \times \left(t - t_{10}\right)\right)}{\sum_{t_{10}-l}^{t_{10}+r} v_t}, \quad (5)$$

where v_t is the measured voltage value at time t subtracting the baseline level, t_{10} is the time when it reaches 10% of the pulse height, and l and r indicate the time length of the signal toward left and right directions from t_{10}, respectively, to calculate the mean-time. l is set to reach the time at the baseline level, while r is a free parameter that was selected to achieve the most efficient particle discrimination. Here, the r value was set to not include the negative part of an AC coupled signal (see Figure 2), which was used for the energy spectrum because it was recorded with finer digitizer resolution (i.e., bigger gain is used) than the DC coupled signal.

The pulse-shape discrimination (PSD) between α and β/γ particles can be realized with the mean-time as a pulse shape parameter due to the difference in the rise and decay times of the two types of events. A similar tendency of PSD was reported for other low temperature scintillating detectors [24]. The separation into two groups of the events in the energy region between 4 and 5 MeV of alpha-equivalent energy can be readily observed from the distribution of mean-time values shown in Figure 4. The energy of α induced events was determined as described in the following section. Although the two peaks have noticeable right-hand tails toward higher mean-time values, normal Gaussian functions were used to fit the distributions. We interpret the right-hand tails as a result of signal pile-up. A parameter of discrimination power (DP) is defined as

$$\text{DP} = \frac{\mu_1 - \mu_2}{\sqrt{\sigma_1^2 + \sigma_2^2}}, \quad (6)$$

where μ_i are the mean values and σ_i are the standard deviations of the Gaussian distributions for α and β/γ events. DP was found to be 7.6.

The averaged pulse shapes for the two groups of events are compared in Figure 5. Templates of α events were obtained by averaging out the ^{232}Th α-decay events pulse profiles with energy release in the crystal 4082 keV (due to the contamination of the crystal by thorium), whereas the events caused by cosmic muons with the same pulse height were selected for the template of β induced events. The normalized pulses of alpha and beta templates are aligned at the time of their maximum values, as shown in Figure 5. Both the rise and decay times of the α and β signals are clearly different. The signals induced by α events have faster rise and faster decay than those of the β events.

According to scintillation measurements of a $CaMoO_4$ crystal at 7–300 K [25, 26], the scintillation decay time of the $CaMoO_4$ crystal reaches hundreds of μs at 7 K. The crystal also shows different light outputs for α and β/γ events [27]. A slowly decaying scintillation mechanism would cause slow generation of phonon in the $CaMoO_4$ crystal. α and β/γ particle events may have different fractions of slow component for phonon generation. This difference in slow phonon generation at mK temperatures may induce different pulse shapes for α and β/γ particle events.

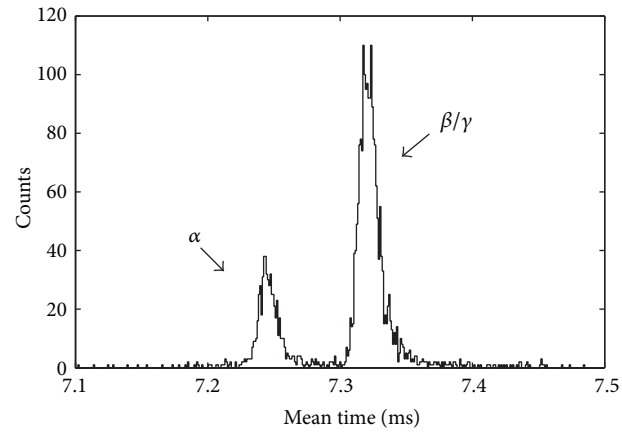

Figure 4: Distribution of mean-time parameter in 4 MeV < E < 5 MeV region of alpha-equivalent energy. Discrimination power was found to be 7.6 from fitting each group of distribution with a normal Gaussian function. Right-hand side tail is noticeable for the two groups toward higher mean-time value.

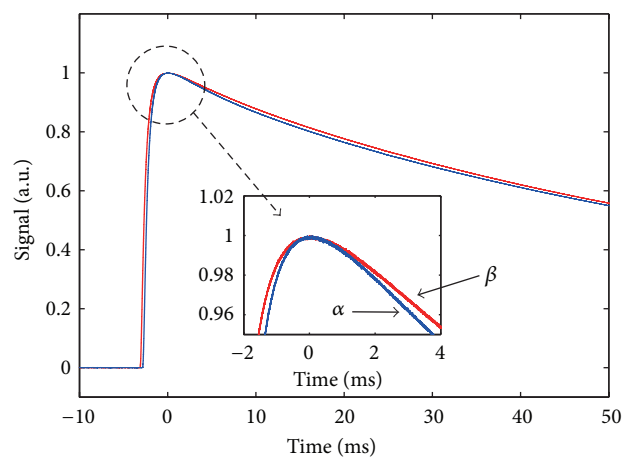

Figure 5: (Color online) averaged pulse shapes of α induced signals from ^{232}Th decays (blue) and the corresponding (i.e., with the same pulse height) muon-induced signals (red). The signals are normalized for their pulse height and shifted in time to align the maximum point of signals.

4. Energy Spectrum

Because athermal phonon absorption in the phonon collector significantly contributes to the signal size [11], the signals have some degrees of position dependence for their pulse height and shape. In this detector, the signals with faster rise-times show bigger pulse heights for the same energy events. This effect can be observed in Figure 3. The distribution of

mean-time values and pulse heights for alpha and gamma-ray full absorption lines has anticorrelated slopes. This negative slope more dominantly appears in the alpha signals, which is likely because the full-energy γ peaks originate from multiple Compton scatterings in the crystal that smear the position dependence on the event location. The pulse height is not an optimal parameter to obtain a high resolution. In the optimal filtering method [28] that is often adopted in high resolution microcalorimeters, the signals are assumed to have one shape but with different amplitudes. Thus, the optimal filtering method is not applicable to provide a high resolution spectrum for the present signals.

In the present analysis, a new parameter LA (left area) was used as an amplitude parameter to reduce the position dependence effect of the large crystal detector. It is defined as

$$\mathrm{LA} = \sum_{t_{10}-l}^{t_{\mathrm{mean}}} v_t, \tag{7}$$

where the variables are as defined in (5). LA is a partial integration for the leading part of a signal. Because the integration range of the LA parameter is set by a shape-dependent parameter, the mean-time, this parameter is less influenced by the pulse shape. For instance, the correlation coefficient between the pulse height and mean-time was −0.62 for 4082 keV α signals, but it was 0.08 between the LA and mean-time.

In a calibration run, a thoriated tungsten rod was used as an external gamma-ray source. The source was placed in the gap between the cryostat and the lead shield.

When a linear energy calibration was applied to gamma-ray peaks, deviations from the linear calibration of less than 0.4% were found for low-energy peaks. A quadratic function with no constant term was used for the calibration of electron-equivalent energy for 511, 583, 911, and 2615 keV peaks for the spectrum shown in Figure 6. The corresponding energy resolutions of the peaks are listed in Table 1.

Figure 7 shows the linearities of the electron and alpha signals. The LA values of the electron and alpha peaks divided by the linear calibration of the gamma-ray peaks are plotted in the upper figure. The LA/energy ratios for the alpha peaks are about 6% larger than those for the gamma-ray peaks. The quadratic fit functions are shown as dotted and dashed lines for gamma and alpha peaks, respectively. The residuals in the lower figure indicate deviations from the quadratic functions for the two groups. With the quadratic calibration, a very small deviation is expected near 3 MeV for electron measurements. It implies that this method can supply an accurate energy calibration at the $Q_{\beta\beta}$ value of the $2\nu\beta\beta$ of ^{100}Mo.

Alpha events can be separated from β/γ events using the mean-time parameter. The energy spectrum of alpha events is shown in Figure 8. An energy calibration for this spectrum was performed with a quadratic function for the alpha peaks as discussed above. These backgrounds were bulk events of alpha decays in the crystal, mainly from radionuclides of U and Th decay chains, most of them are identified as shown in Figure 8. Because this crystal was developed to investigate the scintillation properties of $CaMoO_4$, its internal background was not exceptionally low. The AMoRE collaboration has developed $^{40}Ca^{100}MoO_4$ growing technology with low radioimpurities. Internal alpha activities of about 80 μBq/kg of ^{226}Ra and 70 μBq/kg of ^{228}Th were found in a 196 g $^{40}Ca^{100}MoO_4$ [18].

Not only alpha signals can be rejected efficiently, but also β decays of ^{212}Bi, ^{214}Bi, and ^{208}Tl can be tagged and eliminated from the data by using information about associated alpha-emitting nuclides. Random pile-ups of events (first of all from the $2\nu\beta\beta$) could be a substantial source of background of LTD to search for $0\nu\beta\beta$ due to the poor time resolution [29]. Relatively fast response of the MMC among the LTDs is a certain advantage to discriminate the background.

Table 1: Energy resolutions of gamma-ray full absorption peaks in the calibration measurement.

Energy (keV)	FWHM (keV)
511	7.2 ± 0.6
583	6.5 ± 0.5
911	6.8 ± 0.3
2615	10.9 ± 0.4

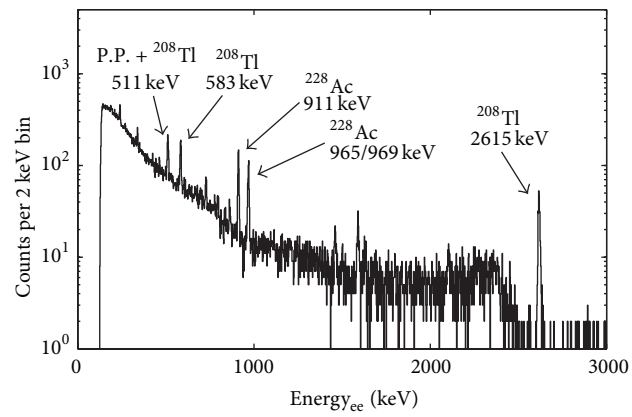

Figure 6: Energy spectrum measured with an external source over 65 h.

5. Conclusion

LTDs made of crystal scintillators containing isotopes of interest have distinct advantages in $0\nu\beta\beta$ searches. Such LTDs make it possible to provide a high detection efficiency to the $0\nu\beta\beta$. Taking the advantage of high resolution sensor technologies, these dielectric detectors in the heat (phonon) measurement can have comparable energy resolution to those of HPGe detectors. The comparison in heat/light measurement channels makes unambiguous separation of alpha events from electron events. As discussed in this report, pulse shape discrimination is also possible using only the phonon measurement. This PSD capability of the phonon sensor increases discrimination power for alpha background signals or can simplify the detector cell design by using only one phonon sensor without a photon sensor that is commonly

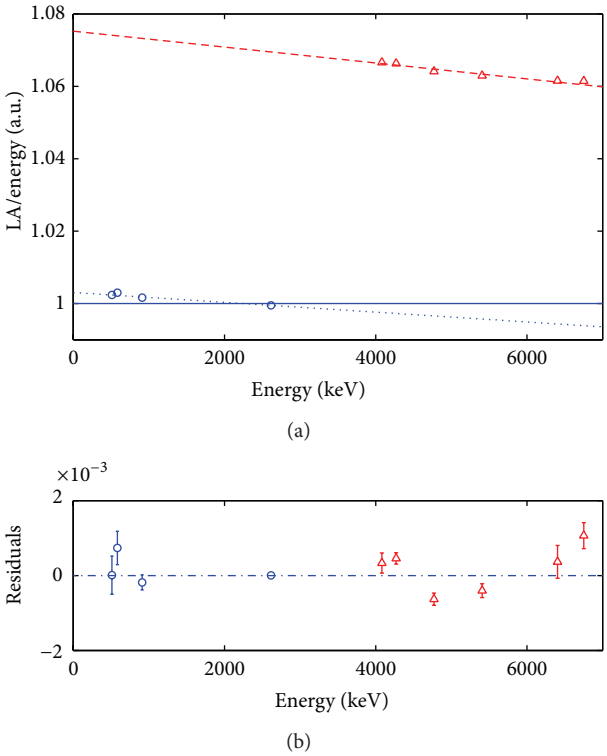

Figure 7: (Color online) ratio of signal amplitude (LA) and energy in linear calibration for γ (circle, blue) and α (triangle, red) peaks (a). Quadratic calibration lines (dotted and dashed lines) are shown for γ and α peaks, respectively. Deviations of the ratios from each quadratic functions are shown in (b).

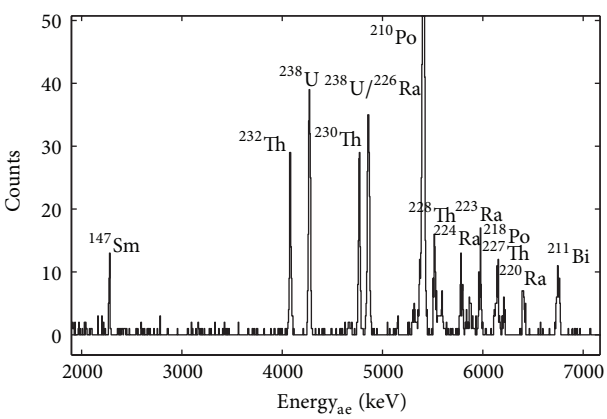

Figure 8: Energy spectrum of bulk alpha events in a background measurement.

used for particle discrimination [30] and will reduce the number of measurement channels.

In comparison with signals from PMTs or conventional semiconductor detectors, phonon signals from a crystal detector in the LTD concept are typically slow. Even though the energy resolution of these detectors does not suffer from the slow signal in the low activity environment of an underground experiment, random coincidence of events leads to an unavoidable background because of the slow rise-time [29]. Two consecutive electron events that occur in a time interval that is much shorter than the signal rise-time can be regarded as a single event. Such randomly coincident events, particularly of $2\nu\beta\beta$, are an unavoidable source of backgrounds in the $0\nu\beta\beta$ taking into account that the $2\nu\beta\beta$ event rate of ^{100}Mo is expected to be about 10 mBq in 1 kg $^{40}Ca^{100}MoO_4$.

In the present experiment, the phonon signals had rise-times of 1.1 ms, which is much faster than the rise-times of LTDs with NTD Ge thermistors. The fast rise-time provides efficient rejection possibility for randomly coincident events [31]. Moreover, a photon detector composed of a 2 inch Ge wafer and an MMC sensor showed a temperature independent rise-time of about 0.2 ms with reasonable energy resolution [32]. Simultaneous measurements with the photon detector will increase the discrimination power not just for alpha events but also for randomly coincident events.

For the AMoRE project, $^{40}Ca^{100}MoO_4$ crystals will be used as the detector material together with MMCs in phonon and photon measurement setups. We aim to reach a zero background with improved energy resolution of a few keV. The first stage experiment is expected to be constructed with a 10 kg prototype detector by 2016. We plan to perform a large scale experiment with 200 kg $^{40}Ca^{100}MoO_4$ crystals in the next 5-6 years. The sensitivity of the experiment to the effective Majorana neutrino mass is estimated to be in the range of 20–50 meV, which corresponds to the inverted scheme of the neutrino mass.

Conflict of Interests

The authors declare that there is no conflict of interests regarding the publication of this paper.

Acknowledgments

This research was funded by Grant no. IBS-R016-G1 and partly supported by the National Research Foundation of Korea Grant funded by the Korean Government (NRF-2011-220-C00006 and NRF-2013K2A5A3000039). F. A. Danevich was supported in part by the Space Research Program of the National Academy of Sciences of Ukraine.

References

[1] J. Beringer, J. F. Arguin, R. M. Barnett et al., "Review of particle physics," *Physical Review D*, vol. 86, Article ID 010001, 2012.

[2] R. N. Mohapatra, S. Antusch, K. S. Babu et al., "Theory of neutrinos: a white paper," *Reports on Progress in Physics*, vol. 70, no. 11, pp. 1757–1867, 2007.

[3] S. R. Elliott and P. Vogel, "Double beta decay," *Annual Review of Nuclear and Particle Science*, vol. 52, pp. 115–151, 2002.

[4] F. T. Avignone, S. R. Elliott, and J. Engel, "Double beta decay, Majorana neutrinos, and neutrino mass," *Reviews of Modern Physics*, vol. 80, p. 481, 2008.

[5] W. Rodejohann, "Neutrino-less double beta decay and particle physics," *International Journal of Modern Physics E*, vol. 20, no. 9, pp. 1833–1930, 2011.

[6] A. Giuliani and A. Poves, "Neutrinoless double-beta decay," *Advances in High Energy Physics*, vol. 2012, Article ID 857016, 38 pages, 2012.

[7] J. J. Gómez-Cadenas, J. Martín-Albo, M. Mezzetto, F. Monrabal, and M. Sorel, "The search for neutrinoless double beta decay," *Rivista del Nuovo Cimento*, vol. 35, no. 2, pp. 29–98, 2012.

[8] C. Enss, *Cryogenic Particle Detection*, vol. 99, Springer, 2005.

[9] H. Bhang, R. S. Boiko, D. M. Chernyak et al., "AMoRE experiment: a search for neutrinoless double beta decay of ^{100}Mo isotope with ^{40}Ca $^{100}MoO_4$ cryogenic scintillation detector," *Journal of Physics: Conference Series*, vol. 375, no. 4, Article ID 042023, 2012.

[10] S. J. Lee, J. H. Choi, F. A. Danevich et al., "The development of a cryogenic detector with $CaMoO_4$ crystals for neutrinoless double beta decay search," *Astroparticle Physics*, vol. 34, no. 9, pp. 732–737, 2011.

[11] G. B. Kim, S. Choi, Y. S. Jang et al., "Thermal model and optimization of a large crystal detector using a metallic magnetic calorimeter," *Journal of Low Temperature Physics*, vol. 176, no. 5-6, pp. 637–643, 2014.

[12] H. J. Kim, A. N. Annenkov, R. S. Boiko et al., "Neutrino-less double beta decay experiment using $Ca_{100}MoO_4$ scintillation crystals," *IEEE Transactions on Nuclear Science*, vol. 57, no. 3, pp. 1475–1480, 2010.

[13] S. Pirro, J. W. Beeman, S. Capelli, M. Pavan, E. Previtali, and P. Gorla, "Scintillating double-beta-decay bolometers," *Physics of Atomic Nuclei*, vol. 69, no. 12, pp. 2109–2116, 2006.

[14] S. Rahaman, V.-V. Elomaa, T. Eronen et al., "Q values of the 76Ge and 100Mo double-beta decays," *Physics Letters B: Nuclear, Elementary Particle and High-Energy Physics*, vol. 662, no. 2, pp. 111–116, 2008.

[15] M. E. Wieser and J. R. D. Laeter, "Absolute isotopic composition of molybdenum and the solar abundances of the p-process nuclides ^{92,94}Mo," *Physical Review C*, vol. 75, Article ID 055802, 2007.

[16] J. Barea, J. Kotila, and F. Iachello, "Limits on neutrino masses from neutrinoless double-β decay," *Physical Review Letters*, vol. 109, no. 4, Article ID 042501, 2012.

[17] J. D. Vergados, H. Ejiri, and F. Šimkovic, "Theory of neutrinoless double-beta decay," *Reports on Progress in Physics*, vol. 75, no. 10, Article ID 106301, 2012.

[18] J. H. So, H. J. Kim, V. V. Alenkov et al., "Scintillation properties and internal background study of $^{40}Ca^{100}MoO_4$ crystal scintillators for neutrino-less double beta decay search," *IEEE Transactions on Nuclear Science*, vol. 59, no. 5, pp. 2214–2218, 2012.

[19] W. S. Yoon, Y. S. Jang, G. B. Kim et al., "High energy resolution cryogenic alpha spectrometers using magnetic calorimeters," *Journal of Low Temperature Physics*, vol. 167, no. 3-4, pp. 280–285, 2012.

[20] W. S. Yoon, G. B. Kim, H. J. Lee et al., "Fabrication of metallic magnetic calorimeter for radionuclide analysis," *Journal of Low Temperature Physics*, vol. 176, no. 5-6, pp. 644–649, 2014.

[21] J. P. Wolfe, *Imaging Phonons: Acoustic Wave Propagation in Solids*, Cambridge University Press, 2005.

[22] S. W. Leman, "Invited review article: physics and Monte Carlo techniques as relevant to cryogenic, phonon, and ionization readout of Cryogenic Dark Matter Search radiation detectors," *Review of Scientific Instruments*, vol. 83, Article ID 091101, 2012.

[23] Y. H. Kim, H. Eguchi, C. Enss et al., "Measurements and modeling of the thermal properties of a calorimeter having a sapphire absorber," *Nuclear Instruments and Methods in Physics Research A: Accelerators, Spectrometers, Detectors and Associated Equipment*, vol. 520, no. 1–3, pp. 208–211, 2004.

[24] C. Arnaboldi, C. Brofferio, O. Cremonesi et al., "A novel technique of particle identification with bolometric detectors," *Astroparticle Physics*, vol. 34, no. 11, pp. 797–804, 2011.

[25] V. B. Mikhailik, S. Henry, H. Kraus, and I. Solskii, "Temperature dependence of $CaMoO_4$ scintillation properties," *Nuclear Instruments and Methods in Physics Research A*, vol. 583, no. 2-3, pp. 350–355, 2007.

[26] V. B. Mikhailik and H. Kraus, "Performance of scintillation materials at cryogenic temperatures," *Physica Status Solidi B*, vol. 247, no. 7, pp. 1583–1599, 2010.

[27] A. N. Annenkov, O. A. Buzanov, F. A. Danevich et al., "Development of CaMoO4 crystal scintillators for a double beta decay experiment with 100Mo," *Nuclear Instruments and Methods in Physics Research A*, vol. 584, no. 2-3, pp. 334–345, 2008.

[28] Y. N. Yuryev, Y. S. Jang, S. K. Kim et al., "Signal processing in cryogenic particle detection," *Nuclear Instruments and Methods in Physics Research A: Accelerators, Spectrometers, Detectors and Associated Equipment*, vol. 635, no. 1, pp. 82–85, 2011.

[29] D. M. Chernyak, F. A. Danevich, A. Giuliani, E. Olivieri, M. Tenconi, and V. I. Tretyak, "Random coincidence of $2\nu2\beta$ decay events as a background source in bolometric $0\nu2\beta$ decay experiments," *European Physical Journal C*, vol. 72, no. 4, pp. 1–6, 2012.

[30] D. Artusa, F. Avignone III, O. Azzolini et al., "Exploring the neutrinoless double beta decay in the inverted neutrino hierarchy with bolometric detectors," http://arxiv.org/abs/1404.4469.

[31] D. M. Chernyak, F. A. Danevich, A. Giuliani et al., "Rejection of randomly coinciding events in ZnMoO TeX scintillating bolometers," *The European Physical Journal C*, vol. 74, p. 2913, 2014.

[32] H. J. Lee, C. S. Kang, S. R. Kim et al., "Development of a scintillation light detector for a cryogenic rare-event-search experiment," submitted in *Nuclear Instruments and Methods in Physics Research Section A*.

Hindawi Publishing Corporation
Advances in High Energy Physics
Volume 2015, Article ID 632131, 11 pages
http://dx.doi.org/10.1155/2015/632131

Research Article

Convoluted ν-Signals on ^{114}Cd Isotope from Astrophysical and Laboratory Neutrino Sources

Vaitsa Tsakstara[1,2]

[1] *Technological Education Institute of Western Macedonia, 51100 Grevena, Greece*
[2] *Division of Theoretical Physics, University of Ioannina, 45110 Ioannina, Greece*

Correspondence should be addressed to Vaitsa Tsakstara; vtsaksta@cc.uoi.gr

Received 9 July 2014; Revised 28 February 2015; Accepted 2 March 2015

Academic Editor: Theocharis Kosmas

At first, we evaluate scattering cross sections of low, and intermediate-energy neutrinos scattered off the ^{114}Cd isotope, the most abundant Cd isotope present also in the COBRA detector (CdTe and CdZnTe materials) which aims to search for double beta decay events and neutrino observations at Gran Sasso laboratory (LNGS). The coherent ν-nucleus channel addressed here is the dominant reaction channel of the neutral current ν-nucleus scattering. Our ν-nucleus cross sections (calculated with a refinement of the quasiparticle random-phase approximation, QRPA) refer to the $gs \rightarrow gs$ transitions for ν-energies $\varepsilon_\nu \leq 100$ MeV. Subsequently, simulated ν-signals on ^{114}Cd isotope are derived. Towards this purpose, the required folded cross section comes out of simulation techniques by employing several low, and intermediate-energy neutrino distributions of the astrophysical ν-sources, like the solar, supernova, and Earth neutrinos, as well as the laboratory neutrinos, the reactor neutrinos, the pion-muon stopped neutrinos, and the β-beam neutrinos.

1. Introduction

In the past few decades neutrinos attracted a great part of the effort of the authors working in Nuclear, Astroparticle Physics and Cosmology [1–8]. Many neutrino experiments like the KamLAND [9], Borexino [10, 11], SNO+ [12], LENA [13], and other experiments, with high precision detectors aim to measure different types of neutrinos as well as neutrino-nucleus cross sections. Measurements in the beta-beam neutrino experiments [14–16] or in the expected to be built near spallation neutron sources (ORLAND experiment, Spallation Source) [17–20] may help answer key questions about the neutrino properties, the evolution of distant massive stars, the structure of the interior of our planet [21–23], and the fundamental electroweak interactions.

In recent terrestrial experiments aiming at neutrino studies through ν-nucleus interactions, the characteristics of the neutrino fluxes emitted by various neutrino sources like the astrophysical ν-sources (supernova, solar, and Earth neutrinos) or the laboratory ν-sources (accelerated β-decay ions in storage rings [15, 16], pion-muon decay at rest, e.g., at Fermilab [24], reactor neutrinos, etc.) are encoded on the nuclear response of the detector materials. On the theoretical side, the nuclear responses of ν-detectors to the energy spectra of the observed neutrino flux could be simulated by convoluted (folded) cross sections. The latter are obtained by using original ν-nucleus cross sections calculations and realistic descriptions for the ν-beam of the studied neutrino source [25–27], that is, reliable ν-energy distributions.

In the present paper, we study extensively the nuclear response to low and intermediate-energy neutrinos of the ^{114}Cd isotope focusing on the computation of flux averaged cross sections of this nucleus for various neutrino energy spectra. The Cd isotopes constitute significant materials of the semiconductors CdZnTe and CdTe detectors of the COBRA experiment which is aiming to search for double beta decay events and neutrino observations at Gran Sasso laboratory (LNGS) [4, 5, 12]. Calculation of the induced ν-signal in such nuclear detectors involves, first, evaluation of the flux of the neutrinos arriving at the detector and, second, folding of the calculated cross section of the neutrino interaction with the nuclear detector [6, 8]. The present

work is an extension of our previous studies which address inelastic cross sections of neutrinos scattered off the Te and Zn isotopes contents of the COBRA detector [6, 8, 28]. We pay special attention to the calculations of the elastic (coherent) neutral current (NC) neutrino-nucleus reaction cross sections for the ^{114}Cd nucleus (the most abundant isotope in the natural Cd). For similar calculations on other Cd isotopes the reader is referred to [29]. As it is well known, in NC ν-nucleus scattering the $gs \rightarrow gs$ transitions represent the dominant reaction channel [6, 30]. In terrestrial experiments the detection of this channel may be achieved through a measurement of the nuclear recoil signal [31–33] which is a rather different signature compared to that of the incoherent channel [1, 3, 6, 8, 34]. Inelastic scattering of neutrinos on nuclei creates different signal and could be studied through the outgoing charged-lepton and extracted nucleons and/or γ-ray emission. These channels have been studied in detail elsewhere (see, e.g., [6, 8, 30]).

For detectors of supernova neutrinos, all neutrino and antineutrino flavours take part in NC scattering on nuclear detectors (specifically heavy flavour neutrinos can be detected too) [4, 5, 35] while only electron-neutrino (ν_e) charged-current reactions are important (only a small portion of ν_x neutrinos has energy above the mass of the x-lepton which constitutes the main detection signal).

The solar neutrinos, which represent a powerful tool to investigate the Sun's deep interior [36, 37], have provided precious information to understand new physics and the interpretation of neutrino oscillations. Future experiments, like the SNO+ [12], are expected to contribute crucially in order to explore the CNO-cycle neutrino flux and clarify the open issue of the Sun's core metalicity.

Recently, geoneutrinos which are $\tilde{\nu}_e$ antineutrinos produced from decays of natural radioactive elements (predominantly ^{40}K and nuclides in the ^{238}U and ^{232}Th chains) mainly in the crust and mantle of the Earth have been successfully detected by the liquid-scintillator experiments of the KamLAND [38] and Borexino Collaborations [39], but the geological information contained in these measurements is still limited [40, 41]. Geoneutrinos are direct messengers of the abundance and matter distribution of radioactive elements deep within our planet, information that provides strong constraints on several phenomena occurring inside the Earth [42, 43]. Concerning the energy distribution of geoneutrinos, up to now little is known due to the fact that this is a new research field, but in the near future experiments like LENA, SNO+, and others, having in their objectives to explore geoneutrinos, are expected to provide us with new data. From the currently known information we imply that their energy range is $0 \leq \varepsilon_\nu \leq 10$ MeV.

It is expected [28] that the response of the Cd isotopes in the particle-bound excitation region, which coincides with the energy range of geoneutrinos, is rather rich and this motivates our present calculations. The next-generation detectors (LENA, Borexino, SNO) are expected to give useful answers to several questions of geological importance regarding the precise geo-ν fluxes and abundances of natural radioactive elements (K, U, and Th) in the Earth's interior [40–43].

One of the main goals of the present work is to focus on the interpretation of various ν-signals generated in nuclear detectors of terrestrial experiments through the investigation of the nuclear response of Cd detector medium to the corresponding neutrino energy spectra. We emphasize on signals coming from geo-, supernova-, solar-, reactor-, pion-muon stopped-neutrinos by using the following basic theoretical ingredients: (i) the calculated coherent total cross sections of the neutral-current reaction $^{114}\mathrm{Cd}(\nu,\nu')^{114}\mathrm{Cd}^*$ computed with a refinement of the quasiparticle random-phase approximation (QRPA), (ii) reliable descriptions of the shapes of neutrino energy distributions provided mostly from numerical simulations of distributions of low energy neutrinos, and (iii) computational tools required for the folding procedure in order to simulate the signal expected to be recorded on Cd detectors as the CdTe or CdZnTe (the detector medium of COBRA experiment) from low-energy ν sources (geo-, reactor-, and solar-neutrinos) and intermediate-energy neutrinos (supernova and laboratory-neutrinos).

The paper is organized as follows. At first (Section 2) the main formalism is described and our cross section calculations are presented. Then, (Section 3), a description of the main characteristics of the low- and intermediate-energy neutrino sources addressed here is briefly summarized and folded cross sections as well as event rates for neutral current neutrino scattering off the ^{114}Cd isotope are discussed. Finally (Section 4), the main conclusions of the present work are extracted.

2. Brief Description of the Formalism

2.1. Angle Differential Coherent ν-Nucleus Cross Section. The angle differential cross section $d\sigma/d\Omega$ of the elastic scattering of a neutrino with energy ε_ν on a nucleus (A, Z) is [34, 44]

$$\frac{d\sigma}{d\Omega} = \frac{G_F^2}{4\pi^2}\varepsilon_\nu^2 (1+\cos\vartheta)\frac{Q_w^2}{4}\mathcal{F}\left(q^2\right)^2, \quad (1)$$

where G_F is the Fermi coupling constant and $\mathcal{F}(q^2)$ contains the nuclear dependence of the cross section given by

$$\mathcal{F}\left(q^2\right) = \frac{1}{Q_w}\left[NF_N\left(q^2\right) + \left(1-4\sin^2\vartheta_W\right)ZF_Z\left(q^2\right)\right]. \quad (2)$$

In (1), ϑ represent the scattering angle and Q_w denotes the weak charge of the target nucleus:

$$Q_w = N + \left(1-4\sin^2\vartheta_W\right)Z, \quad (3)$$

(the weak mixing angle is $\sin^2\vartheta_W \approx 0.231$ [45]).

The ground state elastic nuclear form factors $F_Z(q^2)$ for protons and $F_N(q^2)$ for neutrons are defined by

$$F_k\left(q^2\right) = \frac{k}{4\pi}\int j_0\left(qr\right)\rho_{n,p}\left(r\right)d^3r, \quad k = N, Z \quad (4)$$

and are normalized as $F_{N,Z}(q^2 = 0) = 1$. In (4), $\rho_{n,p}(r)$ denote the neutron (n) and proton (p) charge density distribution

with $j_0(qr) = \sin(qr)/(qr)$ being the zero-order spherical Bessel function (we neglect a small correction from the single-nucleon form factors). The proton density $\rho_p(r)$ is often taken from experiment whenever measured charge densities are available [44, 46]. Moreover, some authors assume $F_N \approx F_Z$. From (1) we can easily obtain the expression with respect to the scattering angle ϑ as

$$\frac{d\sigma(\varepsilon_\nu, \vartheta)}{d\cos\vartheta} = \frac{G_F^2}{8\pi}(1+\cos\vartheta)\,\varepsilon_\nu^2 \cdot \left[f_V^p Z F_Z\left(q^2\right) + f_V^n N F_N\left(q^2\right)\right]^2, \tag{5}$$

where f_V^p and f_V^n stand for the polar-vector coupling for the weak neutral current for proton and neutron, respectively, given by:

$$f_V^p = -\frac{1-4\sin^2\vartheta_W}{2}, \qquad f_V^n = -\frac{1}{2}. \tag{6}$$

From the latter two equations one can imply that the consideration of $F_N(q^2)$ in the cross section is important especially for heavier ν-detection targets. Thus, the coherent cross section depends on the square of the ground state nuclear form factor $\mathcal{F}(q^2)$ at momentum transfer q^2 which (in the extreme-relativistic limit) is given by

$$q^2 = 2\varepsilon_\nu^2(1-\cos\vartheta), \tag{7}$$

or $q = 2\varepsilon_\nu \sin(\vartheta/2)$.

From (2), we see that, since $(1-4\sin^2\vartheta_W \approx 0.04)$ is small, a neutrino scattered elastically on a spin-zero nucleus couples mostly to the neutron distribution, $\rho_n(r)$. A measurement of the cross section for this process would, at some level, provide a determination of the neutron form factor $F_N(q^2)$. Some authors consider that this would be complementary to parity violating experiments because it would provide additional data, obtained at different energy ranges and with different nuclei that could be used to calibrate nuclear structure calculations [34, 44, 46–48].

2.2. Coherent Differential Cross Section with respect to Nuclear Recoil Energy T_A. From an experimental point of view and particularly for the neutrino facilities near spallation sources [18, 33] the expression of the coherent differential cross section with respect to the nuclear recoil energy T_A is also interesting. This is written as [31–33, 49]

$$\frac{d\sigma(\varepsilon_\nu, T_A)}{dT_A} = \frac{G_F^2}{4\pi} Q_W^2 M\left(1-\frac{MT_A}{2\varepsilon_\nu^2}\right) F\left(2MT_A^2\right), \tag{8}$$

where M is the nuclear mass and F denotes the ground state elastic form factor. More accurate expressions, including higher order terms with respect to T_A, can be found in [31–33, 50]. It should be noted that the signal on the coherent neutrino-nucleus scattering experiments is significantly different to that of the incoherent scattering where the signal could be an outgoing particle.

2.3. Total Coherent Cross Section. The total coherent cross section $\sigma_{\text{tot}}(\varepsilon_\nu)$ is obtained by integrating numerically Equation (5) over the angle ϑ ($\vartheta_{\min} = 0$ to $\vartheta_{\max} = \pi$) or (8) over T_A between

$$T_A^{\min} = \frac{T_A}{2} + \sqrt{\frac{T_A}{2}\left(M_A + \frac{T_A}{2}\right)} \tag{9}$$

to $T_A^{\max} = \infty$ [50]. Some authors [48], however, ignoring the momentum dependence of the nuclear form factors take $F_N(q^2) \approx F_Z(q^2) \approx 1$ and in this case the total coherent cross section $\sigma_{\text{tot}}(\varepsilon_\nu)$ is approximately written as

$$\sigma_{\text{tot}}(\varepsilon_\nu) = \frac{G_F^2}{8\pi}\left[Z(4\sin^2\vartheta_W - 1) + N\right]^2 \varepsilon_\nu^2. \tag{10}$$

Also, because $4\sin^2\vartheta_W - 1 \ll 1$ many authors take $\sigma_{\text{tot}} \propto N^2\varepsilon_\nu^2$ [48].

3. Results and Discussion

3.1. Original Cross Section Calculations. The neutral-current scattering of low- and intermediate-energy neutrinos, ν_l, and antineutrinos, $\tilde{\nu}_l$, off the most abundant Cd isotope of the COBRA detectors, that is, the ^{114}Cd isotope (with abundance 28.8%), the main subject of our present work, is represented by the reactions

$$\nu_l(\tilde{\nu}_l) + {}^{114}\text{Cd} \longrightarrow {}^{114}\text{Cd}^* + \nu_l'(\tilde{\nu}_l'), \tag{11}$$

($\ell = e, \mu, \tau$ and ^{114}Cd* denotes an excited state of ^{114}Cd isotope). We mention that the above reactions (also the CC reactions for $\ell = e$) play significant role in astrophysical environment since they affect the electron fraction Y_e of the stellar matter [21–23].

In the first stage of the present work, we evaluate original cross sections for the reactions of (11). These calculations refer to the coherent channel (ground state to ground state transitions) of the target nucleus ^{114}Cd [1, 6, 8, 51–53]. As can be seen from (5) the original cross section identically comes for scattering of neutrinos ν_l and antineutrinos $\tilde{\nu}_l$. However, as we will see in Section 3, the signal on the nuclear detector could be significantly different due to the different ν-energy distributions.

In this work, we use theoretical densities obtained from simple mean-field calculations using the successful Woods-Saxon effective interaction plus the monopole (pairing) Bonn C-D interaction.

The ground state $|J_i^{\pi_i}\rangle = |0^+\rangle$ of the studied (even-even) ^{114}Cd isotope is computed by solving iteratively the BCS equations. In Table 1, we list the values of the pairing parameters ($g_{\text{pair}}^{p,n}$) and the theoretical energy gaps ($\Delta_{p,n}^{\text{th}}$) for protons (p) and neutrons (n) determined at the BCS level for the ^{114}Cd isotope. These parameters renormalise the pairing force and adjust the gaps $\Delta_{p,n}^{\text{th}}$ to the empirical ones $\Delta_{p,n}^{\text{exp}}$ obtained through the application of the three-point formulae (see [8]). The values of the $g_{\text{pair}}^{p,n}$ that adjust the energy gaps in both cases are reliable (see Table 1).

Table 1: Parameters determining the BCS ground state pairing interactions for protons (g^p_{pair}) and neutrons (g^n_{pair}) and the relevant theoretical values of proton (Δ^{th}_p) and neutron (Δ^{th}_n) energy gaps. The latter reproduce well the corresponding (for ^{114}Cd isotope) empirical energy gaps, $\Delta^{\text{exp}}_{p,n}$, listed also in the table, obtained through the three-point formula [6]. The values of the harmonic oscillator size parameter b, used for ^{114}Cd isotope, are also shown.

Isotope	Z, N	Abundance (%)	b (fm)	g^n_{pair}	g^p_{pair}	Δ^{exp}_p	Δ^{th}_p	Δ^{exp}_n	Δ^{th}_n
^{114}Cd	48, 66	28.73	2.214	0.9564	0.9753	1.441	1.44108	1.351	1.35093

Afterwards, the proton and neutron nuclear form factors are obtained from the expression

$$F_k\left(q^2\right) = \frac{1}{k}\sum_j \hat{j}\left\langle (n\ell)\, j\right| j_0\left(qr\right)\left|(n\ell)\, j\right\rangle \left(V^k_j\right)^2, \quad k = N, Z, \tag{12}$$

where V^k_j is the single particle $(n\ell)\,j$-level occupation probability amplitude for protons or neutrons (the summation runs over the 15 active levels of the model space chosen which consists of the major harmonic oscillator shell with quantum number $N = 3, 4, 5$) as well as over the fully occupied core j-levels having $V^k_j = 1$.

In Figure 1, we show the ingredients required for (1) and (5) in order to calculate the differential and integrated coherent cross section for the neutrino reactions of (11). Figure 1(a) shows the theoretical form factors for protons (F_Z) and neutrons (F_N) obtained with our BCS calculations and Figure 2 shows the momentum dependence of $F_{N,Z}(q^2)$ that enters (1) and (5). In this figure, the results obtained by assuming zero momentum transfer ($q \approx 0$), that is, $F_Z(q^2) = F_N(q^2) = \mathscr{F}(q^2) = 1$, are also presented (dash dotted curve). We see that, for energies above about 40 MeV, the two methods give significantly different results; the approximation $F_Z = F_N = \mathscr{F} = 1$ is good only for small momentum transfer (e.g., solar and low-energy SN-neutrinos). This shows also the sensitivity of the total cross sections of the total cross sections on the nuclear form factor.

Figure 2 illustrates the coherent cross sections of ν-^{114}Cd scattering as a function of (i) the momentum transfer q (Figure 2(a)) and (ii) the incoming neutrino energy ε_ν (Figure 2(b)). The original cross sections will be used below for evaluations of flux averaged folded cross sections for various neutrino sources. Towards this purpose, the ν-energy distributions of each source are required. We mention that here we have neglected the threshold energy of the detector (calculations where the threshold energy is considered have been performed in [54]).

In the next subsection, we summarize the main features of the neutrino energy distributions adopted in this work.

3.2. Energy Spectra of Low- and Intermediate-Energy ν-Sources. The real neutrino sources, astrophysical (solar, supernova, and geoneutrinos) and laboratory (β-beam, pion-muon stopped neutrino beams, and reactor neutrinos), with few exceptions such as the ν_μ neutrino beam emerging from the π^+ decay at rest ($\varepsilon_\nu = 29.8$ MeV), the ^{7}Be solar neutrinos ($\varepsilon_\nu = 0.862$ MeV [10, 11]), and so forth, produce neutrinos that present a spectral distribution, characteristic of the source itself (i.e., on the reactions producing the considered neutrinos), and are defined by

$$\frac{dN_\nu\left(\varepsilon_\nu\right)}{d\varepsilon_\nu} \equiv \eta\left(\varepsilon_\nu\right), \tag{13}$$

N_ν denotes the number of neutrinos of the beam. Thus, for example, the ν_e neutrinos originating from pion-muon decay at rest have energy spectra approximately described by the well-known Michel distribution, while the supernova neutrinos are commonly interpreted by using for their energy spectra a two-parameter Fermi-Dirac or power law distributions [6, 8, 28] (see below).

In this section, we summarize briefly the basic features of the currently interesting low-energy astrophysical and laboratory neutrino sources: solar, supernova, geoneutrinos, reactor neutrinos, pion-muon stopped neutrinos, and β-beam neutrinos. We focus on their energy distributions which drop in the neutrino energy range of our original cross sections. These neutrino spectra will be used in the folding procedure in the next section, in order to simulate the nuclear detector response of the ^{114}Cd nucleus and calculate event rates.

3.2.1. Geoneutrinos. Geoneutrinos (or Earth neutrinos) are mainly electron antineutrinos ($\tilde{\nu}_e$) generated upon transmutation of neutron-rich β-decay nuclei, accompanied by emission of an electron (e^-) and release of decay energy (Q_β) according to the reaction [40]

$$(A, Z) \longrightarrow (A, Z+1) + e^- + \tilde{\nu}_e + Q_\beta\,. \tag{14}$$

In the latter reaction A is the mass number and Z the atomic (proton) number of the initial (parent) nucleus. Part of the decay energy, $Q_\beta = Q_\nu + Q_h$, is carried away by antineutrinos (Q_ν) while the remainder is available for heating (Q_h). KamLAND is the first detector to conduct an investigation on geoneutrinos [40]. As it is well known, cosmochemical analysis expects significant amount of radioactive isotopes contained in the Earth and radiogenic heat generation of which totals up to about 20 TW [41].

The abundant radioactive isotopes that are in the present Earth are classified into three groups: (i) isotopes in the ^{238}U decay series, (ii) isotopes in ^{232}Th decay series, and ^{40}K isotope. These isotopes are the geologically important isotopes that heat the Earth's interior (they finally decay into stable nuclei). Radiogenic heat is produced by decays of isotopes, in which electron-type (anti-) neutrinos are emitted.

Figure 3(a) shows the antineutrino spectra from ^{40}K, ^{238}U series, and ^{232}Th series ($\tau_{1/2} = 4.47\times10^9$ year, $\tau_{1/2} = 14.0\times10^9$

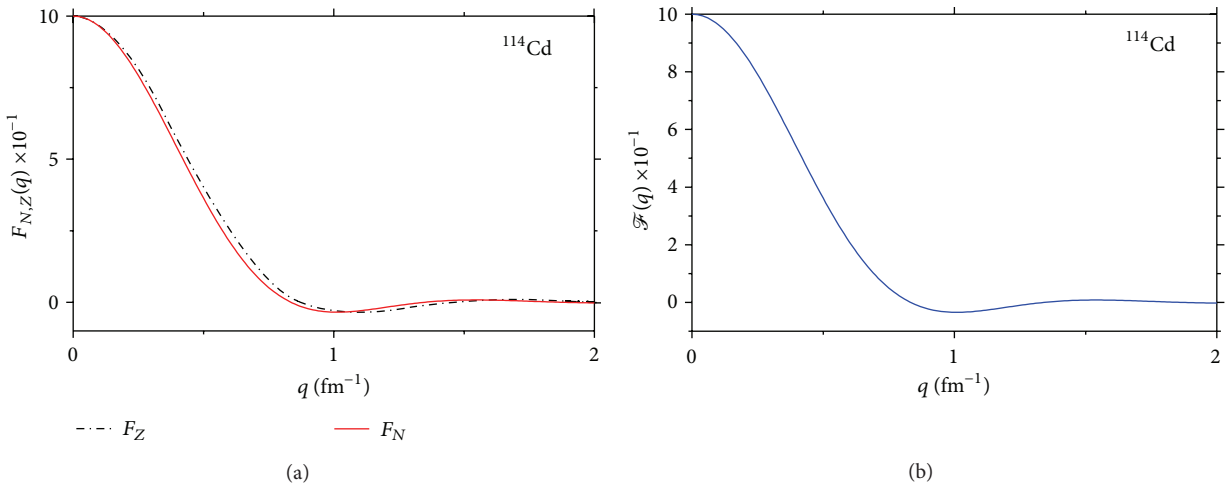

Figure 1: (a) Form factor $\mathscr{F}_{N,Z}(q^2)$ (for neutrons and protons) for ^{114}Cd isotope. (b) The ground state elastic nuclear form factor $F(q^2)$.

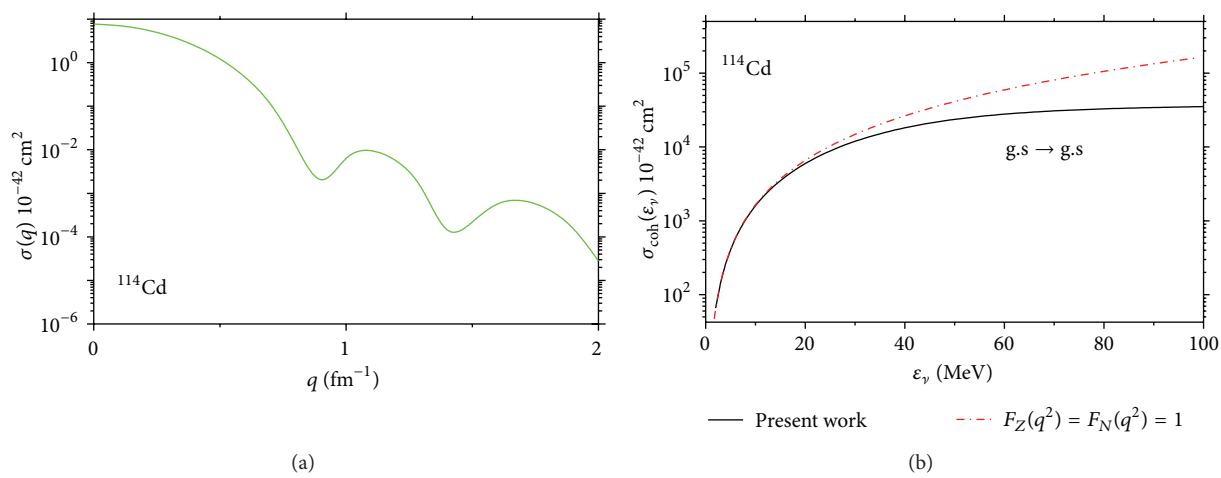

Figure 2: Coherent total cross section for the neutral current reactions $^{114}\mathrm{Cd}(\nu_l, \nu_l')^{114}\mathrm{Cd}^*$, $l = e, \mu, \tau$: (a) as a function of the momentum transfer q and (b) as a function of the incoming neutrino energy ε_ν. The dash dotted curve results by assuming zero momentum transfer; that is, $F_Z(q^2) = F_N(q^2) = \mathscr{F}(q^2) = 1$.

year, and $\tau_{1/2} = 1.28 \times 10^9$ year, resp.). In this neutrino energy distribution $\tilde{\nu}_e$, coming from 82 beta decays in the U series and 70 beta decays in the Th series, are included. Antineutrinos are generated by β-decays of all intermediate radioactive isotopes [40–43].

The most recent measurements from KamLAND [38] and Borexino [39] are reaching the precision where they can start to constrain Earth models. However, these detectors are not sensitive to the neutrino direction. The amount of heat-producing elements in the Earth's mantle is of great interest and hence a detector located away from neutrinos produced in continental crust or on the ocean would be ideal [55]. The next-generation liquid-scintillator neutrino observatory, LENA [13], thanks to its large volume, would be a real breakthrough in geoneutrino detection and geologically significant results could be obtained. LENA could measure the total geoneutrino flux at the level of few percent, by far more precise than other current experiments (e.g., Borexino or KamLAND) could reach. The event and background rates expected for LENA (both in Pyhäsalmi and Fríejus), and projects the precision at which the total geoneutrino flux as well as the U/Th ratio could be measured [13]. The large number of events expected for geoneutrinos will give valuable information on the abundances of Uranium and Thorium and their relative ratio in the Earths crust and mantle.

3.2.2. Reactor Neutrinos. Nuclear reactors have been used as intense ν_e sources in many experiments. In the fission of ^{235}U, ^{239}Pu, and ^{238}U, neutron-rich nuclei are produced and $\tilde{\nu}_e$ antineutrinos are subsequently emitted via β-decay [56, 57]. Experiments using reactor neutrinos are particularly suitable for low Δm measurement because the mean energy of the reactor neutrinos is a few MeV (much smaller than that of accelerator neutrinos). The distance from the reactor core in many reactor experiments is ranged from several tens of meters to 1 km while the overall systematic errors

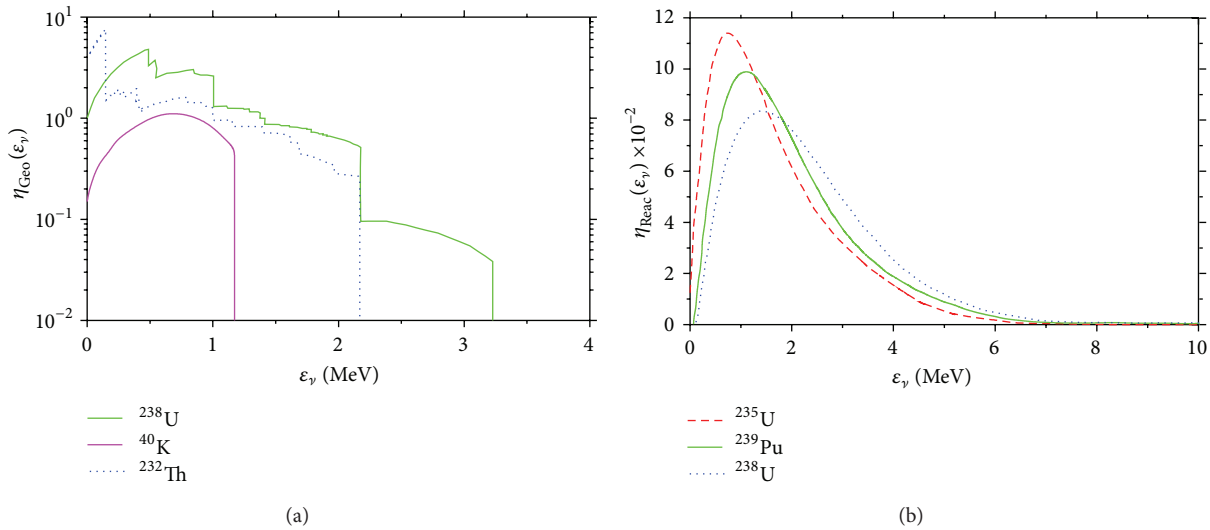

Figure 3: (a) Spectra of the U Series, Th Series, and ^{40}K geoneutrinos. Neutrinos from ^{40}K electron capture are also shown in this figure. (b) Normalized reactor neutrino spectra.

including the ν_e flux uncertainty and detector uncertainty are constrained to within a few % at these experiments.

Nuclear reactors, as sources of $\tilde{\nu}_e$, give fluxes of the order $\sim 10^{13}\,\tilde{\nu}/\text{cm}^2$ sec at distances ~10 m from the reactor core. These antineutrinos have an energy spectrum peaked at very low energies (~0.3 MeV) and extending up to ~10 MeV, characteristic of the β^- decay of the fission products. Figure 3(b) illustrates the reactor neutrino spectra normalized so that the sum over all data-points is equal to one. The fuel composition was adopted to be 62% ^{235}U, 30% ^{239}Pu, and 8% ^{238}U [56, 58].

3.2.3. Solar Neutrinos. Solar neutrinos are ν_e neutrinos produced through weak, electromagnetic, and strong nuclear processes in the interior of our Sun. They have energy $\varepsilon_\nu \leq 18$ MeV and are created either via the well-studied pp-chain reactions or via the CNO-cycle processes [36]. Their energy depends not only on the pertinent nuclear processes, but also on the densities and temperatures in the Sun's environment. The detection of solar neutrinos by terrestrial experiments provides unique information about the interior of the Sun and constitutes excellent probes for astrophysics, nuclear physics, and particle physics searches.

In Figure 4(a), we show the energy spectra of the important ^{8}B and hep neutrino sources predicted by the standard solar model. Each of these spectra has a characteristic shape which is independent of the conditions in the solar interior. The ^{8}B spectrum, on the other hand, is more nearly symmetric, with a peak at 6.4 MeV and a somewhat extended tail. The hep spectrum is rather symmetric and peaks at 9.6 MeV. We mention that measurements of the spectrum of neutrinos that reaches us from the sun provided a decisive test of whether the solar neutrino puzzle is due to our lack of understanding of the solar interior or due to new physics [36, 37].

3.2.4. Pion-Muon Decay at Rest Neutrino Energy Distributions. In the operating pion-muon decay at rest neutrino sources (Fermilab at USA, J-PARC at Japan) and the expected to operate neutrino facilities at the Neutron Spallation Sources (ORNL at USA, and Lund in Sweden), ν_e neutrinos and $\tilde{\nu}_\mu$ antineutrinos are produced from the decay of muons according to the reaction

$$\mu^+ \longrightarrow e^+ + \nu_e + \tilde{\nu}_\mu. \tag{15}$$

The decaying muons result from the decay of slow pions ($\pi^+ \rightarrow \mu^+ + \nu_\mu$) and hence, ν_e and $\tilde{\nu}_\mu$ neutrinos have relatively low energies. Their energy spectra are approximately described by normalized distributions of the form [2, 59]

$$\eta_{\nu_e}(\varepsilon_\nu) = 96\varepsilon_\nu^2 M_\mu^{-4} \left(M_\mu - 2\varepsilon_\nu\right), \tag{16}$$

$$\eta_{\tilde{\nu}_\mu}(\varepsilon_\nu) = 16\varepsilon_\nu^2 M_\mu^{-4} \left(3M_\mu - 4\varepsilon_\nu\right), \tag{17}$$

where $M_\mu = 105.6$ MeV is the muon rest mass (see Figure 4(b)). The maximum energy of ν_e and $\tilde{\nu}_\mu$ in the later equations is $\varepsilon_\nu^{\max} = 52.8$ MeV $= M_\mu/2$ [59, 60]. The distribution of these ν_e neutrinos is known as Michel energy spectrum. The pion-muon decay at rest neutrino beams is not completely pure as, for example, the β-beam neutrinos.

Obviously, the analytic expressions of (16) and (17) are convenient for the required numerical integration in the folding procedure [6, 8, 28, 61–63]. Their energy range and shape roughly resemble those of supernova neutrinos and give us a unique opportunity to study neutrino interactions in this important energy range. This will improve our understanding of SN dynamics and help us to design and calibrate the response of supernova neutrino detectors. We should mention, however, that the pion-muon decay at rest neutrino distributions is closed for high energies while the SN neutrino spectra are open at their high energy tail (see below).

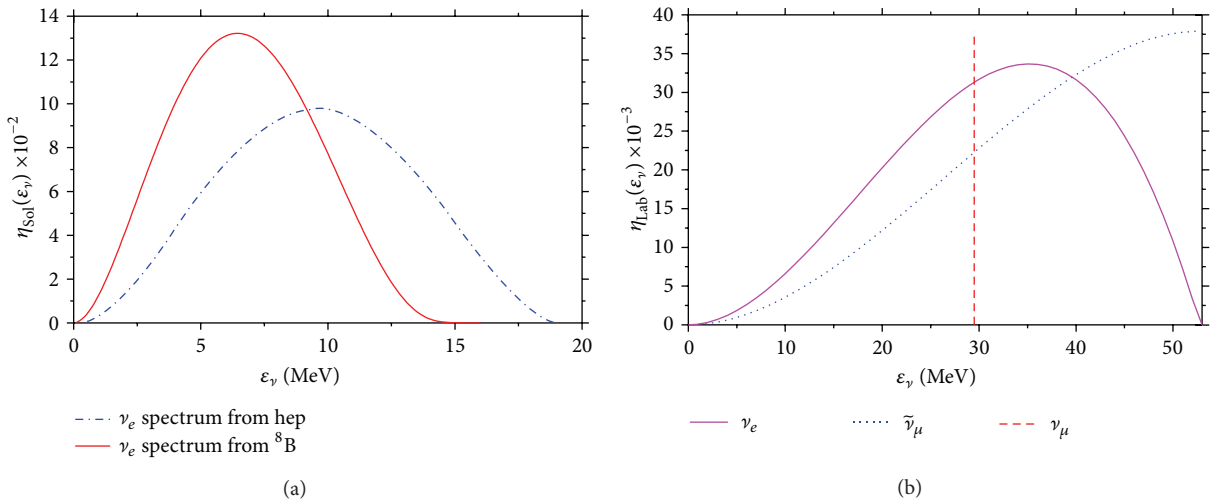

Figure 4: (a) Normalized energy spectrum of ^{8}B and hep ν_e solar neutrinos. (b) Energy spectra of ν_e and $\tilde{\nu}_\mu$ neutrino beams, generated from the muon-decay at rest.

3.2.5. Supernova Neutrinos. According to predictions of recent numerical simulations [64, 65], the creation of the supernova neutrino fluxes is a very complicated process. The shape of SN-neutrino energy distributions is determined by the conditions under which the neutrinos are emitted from the star causing the cooling of the protoneutron star formed at the center of the collapsing star [21, 66–69]. In earlier studies, a thermal spectrum was employed to describe the SN-ν energy distribution [70]. Recent stellar evolution simulations, however, have shown that several effects modify the spectral shape from a purely thermal one [64].

In stellar modelling, authors use analytic expressions that include various modulation effects by inserting a chemical potential μ. Such an expression is as the well-known two-parameter Fermi-Dirac (FD) distribution [64]. A similar expression is the analytically simpler two-parameter Power-Law (PL) energy distribution [64, 65, 71]. Both parametrizations FD and PL yield similar distributions characterized by the temperature T or the average ν-energy $\langle\varepsilon_\nu\rangle$ [8, 28, 72–74]. It is important to note that the flavour-dependent fluxes and spectra emitted by supernovae at any distance from the source can be different from those originally produced, which is mainly due to neutrino oscillations but also due to other phenomena [70].

In Figure 1 of [75, 76] some specific cases of Fermi-Dirac (FD) and Power-law (PL) distributions have been presented for various values of their parameters [64, 65]. Concerning the behaviour of FD and PL distributions throughout their energy range we mention the following features. For the Fermi-Dirac spectral distribution, as the temperature grows both the maximum of the PL distribution shifts to greater neutrino energy and its peak becomes smaller. Also, increasing the degeneracy parameter n_{dg} shifts the spectrum to higher energies [64, 65]. The Power-Law energy distribution is characterized by the pinching parameter α and average energy $\langle\varepsilon_\nu\rangle$. The average energy $\langle\varepsilon_\nu\rangle$ reflects the depth of the stars from where the neutrinos are escaping. As $\langle\varepsilon_\nu\rangle$ grows, the maximum of the distribution shifts to higher neutrino energy ε_ν [65], while as the width parameter w [8] grows (for the same average energy $\langle\varepsilon_\nu\rangle$), both the maximum of the distribution shifts to smaller neutrino energy ε_ν and its peak becomes smaller. For the purposes of the present work, the values of the pinching parameter needed are α =5.1, 3.7, 2.7. The corresponding values of the parameters of $\langle\varepsilon_\nu\rangle$ are shown in Table 2.

It is important to note that the flavour-dependent fluxes and spectra emitted by an SN at any distance from the source can be different from those originally produced mainly due to neutrino oscillations in propagation and also due to other phenomena [70]. The high statistics of neutrino signal from a future galactic SN may allow us to unravel the relevant SN-neutrino scenarios.

The number of the emitted neutrinos can be obtained from the total emitted energy $\mathrm{U}_\nu = 3\times10^{53}$ erg$N_\nu = \mathrm{U}_\nu/\langle E_\nu\rangle$. The (time averaged) neutrino flux at a distance D from the source is $\Phi = N_\nu/(4\pi D^2)$ (for the SN 1987A $D = 10$ kpc $= 3.1\times10^{22}$ cm).

3.2.6. Low-Energy β-Beam Neutrinos. Recently, some accelerated β-radioactive nuclei have been proposed as sources of neutrino beams (beta-beam neutrinos) [14, 15, 77]. Such facilities may produce pure beam neutrinos in which the possible flavors are either the ν_e (for β^+-decaying ions) or the $\tilde{\nu}_e$ (for β^--decaying ions) to search for standard and nonstandard neutrino physics at low and intermediate energies (ν-nucleus interactions, neutrino properties, neutrino oscillations, etc.) and measure ν-nucleus scattering cross sections [15, 77].

For the readers convenience, we summarize here the main features of the low-energy β-beam neutrinos. Their spectra [8, 75, 76] are characterised by the boost velocities (Lorentz factors or γ-factors). For most applications, we derive normalized synthetic neutrino energy distributions $\eta_{bb}(\varepsilon_\nu)$ given by linear combinations of the form

$$\eta_{bb}(\varepsilon_\nu) = \sum_{j=1}^{N} \alpha_j \eta_{\gamma_j}(\varepsilon_\nu), \tag{18}$$

Table 2: Flux averaged coherent cross sections $\langle\sigma_{\text{coh}}\rangle$ (in units 10^{-42} cm^2) for ^{114}Cd isotope obtained in the case of neutrino energy spectra coming from two neutrino sources: (i) supernova neutrinos and (ii) laboratory neutrinos.

Flux averaged cross sections $\langle\sigma_{\text{coh}}\rangle$ (10^{-42} cm^2)										
				Supernova neutrinos					Neutrinos Pion-muon stopped Michel spectrum	
Fermi-Dirac (FD)				Power Law (PL)						
$T =$	3.10	4.14	6.20	$\langle\varepsilon_\nu\rangle =$	12	16	24		$\eta_{\nu_e}(\varepsilon_\nu)$	$\eta_{\tilde{\nu}_\mu}(\varepsilon_\nu)$
$\langle\sigma\rangle =$	2648	4457.52	8648.06	$\langle\sigma\rangle =$	2653.26	4452.93	8658.47	$\langle\sigma\rangle =$	13109.52	15880.76

where N numbers the different Lorentz (γ) factors included in the synthetic spectrum (expressions for the individual distributions $\eta_{\gamma_j}(\varepsilon_\nu)$ are given in [7, 8, 74]). Combinations of the type $\eta_{bb}(\varepsilon_\nu)$ for γ-factors up to 10–12 are used to fit original supernova neutrino spectral distributions, $\eta_{\text{SN}}(\varepsilon_\nu)$, reaching terrestrial detectors by adjusting the weight parameters α_j through the minimization procedure described in [8, 75, 76].

Many authors in recent β-beam neutrino simulations employ the energy spectra of the antineutrinos $\tilde{\nu}_e$ emitted from β^--radioactive $^6_2$He ions according to the reaction

$$^6_2\text{He} \longrightarrow {}^6_3\text{Li} + e^- + \tilde{\nu}_e \tag{19}$$

The Q-value of this reaction is $Q_{\text{He}} = 3.5$ MeV. Another potential β^--radioactive isotope for $\tilde{\nu}_e$ beams is the $^8_3$Li with Q-value $Q_{\text{Li}} = 13.0$ MeV. Interesting β^+-radioactive ion source to be accelerated for producing ν_e beams is the $^{18}_{10}$Ne, which decays according to the reaction [15, 77]

$$^{18}_{10}\text{Ne} \longrightarrow {}^{18}_{9}\text{F} + e^+ + \nu_e \tag{20}$$

The Q-value of this reaction is $Q_{\text{Ne}} = 3.4$ MeV. For ν_e beams another promising β^+-radioactive isotope is the $^8_4$B ($Q_{\text{B}} = 13.9$ MeV).

From the aforementioned potential targets, $^6_2$He and $^{18}_{10}$Ne are considered to have rather low Q-values, so they are good choices for short baseline neutrino studies while $^8_3$Li and $^8_4$B have relatively high Q-values and they are the best choices for a large baseline [13].

Energy spectra of the reactions (19) and (20) for several integer γ-boost factors ($\gamma = 3, 4, \ldots, 15$) are discussed in [8, 74].

3.3. Simulated Neutrino Signals on Nuclear Detectors. As mentioned in Section 1, the characteristics of the arriving at a nuclear detector neutrino flux are concealed in the nuclear response of the detector medium, that is, in the material CdTe or CdZnTe for the case of the COBRA detectors. Theoretically, these features could be simulated by convoluted cross sections calculations carried out as discussed in [64, 65, 71].

In the present work, the convolution (folding) method was performed with the original cross sections obtained as discussed before, in order to compute the flux averaged total cross sections, $\langle\sigma_{\text{tot}}\rangle$, for the low-energy neutrino spectra of the previous section.

For the coherent channel, which is possible only in neutral current neutrino-nucleus reactions studied in the present work, the flux averaged cross section $\langle\sigma_{\text{coh}}\rangle$ is defined as [2]

$$\langle\sigma_{\text{coh}}\rangle = \int_0^\infty \sigma_{\text{coh}}(\varepsilon_\nu)\,\eta(\varepsilon_\nu)\,d\varepsilon_\nu. \tag{21}$$

Due to the dominance of the coherent cross section $\sigma_{\text{coh}}(\varepsilon_\nu)$ throughout the region of the incoming neutrino energy ε_ν, $\langle\sigma_{\text{coh}}\rangle$ is, sometimes, even two or three orders of magnitude larger than the incoherent one, $\langle\sigma_{\text{tot}}^{\text{incoh}}\rangle$ [6, 8, 28, 61].

The flux averaged cross sections obtained for ^{114}Cd with (21) for the neutrino distributions $\eta(\varepsilon_\nu)$ of Section 3 are listed in Tables 2 and 3. In Table 2 the flux averaged cross sections refer to various supernova neutrino scenarios described by the Fermi-Dirac (F-D) and Power-Low (P-L) distributions corresponding to the parameters given in this Table, that is, ν_e neutrinos, $\tilde{\nu}_e$ antineutrinos, and ν_x, $x = \nu_\mu, \nu_\tau, \tilde{\nu}_\mu$, and $\tilde{\nu}_\tau$ [64, 65, 71]. In the last two columns of Table 2 we tabulate the $\langle\sigma_{\text{coh}}\rangle$ calculated for the distributions of (16) and (17). Here the flux averaged cross sections have been calculated as in [30].

In Table 3 we list the flux averaged cross sections evaluated by adopting the neutrino distributions of the geoneutrinos (see Figure 3(a)), of the reactor neutrinos (see Figure 3(b)) and solar neutrinos (see Figure 4(a)) for the ^{8}B-neutrinos and Figure 4(b) for the hep neutrinos).

3.4. Number of Events in nu-Detectors. For another connection of the present theoretical results with the neutrino experiments discussed in Section 1, and specifically COBRA experiment, we estimate the signals created in the ^{114}Cd detector which is given by the expression [6, 78]

$$\sigma_{\text{sign}}(\varepsilon_\nu) = \sigma_{\text{coh}}(\varepsilon_\nu)\,\eta(\varepsilon_\nu). \tag{22}$$

By using our theoretical cross sections $\sigma(\varepsilon_\nu)$ for ^{114}Cd isotope we may evaluate the neutrino fluxes Φ_ν or the scattering event rates, N_{event}, for the COBRA detector.

Our calculations here are based on a mass 100 Kgr of the COBRA detector with detector material CdZnTe or CdTe for the typical detection rate of $N_{\text{event}} = 1$ event hr^{-1}, t. Assuming that N_{Cd} is the total number of nuclei (atoms) of ^{114}Cd in the detector, we have [78]

$$\frac{dN_\nu}{dt} \equiv N_{\text{event}} = N_{\text{Cd}}\Phi_\nu(\varepsilon_\nu)\,\sigma_{\text{tot}}(\varepsilon_\nu). \tag{23}$$

Table 3: Flux averaged coherent cross sections $\langle\sigma_{\text{coh}}\rangle$ (in units 10^{-40} cm^2) for ^{114}Cd isotope obtained in the case of neutrino energy spectra coming from two neutrino sources: (i) geoneutrinos, (ii) reactor neutrinos, and (iii) solar neutrinos.

	Flux averaged cross sections $\langle\sigma_{\text{coh}}\rangle$ (10^{-42} cm^2)							
Detector		Geoneutrinos			Reactor neutrinos		Solar neutrinos	
^{114}Cd	^{40}K	^{238}U	^{232}Th	^{235}U	^{238}U	^{239}Pu	^{8}B	hep
	151.38	1504.40	972.56	192.20	508.90	9604.36	8503.99	9956.57

Table 4: Neutrino coherent fluxes $\Phi_\nu(\varepsilon_\nu)$ (in units 10^9 sec^{-1} cm^2) for ^{114}Cd isotope for the two materials (CdTe and CdZnTe) of the COBRA experiment obtained in the case of supernova neutrinos with mean energies $\langle\varepsilon_\nu\rangle$ = 12, 16, and 24 MeV. N_0 is the Avogadro's number.

	Neutrino coherent fluxes Φ_ν			
Detector medium	Number of atoms	^{114}Cd (Kgr)	$\langle\varepsilon_\nu\rangle$ (MeV)	Φ_ν ($\times 10^9$ sec^{-1} cm^{-2})
			12	1.447
CdTe	$120.11N_0$	13.5	16	0.862
			24	0.449
			12	1.847
CdZnTe	$94.17N_0$	10.6	16	1.100
			24	0.566

The COBRA detector is expected to have a total mass of ^{114}Cd CdZnTe about $m_{\text{Cd}} = 10.6$ Kgr which translates to about $N_{\text{Cd}} = N_{^{114}\text{Cd}} = 94.17N_{\text{Avogadro}}$ atoms (nuclei). The results from (23) neutrino fluxes for the supernova neutrinos with the mean energies $\langle\varepsilon_\nu\rangle = 12$ MeV (electron neutrinos ν_e), $\langle\varepsilon_\nu\rangle = 16$ MeV (electron anti-neutrinos $\tilde{\nu}_e$), and $\langle\varepsilon_\nu\rangle = 24$ MeV ($\nu_x, \tilde{\nu}_x, x = \mu, \tau$) and the $\langle\sigma_{\text{coh}}\rangle$ of Table 2 are shown in Table 4 (first three lines).

Similar calculations will be done assuming that the material of COBRA detector is the CdTe. Again we consider 100 Kgr detector which contains 13.5 Kgr ^{114}Cd or about $N_{\text{Cd}} = N_{^{114}\text{Cd}} = 120.11N_{\text{Avogadro}}$ atoms (nuclei). The results from (23) neutrino flux for the supernova neutrino scenarios adopted above are shown in Table 4 (last three lines).

These results are encouraging for the Cd materials to be used in the future as astrophysical neutrino detectors in addition to their main goal of neutrinoless double β-decay search. We stress, however, that even though the above neutrino fluxes are of the same order with those expected at the Spallation Neutron Source at ORLaND, Oak Ridge [17–19], in choosing a neutrino cross section measurement target other experimental criteria usually lead to more popular choices (Xe, Cs, etc.). For such targets similar calculations to those we performed here for ^{114}Cd could be also done.

4. Conclusions

Astrophysical neutrinos (solar, supernova, and Earth neutrinos) are key particles in investigating the structure and evolution of stars, the astronuclear reactions, and also in deepening our knowledge on the fundamental interactions and the nuclear weak responses. In this work we applied the convolution procedure to calculate flux averaged cross sections and event rates for the above ν-sources based on neutrino-nucleus cross sections obtained with realistic nuclear structure calculations (QRPA method). For the computed folded cross sections we employed specific spectral distributions describing neutrino-energy spectra of supernova and solar neutrinos, geoneutrinos, reactor neutrinos, laboratory neutrinos, and neutrinos produced from the decay of pions and muons at rest.

The flux-averaged total coherent cross sections, $\langle\sigma_{\text{coh}}\rangle$, reflect to some extent the neutrino signals generated in several selected terrestrial detectors from such ν-sources. In this work, we estimated coherent neutrino fluxes for ^{114}Cd which is content of the CdTe and CdZnTe materials of the COBRA detector at LNGS. The goal of this experiment is to search for double beta decay events and neutrino observation.

Conflict of Interests

The author declares that there is no conflict of interests regarding the publication of this paper.

Acknowledgments

The author is grateful to Professor T. S. Kosmas for fruitful and stimulating discussions and to the Division of Theoretical Physics of the University of Ioannina for technical support and computational assistance to perform the present calculations.

References

[1] T. W. Donnelly and R. D. Peccei, "Neutral current effects in nuclei," *Physics Reports*, vol. 50, no. 1, pp. 1–85, 1979.

[2] T. S. Kosmas and E. Oset, "Charged current neutrino-nucleus reaction cross sections at intermediate energies," *Physical Review C: Nuclear Physics*, vol. 53, no. 3, pp. 1409–1415, 1996.

[3] H. Ejiri, "Nuclear spin isospin responses for low-energy neutrinos," *Physics Reports*, vol. 338, no. 3, pp. 265–351, 2000.

[4] K. Zuber, "COBRA—double beta decay searches using CdTe detectors," *Physics Letters B*, vol. 519, no. 1-2, pp. 1–7, 2001.

[5] K. Zuber, "Spectroscopy of low energy solar neutrinos using CdTe detectors," *Physics Letters B*, vol. 571, no. 3-4, pp. 148–154, 2003.

[6] V. Tsakstara and T. S. Kosmas, "Low-energy neutral-current neutrino scattering on ^{128,130}Te isotopes," *Physical Review C*, vol. 83, Article ID 054612, 2011.

[7] V. Tsakstara, T. S. Kosmas, and J. Wambach, "Studying low-energy astrophysical neutrinos with neutrino nucleus cross-section calculations and beta beam neutrino spectra," *Progress in Particle and Nuclear Physics*, vol. 66, no. 2, pp. 424–429, 2011.

[8] V. Tsakstara and T. S. Kosmas, "Analyzing astrophysical neutrino signals using realistic nuclear structure calculations and the convolution procedure," *Physical Review C*, vol. 84, Article ID 064620, 2011.

[9] S. Abe, T. Ebihara, S. Enomoto et al., "Precision measurement of neutrino oscillation parameters with KamLAND," *Physical Review Letters*, vol. 100, no. 22, Article ID 221803, 2008.

[10] G. Bellini, J. Benziger, S. Bonetti et al., "Observation of geo-neutrinos," *Physics Letters B*, vol. 687, no. 4-5, pp. 299–304, 2010.

[11] G. Bellini, J. Benziger, D. Bick et al., "Precision measurement of the ^{7}Be solar neutrino interaction rate in borexino," *Physical Review Letters*, vol. 107, Article ID 141302, 2011.

[12] K. Zuber, "Status of the double beta experiment COBRA," *Progress in Particle and Nuclear Physics*, vol. 57, pp. 235–240, 2006.

[13] M. Wurm, J. F. Beacom, L. B. Bezrukov et al., "The next-generation liquid-scintillator neutrino observatory LENA," *Astroparticle Physics*, vol. 35, no. 11, pp. 685–732, 2012.

[14] P. Zucchelli, "A novel concept for a $\overline{\nu}_e/\nu_e$ neutrino factory: the beta-beam," *Physics Letters B*, vol. 532, no. 3-4, pp. 166–172, 2002.

[15] C. Volpe, "What about a beta-beam facility for low-energy neutrinos?," *Journal of Physics G*, vol. 30, article L1, 2004.

[16] M. S. Athar and S. K. Singh, "$\nu_e(\overline{\nu}_e)$-^{40}Ar absorption cross sections for supernova neutrinos," *Physics Letters B*, vol. 591, no. 1-2, pp. 69–75, 2004.

[17] F. T. Avignone and Y. V. Efremenko, "ORLaND—a neutrino facility at the spallation neutron source," *Nuclear Physics B—Proceedings Supplements*, vol. 87, no. 1–3, pp. 304–308, 2000.

[18] F. T. Avignone III and Y. V. Efremenko, "Neutrino-nucleus cross-section measurements at intense, pulsed spallation sources," *Journal of Physics G: Nuclear and Particle Physics*, vol. 29, no. 11, pp. 2615–2628, 2003.

[19] R. L. Burman and W. C. Louis, "Neutrino physics at meson factories and spallation neutron sources," *Journal of Physics G*, vol. 29, no. 11, article 2499, 2003.

[20] E. Kolbe, K. Langanke, G. Martínez-Pinedo, and P. Vogel, "Neutrino–nucleus reactions and nuclear structure," *Journal of Physics G: Nuclear and Particle Physics*, vol. 29, no. 11, pp. 2569–2596, 2003.

[21] K. Langanke and G. Martinez-Pinedo, "Nuclear weak-interaction processes in stars," *Reviews of Modern Physics*, vol. 75, no. 3, pp. 819–862, 2003.

[22] A. Juodagalvis, K. Langanke, G. Martinez-Pinedo, W. R. Hix, D. J. Dean, and J. M. Sampaio, "Neutral-current neutrino–nucleus cross sections for A~50–65 nuclei," *Nuclear Physics A*, vol. 747, pp. 87–108, 2005.

[23] K. Langanke, "Weak interaction, nuclear physics and supernovae," *Acta Physica Polonica B*, vol. 39, no. 2, pp. 265–281, 2008.

[24] A. A. Aguilar-Arevalo, C. E. Anderson, A. O. Bazarko et al., "Search for core-collapse supernovae using the MiniBooNE neutrino detector," *Physical Review D*, vol. 81, Article ID 032001, 2010.

[25] H. Ejiri, J. Engel, and N. Kudomi, "Supernova-neutrino studies with ^{100}Mo," *Physics Letters Section B*, vol. 530, no. 1–4, pp. 27–32, 2002.

[26] W. C. Haxton, "Nuclear response of water Cherenkov detectors to supernova and solar neutrinos," *Physical Review D*, vol. 36, no. 8, pp. 2283–2292, 1987.

[27] S. W. Bruenn and W. C. Haxton, "Neutrino-nucleus interactions in core-collapse supernovae," *Astrophysical Journal Letters*, vol. 376, no. 2, pp. 678–700, 1991.

[28] V. Tsakstara and T. S. Kosmas, "Nuclear responses of ^{64,66}Zn isotopes to supernova neutrinos," *Physical Review C*, vol. 86, no. 4, Article ID 044618, 10 pages, 2012.

[29] V. Tsakstara and T. S. Kosmas, *Physical Review C*. To be submitted.

[30] K. G. Balasi, E. Ydrefors, and T. S. Kosmas, "Theoretical study of neutrino scattering off the stable even Mo isotopes at low and intermediate energies," *Nuclear Physics A*, vol. 868-869, no. 1, pp. 82–98, 2011.

[31] Y. Giomataris and J. D. Vergados, "A network of neutral current spherical TPCs for dedicated supernova detection," *Physics Letters B*, vol. 634, no. 1, pp. 23–29, 2006.

[32] J. D. Vergados and Y. Giomataris, "Dedicated supernova detection by a network of neutral current spherical TPC detectors," *Physics of Atomic Nuclei*, vol. 70, no. 1, pp. 140–149, 2007.

[33] J. D. Vergados, F. T. Avignone, and I. Giomataris, "Coherent neutral current neutrino-nucleus scattering at a spallation source: a valuable experimental probe," *Physical Review D*, vol. 79, no. 11, Article ID 113001, 2009.

[34] T. S. Kosmas, "Exotic $\mu^- \rightarrow e^-$ conversion in nuclei: energy moments of the transition strength and average energy of the outgoing e^-," *Nuclear Physics A*, vol. 683, no. 1–4, pp. 443–462, 2001.

[35] K. Zuber, "The status of the COBRA double-beta-decay experiment," *Progress in Particle and Nuclear Physics*, vol. 64, no. 2, pp. 267–269, 2010.

[36] J. N. Bachall and R. K. Ulrich, "Solar models, neutrino experiments, and helioseismology," *Reviews of Modern Physics*, vol. 60, p. 297, 1988.

[37] J. N. Bahcall, S. Basu, M. Pinsonneault, and A. M. Serenelli, "Helioseismological implications of recent solar abundance determinations," *The Astrophysical Journal*, vol. 618, no. 2, pp. 1049–1056, 2005.

[38] A. Gando, Y. Gando, K. Ichimura et al., "Partial radiogenic heat model for Earth revealed by geoneutrino measurements," *Nature Geoscience*, vol. 4, no. 9, pp. 647–651, 2011.

[39] G. Bellini, J. Benziger, D. Bick et al., "Measurement of geo-neutrinos from 1353 days of Borexino," *Physics Letters B*, vol. 722, no. 4-5, pp. 295–300, 2013.

[40] P. Vogel and J. F. Beacom, "Angular distribution of neutron inverse beta decay, $\overline{\boldsymbol{\nu}}\mathbf{e} + \vec{\mathbf{p}}\mathbf{e}^+ + \mathbf{n}$," *Physical Review D*, vol. 60, no. 5, Article ID 053003, 1999.

[41] S. Dye, "Geoneutrinos and the radioactive power of the Earth," *Reviews of Geophysics*, vol. 50, no. 3, Article ID RG3007, 2012.

[42] G. Fiorentini, F. Mantovani, and B. Ricci, "Neutrinos and energetics of the Earth," *Physics Letters B*, vol. 557, no. 3-4, pp. 139–146, 2003.

[43] G. Fiorentini, A. Ianni, G. Korga et al., "Nuclear physics for geo-neutrino studies," *Physical Review C*, vol. 81, no. 3, Article ID 034602, 9 pages, 2010.

[44] T. S. Kosmas, J. D. Vergados, O. Civitarese, and A. Faessler, "Study of the muon number violating (μ^-, e^-) conversion in a nucleus by using quasi-particle RPA," *Nuclear Physics, Section A*, vol. 570, no. 3-4, pp. 637–656, 1994.

[45] K. Abe, K. Abe, T. Abe et al., "Improved direct measurement of leptonic coupling asymmetries with polarized Z bosons," *Physical Review Letters*, vol. 86, no. 7, pp. 1162–1166, 2001.

[46] J. Engel, "Nuclear form factors for the scattering of weakly interacting massive particles," *Physics Letters B*, vol. 264, pp. 114–119, 1991.

[47] H. de Vries, C. W. de Jager, and C. de Vries, "Nuclear charge-density-distribution parameters from elastic electron scattering," *Atomic Data and Nuclear Data Tables*, vol. 36, no. 3, pp. 495–536, 1987.

[48] A. Drukier and L. Stodolsky, "Principles and applications of a neutral-current detector for neutrino physics and astronomy," *Physical Review D*, vol. 30, no. 11, article 2295, 1984.

[49] P. Vogel and J. Engel, "Neutrino electromagnetic form factors," *Physical Review D*, vol. 39, no. 11, pp. 3378–3383, 1989.

[50] J. D. Vergados, "Neutral current coherent cross sections-implications on gaseous spherical TPC's for detecting SN and Earth neutrinos," *Journal of Physics: Conference Series*, vol. 309, no. 1, Article ID 012031, 2011.

[51] T. W. Donnelly and J. D. Walecka, "Semi-leptonic weak and electromagnetic interactions in nuclei with application to 16O," *Physics Letters B*, vol. 41, no. 3, pp. 275–280, 1972.

[52] T. W. Donnelly and J. D. Walecka, "Elastic magnetic electron scattering and nuclear moments," *Nuclear Physics, Section A*, vol. 201, no. 1, pp. 81–106, 1973.

[53] E. Kolbe, "Differential cross sections for neutrino scattering on ^{12}C," *Physical Review C*, vol. 54, no. 4, pp. 1741–1748, 1996.

[54] D. K. Papoulias and T. S. Kosmas, "Nuclear aspects of neutral current non-standard ν-nucleus reactions and the role of the exotic $\mu^- \to e^-$ transitions experimental limits," *Physics Letters B*, vol. 728, pp. 482–488, 2014.

[55] A. de Gouvea, K. Pitts, K. Scholberg et al., "Neutrinos," http://arxiv.org/abs/1310.4340v1.

[56] B. R. Davis, P. Vogel, F. M. Mann, and R. E. Schenter, "Reactor antineutrino spectra and their application to antineutrino-induced reactions," *Physical Review C*, vol. 19, no. 6, pp. 2259–2266, 1979.

[57] Y. Declais, H. de Kerret, B. Lefièvre et al., "Study of reactor antineutrino interaction with proton at Bugey nuclear power plant," *Physics Letters B*, vol. 338, no. 2-3, pp. 383–389, 1994.

[58] O. Tengblad, K. Aleklett, R. von Dincklage, E. Lund, G. Nyman, and G. Rudstam, "Integral \̄ gn-spectra derived from experimental β-spectra of individual fission products," *Nuclear Physics A*, vol. 503, no. 1, pp. 136–160, 1989.

[59] W. C. Louis, "Searches for muon-to-electron (anti) neutrino flavor change," *Progress in Particle and Nuclear Physics*, vol. 63, pp. 51–73, 2009.

[60] E. Kolbe and T. S. Kosmas, "Recent highlights on neutrino-nucleus interactions," in *Symmetries in Intermediate and High Energy Physics*, vol. 163 of *Springer Tracts in Modern Physics*, pp. 199–225, Springer, 2000.

[61] T. S. Kosmas and J. D. Vergados, "Cold dark matter in SUSY theories: the role of nuclear form factors and the folding with the LSP velocity," *Physical Review D*, vol. 55, no. 4, pp. 1752–1764, 1997.

[62] V. Tsakstara, T. S. Kosmas, J. Sinatkas, V. C. Chasioti, and P. C. Divari, "The convolution method in neutrino physics searches," *AIP Conference Proceedings*, vol. 963, no. 2, p. 1383, 2007.

[63] V. A. Tsakstara, T. S. Kosmas, V. C. Chasioti, and J. Sinatkas, "On the nuclear response of ^{56}Fe to supernova neutrino spectra," in *Proceedings of the Carpathian Summer School of Physics (CSSP '07)*, vol. 972, pp. 562–565, Sinaia, Romania, August 2007.

[64] H. T. Janka and W. Hillebrand, "Neutrino emission from type II supernovae—an analysis of the spectra," *Astronomy & Astrophysics*, vol. 224, no. 1-2, pp. 49–56, 1989.

[65] M. T. Keil, G. G. Raffelt, and H.-T. Janka, "Monte Carlo study of supernova neutrino spectra formation," *The Astrophysical Journal*, vol. 590, no. 2, pp. 971–991, 2003.

[66] H. A. Bethe, "Supernova mechanisms," *Reviews of Modern Physics*, vol. 62, no. 4, pp. 801–866, 1990.

[67] C. Fröhlich, G. Martínez-Pinedo, M. Liebendörfer et al., "Neutrino-induced nucleosynthesis of A>64 nuclei: the νp process," *Physical Review Letters*, vol. 96, no. 14, Article ID 142502, 2006.

[68] H.-T. Janka and B. Müller, "Neutrino-driven type-II supernova explosions and the role of convection," *Physics Reports*, vol. 256, no. 1–3, pp. 135–156, 1995.

[69] H.-Th. Janka, K. Langanke, A. Mareka, G. Martinez-Pinedo, and B. Mullera, "Theory of core-collapse supernovae," *Physics Reports*, vol. 442, no. 1–6, pp. 38–74, 2007.

[70] B. Dasgupta and A. Dighe, "Collective three-flavor oscillations of supernova neutrinos," *Physical Review D*, vol. 77, Article ID 113002, 2008.

[71] G. G. Raffelt, M. T. Keil, R. Buras, H.-T. Janka, and M. Rampp, "Supernova neutrinos: flavor-dependent fluxes and spectra," http://arxiv.org/abs/astro-ph/0303226.

[72] V. Tsakstara and T. S. Kosmas, "Studying supernovae via their neutrino signatures at nuclear detectors," in *Horizons in World Physics*, vol. 278, chapter 7, pp. 219–254, Nova Science Publishers, 2012.

[73] V. Tsakstara, T. S. Kosmas, P. C. Divari, and J. Sinatkas, "The interpretation of SN−v signals in terrestrial experiments through the folding procedure," *AIP Conference Proceedings*, vol. 1180, pp. 140–144, 2009.

[74] V. Tsakstara and T. S. Kosmas, "Neutrino-nucleus reactions in terrestrial experiments and astrophysics," *Progress in Particle and Nuclear Physics*, vol. 64, no. 2, pp. 407–410, 2010.

[75] N. Jachowicz and G. C. McLaughlin, "Reconstructing supernova-neutrino spectra using low-energy beta beams," *Physical Review Letters*, vol. 96, Article ID 172301, 2006.

[76] N. Jachowicz, G. McLaughlin, and C. Volpe, "Untangling supernova-neutrino oscillations with β-beam data," *Physical Review C*, vol. 77, no. 5, Article ID 055501, 12 pages, 2008.

[77] C. Volpe, "Beta-beams," *Journal of Physics G: Nuclear and Particle Physics*, vol. 34, no. 1, pp. R1–R44, 2007.

[78] V. Tsakstara, T. S. Kosmas, and J. D. Vergados, "Weak responses of neutral current neutrino-nucleus," *Romanian Journal of Physics*, vol. 58, no. 9-10, pp. 1258–1269, 2013.

Hindawi Publishing Corporation
Advances in High Energy Physics
Volume 2014, Article ID 807857, 10 pages
http://dx.doi.org/10.1155/2014/807857

Research Article

CνB Damping of Primordial Gravitational Waves and the Fine-Tuning of the CγB Temperature Anisotropy

A. E. Bernardini and J. F. G. Santos

Departamento de Física, Universidade Federal de São Carlos, P.O. Box 676, 13565-905 São Carlos, SP, Brazil

Correspondence should be addressed to A. E. Bernardini; alexeb@ufscar.br

Received 23 May 2014; Revised 15 July 2014; Accepted 15 July 2014; Published 1 September 2014

Academic Editor: Theocharis Kosmas

Damping of primordial gravitational waves due to the anisotropic stress contribution owing to the cosmological neutrino background (CνB) is investigated in the context of a radiation-to-matter dominated universe. Besides its inherent effects on the gravitational wave propagation, the inclusion of the CνB anisotropic stress into the dynamical equations also affects the tensor mode contribution to the anisotropy of the cosmological microwave background (CγB) temperature. The mutual effects on the gravitational waves and on the CγB are obtained through a unified prescription for a radiation-to-matter dominated scenario. The results are confronted with some preliminary results for the radiation dominated scenario. Both scenarios are supported by a simplified analytical framework, in terms of a scale independent dynamical variable, $k\eta$, that relates cosmological scales, k, and the conformal time, η. The background relativistic (hot dark) matter essentially works as an effective dispersive medium for the gravitational waves such that the damping effect is intensified for the universe evolving to the matter dominated era. Changes on the temperature variance owing to the inclusion of neutrino collision terms into the dynamical equations result in spectral features that ratify that the multipole expansion coefficients C_l^T's die out for $l \sim 100$.

1. Introduction

The theoretical investigation and the phenomenological analysis of anisotropies in the cosmological microwave background (CγB) radiation are recursively considered as a singular valuable check on the validity of simple inflationary cosmological models. The fast growth of primordial masses and of energy density fluctuations is identified as the simplest mechanism for producing cosmological structures and observable CγB temperature anisotropies. In addition, a primordial spectrum of gravitational waves [1, 2] may also have been perturbatively induced during the inflationary epoch. It could, for instance, change the theoretical predictions for cluster abundances and work as a pertinent test for inflationary models as it produces some imprints on radiation tensor modes.

Cosmological tensor fluctuations should produce not only temperature anisotropies but also distinct imprints in the so-called magnetic or B-modes of its polarization field [3], which has been identified through the CγB polarization experiments [1, 2, 4, 5]. Current experiments have indeed been able to put upper limits on polarizations of the CγB that might be owed to a gravitational wave background [6–14].

The observed pattern of temperature anisotropies, when combined with probes of inhomogeneities in matter on large scale structures, and with measurements of the total energy density in the universe, is in striking agreement with the simplest predictions for the spectrum of anisotropies due to gravitational waves produced during inflation. These facts support the inclusion of extra ingredients in the fine-tuning analysis involving the theoretical predictions and the observable data for CγB anisotropies.

The CνB contribution to the dark matter inventory at present can be estimated from the modifications on the matter power spectrum, even for neutrinos behaving like a relativistic fluid at higher redshifts [15]. This phenomenological characteristic is related to the large scale structures, such that effective mass values for neutrinos through the CγB results are inferred through the transfer function in the matter power spectrum at small scales [16–18]. Depending on the current thermodynamic regime, the free-streaming massive neutrinos can affect the cosmological evolution of

tensor modes by increasing the magnitude of the anisotropic stress, which acts as an effective viscosity, absorbing gravitational waves in the low frequency. That is the theoretical point discussed in some previous issues [19–21] where it has been given some emphasis on the cosmological evolution of perturbation tensor modes coupled to cosmological neutrinos in the radiation dominated (RD) universe.

Our aim is to extend such a preliminary approach involving the RD cosmic inventory to a transient, radiation-to-matter dominated (RMD) background universe. We will follow the analytical setup based on the multipole formalism that reproduces the procedure which deals with scalar perturbations [15, 19, 20, 22]. Even in the framework for a RMD scenario, it can be shown that equations can be manipulated in order to avoid explicit (and sometimes confused) dependencies on cosmological scales, k, which, in this case, are absorbed by the scale independent variable, $k\eta$. Besides quantifying the dynamical evolution of gravitational waves and identifying the role of neutrinos and collision terms inherent to the model, one will be able to quantify a modified tensor mode variance for the temperature anisotropy. Once extended to the RMD background scenario, our analysis follows several theoretical prescriptions provided by some preliminary studies like in [15, 19–21].

Our paper is therefore organized as follows. In Section 2, we report about the textbook multipole formalism [22], with the corresponding modifications for reconstructing the pattern of tensor perturbations [19, 20]. In Section 3, we reproduce the framework for including the anisotropic stress effects on the propagation of gravitational waves by assuming physically reliable conditions over the collision parameters. The dynamical evolution of tensor modes and its corresponding potential modifications on the CγB temperature for a RMD environment is therefore quantified. Since the neutrino viscosity underlies an increasing wave damping effect, we expect to have a frequency-dependent absorption of gravitational waves in the frequency range where neutrino decoupling happens. We draw our conclusions in Section 4.

2. Theoretical Preliminaries

As supported by the decomposition theorem [15, 17, 22, 23], the perturbation equations for the cosmological scenario in the synchronous gauge allow one to depict simpler and clearer properties of cosmological tensor perturbations. In general lines, the cosmological evolution of a homogeneous Friedmann-Robertson-Walker (FRW) flat universe with background energy density, $\overline{\rho}(\eta)$, and pressure, $\overline{\mathscr{P}}(\eta)$, is described in terms of the scale factor, $a(\eta)$, through the following components of the Einstein equation:

$$\left(\frac{da/d\eta}{a}\right)^2 = \frac{8\pi}{3}Ga^2\overline{\rho}, \tag{1}$$

$$\frac{d}{d\eta}\left(\frac{da/d\eta}{a}\right) = -\frac{4\pi}{3}Ga^2\left(\overline{\rho}+3\overline{\mathscr{P}}\right), \tag{2}$$

where η is the conformal time defined by $d\eta = dt/a$ and G is the Newtonian constant, and one sets the natural units $c = \hbar = k_B = 1$.

The propagation of gravitational waves is parameterized by the relevant (spatial) components of the perturbed metric written as (one notices the $(-+++)$ signature for the metric)

$$g_{ij} = a^2(\eta)\left[\delta_{ij}+h_{ij}\right], \quad i,j = 1,2,3, \tag{3}$$

while $g_{00} = -1$ and $g_{0i} = 0$. The transverse traceless part of h_{ij} corresponds to gravitational waves [17]. The coupling of tensor modes with matter and radiation is suppressed in case of perfect fluids. However, the inclusion of traceless transverse terms, Π^i_j, into the anisotropic stress tensor, T^i_j, as defined by

$$T^\mu_\nu = \left(\overline{\mathscr{P}}+\delta\overline{\mathscr{P}}\right)g^\mu_\nu + \left(\left(\overline{\rho}+\delta\overline{\rho}\right)+\left(\overline{\mathscr{P}}+\delta\overline{\mathscr{P}}\right)\right)U^\mu U_\nu, \quad \mu,\nu = 0,1,2,3, \tag{4}$$

modifies the isotropic and homogeneous characteristics of perfect fluids, $\overline{\rho}$ and $\overline{\mathscr{P}}$, and provides a natural coupling for observing interactions between the tensor modes, that is, gravitational waves, in the (RMD) cosmological environment. It changes the dynamical behavior of the tensor perturbation components, h_{ij}, through the following equation of motion:

$$\partial_t^2 h_{ij} + \left(\frac{3}{a}\frac{da}{dt}\right)\partial_t h_{ij} - \left(\frac{\nabla^2}{a^2}\right)h_{ij} = 16\pi G\frac{\Pi_{ij}}{a^2}. \tag{5}$$

In this case, the traceless component of the energy-momentum tensor is defined by $\Pi_{ij} = g_{il}\Pi^l_j = g_{il}(T^l_j - \delta^l_j T^k_k/3) = T_{ij} - g_{ij}(\overline{\mathscr{P}}+\delta\overline{\mathscr{P}})$.

By turning (5) into its Fourier space transformed form, one has

$$\ddot{h}_{ij} + 2\mathscr{H}\dot{h}_{ij} + k^2 h_{ij} = 16\pi G\Pi_{ij}, \tag{6}$$

where $\mathscr{H} = \dot{a}/a$, and *dots* correspond to conformal time derivatives. The anisotropic stress Π_{ij} is given by

$$\Pi_{ij} = T_{ij} - \frac{g_{ij}}{3}T^k_k = \frac{a^2\overline{\rho}}{4\pi}\int\left(n_i n_j - \frac{\delta_{ij}}{3}\right)F_\nu d\Omega = \frac{a^2\overline{\rho}_\nu}{4\pi}\mathscr{F}^{(0)}_{ij}, \tag{7}$$

with $\int n_i n_j d\Omega = 4\pi\delta_{ij}/3$.

The analytical multipole decomposition discussed in [19] supports the equations for obtaining $\mathscr{F}^{(0)}_{ij}$. Given a (Fermi-Dirac) momentum distribution, $f_0(q)$, and scalar perturbations, $\Psi(k_i, q, n_j, \eta)$, one defines

$$F_\nu\left(k_i, n_j, \eta\right) \equiv \frac{\int q^3 f_0(q)\,\Psi\left(k_i, q, n_j, \eta\right)dq}{\int q^3 f_0(q)\,dq}, \tag{8}$$

which appears in the Boltzmann equation [19] as

$$\dot{F}_\nu + ik_i n^i F_\nu + 2\dot{h}_{ij}n^i n^j = \frac{4\pi}{a^4\overline{\rho}_\nu}\int q^3\widehat{C}\left[f\right]dq, \tag{9}$$

where the interactions brought up by $\widehat{C}[f]$ will be discussed later. By following the same notation from [19], one finds that

$$\mathscr{F}_{ij}(k_i,\mu,\eta) = \int_0^{2\pi}\left(n_i n_j - \frac{\delta_{ij}}{3}\right)F_\nu d\varphi, \tag{10}$$

where φ is the polar angle such that $d\Omega = \sin\theta d\theta d\varphi$. Upon multiplying (9) by $(n_i n_j - \delta_{ij}/3)$ and integrating over φ, one has [15, 19]

$$\dot{\mathscr{F}}_{ij} + ik\mu\mathscr{F}_{ij} + 2\dot{h}_{lm}\int_0^{2\pi} n^l n^m\left(n_i n_j - \frac{\delta_{ij}}{3}\right)d\varphi = \mathscr{C}_{ij} \tag{11}$$

with $\mu \equiv \cos(\varphi) = \widehat{k}\cdot\widehat{n}$, where an ordinary collision term, $\mathscr{C}_{ij}$, is introduced as

$$\mathscr{C}_{ij} \equiv \frac{4\pi}{a^4\overline{\rho}}\int q^3 dq\int_0^{2\pi} d\varphi\left(n_i n_j - \frac{\delta_{ij}}{3}\right)\widehat{C}[f]. \tag{12}$$

Now performing the Legendre expansion with respect to μ, one obtains

$$\begin{aligned}\mathscr{F}_{ij}(k_i,\mu,\eta) &= \sum_{\ell=0}^{\infty}(-i)^\ell(2\ell+1)\mathscr{F}_{ij}^{(\ell)}(k_i,\eta)P_\ell(\mu),\\ \mathscr{C}_{ij}(k_i,\mu,\eta) &= \sum_{\ell=0}^{\infty}(-i)^\ell(2\ell+1)\mathscr{C}_{ij}^{(\ell)}(k_i,\eta)P_\ell(\mu),\end{aligned} \tag{13}$$

for which the orthogonality relations involving the Legendre polynomials,

$$\int_{-1}^{1} P_\ell P_m\, d\mu = \frac{2}{2\ell+1}\delta_{\ell m}, \tag{14}$$

are prescribed. The zeroth-order multipole contribution that appears in (7) is effectively the unique nonvanishing contribution of F_ν into (10), which is computed from the above multipole expansion for $\mathscr{F}_{ij}(k_i,\mu,\eta)$. It explains the origin of the anisotropic stress contribution written in terms of $\mathscr{F}_{ij}^{(0)}$ into (5).

Finally, by multiplying (11) by $(i^\ell/2)P_\ell$ and integrating it over μ, after performing some straightforward mathematical manipulations, one obtains [19]

$$\dot{\mathscr{F}}_{ij}^{(0)} = -k\,\mathscr{F}_{ij}^{(1)} - \frac{8\pi}{15}\dot{h}_{ij} + \mathscr{C}_{ij}^{(0)}, \tag{15}$$

$$\dot{\mathscr{F}}_{ij}^{(2)} = -\frac{k}{5}\left[3\mathscr{F}_{ij}^{(3)} - 2\mathscr{F}_{ij}^{(1)}\right] - \frac{16\pi}{105}\dot{h}_{ij} + \mathscr{C}_{ij}^{(2)}, \tag{16}$$

$$\dot{\mathscr{F}}_{ij}^{(4)} = -\frac{k}{9}\left[5\mathscr{F}_{ij}^{(5)} - 4\mathscr{F}_{ij}^{(3)}\right] - \frac{8\pi}{315}\dot{h}_{ij} + \mathscr{C}_{ij}^{(4)}, \tag{17}$$

$$\dot{\mathscr{F}}_{ij}^{(\ell)} = -\frac{k}{2\ell+1}\left[(\ell+1)\mathscr{F}_{ij}^{(\ell+1)} - \ell\mathscr{F}_{ij}^{(\ell-1)}\right] + \mathscr{C}_{ij}^{(\ell)}, \quad (\ell \neq 0,2,4). \tag{18}$$

The above equations are constrained by the dynamical behavior of h_{ij}, which turns them into a system of $\ell+1$ decomposed first-order ordinary differential equations completely equivalent to the Boltzmann equation.

Since we are concerned with the fact that the anisotropic stress is only cosmologically relevant for massless particles [23], independently of our previous arguments, the condition of having background neutrinos in ultrarelativistic thermodynamic regime is assumed along the RMD era. In this case one can write $\overline{\rho}_\nu$ in terms of the total energy density, $\overline{\rho}$, and of the rates $R_\nu = \Omega_\nu/\Omega_r \equiv \overline{\rho}_\nu/\overline{\rho}_r$ and $R_{m/\gamma} = \Omega_m/\Omega_\gamma$,

$$\begin{aligned}\overline{\rho}_\nu &= \overline{\rho}_\nu\frac{\overline{\rho}}{\overline{\rho}_m+\overline{\rho}_r} = \frac{1}{1+(\overline{\rho}_m/\overline{\rho}_r)}R_\nu\overline{\rho}\\ &= \frac{1}{1+(\Omega_\gamma/\Omega_r)(\Omega_m/\Omega_\gamma)}R_\nu\overline{\rho} = \frac{1}{1+(1-R_\nu)R_{m/\gamma}}R_\nu\overline{\rho},\end{aligned} \tag{19}$$

where $\overline{\rho} = \overline{\rho}_m + \overline{\rho}_r$, $\Omega_r = \Omega_\nu + \Omega_\gamma$, such that $\Omega_i = 3\rho_i/(8\pi G)$, with $i = r$ (radiation), ν (neutrinos), γ (photons), and m (matter). By substituting (7) with the above-defined parameters into (5), and using (2) for $\overline{\rho}$, one obtains a suitably modified picture of [19] given by

$$\ddot{h}_{ij} + 2\mathscr{H}\dot{h}_{ij} + k^2 h_{ij} = \frac{3}{2\pi}\mathscr{H}^2\frac{R_\nu}{1+(1-R_\nu)R_{m/\gamma}}\mathscr{F}_{ij}^{(0)}, \tag{20}$$

where the inclusion of the elements of the RMD cosmic inventory is evinced by $R_{m/\gamma}$ on the right-hand side (by setting $R_{m/\gamma} = 0$ one is able to recover the results for the RD cosmic inventory as in [19]).

3. Gravitational Waves Coupled to Neutrinos in the RMD Scenario

The background solutions of the Friedmann equation for the RMD universe, with the corresponding equation of state, respectively, represented by $\overline{\mathscr{P}}_r = \overline{\rho}_r/3$ and $\overline{\mathscr{P}}_m = 0$, are given by

$$\overline{\rho}_r = \rho_0\frac{\Omega_r}{a^4}, \qquad \overline{\rho}_m = \rho_0\frac{\Omega_m}{a^3}, \tag{21}$$

where we have neglected the cosmological constant phase. For a RMD cosmological background, the scale factor dependence on the conformal time reproducing the radiation-to-matter transition can be exactly given by

$$a(\eta) = \frac{2\pi G}{3}\Omega_m\eta^2 + \left(\frac{8\pi G}{3}\Omega_r\right)^{1/2}\eta \tag{22}$$

and conveniently rewritten as

$$ka(\eta) = \sqrt{\frac{8\pi G}{3}\Omega_r}\left[\frac{(k\eta)^2}{4k\eta_{\mathrm{eq}}} + k\eta\right], \tag{23}$$

with $\eta_{\mathrm{eq}} = (3\Omega_r/(8\pi G))^{1/2}/\Omega_m$, where a scale independent parameter $k\eta$ has been introduced, and the boundary conditions are set as $a(0) \equiv 0$. Equation (23) also fiducially describes the dynamics deep inside radiation or matter dominated (MD) eras separately. Assuming the above dependence of a on η into the coupled equations of the previous section, one can treat the gravitational waves entering the horizon

even after the time of matter-radiation equality, that is, with the redshift $z < 10^4$. Therefore, besides being applied to the analysis of waves that have entered the horizon well inside the RD era, with $k \gg 0.1\,[\mathrm{Mpc}]^{-1}$, our result can be extended to the analysis of waves with $k \sim 0.1\,[\mathrm{Mpc}]^{-1}$. In addition, from the point of view of the mathematical manipulation/resolution of the equations, the explicit dependence on the cosmological scales, k, will be relegated to the parameter $k\eta_{\mathrm{eq}}$ at (23), so that one can express all the subsequent results in terms of $k\eta$, with η in units of $\eta_0 \approx 1/H_0 \approx 5000\,[\mathrm{Mpc}]$. In this case, $k\eta \sim 1$ corresponds to the horizon crossing parameter.

The system of coupled equations ordinarily defined in terms of $k\eta$ also allows one to depict the behavior of waves deep inside the horizon ($k\eta \gg 1$). Given the scale covariance introduced by $k\eta$ (in place of a factorized dependence on η), it is always possible to rescale the initial value of $h_{ij}(k\eta)$ as to have $h_{ij}(0) = h^{(0)}$. The choice of the initial amplitude after crossing the causal horizon, $h^{(0)}$, is arbitrary and it does not affect our results. The variables $\dot{h}_{ij}$ and $\mathscr{F}_{ij}^{(\ell)}$ are concerned with the information about the effect of damping oscillation. It is attributed to the expansion of the universe, in case of $\dot{h}_{ij}$, and to the interaction with the CνB, in case of $\mathscr{F}_{ij}^{(\ell)}$. Therefore, these terms should be taken into account just after crossing the causal horizon; that is, for $k\eta > k\eta_0 \approx 0$. Because of that, it is reasonable to assume $\dot{h}_{ij}(0) = 0$ and $\mathscr{F}_{ij}^{(\ell)}(0) = 0$. Finally, we also have assumed the standard cosmological values for Ω_i, with $i = \gamma, \nu$ and m, such that $\Omega_\nu/\Omega_\gamma > 0$ and $\Omega_\gamma/\Omega_m \approx 10^{-4}$.

The corresponding dynamical evolution of the gravitational waves, that is, of the tensor modes, h_{ij}, in terms of the scale independent variable, $k\eta$, can be depicted in Figures 1 and 3. Once gravitational waves have entered the horizon ($k\eta \gtrsim 1$), their amplitude dies away (c.f. Figure 1) more rapidly at a universe with the cosmic inventory containing the matter component contribution. By suppressing the contribution due to the neutrino anisotropic stress at (20), one recovers a damped harmonic oscillator- (DHO-) like equation for which the damping factor is given by $\gamma \equiv 2\mathscr{H}$. One can notice that deep inside the MD era the γ factor is two times the value corresponding to that of deep inside the RD era. The amplitude of the gravitational waves is relatively suppressed when it penetrates into the MD era.

The neutrino free-streaming regime is obtained by setting a vanishing collision term, $\mathscr{C}_{ij}^{(\ell)} = 0$, at the evolution equations. Figure 1 shows the results for $R_\nu = 0.4052$ (three neutrino species) and $R_\nu \approx 1$ (not so realistic large number of neutrino degrees of freedom, which includes extra flavor quantum numbers) obtained from numerical calculations involving 1200 multipoles for RD and RMD scenarios. The results are relevant for modes which enter the horizon at the universe's temperature about $T \lesssim 1$ MeV [21]. The anisotropic stress effects are relatively suppressed for modes which enter the horizon at the MD era, as one can observe from the right side of (20). The exception is for the situation where R_ν

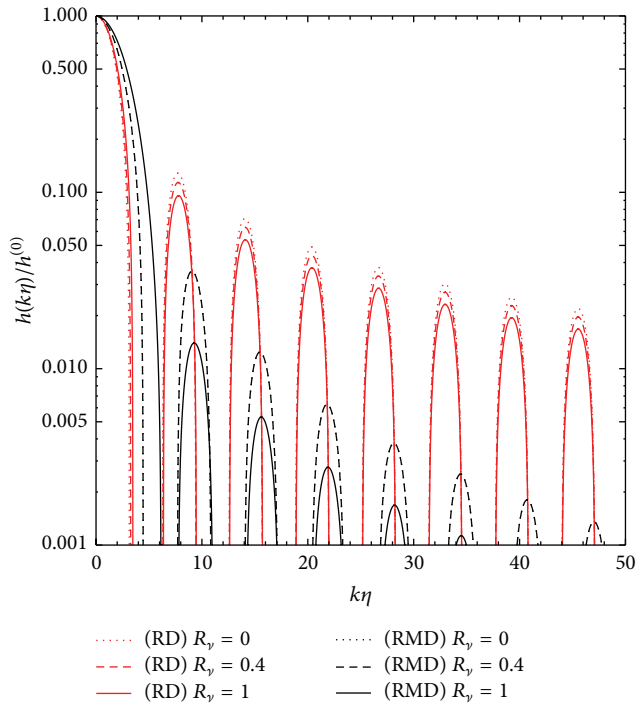

Figure 1: Evolution of the normalized wave amplitude $h_{ij}/h_{ij}^{(0)}$ as function of $k\eta$ for RD (red lines) and RMD (black lines) background cosmic inventories. Results are for vanishing anisotropic stress, with $R_\nu = 0$ (dotted lines), for $R_\nu = 0.4052$ (dashed lines) and for $R_\nu = 1$ (solid lines). The RD curves are scale independent so that $k\eta$ is given in units of $k\eta_0$. The RMD curves are correctly interpreted by observing that $k\eta_{\mathrm{eq}} = 1$, which correspond to scales that have entered the Hubble horizon at the time of matter-radiation equality (see also Figure 7 for comparison). In spite of being more evident for the RMD scenario, in both situations the largely increasing values of R_ν result in a more relevant suppression of the tensor modes during the cosmological evolution. Notice that just for the first peak, solid lines are overpassing dashed- and dotted-lines.

approximates to unity. The amplitude h_{ij} is constant outside the horizon and starts decreasing after the horizon crossing.

The inclusion of the matter background into the cosmic inventory introduces an additional subtle effect on the amplitude of the gravitational waves under the influence of the anisotropic stress. Scales just entering the horizon at late times have the corresponding oscillation modes undergoing a delayed suppression due to the coupling to neutrinos. It propagates to the following oscillation peaks in a kind of translational effect of the oscillation pattern, which is naturally expected if one observes that, in the limit of radiation domination, one has

$$\left|h_{ij}(k\eta)\right| = \frac{\sin(k\eta)}{k\eta}, \tag{24}$$

and, in the limit of matter domination, one has

$$\left|h_{ij}(k\eta)\right| = 3\frac{(\sin(k\eta) - k\eta\cos(k\eta))}{(k\eta)^3}. \tag{25}$$

The reason for such a behavior is engendered by the fact the RMD curves are correctly interpreted only for $k\eta_{\rm eq} = 1$, which correspond to scales that have entered the Hubble horizon at the time of matter-radiation equality. In the Appendix we show the corresponding results for $k\eta_{\rm eq} = 100$. In spite of being evinced for the RMD scenario, increasing values of R_ν result in a more relevant suppression of the tensor modes even for the RD scenario.

In [19] one identifies that for the standard case corresponding to $R_\nu = 0.4052$ for three families of neutrinos, roughly 22% of the intensity of the gravitational waves is absorbed by the CγB environment. In spite of not considering the same steps for numerical integrations as assumed in [19], our results for the RD era agrees with those presented in [19], as it can be depicted in Figures 1 and 2 by comparing dashed and dotted red lines. The effective suppression due to the inclusion of neutrinos can be depicted from Figure 2 where we have computed the time-averaged quantity $D(k)^2 = \langle 2(k\eta)^2|h_{ij}(k\eta)|^2\rangle$ as function of the cosmological scale, k. Such a time-averaged quantity is processed from a cut-off η^*. Although η^* is arbitrary, the time-averaged operation over $(k\eta)^2|h_{ij}(k\eta)|^2$ is effective only for scales entering the horizon at times $\eta \gg \eta^*$.

When the elements for describing the RMD regime are introduced, our results are considerably different, in spite of exhibiting a conceptual agreement with those from [19]. The point is that once the cosmic inventory enters into the MD era, the effects due to anisotropic stress over the corresponding gravitational wave modes are highly suppressed. There is an expected overall suppression of the gravitational wave modes (cf. the black lines depicted in Figures 1 and 2) driven by the MD regime. Likewise, given that the realistic neutrino effects are suppressed, in the RMD scenario the relative rate of absorption of waves turns into a tiny value $\ll$ 0.1% (cf. the dashed and dotted overlapping black lines depicted in Figures 1 and 2). One can notice that the lines obtained for $R_\nu \approx 1$ overpass the lines obtained for $R_\nu \approx 0$ at some ordinary scale $\tilde{k}$. Scale values for which $k > \tilde{k}$ have tried out a sufficient number of oscillating cycles to average $h_{ij}(k\eta)$ and produce some representative damping effect. In this case, the realistic effects produced by neutrinos correspond to a suppression of the power spectrum of gravitational waves for which $k \gg \tilde{k}$.

The maximum amount of damping occurs for the extrapolating limit of $R_\nu \to 1$. In this case, the influence of matter on the cosmic inventory ($R_{m/\gamma} \sim 10^4$) is highly suppressed from (19) and therefore the damping effect increases (cf. solid black lines depicted in Figures 1 and 2). Such a pictorial situation results in an unrealistic scenario for which, however, the absorption rate is roughly similar to that of 43% from [19] (cf. black lines crossing red lines in Figure 2).

Finally, the highest first oscillation peak for the RMD results depicted in Figure 2 appears because of the abovementioned relative delay (phase difference) of the first oscillation damping of the gravitational waves in the RMD era, as depicted in Figure 1 and supported by (24) and (25). Even creating a kind of horizon crossing *fake*-resonance effect, it disappears along the cosmological η evolution. Moreover, the increasing damping caused by the anisotropic stress of the standard (three family) neutrinos is much more effective at the RD regime.

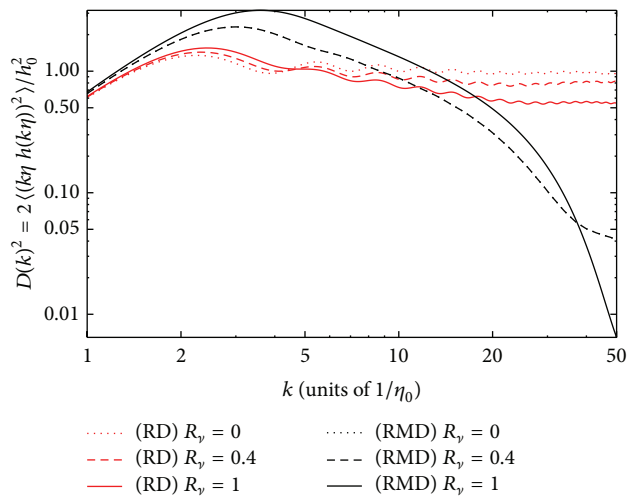

FIGURE 2: Time-averaged values of $2\langle (k\eta)^2|h_{ij}(k\eta)|^2\rangle$ as function of $k[\mathrm{Mpc}^{-1}]$ for RD (red lines) and RMD (black lines) background cosmic inventories. Results are for vanishing anisotropic stress, with $R_\nu = 0$ (dotted lines), for $R_\nu = 0.4(0.4052)$ (dashed lines) and for $R_\nu = 1$ (solid lines). Notice the *fake* resonance effect for modes with $k\eta \gtrsim 1$ followed by the neutrinos damping effect which is more relevant for scales deep inside the horizon.

Turning back to the collision term contributions, we will follow the parametrization from [19] that sets $\widehat{C}[f] = -f_0\Psi/\tau$, where τ is the mean time between collisions. In this case one has $\mathscr{C}_{ij}^{(\ell)} = -\mathscr{F}_{ij}^{(\ell)}/\tau$. The auxiliary parameter in defining the strength of the interactions, $k\tau$, corresponds to the ratio between the wave frequency and the collision frequency. One can compare the effects of including the collision term parameterized by $\tau = 0.01, 0.1, 1$, and 10 in Figures 3 and 4. One should notice that the inclusion of collision effects parameterized by $k\tau$ at $\mathscr{C}_{ij}^{(0)}$ into (18) affects the gravitational wave evolution in a very subtle way. Since one has τ in units of η_0 and k in units of $1/\eta_0$, upon setting $\tau > 10 \gg 1$ one recovers the free-streaming (collisionless) results. Otherwise, small values for $k\tau$ would correspond to very frequent collisions that dominate the dynamical evolution described by (15)–(18). It results in $\mathscr{F}_{ij} \propto e^{-\eta/\tau}$, which leads to an exponential decay suppression of the anisotropic stress. Decreasing values of τ therefore represent increasing collision rates and consequently a less dispersive environment/effect due to the anisotropic stress. Although strong deviations from the standard scenario with $R_\nu = 0.4052$ are unlikely, damping effects as those obtained for $R_\nu = 1$ become effective just when neutrinos enter the free-streaming regime and can be interpreted either as the existence of additional neutrino degrees of freedom (d.o.f) or as the existence of exotic fluid/particles in the early universe.

Figures 3 and 4 also show that, for $k \gg \tilde{k}$, the amount of damping with respect to the vanishing stress contribution in case of RMD era is not regular. It corresponds to a scale

dependent effect. The effects of increasing the frequency of the collisions by diminishing τ can be, at least superficially, quantified. It is important to notice that either in the limit of radiation domination (cf. (24)) or in the limit of matter domination (cf. (25)), where

$$\left|h_{ij}(k\eta)\right| \approx \frac{\sin(k\eta)}{k\eta}\left(1+\mathcal{O}(k\eta)^2\right), \tag{26}$$

scales just entering the horizon lead to nondecaying values for $D(k)^2$. By following the same analogy with a DHO, it is also relevant to notice that $D(k)^2$ parameterizes the damping of the averaged valued of the DHO energy. In fact,

$$(k\eta)^2\left|h_{ij}(k\eta)\right|^2 \propto k^3 P_h(k), \tag{27}$$

where $P_h(k)$ is the power spectrum related to tensor modes [17].

Figure 4 shows the time-averaged quantity, $D(k)^2$, by considering the effective collisions parameterized by $k\tau = 0.01$ and 10. The effect of rare collisions is recovered for $k\tau \sim 10$. As in Figure 2, it is possible to identify the crossing value of $\tilde{k}$ for which the correct interpretation of $D(k)^2$ is pertinent.

To end up, the damping of gravitational waves also affects some spectral features related to the tensor contribution to the anisotropy spectrum. From the analytical multipole decomposition [17], the contribution to the C_l^T's can be written as

$$C_{l,i}^T = \frac{(l-1)\,l\,(l+1)\,(l+2)}{\pi} \times \int_0^\infty dk k^2 \left| \frac{\Theta_{l-2,i}^T}{(2l-1)(2l+1)} + 2\frac{\Theta_{l,i}^T}{(2l-1)(2l+3)} + \frac{\Theta_{l+2,i}^T}{(2l+1)(2l+3)} \right|^2, \tag{28}$$

where i denotes + and × modes. $\Theta_{l,i}^T$ is obtained through

$$\Theta_{l,i}^T = -\frac{1}{2}\int_{\eta^*}^{\eta_0} d\eta j_l\left[k(\eta_0-\eta)\right]\dot{h}_{ij}(k,\eta),$$
$$\Theta_{l,i}^{T(\mathrm{MD})} \approx -\frac{1}{2}\int_{\eta^*}^{\eta_0} d\eta j_l\left[k(\eta_0-\eta)\right]\frac{d}{d\eta}\left[\frac{3j_1(k\eta)}{k\eta}\right]\left(P_h(k)\right)^{1/2}, \tag{29}$$

where the last step stands for the analytical approximation for the MD scenario. In this case, the departing amplitude of the gravitational waves is given in terms of $P_h^{1/2}$.

Substituting the results for Θ_l^T into (28) allows one to compute the tensor imprints on the map of the CγB

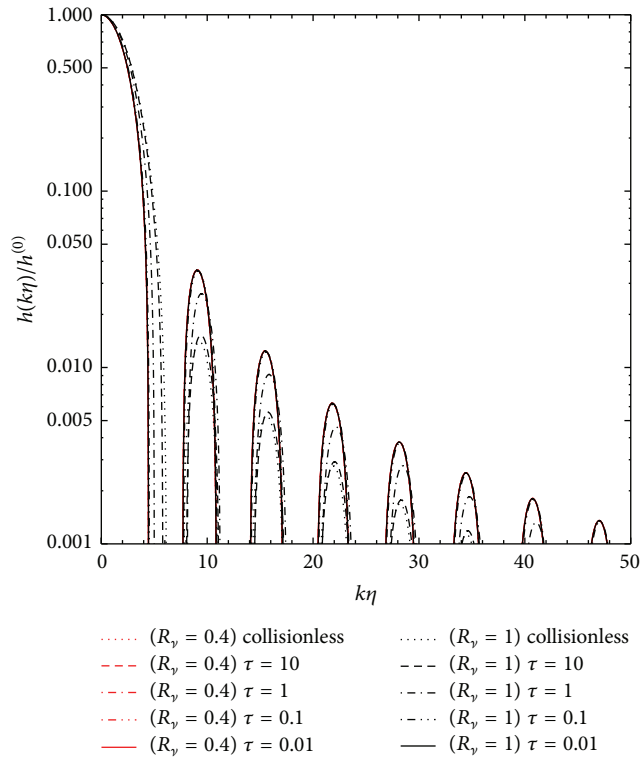

Figure 3: Evolution of the normalized wave amplitude $h_{ij}/h_{ij}^{(0)}$ as function of $k\eta$ for the RMD scenario in case of including the collision terms. Results are for $\tau = 0.01, 0.1, 1$, and 10 and for the collisionless case. τ is given in units of η_0 and k in units of $1/\eta_0$. We have considered three neutrino species with $R_\nu = 0.4052(0.4)$ (red lines) and the extreme case of a huge number of neutrino species with $R_\nu = 1$ (black lines). The RMD curves are correctly interpreted by observing that $k\eta_{\mathrm{eq}} = 1$ (see also Figure 8 for comparison).

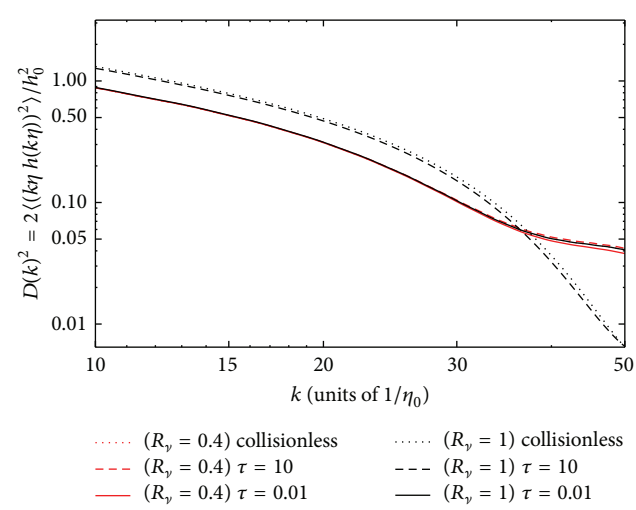

Figure 4: Time-averaged values of $D(k)^2 = 2\langle(k\eta)^2|h_{ij}(k\eta)|^2\rangle$ as function of $k[\mathrm{Mpc}^{-1}]$ for the RMD scenario in case of including the collision term. Results are for $\tau = 0.01$ and 10 and for the collisionless according to the legend, with τ in units of η_0 and k in units of $1/\eta_0$ with red and black lines in correspondence with those from Figure 3.

temperature. After some mathematical manipulations [17], the analytical expression for the RD scenario results in

$$C_l^T = 2\frac{9(l-1)l(l+1)(l+2)}{4\pi}\int_0^\infty dk k^2 P_h(k) \times \left|\int_0^{\eta_0} d(k\eta)\frac{j_2(k\eta)}{k\eta}\left[\frac{j_{j-2}(k[\eta_0-\eta])}{(2l-1)(2l+1)} + 2\frac{j_l(k[\eta_0-\eta])}{(2l-1)(2l+3)} + \frac{j_{l+2}(k[\eta_0-\eta])}{(2l+1)(2l+3)}\right]\right|^2, \quad (30)$$

where we have set the lower limit on the time integral equal to zero since the time η^* at which the modes enter the horizon is assumed to satisfy $\eta^* \ll \eta_0$. We have identically followed the approximations set by [17]. Since one has

$$P_h(k) = \frac{8\pi}{k^3}\frac{H^2}{m_{Pl}^2}, \quad (31)$$

by defining novel integration variables $y \equiv k\eta_0$ and $x \equiv k\eta$, one gets the analytical form given by

$$C_l^T = 36\left(\frac{H_{\text{inf}}}{m_{Pl}}\right)^2 (l-1)l(l+1)(l+2)\int_0^\infty \frac{dy}{y} \times \left|\int_0^y dx\frac{j_2(x)}{x}\left[\frac{j_{l-2}(y-x)}{(2l-1)(2l+1)} + 2\frac{j_l(y-x)}{(2l-1)(2l+3)} + \frac{j_{l+2}(y-x)}{(2l+1)(2l+3)}\right]\right|^2, \quad (32)$$

where H_{inf} is the Hubble rate when the modes crossed the horizon (when $k\eta = 1$ early on), after being modulated by some transfer function that connects MD to RD scenarios [17].

The numerical results obtained for the tensor modes, $h_{ij}(k,\eta)$, allow one to compute the neutrino and collision effect imprints on the map of CγB temperature in the RMD scenario.

After entering the horizon, the amplitude of gravitational waves dies away (cf. Figure 1). The anisotropy spectrum is consequently affected by gravitational waves only on scales larger than the horizon at recombination. This corresponds to angular scales $l \lesssim 100$ in the multipole expansion. The tensor curves that we have obtained in Figure 5 for the same set of parameters introduced into Figure 1 in the RMD era show that C_l^T's die out after $l \gtrsim 100$. The analytical curve is obtained for RD connected to MD scenarios through a transfer function [24]. The coupling to neutrinos suppresses the contribution of tensor modes from the sum of anisotropies. Therefore, if tensor perturbations grow up during the inflationary era, and if the total scalar plus tensor anisotropy spectrum is fit to the large scale structure data, then the small-scale scalar amplitude is smaller than it would be. The presence of the coupled anisotropic stress of neutrinos just shows the effects of the neutrinos (like a fluid) on the variance of temperature due to gravitational waves. In Figure 6 we compare the effects of including the collision term parameterized by $k\tau = 0.01, 0.1, 1$, and 10 assuming three neutrino species, $R_\nu = 0.4052$, and a larger number of neutrino species, $R_\nu = 1$. From Figure 3 one just notices some smooth suppression relative to decreasing of the frequency of collisions ($\tau \gg 1$). The collision frequency also diminishes as like neutrinos go deep inside the free-streaming propagation regime, which intensifies the damping effect.

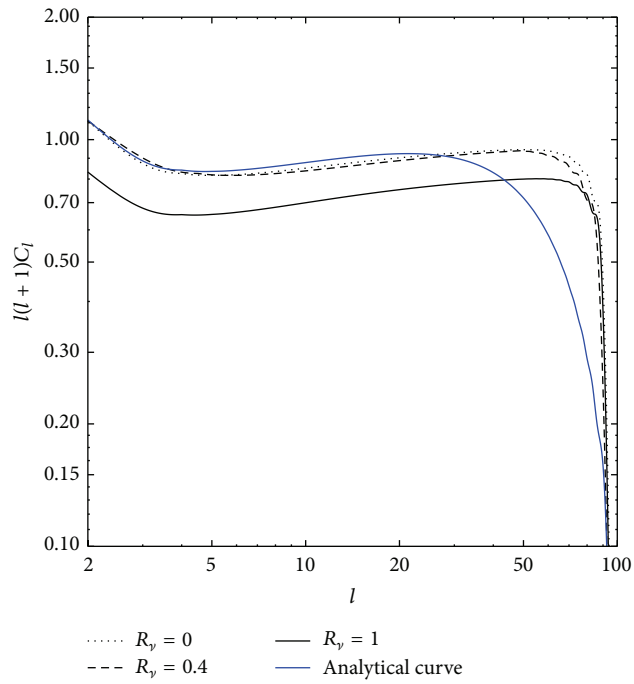

Figure 5: Tensor contribution to the angular power spectrum in the RMD scenario. Results are for vanishing anisotropic stress (dotted lines), for $R_\nu = 0.4\,(0.4052)$ (dashed lines), and for $R_\nu = 1$ (solid lines) for the collisionless case. The blue line corresponds to the analytical results obtained for a vanishing anisotropic stress component, where we have used an analytical transfer function to account for RD and MD scenarios.

Figure 5 shows that for neutrinos with only three flavor degrees of freedom, the modifications on the C_l^T coefficients are minimal. The damping of the angular power spectrum and, more properly, of the temperature variance, C_2^T, is more relevant for $R_\nu \lesssim 1$. The analytical curve reproduces the numerical results up to $l \sim 30$. For larger multipole values, with $l \gg 100$, even numerically, the coefficients C_l^T die out. The sharp fall observed in Figures 5 and 6 is consistent with the multipole decomposition solution.

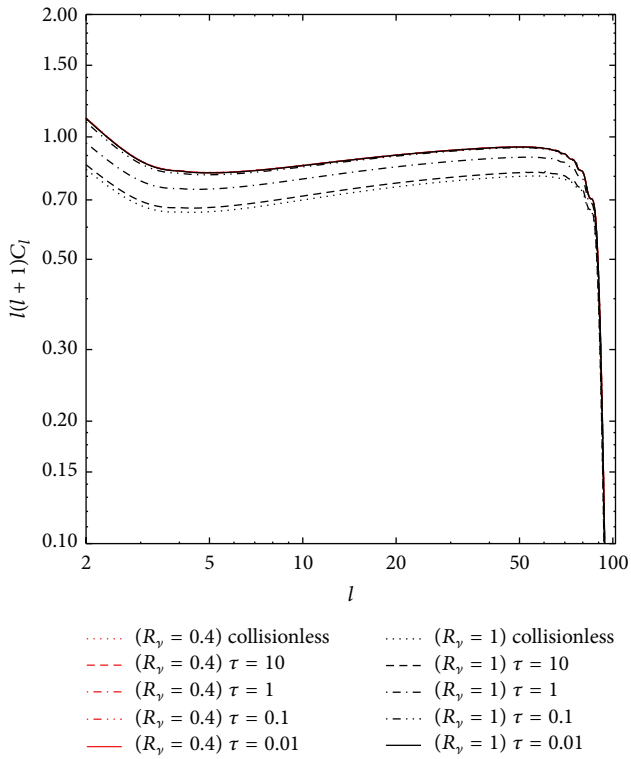

Figure 6: Tensor contribution to the angular power spectrum for the RMD scenario in case of including the collision terms. Results are for $\tau = 0.01, 0.1, 1$, and 10, in units of η_0, and for the collisionless case. Notice that, for decreasing values of the τ parameter, the suppression due to a huge number of neutrinos (d.o.f.) is not so relevant; that is, the increasing collision effect attenuates the damping effect on the tensor mode propagation and it is reflected on the tensor contribution to the angular power spectrum.

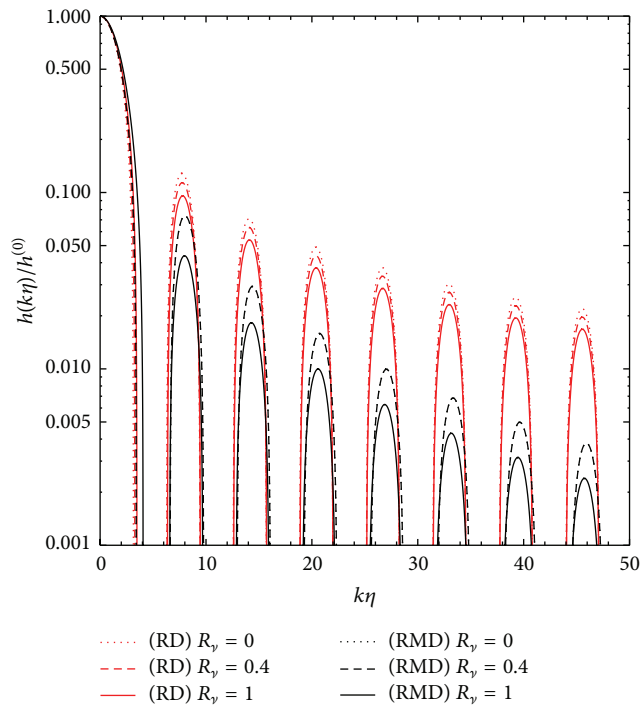

Figure 7: Evolution of the normalized wave amplitude $h_{ij}/h_{ij}^{(0)}$ as function of $k\eta$ for RD (red lines) and RMD (black lines) background cosmic inventories, in correspondence with Figure 1. Again, the RD curves are scale independent and the RMD curves are correctly interpreted by observing that $k\eta_{\rm eq} = 100$, which correspond to scales that have entered the Hubble horizon before the time of matter-radiation equality.

4. Conclusions

The observation of primordial gravitational waves indeed provides a renewed overview about the earliest moments in the history of the universe and on possible new physics at energies many orders of magnitude beyond those accessible at particle accelerators. The recent positive fit-back from experimental physics [1, 2] has indeed provided a crucial evidence for inflation in the early universe, which can also constrain the physics from the grand unification scale to the Planck scale.

Since a universe overfilling viscosity results in gravitational wave damping effects, we have considered the possibility of observing some frequency-dependent absorption in the frequency range where neutrino decoupling is relevant. By mixing analytical and numerical procedures, we have obtained the evolution of tensor modes and its corresponding imprints on the CγB temperature in case of considering a RMD environment in the presence of an overfilling CνB. Departing from the evolution of the gravitational waves from the time of their production, transversing the RD, the relevant modes exhibit a substantial damping on their amplitudes attributed to the expansion of the universe when they enter into the MD era. Meanwhile, the anisotropic stress component of the energy-momentum tensor changes the wave pattern when the cosmological neutrino background CνB is taken into account [25]. It has been noticed that the effective neutrino viscosity introduces some increasing contribution to the overwhelming dynamics during the decoupling period.

The damping effects owing to the influence of the (neutrino) anisotropic stress have been computed for a RMD scenario and compared to previous results for the RD scenario. We have compared the effects of including collision terms with collision frequency parameterized by $\tau = 0.01, 0.1, 1$, and 10 assuming three neutrino species ($R_\nu = 0.4052$) and a larger number of (neutrinos) degrees of freedom ($R_\nu = 1$). The collision dynamics is shown to introduce a tiny shift between two successive peaks of the gravitational wave spectrum.

The connection between the anisotropic stress of neutrinos and its effects on the CγB temperature has also been identified, as it is used to be intermediated by gravitational waves. Our results suggest that an extra number of neutrino degrees of freedom might be related either to some exotic neutrino family or even to some arbitrary composing contribution to the anisotropic stress. In fact, considering $R_\nu = 1$ has intensified the damping effects up to its maximal value, as depicted in the map of the tensor contribution to the angular power spectrum, C_l^T. For decreasing values of the

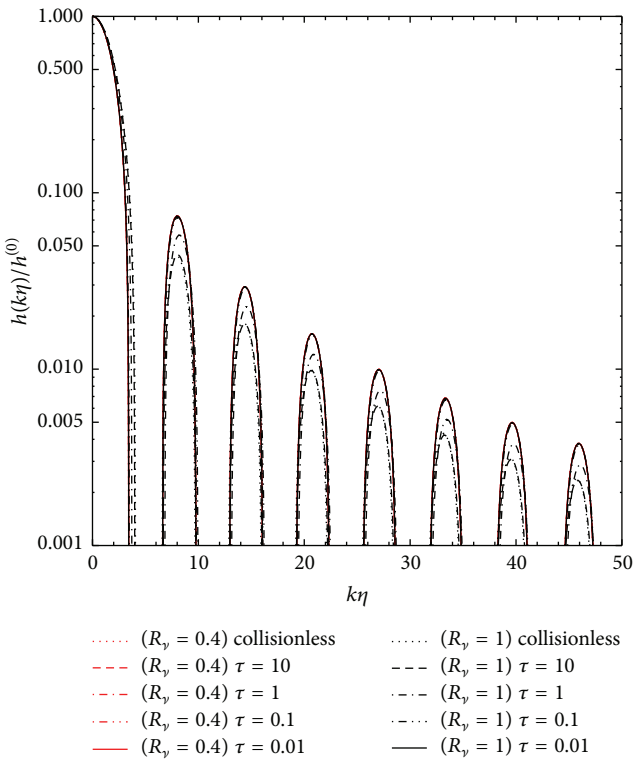

Figure 8: Evolution of the normalized wave amplitude $h_{ij}/h_{ij}^{(0)}$ as function of $k\eta$ for the RMD scenario in case of including the collision term, in correspondence with Figure 3, with RMD curves being correctly interpreted by observing that $k\eta_{\rm eq} = 100$.

collision τ parameter, the suppression of the gravitational wave amplitudes due to a huge number of degrees of freedom related to neutrinos is not so relevant, and the increasing collision frequency attenuates the damping effect on the tensor mode propagation. It has also been reflected on the map of tensor contributions to the angular power spectrum.

Finally, a time-averaged quantity, $D(k)^2$, introduced to implicitly quantify the power spectrum of gravitational waves, has shown that the RMD environment reduces the damping effect for realistic three flavor neutrino scenarios in spite of exhibiting the same maximal rate of damping for hypothesized scenarios with $R_\nu = 1$: a relevant aspect which may be considered in improving the computer programs used to analyze the future facilities.

Appendix

Figures 7 and 8 reveal the intrinsic dependence on the cross horizon driving parameter $k\eta_{\rm eq}$. They correspond to qualitative complementary results to Figures 1 and 3, in case of considering $k\eta_{\rm eq} = 100$ in place of $k\eta_{\rm eq} = 1$. For the RMD scenario, it corresponds to scales that have entered the Hubble horizon before the time of matter-radiation equality.

Conflict of Interests

The authors declare that there is no conflict of interests regarding the publication of this paper.

Acknowledgments

A. E. Bernardini would like to thank the Brazilian Agencies FAPESP (Grant 08/50671-0) and CNPq (Grant 300233/2010-8) for their financial support.

References

[1] D. Hanson, S. Hoover, A. Crites et al., "Detection of B-mode polarization in the cosmic microwave background with data from the south pole telescope," *Physical Review Letters*, vol. 111, Article ID 141301, 2013.

[2] P. A. R. Ade, R. W. Aikin, D. Barkats et al., "Detection of B-mode polarization at degree angular scales by BICEP2," *Physical Review Letters*, vol. 112, no. 24, Article ID 241101, 2014.

[3] W. Hu and M. White, "A CMB polarization primer," *New Astronomy*, vol. 2, pp. 323–344, 1997.

[4] M. Tucci, E. Martinez-Gonzalez, P. Vielva, and J. Delabrouille, "X-ray synchrotron emission from the oblique shock in the jet of the powerful radio galaxy 3C346," *Monthly Notices of the Royal Astronomical Society*, vol. 360, pp. 926–934, 2005.

[5] D. N. Spergel, R. Bean, O. Doré et al., "Three-year Wilkinson Microwave Anisotropy Probe (WMAP) observations: implications for cosmology," *Astrophysical Journal, Supplement Series*, vol. 170, no. 2, pp. 377–408, 2007.

[6] A. Abramovici, W. E. Althouse, R. W. P. Drever et al., "LIGO: the laser interferometer gravitational-wave observatory," *Science*, vol. 256, no. 5055, pp. 325–333, 1992.

[7] B. Abbott, R. Abbott, R. Adhikari et al., "Detector description and performance for the first coincidence observations between LIGO and GEO," *Nuclear Instruments and Methods in Physics Research A: Accelerators, Spectrometers, Detectors and Associated Equipment*, vol. 517, no. 1–3, pp. 154–179, 2004.

[8] B. Caron, A. Dominjon, C. Drezen et al., "The Virgo interferometer," *Classical and Quantum Gravity*, vol. 14, no. 6, pp. 1461–1469, 1997.

[9] F. Acernese, M. Alshourbagy, P. Amico et al., "Status of virgo," *Classical and Quantum Gravity*, vol. 25, Article ID 114045, 2008, http://www.virgo.infn.it/.

[10] H. Lück, "The GEO600 project," *Classical and Quantum Gravity*, vol. 14, p. 1471, 1997.

[11] B. Willke, P. Ajith, B. Allen et al., "The GEO-HF project," *Classical and Quantum Gravity*, vol. 23, p. S207, 2006, http://www.geo600.uni-hannover.de/.

[12] K. Kawabe, "Status of TAMA project," *Classical and Quantum Gravity*, vol. 14, no. 6, pp. 1477–1480, 1997.

[13] K. Danzmann and LISA Study Team, "LISA—an ESA cornerstone mission for a gravitational wave observatory," *Classical and Quantum Gravity*, vol. 14, no. 6, p. 1399, 1997.

[14] P. L. Bender, *Laser Interferometer Space Antenna for the Detection and Observation of Gravitational Waves: Pre-Phase A Report 2nd Edition*, MPQ233, Max-Plank Institut fur Quantenoptik, München, Germany, 1998.

[15] A. E. Bernardini and E. L. D. Perico, "Degenerate Fermi gas perturbations at standard background cosmology," *Journal of Cosmology and Astroparticle Physics*, vol. 2011, p. 10, 2011.

[16] A. D. Dolgov, "Neutrinos in cosmology," *Physics Reports*, vol. 370, no. 4-5, pp. 333–535, 2002.

[17] S. Dodelson, *Modern Cosmology: Anisotropies and Inhomogeneities in the Universe*, Academic Press, New York, NY, USA, 2003.

[18] A. E. Bernardini and V. A. S. V. Bittencourt, "The CνB energy density through the quantum measurement theory," *Astroparticle Physics*, vol. 41, pp. 31–37, 2013.

[19] R. Benini, M. Lattanzi, and G. Montani, "Signatures of the neutrino thermal history in the spectrum of primordial gravitational waves," *General Relativity and Gravitation*, vol. 43, no. 4, pp. 945–958, 2011.

[20] R. Benini, M. Lattanzi, and G. Montani, "A possible signature of cosmic neutrino decoupling in the nHz region of the spectrum of primordial gravitational waves," *Classical and Quantum Gravity*, vol. 27, no. 19, Article ID 194008, 2010.

[21] S. Weinberg, "Damping of tensor modes in cosmology," *Physical Review D*, vol. 69, no. 2, Article ID 023503, 2004.

[22] C. P. Ma and E. Bertschinger, "Cosmological perturbation theory in the synchronous and conformal Newtonian gauges," *The Astrophysical Journal*, vol. 455, pp. 7–25, 1995.

[23] J. Lesgourgues and S. Pastor, "Massive neutrinos and cosmology," *Physics Reports*, vol. 429, no. 6, pp. 307–379, 2006.

[24] M. S. Turner, M. White, and J. E. Lidsey, "Tensor perturbations in inflationary models as a probe of cosmology," *Physical Review D*, vol. 48, no. 10, pp. 4613–4622, 1993.

[25] T. Y. Xia and Y. Zhang, "Analytic spectra of CMB anisotropies and polarization generated by relic gravitational waves with modification due to neutrino free-streaming," *Physical Review D*, vol. 78, Article ID 123005, 2008.

Hindawi Publishing Corporation
Advances in High Energy Physics
Volume 2014, Article ID 469572, 10 pages
http://dx.doi.org/10.1155/2014/469572

Research Article

Residual Symmetries Applied to Neutrino Oscillations at NOνA and T2K

Andrew D. Hanlon,[1] Wayne W. Repko,[1] and Duane A. Dicus[2]

[1] *Department of Physics and Astronomy, Michigan State University, East Lansing, MI 48824, USA*
[2] *Department of Physics and Center for Particles and Fields, University of Texas, Austin, TX 78712, USA*

Correspondence should be addressed to Andrew D. Hanlon; adh58@pitt.edu

Received 3 April 2014; Accepted 24 July 2014; Published 24 August 2014

Academic Editor: Hiro Ejiri

The results previously obtained from the model-independent application of a generalized hidden horizontal $\mathbb{Z}_2$ symmetry to the neutrino mass matrix are updated using the latest global fits for the neutrino oscillation parameters. The resulting prediction for the Dirac CP phase δ_D is in agreement with recent results from T2K. The distribution for the Jarlskog invariant J_ν has become sharper and appears to be approaching a particular region. The approximate effects of matter on long-baseline neutrino experiments are explored, and it is shown how the weak interactions between the neutrinos and the particles that make up the Earth can help to determine the mass hierarchy. A similar strategy is employed to show how NOνA and T2K could determine the octant of $\theta_a(\equiv \theta_{23})$. Finally, the exact effects of matter are obtained numerically in order to make comparisons with the form of the approximate solutions. From this analysis there emerge some interesting features of the effective mass eigenvalues.

1. Introduction

Although there has been significant progress in neutrino physics from oscillation experiments, there remains much work to be done. The reactor angle $\theta_r(\equiv \theta_{13})$ has now been measured to greater accuracy than ever before, and the solar angle $\theta_s(\equiv \theta_{12})$ has been known for some time now. But, the octant of the atmospheric angle ($\theta_a > \pi/2$ or $\theta_a < \pi/2$) or whether this angle is maximal ($\theta_a = \pi/2$) has yet to be answered. Determination of the Dirac CP phase has been improved. Recent results from T2K exclude at 90% C.L. $\delta_D \in [34.2^\circ, 144^\circ]$ for normal hierarchy (NH) and $\delta_D \in [-180^\circ, -174.6^\circ] \cup [-7.2^\circ, 180^\circ]$ for inverted hierarchy (IH) [1]. Finally, the absolute value of the mass squared differences has been carefully measured, but the mass hierarchy is still undetermined (i.e., $m_3 \gg m_2 > m_1$ or $m_2 > m_1 \gg m_3$). Each of these questions will be discussed in this work.

From the improvements in recent global analyses [2–4] it is possible to make more accurate predictions for the distributions of some of the aforementioned parameters of interest. Specifically, each of the residual symmetries, $\mathbb{Z}_2^s$ and $\overline{\mathbb{Z}}_2^s$, can be used to derive a model-independent equation for δ_D (one for each symmetry) [5, 6]. Then using the newly available global fits of the neutrino oscillation parameters in [2], likelihood distributions for δ_D, the Jarlskog invariant [7], and θ_a are obtained.

Using the PMNS mixing matrix, an expression for the probability of a neutrino originally of flavor α to be detected as a neutrino of flavor β, $P(\nu_\alpha \to \nu_\beta)$ is presented (which is a standard result found in many review papers on neutrino physics [8]). Then, using the approximation from [9] it is shown how the earth's matter affects the neutrino beam in long-baseline experiments. This is done by replacing the oscillation parameters with effective values that depend on the energy of the neutrinos, the baseline length, and the density of the matter.

In this paper, a focus is made on the NOνA and T2K experiments. Both of these experiments measure the appearance of ν_e's ($\overline{\nu}_e$'s) from a $\nu_\mu(\overline{\nu}_\mu)$ beam. The probability for this appearance is plotted as a function of energy using the best fits

Table 1: Global fits for neutrino oscillation parameters from [2]. * represents a local minimum at approximately 0.42σ for χ^2.

Parameter	Best fit	1σ range
$\sin^2\theta_s/10^{-1}$ (NH or IH)	3.08	2.91–3.25
$\sin^2\theta_r/10^{-2}$ (NH)	2.34	2.16–2.56
$\sin^2\theta_r/10^{-2}$ (IH)	2.39	2.18–2.60
$\sin^2\theta_a/10^{-1}$ (NH)	4.25	3.98–4.54
$\sin^2\theta_a/10^{-1}$ (IH)	4.37, 5.82*	4.08–4.96 $\oplus$ 5.31–6.10
δ_D/π (NH)	1.39	1.12–1.72
δ_D/π (IH)	1.35	0.96–1.59
$m_{21}^2/10^{-5}$ eV^2 (NH or IH)	7.54	7.32–7.80
$m_{31}^2/10^{-3}$ eV^2 (NH)	2.48	2.42–2.56
$\lvert m_{31}^2\rvert/10^{-3}$ eV^2 (IH)	2.36	2.29–2.43

for the oscillation parameters in [2]. The effects of matter are taken into account using the average matter density along the baseline for the two experiments. This is justified by the fact that there does not appear to be a significant effect due to the variation of the matter density [10]. A comparison is made for this probability with and without CP-violation in an attempt to observe the sensitivity of NOνA and T2K to measurements of δ_D. We have also plotted $P(\nu_\mu \to \nu_e)$ versus $P(\overline{\nu}_\mu \to \overline{\nu}_e)$ which shows that it may be possible for these experiments to determine the neutrino mass hierarchy for some values of the CP phase as discussed in [11, 12].

The update of the analysis of [13] given in [2] gives closer agreement on θ_a with the other two major global analyses [3, 4]. This shows that θ_a is closer to being maximal than originally believed and only excludes the possibility of it being maximal by about 1σ for inverted hierarchy. But, it is clear that the analyses do not agree upon which octant is favored. Fortunately, the plots of $P(\nu_\mu \to \nu_e)$ versus $P(\overline{\nu}_\mu \to \overline{\nu}_e)$ may also serve to determine the octant of θ_a [11, 12].

This work is concluded with a digression into the effective mixing angles and masses in matter. The solar resonance, first described by the MSW effect [14–16], and the atmospheric resonance are readily observed.

2. Distribution of δ_D, J_ν, and θ_a

The equations for δ_D, in terms of the neutrino mixing angles, based on residual symmetries are given by [5, 6]

$$\cos\delta_D = \frac{\left(s_s^2 - c_s^2 s_r^2\right)\left(s_a^2 - c_a^2\right)}{4c_a s_a c_s s_s s_r}, \tag{1a}$$

$$\cos\delta_D = \frac{\left(s_s^2 s_r^2 - c_s^2\right)\left(s_a^2 - c_a^2\right)}{4c_a s_a c_s s_s s_r}, \tag{1b}$$

for $\mathbb{Z}_2^s$ and $\overline{\mathbb{Z}}_2^s$ respectively, where $s_i \equiv \sin\theta_i$ and $c_i \equiv \cos\theta_i$. The latest global fits for the neutrino oscillation parameters from [2] are shown in Table 1.

From this we can obtain a distribution for $\cos\delta_D$ following the procedure in [5, 6] by using

$$\frac{dP\left(\cos\delta_D\right)}{d\cos\delta_D} = \int \delta_D^p \mathbb{P}\left(s_a^2\right)\mathbb{P}\left(s_s^2\right)\mathbb{P}\left(s_r^2\right)\mathrm{d}s_a^2\mathrm{d}s_s^2\mathrm{d}s_r^2, \tag{2}$$

where $\delta_D^p \equiv \delta(\cos\delta_D - \overline{c}_D)$, the $\mathbb{P}$'s are proportional to $\exp(-\chi^2/2)$, and $\overline{c}_D \equiv$ RHS of (1a), (1b). Because it is preferable to get a distribution with respect to δ_D rather than $\cos\delta_D$ we use

$$\frac{dP\left(\delta_D\right)}{d\delta_D} = \left|s_D\right|\frac{dP\left(c_D\right)}{dc_D}, \tag{3}$$

where $c_D \equiv \cos\delta_D$ and $s_D \equiv \sin\delta_D$. Since this is a numerical integral, the delta function cannot be used as it is normally defined (unless integrated out of the equation prior to the numerical calculation). The integral was evaluated using a Monte Carlo algorithm and the results are shown in Figure 1(a). The domain of δ_D in (3) is $[-180^\circ, 0^\circ]$, but the distributions in Figure 1(a) can be reflected about $\delta_D = 0^\circ$ to account for the full interval $[-180^\circ, 180^\circ]$. Therefore, these distributions have been normalized to 1/2 over the domain shown in the figures. This means that each of the residual symmetries will have two peak predictions for the CP phase (equidistant from 0°). The IH χ^2 curve for θ_a in [2] is closer to being symmetric about $\sin^2\theta_a = 0.5$. This is very prevalent in the results shown in Figure 1(a) given that the IH plots are close to being symmetric about $\delta_D = -90^\circ$. But, since the NH global fit favors the lower octant for θ_a by at least 2σ [2] the predicted distributions for NH tend to prefer one side of $\delta_D = -90^\circ$. But in both cases the results for $\mathbb{Z}_2^s$ are in agreement with the best fit value of $\delta_D = -90^\circ$ from T2K's latest results [1].

The same method is applied to the Jarlskog invariant $J_\nu \equiv c_a s_a c_s s_s c_r^2 s_r s_D$ [7]; that is,

$$\frac{dP\left(J_\nu\right)}{dJ_\nu} = \int \delta_{J_\nu}^p \mathbb{P}\left(s_a^2\right)\mathbb{P}\left(s_s^2\right)\mathbb{P}\left(s_r^2\right)\mathrm{d}s_a^2\mathrm{d}s_s^2\mathrm{d}s_r^2, \tag{4}$$

with $\delta_{J_\nu}^p \equiv \delta(J_\nu - c_a s_a c_s s_s c_r^2 s_r s_D)$. This distribution is shown in Figure 1(b). When calculating these distributions, δ_D is taken to be in the interval $[0, 180^\circ]$ and is even about the vertical axis to extend δ_D to include $[-180^\circ, 0^\circ]$. To account for this, the figures are labeled for the distribution of $|J_\nu|$, and they can therefore be normalized to one. As compared with our previous results in [6], $\overline{\mathbb{Z}}_2^s$ is beginning to favor the region that $\mathbb{Z}_2^s$ prefers. Also, the region predicted by $\mathbb{Z}_2^s$ has become slightly narrower and it now excludes $|J_\nu| < 0.024$.

Finally, this method is again applied similarly to θ_a by first using (1a), (1b) to solve for $\tan 2\theta_a$

$$\tan 2\theta_a = \frac{c_s^2 s_r^2 - s_s^2}{2c_s s_s s_r \cos\delta_D}, \tag{5a}$$

$$\tan 2\theta_a = \frac{c_s^2 - s_s^2 s_r^2}{2c_s s_s s_r \cos\delta_D}, \tag{5b}$$

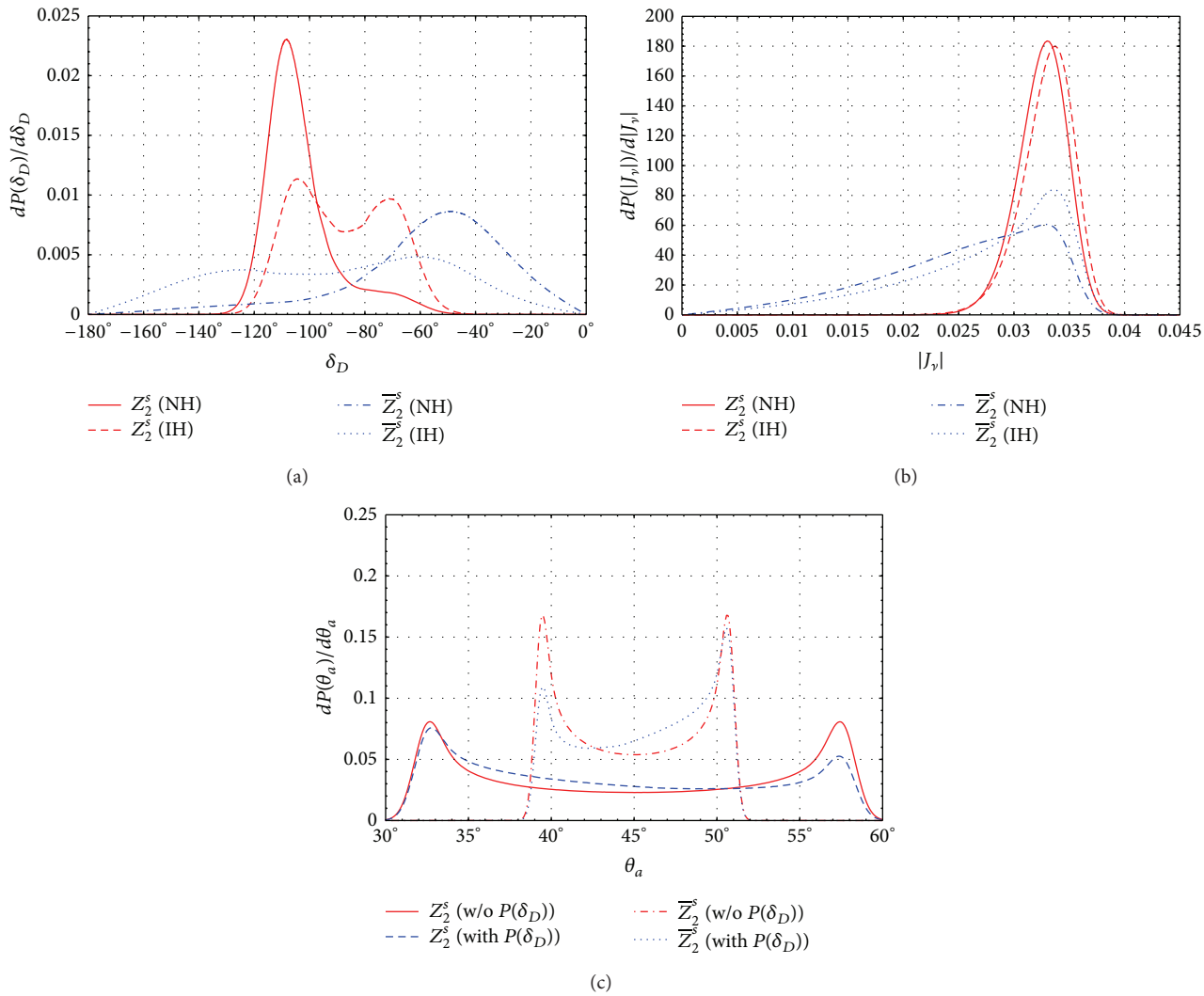

Figure 1: Predicted distributions for (a) δ_D, (b) J_ν, and (c) θ_a (NH) using the global analysis in [2].

for $\mathbb{Z}_2^s$ and $\overline{\mathbb{Z}}_2^s$, respectively. Then we have

$$\frac{dP(\tan 2\theta_a)}{d\tan 2\theta_a} = \int \delta_{\theta_a}^p \mathbb{P}(s_s^2)\,\mathbb{P}(s_r^2)\,\mathbb{P}(\delta_D)\,\mathrm{d}s_s^2\mathrm{d}s_r^2\mathrm{d}\delta_D, \quad (6)$$

with $\delta_{\theta_a}^p \equiv \delta(\tan 2\theta_a - \bar{t}_{\theta_a})$, where $\bar{t}_{\theta_a} \equiv$ RHS of (5a), (5b). To get a distribution for θ_a we use

$$\frac{dP(\theta_a)}{d\theta_a} = 2\sec^2(2\theta_a)\,\frac{dP(\tan 2\theta_a)}{d\tan 2\theta_a}. \quad (7)$$

The distribution is shown in Figure 1(c), where plots are made with and without using the prior on δ_D from [2]. When no prior on δ_D is used, $\mathbb{P}(\delta_D)$ becomes evenly distributed in $[0, 2\pi)$. As previously discussed in [6], θ_a is symmetric about $\theta_a = 45^\circ$ when there is no prior on δ_D. In addition, the distributions using the prior on δ_D have also become more symmetric, as a result of the χ^2 for $\cos\delta_D$ also having become more symmetric about zero.

3. ν_μ to ν_e Oscillation

Now that we have a distribution for all the neutrino oscillation parameters, an attempt can be made to predict the results of an experiment measuring the number of ν_μ's that oscillate into ν_e's over some distance. First, the expression for this probability, $P(\nu_\mu \to \nu_e)$, must be found. Denoting the weak eigenstates of the neutrino by $|\nu_\alpha\rangle$ and the neutrino mass eigenstates by $|\nu_i\rangle$, then

$$(U_{\mathrm{PMNS}})_{\alpha j} \equiv \langle \nu_\alpha \mid \nu_j \rangle \quad (8)$$

defines the PMNS mixing matrix, U_{PMNS}. The standard parametrization is given by [9]

$$U_{\mathrm{PMNS}} = U\mathscr{P}, \quad (9)$$

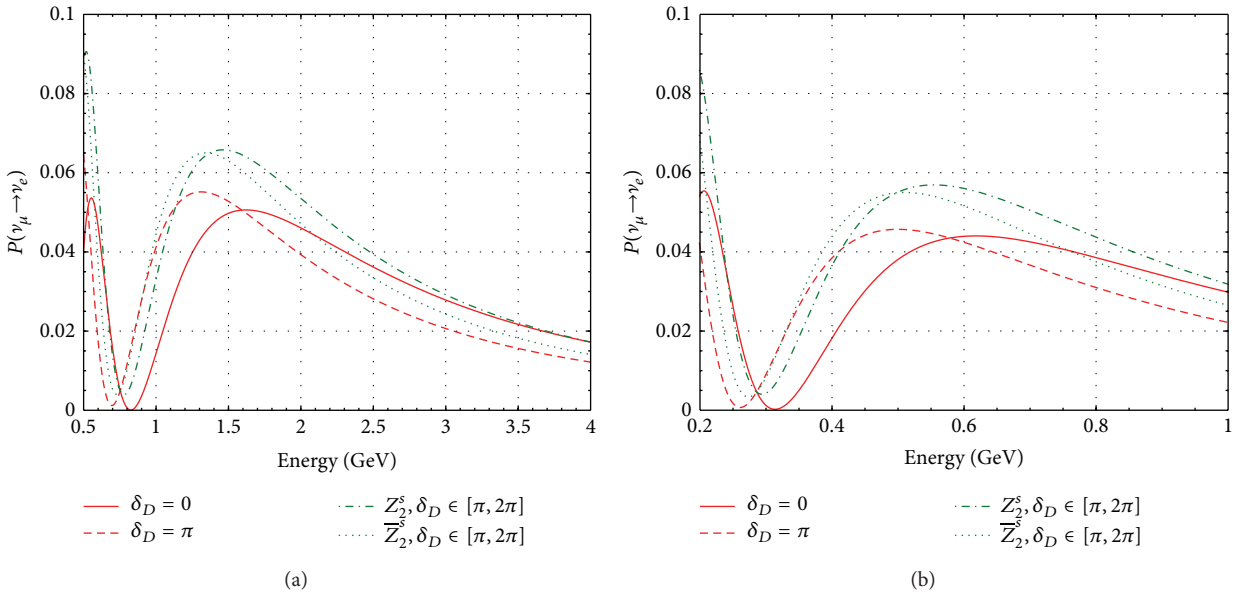

FIGURE 2: $P(\nu_\mu \to \nu_e)$ as a function of energy at (a) NOνA and (b) T2K, using the best fits from [2] with normal hierarchy.

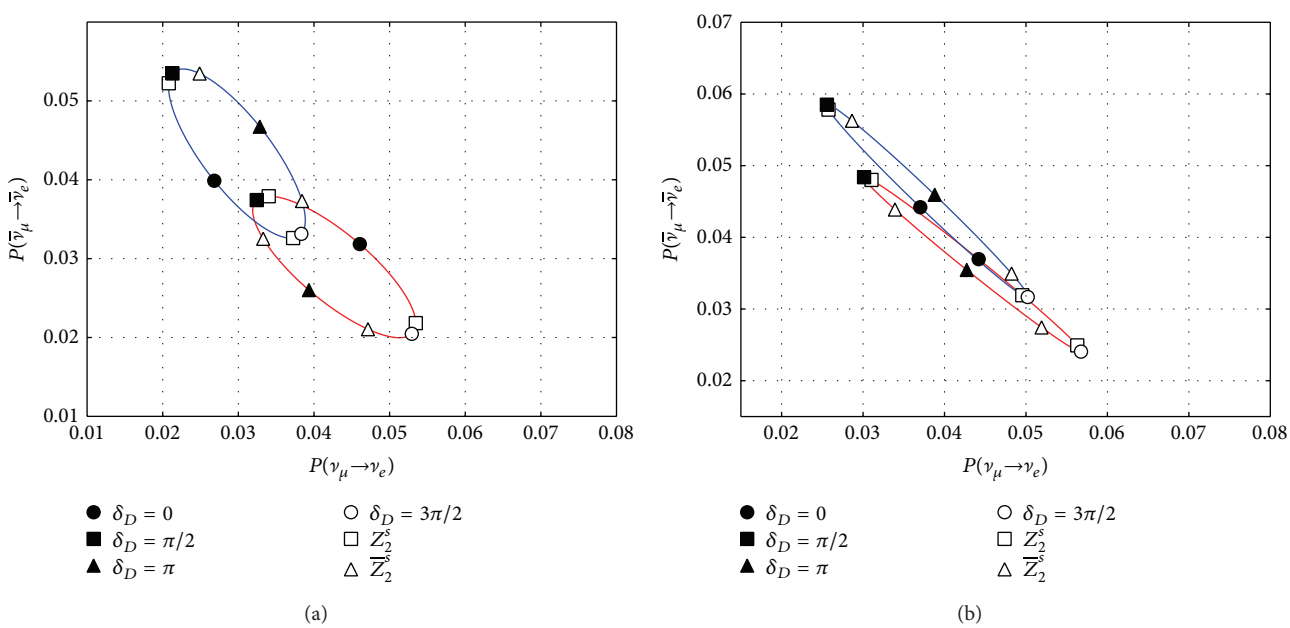

FIGURE 3: Plot of $P(\nu_\mu \to \nu_e)$ versus $P(\overline{\nu}_\mu \to \overline{\nu}_e)$ to show the sensitivity of (a) NOνA and (b) T2K to determine the mass hierarchy assuming $\theta_a < \pi/2$. The red ellipse (lower right corner) corresponds to NH, and the blue ellipse (upper left corner) corresponds to IH.

where

$$U = \begin{pmatrix} c_s c_r & s_s c_r & s_r e^{-i\delta_D} \\ -s_s c_a - c_s s_a s_r e^{i\delta_D} & c_s c_a - s_s s_a s_r e^{i\delta_D} & s_a c_r \\ s_s s_a - c_s c_a s_r e^{i\delta_D} & -c_s s_a - s_s c_a s_r e^{i\delta_D} & c_a c_r \end{pmatrix}, \quad (10)$$

$$\mathscr{P} = \operatorname{diag}\left(1, e^{i\alpha_{21}/2}, e^{i\alpha_{31}/2}\right).$$

From [8],

$$\operatorname{Amp}\left(\nu_\alpha \longrightarrow \nu_\beta\right) = \sum_i U_{\alpha i}^* e^{-i m_i^2 (L/2E)} U_{\beta i}, \quad (11)$$

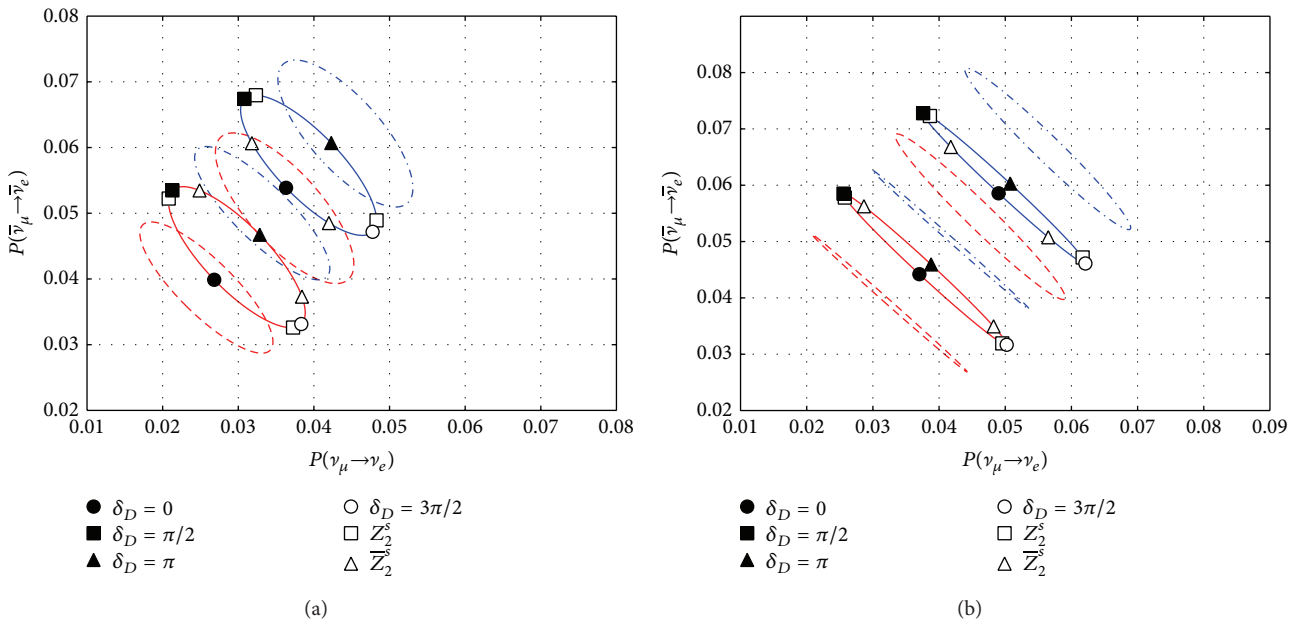

FIGURE 4: Plot of $P(\nu_\mu \to \nu_e)$ versus $P(\bar{\nu}_\mu \to \bar{\nu}_e)$ to show the sensitivity of (a) NOνA and (b) T2K to determine the octant of θ_a assuming inverted hierarchy. The red ellipses (lower left corner) correspond to $\theta_a < \pi/4$, while the blue ellipses (upper right corner) correspond to $\theta_a > \pi/4$. The dashed ellipses correspond to the $\pm 1\sigma$ values.

which leads to

$$\begin{aligned} P\left(\overset{(-)}{\nu}_\alpha \longrightarrow \overset{(-)}{\nu}_\beta\right) &= \delta_{\alpha\beta} - 4\sum_{i>j} \Re\left(U_{\alpha i}^* U_{\beta i} U_{\alpha j} U_{\beta j}^*\right) \sin^2\left(\Delta m_{ij}^2 \frac{L}{4E}\right) \\ &\overset{+}{(-)} 2\sum_{i>j} \Im\left(U_{\alpha i}^* U_{\beta i} U_{\alpha j} U_{\beta j}^*\right) \sin\left(\Delta m_{ij}^2 \frac{L}{2E}\right), \end{aligned} \tag{12}$$

where $\Delta m_{ij}^2 \equiv m_i^2 - m_j^2$, m_i is the ith mass eigenvalue, L is the distance propagated by the neutrino, and E is the energy of the neutrino. Notice that this probability does not depend on the Majorana phases, and therefore a discussion on these phases will not be pursued here.

Making the following definition [9]:

$$\Delta_{ij} \equiv \frac{\Delta m_{ij}^2}{2E} L \tag{13}$$

and noting that $\Delta_{32} = \Delta_{31} - \Delta_{21}$, then

$$\begin{aligned} P\left(\overset{(-)}{\nu}_\mu \longrightarrow \overset{(-)}{\nu}_e\right) &= 4 s_s^2 c_r^2 \left(s_s^2 s_r^2 s_a^2 + c_s^2 c_a^2 - 2 c_s c_a s_s s_r s_a c_D\right) \\ &\quad \times \sin^2\left(\frac{\Delta_{21}}{2}\right) + 4 s_r^2 s_a^2 c_r^2 \sin^2\left(\frac{\Delta_{31}}{2}\right) + 2 s_s s_r c_r^2 s_a \\ &\quad \times \left(c_s c_a c_D - s_s s_r s_a\right) \\ &\quad \times \left[4\sin^2\left(\frac{\Delta_{21}}{2}\right)\sin^2\left(\frac{\Delta_{31}}{2}\right) + \sin\left(\Delta_{21}\right)\sin\left(\Delta_{31}\right)\right] \\ &\quad \overset{+}{(-)} 4 J_\nu \left[\sin^2\left(\frac{\Delta_{21}}{2}\right)\sin\left(\Delta_{31}\right) \right. \\ &\quad \left. - \sin^2\left(\frac{\Delta_{31}}{2}\right)\sin\left(\Delta_{21}\right)\right]. \end{aligned} \tag{14}$$

The last term includes the Jarlskog invariant [7] defined above.

3.1. Matter Effects. As electron neutrinos propagate through the earth, they can interact with electrons via W-exchange. In addition, all three neutrino flavors can interact with electrons, protons, or neutrons via Z-exchange. Assuming electrically neutral matter, the Z-exchange between the neutrinos and protons will exactly cancel with the Z-exchange between the neutrinos and electrons [8]. The contribution from Z-exchange can be dropped, because it only adds a multiple of the identity matrix to the Hamiltonian [9]. Then, under the assumption that $E \ll M_W$, the effect of W-exchange can be accounted for by modifying the Hamiltonian for neutrinos [17]

$$H = \frac{1}{2E} U \begin{pmatrix} 0 & 0 & 0 \\ 0 & \Delta m_{21}^2 & 0 \\ 0 & 0 & \Delta m_{31}^2 \end{pmatrix} U^\dagger + \frac{1}{2E} \begin{pmatrix} a & 0 & 0 \\ 0 & 0 & 0 \\ 0 & 0 & 0 \end{pmatrix}, \tag{15}$$

where $a \equiv 2\sqrt{2} G_F N_e E$ and N_e is the density of electrons. For antineutrinos, the Hamiltonian is simply the complex conjugate of (15) with $a \to -a$.

One way to proceed is to diagonalize the Hamiltonian exactly, which has been done analytically [17–19]. However, this does not give much physical insight into the effects of matter on neutrino oscillations. Approximations in which the mixing angles and mass eigenvalues are replaced by effective values do not modify any of the equations, and therefore it becomes clear how matter affects neutrinos. A number of approximation schemes have been developed [20–26]. One of the most commonly used of these are the equations derived in [26]. But, due to the large value of θ_r measured at Daya Bay [27], the approximation in [26] begins to fail as is shown in [9]. In the approximation that is used here, the form of (14) can be used with the following modifications [9]:

$$\begin{aligned} \theta_s &\longrightarrow \theta_s', \qquad \theta_r \longrightarrow \theta_r', \\ \Delta m_{21}^2 &\longrightarrow \lambda_2 - \lambda_1, \qquad \Delta m_{31}^2 \longrightarrow \lambda_3 - \lambda_1, \end{aligned} \tag{16}$$

with

$$\tan\left(2\theta_s'\right) = \frac{\left(\Delta m_{21}^2/c_r^2\right)\sin\left(2\theta_s\right)}{\left(\Delta m_{21}^2/c_r^2\right)\cos\left(2\theta_s\right) - a}, \tag{17a}$$

$$\tan\left(2\theta_r'\right) = \frac{\left(\Delta m_{31}^2 - \Delta m_{21}^2 s_s^2\right)\sin\left(2\theta_r\right)}{\left(\Delta m_{31}^2 - \Delta m_{21}^2 s_s^2\right)\cos\left(2\theta_r\right) - a}, \tag{17b}$$

$$\begin{aligned} \lambda_\pm' \equiv \Big(&\left(\Delta m_{21}^2 + a c_r^2\right) \\ &\pm\sqrt{\left(\Delta m_{21}^2 - a c_r^2\right)^2 + 4 a c_r^2 s_s^2 \Delta m_{21}^2}\Big)(2)^{-1}, \end{aligned} \tag{17c}$$

$$\begin{aligned} \lambda_\pm'' \equiv \Big(&\lambda + \left(\Delta m_{31}^2 + a s_r^2\right) \\ &\pm\sqrt{\left[\lambda - \left(\Delta m_{31}^2 + a s_r^2\right)\right]^2 + 4 a^2 s c_r^2 s_r^2}\Big)(2)^{-1}, \end{aligned} \tag{17d}$$

where for neutrinos let

$$\begin{aligned} &\lambda \equiv \lambda_+', \qquad s \equiv s_s'^2, \qquad \lambda_1 \approx \lambda_-', \\ &\lambda_2 \approx \lambda_\mp'', \qquad \lambda_3 \approx \lambda_\pm'', \end{aligned} \tag{18}$$

and for antineutrinos let

$$\begin{aligned} &\lambda \equiv \lambda_-', \qquad s \equiv c_s'^2, \qquad a \longrightarrow -a, \\ &\lambda_1 \approx \lambda_\mp'', \qquad \lambda_2 \approx \lambda_+', \qquad \lambda_3 \approx \lambda_\pm'', \end{aligned} \tag{19}$$

with the upper sign for normal hierarchy and the lower sign for inverted hierarchy.

It is helpful to show a and Δ_{ij} in conventional units. Following [9]

$$\Delta_{ij} = 2.534\left(\frac{\Delta m_{ij}^2}{[\mathrm{eV}^2]}\right)\left(\frac{[\mathrm{GeV}]}{E}\right)\left(\frac{L}{[\mathrm{km}]}\right), \tag{20a}$$

$$a = \left(7.63\times10^{-5}\left[\mathrm{eV}^2\right]\right)\left(\frac{\rho}{[\mathrm{g/cm}^3]}\right)\left(\frac{E}{[\mathrm{GeV}]}\right). \tag{20b}$$

3.2. NOνA and T2K. NOνA is a long-baseline neutrino oscillation experiment located in northern Minnesota. It has a baseline length of 810 km, an average matter density of 2.8 g/cm^3 along this baseline, and a peak neutrino energy around 2 GeV [11]. T2K is another neutrino oscillation experiment with similar goals to that of NOνA. Its baseline length is 295 km and has an average matter density of 2.6 g/cm^3, and the neutrino beam energy peaks around 0.6 GeV [28].

With the use of the effective mixing angles derived in the previous section, the probability of the appearance of a $\nu_e(\overline{\nu}_e)$ from a $\nu_\mu(\overline{\nu}_\mu)$ beam can be determined for any matter density. Using the length and matter density for the two experiments in question, plots of these probabilities are shown in Figure 2 as a function of energy.

It is not entirely apparent that the approximation [9] is valid for different values of the *CP* phase or the vacuum mixing angles; therefore, a comparison is made between this approximation and the exact results in the Appendix. In this comparison, the exact results are found by numerically diagonalizing the Hamiltonian. As it turns out, the approximation is very good for the energies and densities considered here.

4. Determination of the Mass Hierarchy and the Octant of θ_a

As has been mentioned previously, a major goal of neutrino oscillation experiments is to determine the mass hierarchy. If *CP* was a good symmetry, then there would be no observable difference between $P(\nu_\mu \to \nu_e)$ and $P(\overline{\nu}_\mu \to \overline{\nu}_e)$ when the neutrinos are propagating through a vacuum. However, interestingly enough, the matter effects discussed previously emulate the effects of *CP*-violation. Therefore, there is an observable difference between $P(\nu_\mu \to \nu_e)$ and $P(\overline{\nu}_\mu \to \overline{\nu}_e)$ even if *CP* is a good symmetry. Without the effects of matter the difference between oscillation probabilities for normal hierarchy versus inverted hierarchy is minimal. Thus it is because of the interactions with matter that allow for a discernible difference between normal and inverted hierarchy.

It is possible that actual *CP*-violation is substantially cancelled by this matter induced *CP*-violation. This would be very unfortunate, because it would make the determination of the *CP* phase more difficult than expected. A plot for $P(\nu_\mu \to \nu_e)$ versus $P(\overline{\nu}_\mu \to \overline{\nu}_e)$ is shown in Figure 3 for NOνA and T2K using the best fits from [2]. It can be seen that there are many values of the *CP* phase that will allow NOνA to make a serious determination of the true mass hierarchy. This will occur if $\delta_D \in [\pi, 2\pi]$ with NH being the true hierarchy or $\delta_D \in [0, \pi]$ with IH being the true hierarchy. And since T2K has excluded most of $\delta_D \in [0, \pi]$ at 90% C.L. [1], hopefully the true mass hierarchy is normal. From Figure 3(b) it appears that T2K will not be able to determine the mass hierarchy in this manner.

In addition, it may also be possible to determine the octant of θ_a from similar plots. These are shown in Figure 4. It appears that every value of the *CP* phase could at least give some indication of the true octant of θ_a, but the best values

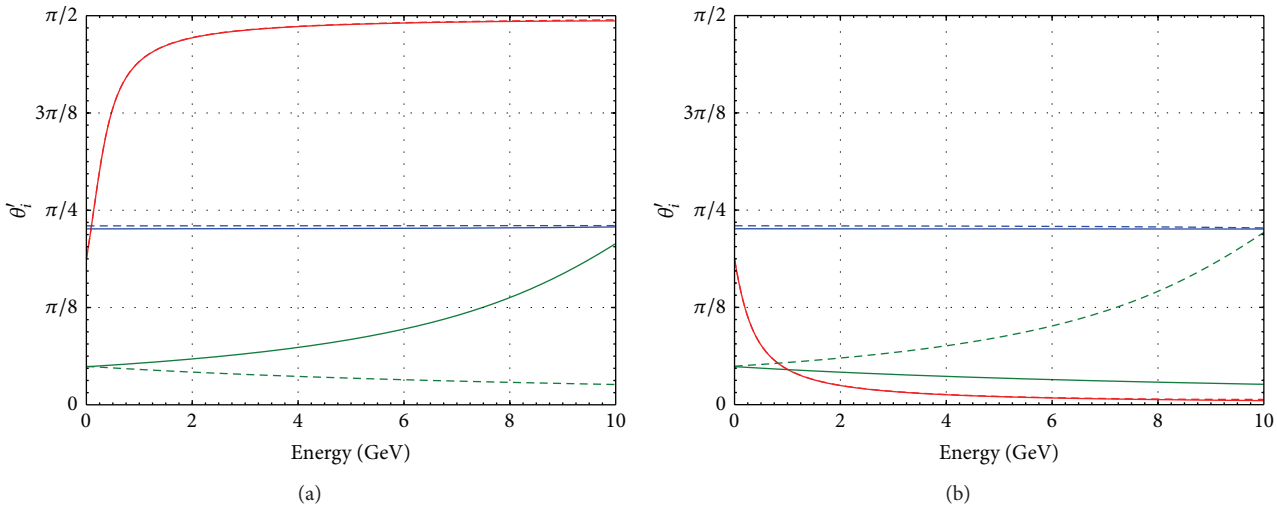

Figure 5: Plots of the effective mixing angles as a function of energy using data from [2]. For (a) NOνA and neutrinos, (b) NOνA and antineutrinos. Red = θ_s', blue = θ_a', and green = θ_r'. The solid lines are for normal hierarchy, and the dashed lines are for inverted hierarchy. In the cases where the dashed line is not visible, it's because the solid line is on top of it.

would be $\delta_D = 0$ for the lower octant and $\delta_D = \pi$ for the higher octant.

The ellipses were created by using (14) with the matter effect modifications of (16), for all possible values of δ_D (i.e., $\delta_D \in [0, 2\pi]$). The $\square$ and the $\triangle$ symbols correspond to the predicted values for δ_D, based on $\mathbb{Z}_2^s$ and $\overline{\mathbb{Z}}_2^s$, respectively. The predicted values are determined by using the best fits from [2] in (1a), (1b).

5. Effective Masses and Mixing Angles in Matter

The values of the effective mixing angles are plotted in Figure 5 and the mass eigenvalues in Figure 6, as functions of energy using the matter density for the NOνA experiment. The plots for T2K are excluded here, because they do not differ much from the ones for NOνA. Also, these particular plots consider $\delta_D = 0$, because the results depend very little on the CP phase. These have been plotted by numerically diagonalizing the Hamiltonian. It is assumed that the diagonalization matrix will have the same form as the standard parameterization of the PMNS mixing matrix.

The approximation introduced in Section 3.1 implies that the CP phase and θ_a' do not vary much, if at all, due to interactions with matter (which can be observed in Figure 5). It also implies certain characteristics of the variations of the other two mixing angles. From (17a), θ_s' should be independent of the mass hierarchy, and taking the limit $a \to \infty$, then $\theta_s' \to \pi/2$ (0) for ν ($\overline{\nu}$). This behavior is easily observed in Figure 5. From (17b), θ_r' should have similar asymptotic behavior as θ_s' for normal hierarchy, while it should reverse its behavior for inverted hierarchy. These features are approximately shown in Figure 5, but at the energies shown, θ_r' is not able to approach its asymptotic limit. Therefore, these results appear to agree with the approximation in [9].

The effective neutrino masses are found from multiplying the eigenvalues of the Hamiltonian by $2E$. These plots are shown in Figure 6 for NOνA. There are some interesting characteristics of these plots. The first and most obvious are two resonances referred to as the solar resonance and the atmospheric resonance which represent the condition for maximal oscillation probability. This phenomenon was first understood with the introduction of the MSW effect [14, 15]. The first peak of $\sin^2(2\theta_s')$ is the solar resonance and corresponds to an approach of $|\lambda_1|$ and $|\lambda_2|$ followed by a repulsion. The first peak of $\sin^2(2\theta_r')$ is the atmospheric resonance and corresponds to an approach of $|\lambda_2|$ and $|\lambda_3|$ followed by a repulsion. If the absolute value of the mass eigenvalues crosses, then no resonance can be seen there. If we do not take the absolute value of the mass eigenvalues, then they will never cross each other. This is a wonderful example of level repulsion in quantum mechanics. For more details on these resonances, including a derivation of the resonance condition, see [14–16, 29].

6. Conclusions

Predicted distributions for δ_D, J_ν, and θ_a were updated using the residual symmetries $\mathbb{Z}_2^s$ and $\overline{\mathbb{Z}}_2^s$. It was found that the greater uncertainty in the octant of θ_a for IH shown in [2] forced the distributions of δ_D for IH to have nearly equal contributions on either side of $\delta_D = -90^\circ$. This had no significant effect on the distribution for J_ν and the prediction for J_ν has improved.

By including the effects of matter into the oscillation probabilities, it was shown in Section 4 how NOνA stands a good chance of determining the mass hierarchy

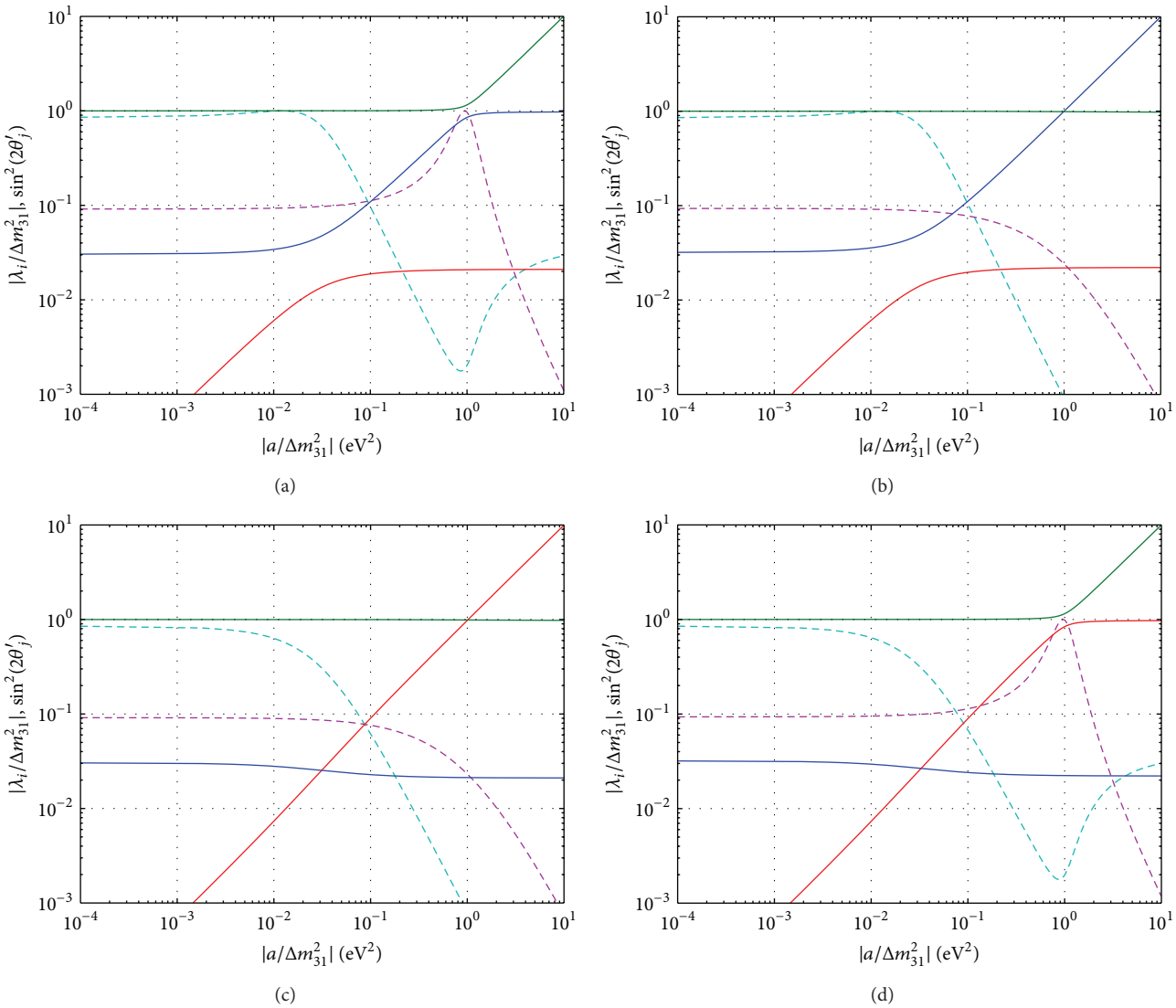

Figure 6: Effective masses for NOνA. The major focus of these plots should be on the solar and atmospheric resonances corresponding to a level repulsion. (a) ν and NH, (b) ν and IH, (c) $\overline{\nu}$ and NH, and (d) $\overline{\nu}$ and IH. Red = λ_1, blue = λ_2, green = λ_3, cyan-dashed = $\sin^2(2\theta_s)$, and magenta-dashed = $\sin^2(2\theta_r)$.

if $\delta_D \in [\pi, 2\pi]$ and the true hierarchy is normal or if $\delta_D \in [0, \pi]$ and the true hierarchy is inverted. It was also shown that both NOνA and T2K may be capable of nailing down the octant of θ_a.

The effects of matter were also shown to give rise to two resonances: the solar resonance and the atmospheric resonance. This behavior can be seen to agree with the approximation used throughout this work [9].

Appendix

Comparison with Solving for Matter Effects Exactly

Here a comparison is made between the approximation used [9] and exact results found from numerically diagonalizing the Hamiltonian. Each plot for $P(\nu_\mu \to \nu_e)$ and $P(\overline{\nu}_\mu \to \overline{\nu}_e)$ above has been redone without any approximation. The plots in Figure 7 show the difference between these two methods. It is clear that the approximation is indeed very good, with a maximum difference around 0.0001.

Conflict of Interests

The authors declare that there is no conflict of interests regarding the publication of this paper.

Acknowledgments

The authors would like to thank Shao-Feng Ge for the contributions in the early stages of this work. Wayne W. Repko would also like to thank Kendall Mahn for some

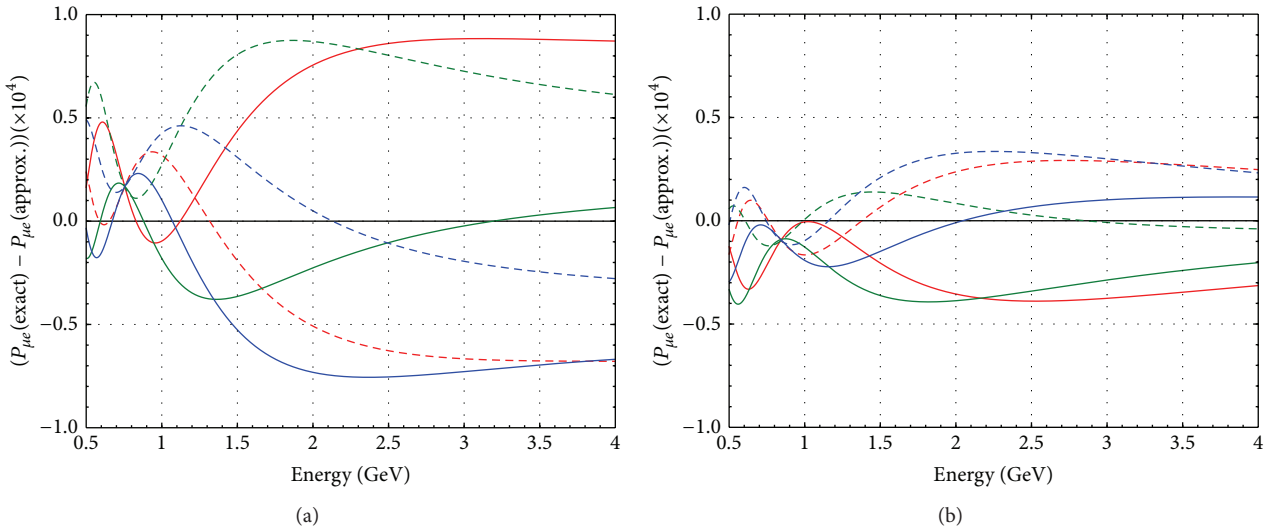

Figure 7: Comparison between the exact results and the approximation used throughout the paper. For (a) NOνA and neutrinos and (b) NOνA and antineutrinos. Red = ($\delta_D = 0$), red-dash = ($\delta_D = \pi$), green = $\mathbb{Z}_2^s, \delta_D \in [0, \pi]$, green-dash: = $\mathbb{Z}_2^s, \delta_D \in [\pi, 2\pi]$, blue: = $\overline{\mathbb{Z}}_2^s, \delta_D \in [0, \pi]$, and blue-dash: = $\overline{\mathbb{Z}}_2^s, \delta_D \in [\pi, 2\pi]$.

helpful conversations. All plots in this paper were produced using matplotlib [30]. Wayne W. Repko was supported in part by the National Science Foundation under Grant no. PHY-1068020. Duane A. Dicus was supported in part by the U.S. Department of Energy under Award no. DE-FG02-12ER41830.

References

[1] K. Abe, J. Adam, H. Aihara et al., "Observation of electron neutrino appearance in a Muon neutrino beam," *Physical Review Letters*, vol. 112, Article ID 061802, 2014.

[2] F. Capozzi, G. Fogli, E. Lisi et al., "Status of three-neutrino oscillation parameters, circa 2013," *Physical Review D*, vol. 89, Article ID 093018, 2013.

[3] D. Forero, M. Tortola, and J. Valle, "Global status of neutrino oscillation parameters after Neutrino-2012," *Physical Review D*, vol. 86, Article ID 073012, 2012.

[4] M. Gonzalez-Garcia, M. Maltoni, J. Salvado, and T. Schwetz, "Global fit to three neutrino mixing: critical look at present precision," *Journal of High Energy Physics*, vol. 2012, article 123, 2012.

[5] S.-F. Ge, D. A. Dicus, and W. W. Repko, " Residual Symmetries for Neutrino Mixing with a Large theta_13 and Nearly Maximal delta_D," *Physical Review Letters*, vol. 108, Article ID 041801, 2012.

[6] A. D. Hanlon, S.-F. Ge, and W. W. Repko, "Phenomenological consequences of residual $\mathbb{Z}_2^s$ and $\mathbb{Z}_2^s$ symmetries," *Physics Letters B*, vol. 729, pp. 185–191, 2014.

[7] C. Jarlskog, "Commutator of the quark mass matrices in the standard electroweak model and a measure of maximal CP nonconservation," *Physical Review Letters*, vol. 55, p. 1039, 1985.

[8] B. Kayser, "Neutrino physics," eConf C040802, L004, http://arxiv.org/abs/hep-ph/0506165.

[9] S. K. Agarwalla, Y. Kao, and T. Takeuchi, "Analytical approximation of the neutrino oscillation probabilities at large θ_{13}," http://arxiv.org/abs/1302.6773.

[10] M. Koike and J. Sato, "Effects of matter density fluctuation in long baseline neutrino oscillation experiments," *Modern Physics Letters A*, vol. 14, no. 19, pp. 1297–1302, 1999.

[11] R. Patterson, "The NOvA experiment: status and outlook," *Nuclear Physics B—Proceedings Supplements*, vol. 235-236, pp. 151–157, 2013.

[12] S. K. Agarwalla, S. Prakash, and S. U. Sankar, "Resolving the octant of θ_{23} with T2K and NOνA," *Journal of High Energy Physics*, vol. 2013, article 131, 2013.

[13] G. L. Fogli, E. Lisi, A. Marrone, D. Montanino, A. Palazzo, and A. M. Rotunno, "Global analysis of neutrino masses, mixings and phases: entering the era of leptonic CP violation searches," *Physical Review D*, vol. 86, Article ID 013012, 2012.

[14] L. Wolfenstein, "Neutrino oscillations in matter," *Physical Review D*, vol. 17, pp. 2369–2374, 1978.

[15] S. Mikheev and A. Y. Smirnov, "Resonant amplification of ν oscillations in matter and solar-neutrino spectroscopy," *Il Nuovo Cimento C*, vol. 9, no. 1, pp. 17–26, 1986.

[16] A. Y. Smirnov, "The MSW effect and matter effects in neutrino oscillations," *Physica Scripta*, vol. 2005, no. T121, pp. 57–64, 2005.

[17] K. Kimura, A. Takamura, and H. Yokomakura, "Exact formulas and simple dependence of neutrino oscillation probabilities in matter with constant density," *Physical Review D*, vol. 66, Article ID 073005, p. 073005, 2002.

[18] H. W. Zaglauer and K. H. Schwarzer, "The mixing angles in matter for three generations of neutrinos and the MSW mechanism," *Zeitschrift für Physik C: Particles and Fields*, vol. 40, no. 2, pp. 273–282, 1988.

[19] K. Kimura, A. Takamura, and H. Yokomakura, "Exact formula of probability and CP violation for neutrino oscillations in matter," *Physics Letters B*, vol. 537, pp. 86–94, 2002.

[20] J. Arafune, M. Koike, and J. Sato, "CP violation and matter effect in long baseline neutrino oscillation experiments," *Physical Review D*, vol. 56, p. 3093, 1997.

[21] M. Freund, "Analytic approximations for three neutrino oscillation parameters and probabilities in matter," *Physical Review D*, vol. 64, Article ID 053003, 2001.

[22] O. Peres and A. Y. Smirnov, "Atmospheric neutrinos: LMA oscillations, *Ue*3 induced interference and CP-violation," *Nuclear Physics B*, vol. 680, Article ID 0309312, pp. 479–509, 2004.

[23] E. K. Akhmedov, R. Johansson, M. Lindner, T. Ohls-son, and T. Schwetz, "Series expansions for three-flavor neutrino oscillation probabilities in matter," *Journal of High Energy Physics*, vol. 2004, article 078, 2004.

[24] E. K. Akhmedov, M. Tortola, and J. Valle, "A simple analytic three-flavour description of the day-night effect in the solar neutrino flux," *Journal of High Energy Physics*, vol. 2004, no. 5, article 057, 2004.

[25] E. K. Akhmedov and V. Niro, "An accurate analytic description of neutrino oscillations in matter," *Journal of High Energy Physics*, vol. 2008, no. 12, article 106, 2008.

[26] A. Cervera, A. Donini, M. Gavela et al., "Golden measurements at a neutrino factory," *Nuclear Physics B*, vol. 579, no. 1-2, pp. 17–55, 2000.

[27] D. A. Dwyer, "The improved measurement of electron-antineutrino disappearance at daya bay," http://arxiv.org/abs/1303.3863.

[28] K. Hagiwara, N. Okamura, and K.-I. Senda, "The earth matter effects in neutrino oscillation experiments from Tokai to Kamioka and Korea," *Journal of High Energy Physics*, vol. 82, 2011.

[29] J. Beringer, J.-F. Arguin, R. M. Barnett et al., "Review of particle physics," *Physical Review D*, vol. 86, no. 1, Article ID 010001, 2012.

[30] J. D. Hunter, "Matplotlib: a 2D graphics environment," *Computing in Science & Engineering*, vol. 9, pp. 90–95, 2007.

Hindawi Publishing Corporation
Advances in High Energy Physics
Volume 2014, Article ID 305298, 7 pages
http://dx.doi.org/10.1155/2014/305298

Research Article

Tests of Lorentz Symmetry in Single Beta Decay

Jorge S. Díaz

Institute for Theoretical Physics, Karlsruhe Institute of Technology, 76128 Karlsruhe, Germany

Correspondence should be addressed to Jorge S. Díaz; jorge.diaz@kit.edu

Received 4 July 2014; Accepted 30 July 2014; Published 24 August 2014

Academic Editor: Theocharis Kosmas

Low-energy experiments studying single beta decay can serve as sensitive probes of Lorentz invariance that can complement interferometric searches for deviations from this spacetime symmetry. Experimental signatures of a dimension-three operator for Lorentz violation which are unobservable in neutrino oscillations are described for the decay of polarized and unpolarized neutrons as well as for measurements of the spectral endpoint in beta decay.

1. Introduction

The foundations of modern physics assume the invariance of physical laws under rotations and boosts, known as Lorentz symmetry. In our search for new physics, the possibility of minute violations of Lorentz invariance has become an active field of study by the development of theoretical formalisms and mainly by searching for key signatures in a wide range of experiments [1]. Precise studies of beta decay offer the opportunity to search for physics beyond the Standard Model. For instance, many experiments measuring the decay of neutrons are searching for unconventional couplings in weak interactions leading to new sources of CP violation [2]. Similarly, the search for a distortion in the spectrum of tritium decay would provide an absolute measurement of the neutrino mass. These experiments can also search for deviations from the exact Lorentz symmetry. The interferometric nature of quantum oscillations gives neutral mesons [3] and neutrinos [4] a remarkable sensitivity to signals of new physics; nonetheless, there are certain signals that are unobservable in these experiments. For neutrinos, it has been shown that beta decay experiments have unique sensitivity to the so-called *countershaded* operators, which produce no effects in oscillations nor modifications of the neutrino velocity; therefore, their effects can only be studied via weak decays [5].

This paper describes the relevant signatures of Lorentz and CPT violation in single beta decay experiments. High-precision measurements of beta decay spectra for the determination of neutron and neutrino properties offer an attractive opportunity to test Lorentz invariance by searching for distinctive signals that could arise in current and future experiments. Observable effects can also appear in double beta decays [6]. Systematic searches for Lorentz violation in experiments use a general framework based on effective field theory known as the Standard Model Extension (SME) [7–9]. This framework incorporates coordinate-independent terms that break Lorentz symmetry in the Standard Model action in the form of conventional operators contracted with controlling coefficients for Lorentz violation. These terms can trigger observable signals under the rotation and/or the boost of the relevant experimental system. The spontaneous breakdown of Lorentz symmetry at high energies in some string-theory scenarios [10] suggests that the SME coefficients should be small due to the relevant energy scale suppression, such as the Planck scale. Nevertheless, potentially large deviations from Lorentz symmetry have been considered in systems involving weak decays [5] and matter-gravity couplings [11].

For neutrinos, the SME has been used to search for signatures of Lorentz violation in oscillations [12, 13] using accelerators [14–20], atmospheric neutrinos [21, 22], and reactors [23, 24], reaching impressive sensitivity. Neutrino oscillations are powerful tools to test Lorentz symmetry; nonetheless, there are operators that are unobservable in these types of experiments. For these oscillation-free operators, other kinematical effects must be invoked such as modifications

of the neutrino velocity, which lead to Cherenkov radiation and threshold effects [25]. In these scenarios, the effects of Lorentz violation can be enhanced by the neutrino energy and propagation time, which makes astrophysical sources sensitive probes of Lorentz symmetry [26], particularly when operators of arbitrary dimension are incorporated in the action [27].

The fundamental role of beta decay experiments is the study of countershaded operators that are oscillation-free terms of mass dimension three in the Lagrangian which are controlled by the SME coefficient $a_{\rm of}^{(3)}$. These CPT-odd operators leave the neutrino velocity unchanged, and their experimental signatures are unaffected by the neutrino energy [27]. This feature makes beta decay experiments unique probes of Lorentz symmetry [5]. For illustration purposes, some neutron experiments such as *a*CORN [28], *a*SPECT [29], and PERKEO [30] are discussed; nevertheless, several observable signatures can be studied by other experiments including *ab*BA [31], emiT [32], N*ab* [33], nTRV [34], PERC [35], and UCNB [36]. Similarly, the analysis of tritium decay can be applied to experiments for neutrino mass measurements, Mainz [37], Troitsk [38], and Karlsruhe Tritium Neutrino experiment (KATRIN) [39] as well as the Princeton Tritium Observatory for Light, Early-Universe, Massive-Neutrino Yield (PTOLEMY) [40] proposed to search for the cosmic neutrino background.

2. Beta Decay

At low energies, the transition amplitude describing nuclear beta decay is well described by the Fermi four-fermion interaction of the form

$$i\mathcal{M} = \frac{iG_F}{\sqrt{2}} V_{ud} \left[\overline{u}(p)\gamma_\alpha (1-\gamma_5) v(q)\right] J^\alpha, \tag{1}$$

where J^α is the current describing the nuclear states, the spinor $\overline{u}(p)$ corresponds to the emitted electron of 4-momentum $p^\alpha = (E, \mathbf{p})$ and mass m_e, and the antineutrino of mass m_ν and 4-momentum $q^\alpha = (\omega, \mathbf{q})$ is given by spinor $v(q)$. The constant factors are the Fermi constant G_F and the relevant element of the CKM matrix $V_{ud} \approx \cos\theta_C$. In this work we are interested in the potential breakdown of Lorentz invariance in the neutrino sector [25]. Recent studies have also considered Lorentz-violating effects in weak decays arising in the gauge sector [41, 42]. The emitted antineutrino escapes unmeasured in beta decay experiments; however, imprints of its behavior can be inferred from the decay products experimentally accessible. The effects of Lorentz violation are controlled by the four components of the coefficient $a_{\rm of}^{(3)}$, which, in the spherical basis introduced in [27], are denoted by $(a_{\rm of}^{(3)})_{00}$, $(a_{\rm of}^{(3)})_{10}$, $\mathrm{Re}(a_{\rm of}^{(3)})_{11}$, and $\mathrm{Im}(a_{\rm of}^{(3)})_{11}$. To date, only theoretically estimated bounds exist on $(a_{\rm of}^{(3)})_{00}$ and $(a_{\rm of}^{(3)})_{10}$ [1, 5, 27], whereas the real and imaginary parts of $(a_{\rm of}^{(3)})_{11}$ remain unexplored. Below we present the signatures of these four coefficients so they can be directly studied in experiments.

3. Neutron Decay

For the transition amplitude in (1) describing beta decay of a neutron we write the nuclear current in the form

$$J^\alpha = \overline{u}_p \gamma^\alpha (1+\lambda\gamma_5) u_n, \tag{2}$$

where u_n and $\overline{u}_p$ represent the neutron and proton, respectively, and $\lambda = g_A/g_V$ is the ratio between the axial and vector couplings. It is important to emphasize that Lorentz violation modifies the neutrino dispersion relations and the spinor solutions satisfy a modified equation of motion.

The sum over the final spin states allowing for a polarized neutron in the direction $\hat{\mathbf{n}}$ can be written in terms of the electron energy E and velocity $\boldsymbol{\beta}$ in the form [43]

$$\sum_{\rm spin} |\mathcal{M}|^2 = 16 M_n^2 C E \omega \left(1 + a\boldsymbol{\beta}\cdot\hat{\tilde{\mathbf{q}}} + A\hat{\mathbf{n}}\cdot\boldsymbol{\beta} + B\hat{\mathbf{n}}\cdot\hat{\tilde{\mathbf{q}}}\right), \tag{3}$$

where Lorentz-violating effects appear in the form of an effective momentum $\hat{\tilde{\mathbf{q}}} = (\mathbf{q} + \mathbf{a}_{\rm of}^{(3)} - \mathring{a}_{\rm of}^{(3)}\hat{\mathbf{q}})/\omega$ for the antineutrino, with the isotropic component of $a_{\rm of}^{(3)}$ denoted by $\mathring{a}_{\rm of}^{(3)} = (a_{\rm of}^{(3)})_{00}/\sqrt{4\pi}$. The constant factor is given by $C = G_F^2 |V_{ud}|^2 (1+3\lambda^2)$, the nucleon mass is M_n, and the correlation parameters are given by the conventional definitions [2]

$$a = \frac{1-\lambda^2}{1+3\lambda^2}, \qquad A = -\frac{2\lambda(\lambda+1)}{1+3\lambda^2}, \qquad B = 2\frac{\lambda(\lambda-1)}{1+3\lambda^2}. \tag{4}$$

The decay rate is given by

$$d\Gamma = \frac{1}{4M_n^2} \int \frac{d^3p}{(2\pi)^3 2E} \frac{d^3q}{(2\pi)^3 2\omega} F(Z,E) \times \sum_{\rm spin} |\mathcal{M}|^2 2\pi\delta(E_A - E_B - E - \omega), \tag{5}$$

where the Fermi function has been included to incorporate the electrostatic interaction between the proton ($Z = 1$) and the outgoing electron. Integrating over the antineutrino energy ω and using $d^3p = |\mathbf{p}| E\, dE\, d\Omega_e$ and $d^3q = (\omega^2 + 2\omega\mathring{a}_{\rm of}^{(3)}) d\omega d\Omega_{\overline{\nu}}$, we can write the electron differential spectrum

$$\frac{d\Gamma}{d\Omega_e\, d\Omega_{\overline{\nu}}\, dT} = \frac{C}{(2\pi)^5} F(Z,E) |\mathbf{p}| E \left(\omega_0^2 + 2\omega_0 \mathring{a}_{\rm of}^{(3)}\right) \times \left(1 + a\boldsymbol{\beta}\cdot\hat{\tilde{\mathbf{q}}} + A\hat{\mathbf{n}}\cdot\boldsymbol{\beta} + B\hat{\mathbf{n}}\cdot\hat{\tilde{\mathbf{q}}}\right), \tag{6}$$

with $\omega_0 = T_0 - T$. The kinetic energy of the electron is given by $T = E - m_e$, and T_0 denotes the maximum kinetic energy available in the decay.

3.1. Unpolarized Neutrons. Experiments with unpolarized neutrons ($\hat{\mathbf{n}} = 0$) can be classified into two categories: those that only measure the electron spectrum and those in which the relative orientation between the two emitted leptons can be identified, relevant to the measurement of the electron-antineutrino asymmetry a defined in (4). The signatures of Lorentz violation for these two cases are presented below.

3.1.1. Spectrum Measurements. For experiments with unpolarized neutrons that only measure the outgoing electrons, the directions of the two final leptons can be integrated to reduce the spectrum (6) to the form

$$\frac{d\Gamma}{dT} = \frac{C}{2\pi^3} F(Z,T)\,|\mathbf{p}|\,(T+m_e)\left(\omega_0^2 + 2\mathring{a}_{\mathrm{of}}^{(3)}\omega_0\right). \quad (7)$$

This expression shows that the Lorentz-violating modification to the antineutrino spinors (3) plays no role and the isotropic effect is purely kinematic due to the modified antineutrino phase space. The effect of Lorentz violation appears as a small perturbation of the beta decay spectrum, similar to the effect in two-neutrino double beta decay [6]. The energy dependence of the modification introduced by the isotropic coefficient $\mathring{a}_{\mathrm{of}}^{(3)}$ can be used to determine the relevant energy for studying this modification, thus serving as a guide for a future experimental search of this effect.

The exact value requires a numerical solution due to the involved energy dependence of the Fermi function; nevertheless, a reasonable estimate can be obtained by considering that, for neutron decay, this function remains almost constant for energies above 200 keV. Using this approximation, the maximum of the Lorentz-invariant spectrum satisfies the cubic equation

$$0 = 4T^3 + 2(5m_e - T_0)T^2 + m_e(5m_e - 4T_0)T - m_e^2 T_0. \quad (8)$$

Using $T_0 = 780$ keV and $m_e = 511$ keV, we find that, in the absence of Lorentz violation, the spectrum has its maximum at 246 keV. In the presence of Lorentz violation, the maximum gets shifted. Instead of the cubic equation (8), the maximum of the modified spectrum satisfies the quartic equation

$$\begin{aligned} 0 = {} & 4T^4 + 2\left(5m_e - 3T_0 - 3\mathring{a}_{\mathrm{of}}^{(3)}\right)T^3 \\ & + \left(2T_0^2 + 5m_e^2 - 14m_eT_0 + 4\mathring{a}_{\mathrm{of}}^{(3)}T_0 - 14m_e\mathring{a}_{\mathrm{of}}^{(3)}\right)T^2 \\ & + 2m_e\left(2T_0^2 - 3m_eT_0 - 3m_e\mathring{a}_{\mathrm{of}}^{(3)} + 4\mathring{a}_{\mathrm{of}}^{(3)}T_0\right)T \\ & + \left(2m_e^2\mathring{a}_{\mathrm{of}}^{(3)}T_0 + m_e^2T_0^2\right). \end{aligned} \quad (9)$$

Here we find a method to search for a nonzero value of the coefficient $\mathring{a}_{\mathrm{of}}^{(3)}$: the maximum of the spectrum can be experimentally determined and its value can be replaced in (9), which gives a linear equation for $\mathring{a}_{\mathrm{of}}^{(3)}$.

It should be noticed that this shift in the maximum of the spectrum can be small and the application of the method mentioned above will depend on the resolution of the experiment. An equivalent method is the search for a direct deviation of the experimental spectrum from the expected prediction in the absence of Lorentz violation. This deviation or *residual spectrum* reaches its maximum at a well defined energy T_m which is independent of the size of $\mathring{a}_{\mathrm{of}}^{(3)}$ and satisfies the cubic equation

$$\begin{aligned} 0 = {} & 3T_m^3 + (7m_e - 2T_0)T_m^2 \\ & + m_e(3m_e - 4T_0)T_m - m_e^2T_0. \end{aligned} \quad (10)$$

For the numerical values used before, we find that the effect of a nonzero coefficient $\mathring{a}_{\mathrm{of}}^{(3)}$ is maximal at $T_m = 406$ keV; hence, this is the region of the spectrum where deviations from the conventional spectrum should be explored. The size of the deviation corresponds to a direct measurement of the magnitude of the coefficient $\mathring{a}_{\mathrm{of}}^{(3)}$.

3.1.2. Electron-Antineutrino Asymmetry. The decay of unpolarized neutrons is also used to measure the antineutrino-electron asymmetry a in (3). The aCORN experiment has a proton detector and an electron detector aligned perpendicular to the neutron beam, in which only decay products emitted along the axis of the detectors are analyzed [28]. The design of the experiment allows identifying events in which the two leptons emitted are parallel N_+ and antiparallel N_-, which can be determined from the spectrum and time-of-flight measurements. Since the directionality of the emitted antineutrino can be inferred from the measurement, we have access to the anisotropic coefficients $(a_{\mathrm{of}}^{(3)})_{1m}$, with $m = 0, \pm 1$.

Let us define the number of events in a given direction as

$$\begin{aligned} N(T) &= \frac{d\Gamma}{dT\,d\Omega_e\,d\Omega_{\bar{\nu}}} \\ &= \widetilde{C}(T)\left(1 + a\boldsymbol{\beta}\cdot\hat{\bar{\mathbf{q}}}\right)\left(1 + \frac{2a_{\mathrm{of}}^{(3)}}{\omega_0}\right), \end{aligned} \quad (11)$$

where we have defined the function $\widetilde{C}(T) = CF(Z,T)|\mathbf{p}|E\omega_0^2/(2\pi)^5$ and the coefficient $a_{\mathrm{of}}^{(3)}$ involves isotropic $(a_{\mathrm{of}}^{(3)})_{00}$ and anisotropic components $(a_{\mathrm{of}}^{(3)})_{1m}$. The experimental asymmetry a_{exp} is defined as

$$a_{\mathrm{exp}} = \frac{N_+ - N_-}{N_+ + N_-}, \quad (12)$$

which provides a direct measure of the parameter a defined in (4). From the number of events in a determined orientation given by (11), we find that at leading order the experimental asymmetry (12) becomes

$$a_{\mathrm{exp}} = a\,|\boldsymbol{\beta}| + \sqrt{\frac{3}{\pi}}\frac{\left(a^2\boldsymbol{\beta}^2 - 1\right)}{\omega_0}\left(a_{\mathrm{of}}^{(3)}\right)_{10}^{\mathrm{lab}}, \quad (13)$$

where the first term corresponds to the conventional expression for determining the parameter a, with the electron speed given in terms of its kinetic energy as $|\boldsymbol{\beta}| = \sqrt{T(T+2m_e)}/(T+m_e)$. The second term in (13) corresponds to the Lorentz-violating part written in the laboratory frame. Direct comparison between different experimental searches for Lorentz violation in a physically meaningful way requires a common reference frame, for which the Sun-centered frame is widely used in the literature for reporting constraints on SME coefficients [1]. The transformation to this frame is obtained by a sequence of rotations of the form [27]

$$\left(a_{\mathrm{of}}^{(3)}\right)_{10}^{\mathrm{lab}} = \sum_m e^{im\omega_\oplus T_\oplus} d_{0m}^{(1)}(-\chi)\left(a_{\mathrm{of}}^{(3)}\right)_{1m}, \quad (14)$$

where $d_{0m}^{(1)}(-\chi)$ are the little Wigner matrices and χ is the colatitude of the experiment. The dependence on the sidereal

time $T_\oplus$ is a consequence of the variation of the coupling between the SME coefficient and the antineutrino direction of propagation due to the Earth rotation with frequency $\omega_\oplus \simeq 2\pi/(23\,\mathrm{h}\ 56\ \mathrm{min})$. The explicit form of expression (14) is

$$\begin{aligned}\left(a_{\mathrm{of}}^{(3)}\right)_{10}^{\mathrm{lab}} &= \cos\chi\left(a_{\mathrm{of}}^{(3)}\right)_{10} \\ &\quad + \sqrt{2}\sin\chi\,\mathrm{Im}\left(a_{\mathrm{of}}^{(3)}\right)_{11}\sin\omega_\oplus T_\oplus \\ &\quad - \sqrt{2}\sin\chi\,\mathrm{Re}\left(a_{\mathrm{of}}^{(3)}\right)_{11}\cos\omega_\oplus T_\oplus.\end{aligned} \tag{15}$$

Equation (13) shows that the effect of Lorentz violation becomes more noticeable near the endpoint; however, for electron energies above 400 keV the measurement of the asymmetry becomes hard because the low energy of the protons makes the proper identification of N_+ and N_- using the proton time-of-flight method difficult. In order to properly measure the asymmetry, the beta spectrometer runs in the range 50 to 350 keV [28].

Another experiment designed to measure the parameter a is aSPECT, in which a magnetic field perpendicular to the neutron beam guides the protons emitted in the decay towards a proton detector for a precise measurement of the proton spectrum [29]. Protons emitted in the opposite direction of the detector are reflected by an electrostatic mirror; thus, the detector can examine protons emitted in all directions. This feature of the experimental setup makes aSPECT insensitive to the Lorentz-violating anisotropies produced by the coefficients $(a_{\mathrm{of}}^{(3)})_{1m}$. Nonetheless, data collected with the electrostatic mirror switched off allowing that only a 2π coverage can be used to implement a search for anisotropies [44].

3.2. Polarized Neutrons. Experiments with polarized neutrons that measure both the beta electron and the recoiling proton can reconstruct the direction of the emitted antineutrino. Experiments such as abBA [31], emiT [32], PERC [35], PERKEO [30], and UCNB [36] could access anisotropic effects due to Lorentz violation. For instance, unconventional energy- and direction-dependent effects could be studied by an experimental setup for the measurement of the spin-antineutrino asymmetry parameter B in (3).

For the decay of polarized neutrons, Lorentz-violating effects appear due to the modified spinor solutions as well as the unconventional antineutrino phase space. Although the antineutrino escapes unmeasured, the direction of its momentum can be inferred if both the electron and the proton are emitted in the same direction because conservation of momentum along the neutron spin axis can be used to write

$$\begin{aligned}0 &= \hat{\mathbf{n}}\cdot\mathbf{q} + \hat{\mathbf{n}}\cdot\mathbf{p} + \hat{\mathbf{n}}\cdot\mathbf{k} \\ &= |\mathbf{q}|\cos\theta_{\bar{\nu}} + |\mathbf{p}|\cos\theta_e + |\mathbf{k}|\cos\theta_p.\end{aligned} \tag{16}$$

For this reason, an asymmetry for coincident events in which both the electron and the proton are emitted in the same direction is appropriate for the determination of the parameter B that appears with the antineutrino momentum [45].

The number of events in which the electron and the proton are emitted along the direction of the neutron spin is $N^{++} = Q^{++}\widetilde{C}(T)$, where

$$\begin{aligned}Q^{++} &= \int_{\Omega_e^+} d\Omega_e \int_{\Omega_{\bar{\nu}}^-} d\Omega_{\bar{\nu}}\left(1 + \frac{2a_{\mathrm{of}}^{(3)}}{\omega_0}\right) \\ &\quad \times\left(1 + a\boldsymbol{\beta}\cdot\hat{\tilde{\mathbf{q}}} + A\hat{\mathbf{n}}\cdot\boldsymbol{\beta} + B\hat{\mathbf{n}}\cdot\hat{\tilde{\mathbf{q}}}\right).\end{aligned} \tag{17}$$

The integration ranges for the electron and the antineutrino are related by the constraint (16), which implies that when the proton is emitted perpendicular to the neutron spin then the antineutrino polar angle $\theta_{\bar{\nu}}$ can take the maximum value $\cos\theta_{\bar{\nu}} = -r\cos\theta_e$, with $r = \sqrt{T(T+2m_e)}/(T_0 - T)$. The integration regions are given by $\Omega_{\bar{\nu}}^- : \phi_{\bar{\nu}} \in [0, 2\pi]$, $\cos\theta_{\bar{\nu}} \in [-1, -r\cos\theta_e]$ and $\Omega_e^+ : \phi_e \in [0, 2\pi]$, $\cos\theta_e \in [0, \cos\theta_e^{\max}]$, where we have defined $\cos\theta_e^{\max} = 1(r^{-1})$ for $r < 1$ ($r > 1$). The number of events in which the electron and the proton are emitted against the direction of the neutron spin $N^{--} = Q^{--}\widetilde{C}(T)$ is found directly from N^{++} by reversing the sign of the parameters A and B. We can now define the following experimental asymmetry:

$$B_{\mathrm{exp}} = \frac{N^{--} - N^{++}}{N^{--} + N^{++}} = \frac{Q^{--} - Q^{++}}{Q^{--} + Q^{++}}. \tag{18}$$

Depending on the range of the parameter r and keeping leading-order terms, the experimental asymmetry can be written in the form $B_{\mathrm{exp}} = (B_{\mathrm{exp}})_0 + \delta B_{\mathrm{exp}}$, where the conventional asymmetry takes the form [45]

$$\left(B_{\mathrm{exp}}\right)_0 = \frac{4}{3}\begin{cases}\dfrac{\left[A\beta(2r-3) + B\left(3 - r^2\right)\right]}{8 - 4r + a\beta\left(r^2 - 2\right)}, & r < 1 \\ \dfrac{-A\beta + 2Br}{4r - a\beta}, & r > 1,\end{cases} \tag{19}$$

and the Lorentz-violating modification can be written as

$$\begin{aligned}\delta B_{\mathrm{exp}} &= \delta B_{\mathscr{C}} + \delta B_{\mathscr{A}_s}\sin\omega_\oplus T_\oplus \\ &\quad + \delta B_{\mathscr{A}_c}\cos\omega_\oplus T_\oplus,\end{aligned} \tag{20}$$

which explicitly shows the sidereal-time dependence of this quantity. The amplitudes $\delta B_{\mathscr{C}}$, $\delta B_{\mathscr{A}_s}$, and $\delta B_{\mathscr{A}_c}$ are functions of the location of the apparatus and the electron energy. They are explicitly presented in Appendix A.1.

4. Spectrum Endpoint Measurements

Direct measurements of the neutrino mass m_ν can be performed by searching for a spectral distortion near the endpoint of beta decay, for which tritium appears as an ideal isotope [46]. In an isotropic decay, the anisotropies produced by Lorentz violation are usually unobservable; nonetheless, the use of inhomogeneous magnetic fields for guiding electrons into electrostatic filters (MAC-E) allows selecting electrons emitted in determined directions. Superconducting magnets produce the guiding magnetic field for the electrons isotropically emitted from the decay of gaseous tritium.

Electrons with very long paths within the tritium source exhibit a high scattering probability; therefore, only electrons with short paths are accepted to be analyzed. Varying the magnetic field from a value in the tritium source B_S to a maximum value $B_{\max}$ creates a cone of acceptance of aperture θ_0, with

$$\sin\theta_0 = \sqrt{\frac{B_S}{B_{\max}}}. \tag{21}$$

Electrons emitted at angles $\theta > \theta_0$ are reflected due to a magnetic mirror effect. This selection is what permits the study of anisotropic effects.

Given the configuration of tritium-decay experiments, the sequence of rotations implemented for relating the components of $a^{(3)}_{\text{of}}$ in the laboratory frame to the relevant components in the Sun-centered frame differs from the one used in the previous section and it takes the explicit form [5]

$$\begin{aligned}\left(a^{(3)}_{\text{of}}\right)^{\text{lab}} &= \sum_{jm} e^{im\omega_\oplus T_\oplus} \sum_{m'm''} Y_{jm'}(\theta,\phi)\, d^{(j)}_{m'm''}(-\pi/2) \\ &\quad\times e^{-im''\xi} d^{(j)}_{m''m}(-\chi)\left(a^{(3)}_{\text{of}}\right)_{jm},\end{aligned} \tag{22}$$

where the extra rotations implemented in this transformation set the laboratory z-axis along the direction of the axis of the experiment determined by the magnetic field in the decay region. The spherical harmonics $Y_{jm'}(\theta,\phi)$ are written in this laboratory frame and ξ indicates the angle formed by the magnetic field at the tritium source measured counterclockwise from the local north. This choice allows us to make use of symmetry properties of the spherical harmonics to perform the integration within the acceptance cone $\Delta\Omega : \theta \in [0,\theta_0]$, $\phi \in [0, 2\pi]$ with ease.

Conventionally, near the endpoint, the spectrum takes the form

$$\frac{d\Gamma}{dT} = 3C_R\left[(\Delta T)^2 - \frac{1}{2}m_\nu^2\right], \tag{23}$$

where C_R is approximately constant and $\Delta T = T_0 - T$ denotes the kinetic energy of the electron measured from the point T_0 where the spectrum would end in the absence of neutrino mass. In the presence of Lorentz violation, the spectrum gets modified by the four components of the coefficient $a^{(3)}_{\text{of}}$ in the form $T_0 \to T_0 + \delta T$, with

$$\begin{aligned}\delta T &= \frac{1}{\Delta\Omega}\int_{\Delta\Omega} d\Omega_{\bar\nu}\left(a^{(3)}_{\text{of}}\right)^{\text{lab}} \\ &= \delta T_{\mathscr{C}} + \delta T_{\mathscr{A}_s}\sin\omega_\oplus T_\oplus + \delta T_{\mathscr{A}_c}\cos\omega_\oplus T_\oplus,\end{aligned} \tag{24}$$

which shows the sidereal-time dependence of this modification. The amplitudes $\delta T_{\mathscr{C}}$, $\delta T_{\mathscr{A}_s}$, and $\delta T_{\mathscr{A}_c}$ are explicitly presented in Appendix A.2. The energy independence of δT allows a direct determination of the integrated spectrum

$$\begin{aligned}\Gamma(T) &= \int_T^{T_{\text{eff}}} \frac{d\Gamma}{dT'}dT' \\ &= C_R\left[(T_{\text{eff}} - T)^3 - \frac{3}{2}m_\nu^2(T_{\text{eff}} - T)\right],\end{aligned} \tag{25}$$

where the effective null-mass endpoint energy $T_{\text{eff}} = T_0 + \delta T$ is a fit parameter that, in the presence of Lorentz violation, depends on the orientation of the experiment and the location of the laboratory and varies with sidereal time. The use of MAC-E filters was implemented in the past by the Mainz [37] and Troitsk [38] experiments, and unprecedent sensitivity will be achieved in KATRIN [39]. These experiments appear as ideal setups to search for the signals of Lorentz violation described here.

The study of Lorentz-violating neutrinos shows interesting features absent in other sectors. In particular, the incorporation of Dirac and Majorana couplings as well as the implementation of the seesaw mechanism that suppresses the left-right handed mixing produces terms in the Hamiltonian which appear as the product of the neutrino mass and a Majorana coefficient for CPT-even Lorentz violation [27]. Some of these mass-induced coefficients $(c^{(2)}_{\text{eff}})_{jm}$ modify the neutrino mass measured as the parameter in spectrum (23) in the form $m_\nu^2 \to m_\nu^2 + \delta m^2$, where the Lorentz-violating modification can be written in the form

$$\delta m^2 = m^2_{\mathscr{C}} + m^2_{\mathscr{A}_s}\sin\omega_\oplus T_\oplus + m^2_{\mathscr{A}_c}\cos\omega_\oplus T_\oplus, \tag{26}$$

to explicitly show the sidereal-time dependence of this parameter that mimics a neutrino mass. The amplitudes $m^2_{\mathscr{C}}$, $m^2_{\mathscr{A}_s}$, and $m^2_{\mathscr{A}_c}$ are explicitly presented in Appendix A.3. This result shows that the experimental mass-squared parameter m^2 measured in the experiment includes the actual neutrino mass m_ν and a Lorentz-violating component that depends on the orientation and location of the laboratory as well as sidereal time. Since there is no restriction on the sign of δm^2, the coefficients $(c^{(2)}_{\text{eff}})_{jm}$ could even produce a negative m^2 without a tachyonic neutrino [47].

5. Conclusions

In this paper, the low-energy signatures of Lorentz invariance violation in neutrinos in the context of the Standard Model Extension have been presented. The main focus is on a particular type of countershaded operator [5] that is unobservable in neutrino oscillations and modifications to the neutrino velocity. The main features that could arise in measurements of neutron decay as well as studies of the endpoint of beta decay are described. Different experimental setups can be sensitive to the effects of this type of Lorentz violation, including a distortion of the entire beta spectrum in neutron decay, modifications to the measurement of the antineutrino-electron correlation in the decay of unpolarized neutrons, a correction to the electron-proton coincidence asymmetry in the decay of polarized neutrons, and a shift in the endpoint energy of the beta decay spectrum. A remark on the effects of a mass-induced coefficient is also presented in the context of tritium decay because these coefficients can mask the effects of the actual neutrino mass in novel ways.

Experimental signatures of the breakdown of Lorentz symmetry in the neutrino sector have been mostly explored using high-energy and interferometric phenomena; nonetheless, the high precision of low-energy experiments studying

single beta decay can play a key complementary role in the search for deviations from exact Lorentz in variance.

Appendix

A. Sidereal Amplitudes

A.1. Sidereal Amplitudes for δB. The amplitudes for the sidereal decomposition of the Lorentz-violating experimental asymmetry defined in (20) are given by

$$\begin{aligned}\delta B_{\mathscr{C}} &= \sqrt{\frac{3}{\pi}} f(T) \cos\chi \left(a_{\mathrm{of}}^{(3)}\right)_{10},\\ \delta B_{\mathscr{A}_s} &= \sqrt{\frac{6}{\pi}} f(T) \sin\chi \,\mathrm{Im}\left(a_{\mathrm{of}}^{(3)}\right)_{11},\\ \delta B_{\mathscr{A}_c} &= -\sqrt{\frac{6}{\pi}} f(T) \sin\chi \,\mathrm{Re}\left(a_{\mathrm{of}}^{(3)}\right)_{11},\end{aligned} \tag{A.1}$$

where $f(T)$ is a function of the electron's kinetic energy and other parameters. Depending on the value of the factor r, the function $f(T)$ takes the form

$$f(T) = \begin{cases} \left((A\beta - Br)\left(2 - r^2\right) - \left(B_{\mathrm{exp}}\right)_0 \right. \\ \quad \times \left[\left(\frac{2r^2}{3} + \frac{2\beta r}{3} - \beta - 2 \right) + a\beta \left(1 - \frac{2r^3}{5} \right) \right] \Big) \\ \quad \times \left(8 - 4r + a\beta\left(r^2 - 2\right)\right)^{-1}, \quad r < 1 \\ \dfrac{(A\beta - Br) + \left(B_{\mathrm{exp}}\right)_0 \left[2\beta/3 + 8r/3 - 6a\beta/5\right]}{4r - a\beta}, \\ \qquad\qquad r < 1. \end{cases} \tag{A.2}$$

A.2. Sidereal Amplitudes for δT. The amplitudes for the sidereal decomposition of the Lorentz-violating shift of the endpoint energy defined in (24) are given by

$$\begin{aligned}\delta T_{\mathscr{C}} &= \mathring{a}_{\mathrm{of}}^{(3)} - \sqrt{\frac{3}{4\pi}} \cos^2\frac{\theta_0}{2} \sin\chi \cos\xi \left(a_{\mathrm{of}}^{(3)}\right)_{10},\\ \delta T_{\mathscr{A}_s} &= -\sqrt{\frac{3}{2\pi}} \cos^2\frac{\theta_0}{2} \left(\sin\xi \,\mathrm{Re}\left(a_{\mathrm{of}}^{(3)}\right)_{11} \right.\\ &\qquad \left. - \cos\xi \cos\chi \,\mathrm{Im}\left(a_{\mathrm{of}}^{(3)}\right)_{11}\right),\\ \delta T_{\mathscr{A}_c} &= -\sqrt{\frac{3}{2\pi}} \cos^2\frac{\theta_0}{2} \left(\sin\xi \,\mathrm{Im}\left(a_{\mathrm{of}}^{(3)}\right)_{11} \right.\\ &\qquad \left. + \cos\xi \cos\chi \,\mathrm{Re}\left(a_{\mathrm{of}}^{(3)}\right)_{11}\right).\end{aligned} \tag{A.3}$$

A.3. Sidereal Amplitudes for δm^2. The amplitudes for the sidereal decomposition of the Lorentz-violating shift of the neutrino mass parameter defined in (26) are given by

$$\begin{aligned}m_{\mathscr{C}}^2 &= \sqrt{\frac{3}{\pi}} \cos^2\frac{\theta_0}{2} \sin\chi \cos\xi \left(c_{\mathrm{eff}}^{(2)}\right)_{10},\\ m_{\mathscr{A}_s}^2 &= \sqrt{\frac{6}{\pi}} \cos^2\frac{\theta_0}{2}\\ &\qquad \times \left[\sin\xi \,\mathrm{Re}\left(c_{\mathrm{eff}}^{(2)}\right)_{11} - \cos\chi \cos\xi \,\mathrm{Im}\left(c_{\mathrm{eff}}^{(2)}\right)_{11}\right],\\ m_{\mathscr{A}_c}^2 &= \sqrt{\frac{6}{\pi}} \cos^2\frac{\theta_0}{2}\\ &\qquad \times \left[\sin\xi \,\mathrm{Im}\left(c_{\mathrm{eff}}^{(2)}\right)_{11} + \cos\chi \cos\xi \,\mathrm{Re}\left(c_{\mathrm{eff}}^{(2)}\right)_{11}\right].\end{aligned} \tag{A.4}$$

Conflict of Interests

The author declares that there is no conflict of interests regarding the publication of this paper.

Acknowledgment

This work was supported in part by the Helmholtz Alliance for Astroparticle Physics (HAP) under Grant no. HA-301.

References

[1] V. A. Kostelecký and N. Russell, "Data tables for Lorentz and CPT violation," *Reviews of Modern Physics*, vol. 83, article 11, 2011.

[2] J. S. Nico and W. M. Snow, "Fundamental neutron physics," *Annual Review of Nuclear and Particle Science*, vol. 55, pp. 27–69, 2005.

[3] V. A. Kostelecký, "Sensitivity of *CPT* tests with neutral mesons," *Physical Review Letters*, vol. 80, p. 1818, 1998.

[4] V. A. Kostelecký and M. Mewes, "Lorentz and *CPT* violation in neutrinos," *Physical Review D*, vol. 69, Article ID 016005, 2004.

[5] J. S. Díaz, V. A. Kostelecký, and R. Lehnert, "Relativity violations and beta decay," *Physical Review D*, vol. 88, Article ID 071902(R), 2013.

[6] J. S. Díaz, "Limits on Lorentz and *CPT* violation from double beta decay," *Physical Review D*, vol. 89, Article ID 036002, 2014.

[7] D. Colladay and V. A. Kostelecký, "CPT violation and the standard model," *Physical Review D*, vol. 55, article 6760, 1997.

[8] D. Colladay and V. A. Kostelecký, "Lorentz-violating extension of the standard model," *Physical Review D*, vol. 58, Article ID 116002, 1998.

[9] V. A. Kostelecký, "Gravity, Lorentz violation, and the standard model," *Physical Review D*, vol. 69, Article ID 105009, 2004.

[10] V. A. Kostelecký and S. Samuel, "Spontaneous breaking of Lorentz symmetry in string theory," *Physical Review D*, vol. 39, p. 683, 1989.

[11] V. A. Kostelecký and J. Tasson, "Matter-gravity couplings and Lorentz violation," *Physical Review D*, vol. 83, Article ID 016013, 2011.

[12] V. A. Kostelecký and M. Mewes, "Lorentz violation and short-baseline neutrino experiments," *Physical Review D*, vol. 70, Article ID 076002, 2004.

[13] J. S. Díaz, V. A. Kostelecký, and M. Mewes, "Perturbative Lorentz and *CPT* violation for neutrino and antineutrino oscillations," *Physical Review D*, vol. 80, Article ID 076007, 2009.

[14] L. B. Auerbach, R. L. Burman, and D. O. Caldwell, "Tests of Lorentz violation in $\overline{\nu}_\mu \rightarrow \overline{\nu}_e$ oscillations," *Physical Review D*, vol. 72, Article ID 076004, 2005.

[15] A. A. Aguilar-Arevalo, C. E. Anderson, A. O. Anderson et al., "Test of Lorentz and CPT violation with short baseline neutrino oscillation excesses," *Physics Letters B*, vol. 718, pp. 1303–1308, 2013.

[16] T. Katori [MiniBooNE Collaboration], "Tests of lorentz and cpt violation with miniboone neutrino oscillation excesses," *Modern Physics Letters A*, vol. 27, Article ID 1230024, 21 pages, 2012.

[17] P. Adamson, D. J. Auty, D. S. Ayres et al., "Testing Lorentz invariance and CPT conservation with NuMI neutrinos in the MINOS near detector," *Physical Review Letters*, vol. 101, Article ID 151601, 2008.

[18] P. Adamson, D. S. Ayres, G. Barr et al., "Search for Lorentz invariance and *CPT* violation with muon antineutrinos in the MINOS Near Detector," *Physical Review D*, vol. 85, no. 3, Article ID 031101, 2012.

[19] P. Adamson, D. J. Auty, D. S. Ayres [MINOS Collaboration] et al., "Search for Lorentz invariance and CPT violation with the MINOS far detector," *Physical Review Letters*, vol. 105, Article ID 151601, 2010.

[20] B. Rebel and S. Mufson, "The search for neutrino–antineutrino mixing resulting from Lorentz invariance violation using neutrino interactions in MINOS," *Astroparticle Physics*, vol. 48, pp. 78–81, 2013.

[21] R. Abbasi, Y. Abdou, T. Abu-Zayyad et al., "Search for a Lorentz-violating sidereal signal with atmospheric neutrinos in IceCube," *Physical Review D*, vol. 82, Article ID 112003, 2010.

[22] T. Akiri, "Sensitivity of atmospheric neutrinos in Super-Kamiokande to Lorentz violation," http://arxiv.org/abs/1308.2210.

[23] Y. Abe, C. Aberle, J. C. dos Anjos et al., "First test of Lorentz violation with a reactor-based antineutrino experiment," *Physical Review D*, vol. 86, no. 11, Article ID 112009, 2012.

[24] J. S. Díaz, T. Katori, J. Spitz, and J. M. Conrad, "Search for neutrino–antineutrino oscillations with a reactor experiment," *Physics Letters B*, vol. 727, no. 4-5, pp. 412–416, 2013.

[25] J. S. Díaz, "Neutrinos as probes of Lorentz invariance," *Advances in High Energy Physics*, vol. 2014, Article ID 962410, 11 pages, 2014.

[26] J. S. Díaz, V. A. Kostelecký, and M. Mewes, "Testing relativity with high-energy astrophysical neutrinos," *Physical Review D*, vol. 89, Article ID 043005, 2014.

[27] V. A. Kostelecký and M. Mewes, "Neutrinos with Lorentz-violating operators of arbitrary dimension," *Physical Review D*, vol. 85, Article ID 096005, 2012.

[28] G. Noid, Indiana University, 2010.

[29] S. Baeßler, F. Ayala Guardia, M. Borg et al., "First measurements with the neutron decay spectrometer a SPECT," *The European Physical Journal A*, vol. 38, pp. 17–26, 2008.

[30] B. Märkisch, H. Abele, D. Dubbers et al., "The new neutron decay spectrometer Perkeo III," *Nuclear Instruments and Methods in Physics Research A: Accelerators, Spectrometers, Detectors and Associated Equipment*, vol. 611, pp. 216–218, 2009.

[31] L. Barrón-Palos, E. Chávez, C. Crawford et al., "A measurement of correlation parameters in the decay of polarized free neutrons: the *abBA* experiment," *Journal of Physics: Conference Series*, vol. 239, no. 1, Article ID 012013, 2010.

[32] L. J. Lising, S. R. Hwang, J. M. Adams et al., "New limit on the *D* coefficient in polarized neutron decay," *Physical Review C*, vol. 62, Article ID 055501, 2000.

[33] D. Pocanic, R. Alarcon, L. P. Alonzi et al., "Nab: measurement principles, apparatus and uncertainties," Nuclear Instruments and Methods in Physics Research, 2009, http://arxiv.org/abs/0810.0251.

[34] A. Kozela, G. Ban, A. Białek et al., "Measurement of the transverse polarization of electrons emitted in free-neutron decay," *Physical Review Letters*, vol. 102, Article ID 172301, 2009.

[35] D. Dubbers, H. Abele, S. Baeßler et al., "A clean, bright, and versatile source of neutron decay products," *Nuclear Instruments and Methods in Physics Research A: Accelerators, Spectrometers, Detectors and Associated Equipment*, vol. 596, no. 2, pp. 238–247, 2008.

[36] L. Broussard, "UCNB: the neutrino asymmetry in polarized ultracold neutron decay," *AIP Conference Proceedings*, vol. 1560, pp. 149–151, 2013.

[37] C. Kraus, B. Bornschein, L. Bornschein et al., "Final results from phase II of the Mainz neutrino mass searchin tritium β decay," *The European Physical Journal C*, vol. 40, pp. 447–468, 2005.

[38] V. N. Aseev, A. I. Belesev, A. I. Berlev et al., "Upper limit on the electron antineutrino mass from the Troitsk experiment," *Physical Review D*, vol. 84, Article ID 112003, 2011.

[39] J. Angrik et al., [KATRIN Collaboration], FZKA-7090, 2005.

[40] S. Betts, W. R. Blanchard, R. H. Carnevale et al., "Development of a relic neutrino detection experiment at PTOLEMY: princeton tritium observatory for light, early-universe, massive-neutrino yield," http://arxiv.org/abs/1307.4738.

[41] J. P. Noordmans, H. W. Wilschut, and R. G. E. Timmermans, "Lorentz violation in neutron decay and allowed nuclear $\boldsymbol{\beta}$ decay," *Physical Review C*, vol. 87, Article ID 055502, 2013.

[42] B. Altschul, "Contributions to pion decay from Lorentz violation in the weak sector," *Physical Review D*, vol. 88, Article ID 076015, 2013.

[43] J. D. Jackson, S. B. Treiman, and H. W. Wyld Jr., "Possible tests of time reversal invariance in beta decay," *Physical Review*, vol. 106, no. 3, pp. 517–521, 1957.

[44] W. Heil, Private communication, 2013.

[45] F. Glück, I. Joób, and J. Lastc, "Measurable parameters of neutron decay," *Nuclear Physics A*, vol. 593, no. 2, pp. 125–150, 1995.

[46] E. J. Konopinski, "H^3 and the mass of the neutrino," *Physical Review*, vol. 72, no. 6, pp. 518–519, 1947.

[47] A. Chodos, A. I. Hauser, and V. A. Kostelecký, "The neutrino as a tachyon," *Physics Letters B*, vol. 150, no. 6, pp. 431–435, 1985.

Hindawi Publishing Corporation
Advances in High Energy Physics
Volume 2014, Article ID 724315, 7 pages
http://dx.doi.org/10.1155/2014/724315

Research Article

Constraints on Heavy Neutrino and SUSY Parameters Derived from the Study of Neutrinoless Double Beta Decay

Andrei Neacsu[1,2] and Sabin Stoica[1,2]

[1] *Horia Hulubei Foundation, P.O. Box MG-12, Magurele, Bucharest 077125, Romania*
[2] *Horia Hulubei National Institute for Physics and Nuclear Engineering, P.O. Box MG-6, Magurele, Bucharest 077125, Romania*

Correspondence should be addressed to Andrei Neacsu; nandrei@theory.nipne.ro

Received 4 April 2014; Accepted 26 May 2014; Published 16 June 2014

Academic Editor: Theocharis Kosmas

New constraints on the lepton number violating (LNV) parameters are derived from the analysis of the neutrinoless double beta ($0\nu\beta\beta$) decay in the hypothesis that this process would occur through the exchange of heavy neutrinos and/or SUSY particles. For derivation, we use new values of both phase space factors (PSFs) and nuclear matrix elements (NMEs) calculated with numerical codes developed recently, as well as the most recent experimental lifetimes. The NMEs are computed with a shell model (ShM) code for ^{48}Ca, ^{76}Ge, and ^{82}Se nuclei, while at present similar ShM results are available only for the first nucleus. We compare our results with similar ones from literature, obtained with ShM, QRPA, and IBM-2 methods, and conclude that more results are needed for a relevant analysis on the validity of NMEs associated with these decay mechanisms.

1. Introduction

Neutrinoless double beta ($0\nu\beta\beta$) decay is a beyond standard model (BSM) process by which an even-even nucleus transforms into another even-even nucleus with the emission of two electrons/positrons but no antineutrinos/neutrinos in the final states. Its study is important since it would clarify the question about the lepton number violation, decide on the neutrinos character (are they distinguished or not from their antiparticles?), and give a hint on the scale of their absolute masses. Moreover, the study of $0\nu\beta\beta$ decay has a broader potential to search for other BSM phenomena, such as new neutrino flavors and exotic particles. The great interest in understanding these fundamental issues has led to many theoretical and experimental investigations of this process. The reader can find up-to-date information on these studies in several recent reviews [1–6], which also contain therein a comprehensive list of references in the domain.

One of the open issues concerning the $0\nu\beta\beta$ decay is related to the possible mechanisms responsible for its occurrence. The exchange of a light Majorana neutrino in the presence of left handed (LH) weak interaction is still the most popular and studied mechanism. However, other mechanisms have also been considered, for example, the exchange of heavy neutrinos [7, 8] and SUSY particles [3, 9], which could also contribute to the total $0\nu\beta\beta$ decay rate. On the other hand, constraints on heavy neutrino and SUSY parameters can be now derived at hadron colliders, as well, by analyzing same sign dilepton decay channels, which are triggered by processes that violate the lepton number conservation by two units (like $0\nu\beta\beta$ decay). Indeed, the CMS, ATLAS, and LHCb experiments at LHC include now in their data analysis the search of such channels, and the first results were already reported [10–13]. Thus, complementary information that allows the constraint of various LNV parameters can also be obtained now from high-energy experiments.

For all mechanisms, the $0\nu\beta\beta$ lifetimes can be expressed in a good approximation as a product of a phase space factor, a nuclear matrix element related to the nuclear structure of the parent and daughter nuclei, and a LNV parameter related to the BSM mechanism considered. These three factors can be identified in (1) and (2) from the next section. Hence, to

extract reliable upper limits for the LNV parameters, we need accurate calculation of both PSFs and NMEs factors, as well as reliable measurements of the lifetimes.

The largest uncertainties in the theoretical calculations for double beta decay (DBD) arise from the calculated values of the NMEs. For the LH light neutrino exchange mechanism, the NMEs are currently computed by several methods, the present most employed ones being the proton-neutron quasi-random phase approximation (pnQRPA) [14–20], interacting shell model (ISM) [21–25], interacting boson model (IBM) [26–28], projected Hartree Fock Bogoliubov (PHFB) [29], and energy density functional (EDS) [30] methods. At present, there are still large discrepancies between the NMEs values computed with different methods and by different groups, which have been widely discussed in literature (see, e.g., [5, 6]) for the light neutrino exchange mechanism. At present, for heavy neutrino and SUSY exchange mechanisms, there are fewer NME calculations, performed with QRPA [31, 32] and IBA-2 [28] and ShM methods [33, 34]. The discrepancies between the existing NME values associated with heavy neutrino or SUSY mechanisms are even larger than those in the case of LH light neutrino exchange, so there is a need for new calculations.

In this paper, we report new constraints on the heavy neutrino and SUSY parameters derived from the analysis of the neutrinoless double beta decay of three experimentally interested nuclei, ^{48}Ca, ^{76}Ge, and ^{82}Se, in the hypothesis that this process would occur through the exchange of such particle. The computation of the NMEs is performed with a ShM code developed recently and presented in detail in [35, 36]. Also, we estimate the uncertainties introduced in calculations by the use of different NN interactions and SRC parameterizations and found that the calculated NME values depend significantly on these nuclear ingredients. We compare our results with other previous ones from literature performed with ShM, QRPA, and IBM-2 approaches and discuss the discrepancies. We remark that, until now, large scale ShM calculations of NMEs corresponding to these mechanisms are available only for ^{48}Ca, and they differ significantly from the IBM-2 calculations. In order to understand these discrepancies, more ShM calculations of the NMEs for these (less discussed) $0\nu\beta\beta$ decay mechanisms, including other nuclei, are needed.

The values of the PSFs are taken from our recent work [37], which are very close to those reported in [38, 39]. We mention that PSFs for DBD have been calculated since long time [40, 41], but they were less discussed, being considered to be computed with enough precision. Recently, they were recalculated with improved approaches [38, 39, 42] and several discrepancies were revealed as compared to the old calculations, which should be taken into account for accurate predictions of $0\nu\beta\beta$ lifetimes and derivation of LNV parameters.

The paper is organized as follows. In the next section, we present the formulae for the $0\nu\beta\beta$ decay lifetimes together with the relevant expressions for the PSFs and NMEs which have to be computed for deriving the LNV parameters, for heavy neutrino and SUSY mechanisms. In Section 3, we present and discuss our results, while in the last section we formulate the conclusions of our work.

2. Formalism

In this section, we give a short description of the heavy neutrino and SUSY formalisms, displaying the PSF and NME formulas that have to be computed. As we already mentioned, the expressions of the $0\nu\beta\beta$ lifetimes can be written as a product of three terms: a phase space, a nuclear matrix elements, and a term related to the corresponding LNV mechanism:

$$\left(T_{1/2}^{0\nu}\right)^{-1} = G^{0\nu}\left(Q_{\beta\beta}, Z\right)\sum_{k}\left(\left|M_{k}^{0\nu}\right|^{2}\right)\left(\eta_{k}\right)^{2}, \tag{1}$$

where k is an index which denotes the mechanisms that can contribute to the $0\nu\beta\beta$ decay. In this work, we refer to the heavy neutrino and SUSY exchange mechanisms, so the lifetime reads

$$\begin{aligned}\left(T_{1/2}^{0\nu}\right)^{-1} = G^{0\nu}\left(Q_{\beta\beta}, Z\right)\Big(&\left|M_{N}^{0\nu}\right|\left\langle\eta_{N}\right\rangle + \left|M_{\lambda'}^{0\nu}\right|\left\langle\eta_{\lambda'}\right\rangle \\ &+ \left|M_{q}^{0\nu}\right|\left\langle\eta_{q}\right\rangle\Big)^{2},\end{aligned} \tag{2}$$

where $G^{0\nu}$ is the phase space factor for this decay mode, depending on the energy decay $Q_{\beta\beta}$ and nuclear charge Z. $M_{N,\lambda',q}^{0\nu}$ are the NMEs associated with the heavy neutrino (N) exchange mechanism and with the gluino (λ') and squark-neutrino (q) exchange mechanisms. The last mechanisms may appear in SUSY theories with R-parity violation [3]. $\eta_{N,\lambda',q}$ are the corresponding coupling parameters associated with these mechanisms.

For the $0\nu\beta\beta$ decay, the expression of the PSFs reads

$$G_{0\nu} = \frac{2}{4g_{A}^{4}R^{2}\ln 2}\int_{m_{e}c^{2}}^{T_{0}-m_{e}c^{2}} f_{11}^{(0)} w_{0\nu}\, d\epsilon_{1}, \tag{3}$$

where $f_{11}^{(0)}$ are the solutions of the Dirac equation and

$$w_{0\nu} = \frac{g_{A}^{4}\left(G\cos\theta_{C}\right)^{4}}{16\pi^{5}}\left(m_{e}c^{2}\right)^{2}\left(\hbar c^{2}\right)\left(p_{1}c\right)\left(p_{2}c\right)\epsilon_{1}\epsilon_{2}, \tag{4}$$

where g_A ($g_A = 1.25$) is the axial-vector coupling constant, $G = 1.16637 \times 10^{-5}\,\mathrm{GeV}^{-2}$ is the Fermi constant, θ_C is the Cabbibo angle, m_e is the electron rest mass, while p_1, p_2 and ϵ_1, ϵ_2 are the electron momenta and energies, respectively. In (3), it is convenient to redefine the PSFs by a renormalization that eliminates the constant g_A and correlates (by dividing by $4R^2$, R the nuclear radius) the dimension of $G_{0\nu}$ with the NMEs which are dimensionless, such that the PSFs are expressed in [yr^{-1}].

Concerning the NMEs, their expressions can be written, in general, as a sum of three components:

$$M^{0\nu} = M_{\mathrm{GT}}^{0\nu} - \left(\frac{g_{V}}{g_{A}}\right)^{2}\cdot M_{F}^{0\nu} - M_{T}^{0\nu}, \tag{5}$$

where $M_{\mathrm{GT}}^{0\nu}$, $M_{F}^{0\nu}$, and $M_{T}^{0\nu}$ are the Gamow-Teller (GT), Fermi (F), and Tensor (T) components, respectively.

Due to the two-body nature of the transition operator, the NMEs can be expressed as a sum of products of two-body transition densities (TBTDs) and matrix elements of the two-body transition operators for two-particle states, shortly, two-body matrix elements (TBMEs) [35, 36]. Consider

$$M_{\alpha}^{0\nu} = \sum_{j_p j_{p'} j_n j_{n'} J_\pi} \mathrm{TBTD}\left(j_p j_{p'}, j_n j_{n'}; J_\pi\right) \times \left\langle j_p j_{p'}; J_\pi \left\| \tau_{-1}\tau_{-2} O_{12}^{\alpha} \right\| j_n j_{n'}; J_\pi \right\rangle, \tag{6}$$

where $|jj'; J^\pi\rangle$ represent the antisymmetrized two-particle states and O_{mn}^{α} are DBD transition operators ($\alpha = \mathrm{GT}, F, T$). Since the NN effective interaction can be treated by means of a central (single-particle) potential, the NMEs can be conveniently calculated using Moshinsky's transformations between the relative and center of mass (CM) coordinates and the proper use of nuclear states in different coupling notations. The calculation of the matrix elements of these operators can be decomposed into products of reduced matrix elements within the spin and relative coordinates subspaces [21, 35]. The expressions of the two-body transition operators are

$$O_{12}^{\mathrm{GT}} = \sigma_1 \cdot \sigma_2 H(r), \qquad O_{12}^{F} = H(r),$$
$$O_{12}^{T} = \sqrt{\frac{2}{3}}\left[\sigma_1 \times \sigma_2\right]^2 \cdot \frac{r}{R} H(r)\, C^{(2)}(\hat{r}), \tag{7}$$

where σ are the Pauli spin operators and $C^{(2)}(\hat{r})$ is the center of mass operator. The expressions for the neutrino potentials H_α in the case of heavy neutrino mechanisms are

$$H_\alpha(r) = \frac{2R}{\pi m_e m_p} \int_0^\infty j_k(qr)\, h_\alpha\left(q^2\right) q^2 dq, \tag{8}$$

where m_p is the proton mass and j_k ($k = 0$ for $\alpha = \mathrm{GT}, F$, and $k = 2$ for $\alpha = T$) are the Bessel spherical functions. The expressions of h_α ($\alpha = \mathrm{GT}, F, T$) are

$$h_F\left(q^2\right) = G_V^2\left(q^2\right), \tag{9}$$

$$h_{\mathrm{GT}}\left(q^2\right) = \frac{G_A^2\left(q^2\right)}{g_A^2}\left[1 - \frac{2}{3}\frac{q^2}{q^2+m_\pi^2} + \frac{1}{3}\left(\frac{q^2}{q^2+m_\pi^2}\right)^2\right] + \frac{2}{3}\frac{G_M^2\left(q^2\right)}{g_A^2}\frac{q^2}{4m_p^2}, \tag{10}$$

$$h_T\left(q^2\right) = \frac{G_A^2\left(q^2\right)}{g_A^2}\left[\frac{2}{3}\frac{q^2}{q^2+m_\pi^2} - \frac{1}{3}\left(\frac{q^2}{q^2+m_\pi^2}\right)^2\right] + \frac{1}{3}\frac{G_M^2\left(q^2\right)}{g_A^2}\frac{q^2}{4m_p^2}, \tag{11}$$

where m_π is the pion mass and

$$G_M\left(q^2\right) = \left(\mu_p - \mu_n\right) G_V\left(q^2\right), \tag{12}$$

with $(\mu_p - \mu_n) = 4.71$. The expressions (9)–(11) include the following nuclear effects: (i) finite nucleon size (FNS) effects through the nucleon form factors G_A, G_V and (ii) higher order current (HOC) effects by the second and third terms in the h_{GT} expression and by the appearance of the h_T contribution.

The G_V and G_A form factors which take into account the finite size of the nucleons effect are

$$G_A\left(q^2\right) = g_A\left(\frac{\Lambda_A^2}{\Lambda_A^2 + q^2}\right)^2, \qquad G_V\left(q^2\right) = g_V\left(\frac{\Lambda_V^2}{\Lambda_V^2 + q^2}\right)^2. \tag{13}$$

For the vector and axial coupling constants, the majority of calculations take $g_V = 1$ and the unquenched value $g_A = 1.25$, while the values of the vector and axial vector form factors are $\Lambda_V = 850$ MeV and $\Lambda_A = 1086$ MeV [1], respectively.

For the SUSY mechanisms, only the GT and T components of the $M^{0\nu}$ are contributing. For the gluino exchange mechanism (SUSY1), the radial neutrino potentials H_α have a similar form as that for the heavy neutrino mechanism (9), but with different h_α factors [3, 14]:

$$\mathscr{M}_{\lambda'}^{0\nu} = c^{1\pi}\left(M_{\mathrm{GT}}^{1\pi} - M_T^{1\pi}\right) + c^{2\pi}\left(M_{\mathrm{GT}}^{2\pi} - M_T^{2\pi}\right), \tag{14}$$

with

$$c^{1\pi} = -\frac{2}{9}\frac{\sqrt{2} f_\pi m_\pi^4}{m_p^3 m_e\left(m_u + m_d\right)}\frac{g_s F_P}{g_A^2}, \qquad c^{2\pi} = \frac{1}{18}\frac{f_\pi^2 m_\pi^4}{m_p^3 m_e\left(m_u + m_d\right)^2}\frac{g_s^2}{g_A^2}, \tag{15}$$

where m_π is the charged-pion mass, 139.6 MeV, $f_\pi = 0.668 m_\pi$ MeV, m_u and m_d are the up and down quark masses $(m_u + m_d) = 11.6$ MeV, $m_p = 938.27$ MeV, $m_e = 0.511$ MeV, $g_s = 13.4$, and $F_P \approx 4.41$ [3]. Computing the expressions from (15), we obtain $c^{1\pi} = -85.33$ and $c^{2\pi} = 365.72$. Consider

$$H_\alpha^{1\pi}(r) = -\frac{2R}{\pi}\int_0^\infty j_k(qr)\, h_\alpha^{1\pi}\left(q^2\right) dq, \qquad H_\alpha^{2\pi}(r) = -\frac{4R}{\pi}\int_0^\infty j_k(qr)\, h_\alpha^{2\pi}\left(q^2\right) dq, \tag{16}$$

with

$$h_\alpha^{1\pi}\left(q^2\right) = \frac{G_A^2\left(q^2\right)}{g_A^2}\frac{q^4/m_\pi^4}{1 + q^2/m_\pi^2}, \qquad h_\alpha^{2\pi}\left(q^2\right) = \frac{G_A^2\left(q^2\right)}{g_A^2}\frac{q^4/m_\pi^4}{\left(1 + q^2/m_\pi^2\right)^2}. \tag{17}$$

For the squark-neutrino mechanism (SUSY2), H_α has an expression similar to the light neutrino mechanism:

$$H_\alpha(r) = \frac{2R}{\pi}\int_0^\infty j_k(qr)\frac{h_\alpha\left(q^2\right)}{q + \langle E\rangle} G_\alpha\left(q^2\right) q\, dq, \tag{18}$$

Table 1: $0\nu\beta\beta$ NMEs values for heavy neutrino mechanism and comparison to other results in the literature.

	No SRC	Jastrow	AV-18	CD-BONN
^{48}Ca (GXPF1A)	91.5	23.7	47.5	70.3
^{48}Ca (KB3G)	106.8	29.7	56.8	82.8
^{48}Ca [34]			52.9	75.5
^{48}Ca [28]		16.3	46.3	76.0
^{76}Ge (JUN45)	255.7	73.1	137.8	199.2
^{76}Ge [31]^{a} , [32]^{b}		32.6^{a}	233^{b}	351^{b}
^{76}Ge [28]		48.1	107	163
^{82}Se (JUN45)	237.3	66.1	126.9	184.5
^{82}Se [31]^{a} , [32]^{b}		30.0^{a}	226^{b}	340^{b}
^{82}Se [28]		35.6	84.4	132

The indices a and b are used to indicate different calculations performed by the Tubingen group.

Table 2: $0\nu\beta\beta$ NMEs values for SUSY1 mechanism and comparison to other results in the literature.

	No SRC	Jastrow	AV-18	CD-BONN
^{48}Ca (GXPF1A)	643.7.2	242.4	417.2	548.2
^{48}Ca (KB3G)	750.1	293.3	492.47	641.7
^{48}Ca [34]			453	618
^{48}Ca [43]	392	147		
^{76}Ge (JUN45)	1762.1	678.3	1156.2	1509.4
^{76}Ge [43]^{a}, [32]^{b}	1831^{a}	625^{a}	587^{b}	515^{b}
^{82}Se (JUN45)	1628.0	612.8	1062.5	1393.5
^{82}Se [43]^{a}, [32]^{b}	1667^{a}	583^{a}	574^{b}	504^{b}

The indices a and b are used to indicate different calculations performed by the Tubingen group.

where $\langle E\rangle$ is the energy used in the closure approximation and represents the average excitation energy of the states in the intermediate odd-odd nucleus that contribute to the decay. The h_α factors have in this case the following expressions [3, 14]:

$$h_{\mathrm{GT},T} = -\frac{1}{6}\frac{m_\pi^2}{m_e\left(m_u+m_d\right)}\frac{q^2/m_\pi^2}{\left(1+q^2/m_\pi^2\right)^2}. \tag{19}$$

For computing the radial matrix elements $\langle nl|H_\alpha|n'l'\rangle$, we use the harmonic oscillator wave functions $\psi_{nl}(lr)$ and $\psi_{n'l'}(r)$ corrected by a factor $[1+f(r)]$, which takes into account the SRCs induced by the nuclear interaction:

$$\psi_{nl}(r) \longrightarrow \left[1+f(r)\right]\psi_{nl}(r). \tag{20}$$

For the correlation function, we take the functional form

$$f(r) = -c\cdot e^{-ar^2}\left(1-br^2\right), \tag{21}$$

where a, b, and c are constants which have particular values in different parameterizations. In this work, we consider the Miller-Spencer (MS) [44], AV18 [45], and CD-Bonn [46, 47] parameterizations.

Table 3: $0\nu\beta\beta$ NMEs values for SUSY2 mechanism and comparison to other results in the literature.

$M^{0\nu}$	No SRC	Jastrow	AV-18	CD-BONN
^{48}Ca (GXPF1A)	65.1	46.4	65.0	70.0
^{48}Ca (KB3G)	72.9	51.8	72.9	78.6
^{48}Ca [34]			81.8	86.7
^{76}Ge (JUN45)	281.7	233.4	283.5	296.8
^{76}Ge [32]			594	612
^{82}Se (JUN45)	253.6	208.6	255.7	268.1
^{82}Se [32]			578	595

3. Numerical Results and Discussions

We calculate first the NMEs for the three nuclei, that is, ^{48}Ca, ^{76}Ge, and ^{82}Se, and the three mechanisms mentioned above, using the code described in detail in [35, 36]. For ^{48}Ca, we performed calculations with two different NN interactions, GXPF1A [51] and KB3G [52] interactions, while for the other two isotopes we used the JUN45 [53] NN interaction. In the case of ^{48}Ca, our model space includes the whole fp shell $f_{7/2}$, $p_{3/2}$, $f_{5/2}$, and $p_{1/2}$, while, for ^{76}Ge and ^{82}Se, the model space is jj44, including the following orbitals $f_{5/2}$, $p_{3/2}$, $p_{1/2}$, and $g_{9/2}$. For the nuclear parameters involved in calculations, we used the values mentioned in the previous section and, for the nuclear radius, $R = r_0A^{1/3}$, we used $r_0 = 1.2fm$. The results are presented in Tables 1, 2, and 3. One can see that there are significant differences between the results when using different NN interactions and different SRC parameterizations. Indeed, especially for the short-range exchange mechanisms, as the heavy neutrino and gluino (SUSY1) ones, one expects the results to be sensitive to the NN interaction and to the type of SRC parameterizations. The uncertainties in the NME calculated values due to the use of different NN interactions are in the range of (10–16)%. The uncertainties due to the use of different SRC parameterizations are larger; sometimes differences between results are larger than 100%, especially when comparing the NME values obtained with MS [44] parameterizations with those obtained with softer parameterizations, such as AV18 [45] and CD-Bonn [46, 47]. Further, we compare our results with other similar ones found in literature. To the best of our knowledge, explicit values of NMEs calculated with large scale ShM approaches are reported only in [34] and for one nucleus, ^{48}Ca. Our results agree within ~10% with those from [34], for all three mechanisms. At this point, it is worth mentioning that the GT and tensor contributions in (5) must have a relative opposite sign, such that the adding of the tensor contribution decreases the $M^{0\nu}$ total value. Hence, one has to pay attention when applying formula (5) because the GT and tensor contributions can come out from numerical calculations with opposite signs. In this respect, we suspect that our NME values agree even better with those from [34]. For the other two isotopes, that is, ^{76}Ge and ^{82}Se, we compare our (ShM) results with QRPA [31, 32, 43] and IBM-2 [28] results. For the heavy neutrino and SUSY2 mechanisms, the differences between our NME values and NME values

Table 4: Upper limits for Majorana neutrino mass parameters together with the other components of the $0\nu\beta\beta$ decay halftimes: the experimental lifetimes lower limits, the phase space factors, and the nuclear matrix elements.

	$T^{0\nu}_{\text{exp}}$ [yr]	$G^{0\nu}$ [yr^{-1}]	$M^{0\nu}_{N}$	$M^{0\nu}_{\lambda'}$	$M^{0\nu}_{q}$	$\langle\eta_N\rangle$	$\langle\eta_{\lambda'}\rangle$	$\langle\eta_q\rangle$
^{48}Ca*	$5.8\cdot10^{22}$ [48]	$2.46E-14$	70.3	548.2	70	$2.42\cdot10^{-7}$	$3.10\cdot10^{-8}$	$2.42\cdot10^{-7}$
^{48}Ca†	$5.8\cdot10^{22}$ [48]	$2.46E-14$	82.8	641.7	78.6	$2.05\cdot10^{-7}$	$2.64\cdot10^{-8}$	$2.16\cdot10^{-7}$
^{76}Ge	$2.1\cdot10^{25}$ [49]	$2.37E-15$	199.2	1509.4	296.8	$0.14\cdot10^{-7}$	$0.19\cdot10^{-8}$	$0.10\cdot10^{-7}$
^{82}Se	$3.6\cdot10^{23}$ [50]	$1.01E-14$	184.5	1393.5	268.1	$0.58\cdot10^{-7}$	$0.76\cdot10^{-8}$	$0.40\cdot10^{-7}$

*Denotes GXPF1A [51] effective interaction and †KB3G [52] effective interaction.

calculated with QRPA and IBM-2 methods are significant, but they are similar (in magnitude) to those encountered usually in the case of light neutrino exchange mechanism. For the SUSY1 mechanism, our results compare differently with the QRPA results reported by Tuebingen group in [32, 43], the only ones found in literature. We note that the agreement is good when comparing with the results of [43], where the MS parameterizations of the SRCs are employed, and it is bad when comparing with those of [32], where AV18 and CD-Bonn parameterizations for SRCs are used. As a conclusion, it turns out that more results for the NMEs associated with heavy neutrino and SUSY mechanisms, performed with different methods and including more nuclei, are needed for a relevant analysis of their validity.

In Table 4, we present new upper limits for the LNV parameters associated with the studied $0\nu\beta\beta$ decay mechanisms, in the hypothesis of a single dominance mechanism. The PSFs values are taken from [37] and we mention that they are very close to PSF values reported in [38, 39]. The PSFs have been calculated since long time [40, 41] but they were less discussed, being considered to be computed with enough precision. Recently, they were recalculated with improved approaches, by using exact electron Dirac wave functions, taking into account the finite nuclear size and electron screening effects [38] and, in addition, a realistic Coulomb potential [39, 42], and differences/discrepancies were found in several cases between the old and the recent PSF values. For the three isotopes considered in this work, the new PSF values differ from older calculations (e.g., from those reported in [41, 54–56]) up to 10%, justifying hence their use in a precise derivation of LNV parameters. The uncertainties in NME values reflect on the precision of derivation the LNV parameters. According to the consensus agreed upon in literature that softer SRC parameterizations are indicated, we adopt the NME values calculated with the CD-Bonn parameterization and derive the LNV parameters for the three nuclei and the three mechanisms considered. These results are presented in Table 4. For derivation, we used the most recent results for the experimental lifetimes, reported in references indicated in parenthesis. For ^{48}Ca, our limits for the LNV parameters are close to those reported in [34], while for the other two nuclei they differ from other results from literature [28, 32, 34, 43], derived with NMEs values calculated with QRPA and IBM-2 methods. As we already mentioned, information on LNV parameters for the heavy neutrino mechanism can be now extracted, as well, from the data analysis of the same sign dilepton channels at the LHC experiments. Thus, we expect that complementary information from both low- and high-energy experiments could be used in the future for better constraining of the LNV parameters.

4. Conclusions

We report new constraints for the heavy neutrino and SUSY parameters derived from an analysis of $0\nu\beta\beta$ decay of three experimentally interesting nuclei, ^{48}Ca, ^{76}Ge, and ^{82}Se. To the best of our knowledge, for the last two isotopes, no other large scale ShM results for these mechanisms are available so far. For deduction of these parameters, precise values of the NMEs and PSFs which enter the lifetime formulae are needed, as well as accurate experimental measurements of the lifetimes. The NME calculations are performed with a recent ShM code described widely in [35, 36]. The PSFs are taken from our most recent calculations reported in [37]. For SUSY mechanisms, we discuss two mechanisms associated with possible R-parity breaking in SUSY theories, a short-range one with exchange of heavy Majorana neutrino and scalar SUSY particles (gluinos and squarks and/or neutralinos and selectrons) and a long-range one involving exchange of both heavy squarks and light Majorana neutrinos—"squark-neutrino" mechanism. First, we calculated the NMEs using different nuclear ingredients. For ^{48}Ca, we use two different NN interactions, GXPF1A and KB3G, and found differences between the results within 10%. Also, we performed the calculations using three different parameterizations for the SRCs and found a significant dependence of the results on the way the SRCs are introduced in calculations. Further, we compare our (ShM) results with similar results from literature. For ^{48}Ca, our results are in good agreement with the results from [34], for all three mechanisms. For the other two isotopes, ^{76}Ge and ^{82}Se, we compare our (ShM) NMEs with those computed by QRPA [31, 32, 43] and IBM-2 [28] methods. For the heavy neutrino and SUSY2 mechanisms, the differences between our results and the results from those references are significant but similar (up to a factor of two) to those encountered usually in literature in the case of light neutrino exchange mechanism. For the SUSY1 mechanism, our results compare differently with QRPA results, reported by Tuebingen group. There is a good agreement with the results from [43], when the MS SRC parameterization is employed, but the agreement is bad when comparing with the values from [32], when softer SRC parameterizations are employed. As a conclusion, it turns out that more results for the NMEs associated with these $0\nu\beta\beta$ decay mechanisms, alternative to the light neutrino exchange one, performed with different nuclear methods and including more nuclei,

are needed for a relevant analysis of their validity. Then, we derived upper limits of the LNV parameters associated with the three mechanisms, in the hypothesis of one single dominance mechanism, using NMEs values computed with CD-Bonn parameterization. Finally, it is worth noting that information on LNV parameters can now be provided by LHC experiments at CERN from the analysis of the same sign dilepton channels. Thus, there is now the possibility to gather complementary information from both low- and high-energy experiments and use it to better constrain LNV parameters.

Conflict of Interests

The authors declare that there is no conflict of interests regarding the publication of this paper.

Acknowledgments

The authors thank J. Menendez for useful discussions. This work was done with the support of the MEN and UEFISCDI through the Project IDEI-PCE-3-1318, Contract no. 58/28.10/2011.

References

[1] F. T. Avignone, S. R. Elliott, and J. Engel, "Double beta decay, Majorana neutrinos, and neutrino mass," *Reviews of Modern Physics*, vol. 80, no. 2, pp. 481–516, 2008.

[2] H. Ejiri, "Double beta decays and neutrino nuclear responses," *Progress in Particle and Nuclear Physics*, vol. 64, no. 2, pp. 249–257, 2010.

[3] J. D. Vergados, H. Ejiri, and F. Šimkovic, "Theory of neutrinoless double-beta decay," *Reports on Progress in Physics*, vol. 75, no. 10, Article ID 106301, 2012.

[4] W. Rodejohann, "Neutrinoless double-beta decay and neutrino physics," *Journal of Physics G: Nuclear and Particle Physics*, vol. 39, no. 12, Article ID 124008, 2012.

[5] A. Faessler, V. Rodin, and F. Simkovic, "Nuclear matrix elements for neutrinoless double-beta decay and double-electron capture," *Journal of Physics G: Nuclear and Particle Physics*, vol. 39, no. 12, Article ID 124006, 2012.

[6] P. Vogel, "Nuclear structure and double beta decay," *Journal of Physics G: Nuclear and Particle Physics*, vol. 39, no. 12, Article ID 124002, 2012.

[7] R. N. Mohapatra and J. C. Pati, "Left-right gauge symmetry and an "isoconjugate & model of CP violation," *Physical Review D*, vol. 11, no. 3, pp. 566–571, 1975.

[8] M. Doi, T. Kotani, H. Nishiura, and E. Takasugia, "Double beta decay," *Progress of Theoretical Physics*, vol. 69, no. 2, pp. 602–635, 1983.

[9] M. Hirsch, H. V. Klapdor-Kleingrothaus, and S. G. Kovalenko, "Supersymmetry and neutrinoless double beta decay," *Physical Review D*, vol. 53, no. 3, pp. 1329–1348, 1996.

[10] CMS Collaboration, "Search for new physics with same-sign isolated dilepton events with jets and missing transverse energy at the LHC," *Journal of High Energy Physics*, vol. 2011, article 77, 2011.

[11] ATLAS Collaboration, "Inclusive search for same-sign dilepton signatures in pp collisions at $\sqrt{S} = 7$ TeV with the ATLAS detector," *Journal of High Energy Physics*, vol. 2011, article 107, 2011.

[12] LHCb Collaboration, "Search for Lepton number violating decays $B^+ \to \pi^-\mu^+\mu^+$ and $B^+ \to K^-\mu^+\mu^+$," *Physical Review Letters*, vol. 108, Article ID 101601, 2012.

[13] LHCb Collaboration, "Searches for Majorana neutrinos in B^- decays," *Physical Review D*, vol. 85, p. 112004, 2012.

[14] F. Simkovic, A. Faessler, H. Muther, V. Rodin, and M. Stauf, "$0\nu\beta\beta$-decay nuclear matrix elements with self-consistent short-range correlations," *Physical Review C*, vol. 79, Article ID 055501, 2009.

[15] V. A. Rodin, A. Faessler, F. Simkovic, and P. Vogel, "Uncertainty in the $0\nu\beta\beta$ decay nuclear matrix elements ," *Physical Review C*, vol. 68, Article ID 044302, 2003.

[16] V. A. Rodin, A. Faessler, F. Simkovic, and P. Vogel, "Assessment of uncertainties in QRPA $0\nu\beta\beta$-decay nuclear matrix elements," *Nuclear Physics A*, vol. 766, pp. 107–131, 2006.

[17] V. A. Rodin, A. Faessler, F. Simkovic, and P. Vogel, "Erratum to: "Assessment of uncertainties in QRPA $0\nu\beta\beta$-decay nuclear matrix elements" [Nucl. Phys. A 766 (2006) 107]," *Nuclear Physics A*, vol. 793, no. 1–4, pp. 213–215, 2007.

[18] M. Kortelainen and J. Suhonen, "Nuclear matrix elements of $0\nu\beta\beta$ decay with improved short-range correlations," *Physical Review C*, vol. 76, Article ID 024315, 2007.

[19] F. Šimkovic, A. Faessler, V. Rodin, P. Vogel, and J. Engel, "Anatomy of the $0\nu\beta\beta$ nuclear matrix elements," *Physical Review C*, vol. 77, no. 4, Article ID 045503, 2008.

[20] S. Stoica and H. V. Klapdor-Kleingrothaus, "Critical view on double-beta decay matrix elements within Quasi Random Phase Approximation-based methods," *Nuclear Physics A*, vol. 694, no. 1-2, pp. 269–294, 2001.

[21] M. Horoi and S. Stoica, "Shell model analysis of the neutrinoless double-β decay of ^{48}Ca," *Physical Review C*, vol. 81, no. 2, Article ID 024321, 2010.

[22] E. Caurier, A. P. Zuker, A. Poves, and G. Martinez-Pinedo, "Full *pf* shell model study of $A = 48$ nuclei," *Physical Review C*, vol. 50, article 225, 1994.

[23] J. Retamosa, E. Caurier, and F. Nowacki, "Neutrinoless double beta decay of ^{48}Ca," *Physical Review C*, vol. 51, article 371, 1995.

[24] E. Caurier, J. Menéndez, F. Nowacki, and A. Poves, "Influence of pairing on the nuclear matrix elements of the neutrinoless $\beta\beta$ decays," *Physical Review Letters*, vol. 100, no. 5, Article ID 052503, 2008.

[25] J. Menéndez, A. Poves, E. Caurier, and F. Nowacki, "Disassembling the nuclear matrix elements of the neutrinoless $\beta\beta$ decay," *Nuclear Physics A*, vol. 818, no. 3-4, pp. 139–151, 2009.

[26] J. Barea and F. Iachello, "Neutrinoless double-β decay in the microscopic interacting boson model," *Physical Review C*, vol. 79, no. 4, Article ID 044301, 2009.

[27] J. Barea, J. Kotila, and F. Iachello, "Limits on neutrino masses from neutrinoless double-β decay," *Physical Review Letters*, vol. 109, no. 4, Article ID 014315, 2012.

[28] J. Barea, J. Kotila, and F. Iachello, "Nuclear matrix elements for double-β decay," *Physical Review C*, vol. 87, Article ID 014315, 2013.

[29] P. K. Rath, R. Chandra, K. Chaturvedi, P. K. Raina, and J. G. Hirsch, "Uncertainties in nuclear transition matrix elements for neutrinoless $\beta\beta$ decay within the projected-Hartree-Fock-Bogoliubov model," *Physical Review C*, vol. 82, no. 6, Article ID 064310, 2010.

[30] T. R. Rodriguez and G. Martinez-Pinedo, "Energy density functional study of nuclear matrix elements for neutrinoless $\beta\beta$ Decay," *Physical Review Letters*, vol. 105, Article ID 252503, 2010.

[31] F. Šimkovic, G. Pantis, J. D. Vergados, and A. Faessler, "Additional nucleon current contributions to neutrinoless double β decay," *Physical Review C*, vol. 60, no. 5, Article ID 055502, 1999.

[32] A. Faessler, G. L. Fogli, E. Lisi, A. M. Rotunno, and F. Åimkovic, "Multi-isotope degeneracy of neutrinoless double-β decay mechanisms in the quasiparticle random-phase approximation," *Physical Review D*, vol. 83, no. 11, Article ID 113015, 2011.

[33] M. Blennow, E. Fernandez-Martinez, J. Lopez-Pavon, and J. Menendez, "Neutrinoless double beta decay in seesaw models," *Journal of High Energy Physics* , vol. 2010, article 96, 2010.

[34] M. Horoi, "Shell model analysis of competing contributions to the double-β decay of ^{48}Ca," *Physical Review C*, vol. 87, Article ID 014320, 2013.

[35] A. Neacsu, S. Stoica, and M. Horoi, "Fast, efficient calculations of the two-body matrix elements of the transition operators for neutrinoless double-β decay," *Physical Review C*, vol. 86, no. 6, Article ID 067304, 2012.

[36] A. Neacsu and S. Stoica, "Study of nuclear effects in the computation of the $0\nu\beta\beta$ decay matrix elements," *Journal of Physics G: Nuclear and Particle Physics*, vol. 41, no. 1, Article ID 015201, 2014.

[37] S. Stoica and A. Neacsu, "Constraints on light neutrino parameters derived from the study of neutrinoless double beta decay," *Advances in High Energy Physics*, vol. 2014, Article ID 745082, 7 pages, 2014.

[38] J. Kotila and F. Iachello, "Phase-space factors for double-β decay," *Physical Review C*, vol. 85, no. 3, Article ID 034316, 2012.

[39] S. Stoica and M. Mirea, "New calculations for phase space factors involved in double-β decay," *Physical Review C*, vol. 88, Article ID 037303, 2013.

[40] H. Primakoff and S. P. Rosen, "Double beta decay," *Reports on Progress in Physics*, vol. 22, no. 1, article 305, pp. 121–166, 1959.

[41] J. Suhonen and O. Civitarese, "Weak-interaction and nuclear-structure aspects of nuclear double beta decay," *Physics Report*, vol. 300, no. 3-4, pp. 123–214, 1998.

[42] T. E. Pahomi, A. Neacsu, M. Mirea, and S. Stoica, "Phase space calculations for beta- beta- decays to final excited 2+1 states," *Romanian Reports in Physics*, vol. 66, no. 2, pp. 370–375, 2014.

[43] A. Wodecki, W. A. Kaminski, and F. Simkovic, "Grand unified theory constrained supersymmetry and neutrinoless double β decay," *Physical Review D*, vol. 60, Article ID 115007, 1999.

[44] T. Tomoda, "Double beta decay," *Reports on Progress in Physics*, vol. 54, no. 1, pp. 53–126, 1991.

[45] C. Giusti, H. Müther, F. D. Pacati, and M. Stauf, "Short-range and tensor correlations in the 16O(e,e$'$ pn) reaction," *Physical Review C*, vol. 60, no. 5, Article ID 054608, 1999.

[46] H. Muther and A. Polls, "Correlations derived from modern nucleon-nucleon potentials," *Physical Review C*, vol. 61, Article ID 014304, 1999.

[47] H. Muther, "Two-body correlations in nuclear systems," *Progress in Particle and Nuclear Physics*, vol. 45, no. 1, pp. 243–334, 2000.

[48] S. Umehara, T. Kishimoto, I. Ogawa et al., "Neutrino-less double-β decay of ^{48}Ca studied by CaF_2(Eu) scintillators," *Physical Review C*, vol. 78, Article ID 058501, 2008.

[49] C. Macolino and GERDA Collaboration, "Results on neutrinoless double-beta decay from GERDA phase I," *Modern Physics Letters A*, vol. 29, no. 1, p. 1430001, 2014.

[50] A. S. Barabash and V. B. Brudanin, "Investigation of double-beta decay with the NEMO-3 detector," *Physics of Atomic Nuclei*, vol. 74, no. 2, pp. 312–317, 2011.

[51] M. Honma, T. Otsuka, B. A. Brown, and T. Mizusaki, "New effective interaction for pf nuclei and its implications for the stability of the $N = Z = 28$ closed core," *Physical Review C*, vol. 69, no. 3, Article ID 034335, 2004.

[52] T. T. S. Kuo and G. E. Brown, "Reaction matrix elements for the 0f-1p shell nuclei," *Nuclear Physics A*, vol. 114, no. 2, pp. 241–279, 1968.

[53] M. Honma, T. Otsuka, T. Mizusaki, and M. Hjorth-Jensen, "New effective interaction for f_5pg_9-shell nuclei," *Physical Review C*, vol. 80, no. 6, Article ID 064323, 2009.

[54] M. Doi, T. Kotani, and E. Takasugi, "Double beta decay and majorana neutrino," *Progress of Theoretical Physics Supplements*, vol. 83, pp. 1–175, 1985.

[55] M. Doi and T. Kotani, "Neutrino emitting modes of double beta decay," *Progress of Theoretical Physics*, vol. 87, no. 5, pp. 1207–1231, 1992.

[56] M. Doi and T. Kotani, "Neutrinoless modes of double beta decay," *Progress of Theoretical Physics*, vol. 89, pp. 139–159, 1993.

Hindawi Publishing Corporation
Advances in High Energy Physics
Volume 2014, Article ID 320287, 8 pages
http://dx.doi.org/10.1155/2014/320287

Research Article

Study on the Neutrino Oscillation with a Next Generation Medium-Baseline Reactor Experiment

Chang Dong Shin and Kyung Kwang Joo

Department of Physics, Chonnam National University, Gwangju 500-757, Republic of Korea

Correspondence should be addressed to Kyung Kwang Joo; kkjoo@chonnam.ac.kr

Received 25 February 2014; Accepted 15 April 2014; Published 12 May 2014

Academic Editor: Theocharis Kosmas

For over fifty years, reactor experiments have played an important role in neutrino physics, in both discoveries and precision measurements. One of the methods to verify the existence of neutrino is the observation of neutrino oscillation phenomena. Electron antineutrinos emitted from a reactor provide the measurement of the small mixing angle θ_{13}, providing rich programs of neutrino properties, detector development, nuclear monitoring, and application. Using reactor neutrinos, future reactor neutrino experiments, more precise measurements of θ_{12}, Δm^2_{12}, and mass hierarchy will be explored. The precise measurement of θ_{13} would be crucial for measuring the CP violation parameters at accelerators. Therefore, reactor neutrino physics will assist in the complete understanding of the fundamental nature and implications of neutrino masses and mixing. In this paper, we investigated several characteristics of RENO-50, which is a future medium-baseline reactor neutrino oscillation experiment, by using the GloBES simulation package.

1. Introduction

Over the last decade, great progress has been made in understanding the neutrino sector of elementary particle physics. The discovery of neutrino oscillations is a direct indication of physics beyond the standard model. It provides a unique new window to explore physics at the Grand Unification Energy scale. While the absolute neutrino mass has not yet been measured, neutrino oscillation implies that neutrinos have a nonzero mass and are mixed together. Neutrino oscillations are described by the three Pontecorvo-Maki-Nakagawa-Sakata (PMNS) mixing angles (θ_{12}, θ_{23}, and θ_{13}), one CP violating phase, and two independent mass squared differences (Δm^2_{31}, Δm^2_{21}) [1, 2]. The mixing angles, (θ_{12}, θ_{23}, and θ_{13}), have been measured using atmospheric, solar, accelerator beam, and reactor neutrino experiments. Among the mixing angles, (θ_{12}, θ_{23}), the values are relatively well measured. θ_{12} was measured using solar neutrinos and the KamLAND experiment [3, 4], while θ_{23} was measured using atmospheric neutrinos and the long baseline accelerator K2K experiment [5, 6]. However, for the θ_{13} value, until the year 2012, the best upper limit was set by the Chooz reactor antineutrino disappearance experiment [7]. The reactor experiments (Double Chooz, Daya Bay, and RENO) have measured θ_{13} and provide accurate information on $\sin^2 2\theta_{13}$ [8–10]. In addition, reactor neutrino experiments make accurate measurements of reactor neutrino fluxes and spectra to search for sterile neutrinos [11–13]. Also, future accelerator based neutrino experiments will provide a rich program of measuring CP violation and matter effects. However, in the long baseline experiments, degeneracies and parameter correlations occur among θ_{13}, the CP violation phase (δ_{CP}), neutrino mass hierarchy, and θ_{23}. The possibility of measuring the CP violation effect can be fulfilled only if the value of θ_{13} is precisely measured. Combining the results from the accelerator and reactor-based experiments could offer the first glimpse of δ_{CP} without the necessity for long running accelerators with antineutrino beams [14].

After the RENO experiment, RENO collaboration plans to construct an underground detector of RENO-50 consisting of 18,000 tons of ultralow-radioactivity unloaded liquid scintillator (LS) and high quantum efficiency (QE) photomultiplier tubes (PMTs). At ~50 km from the reactor center, the neutrino oscillation takes place maximally due to θ_{12}. An

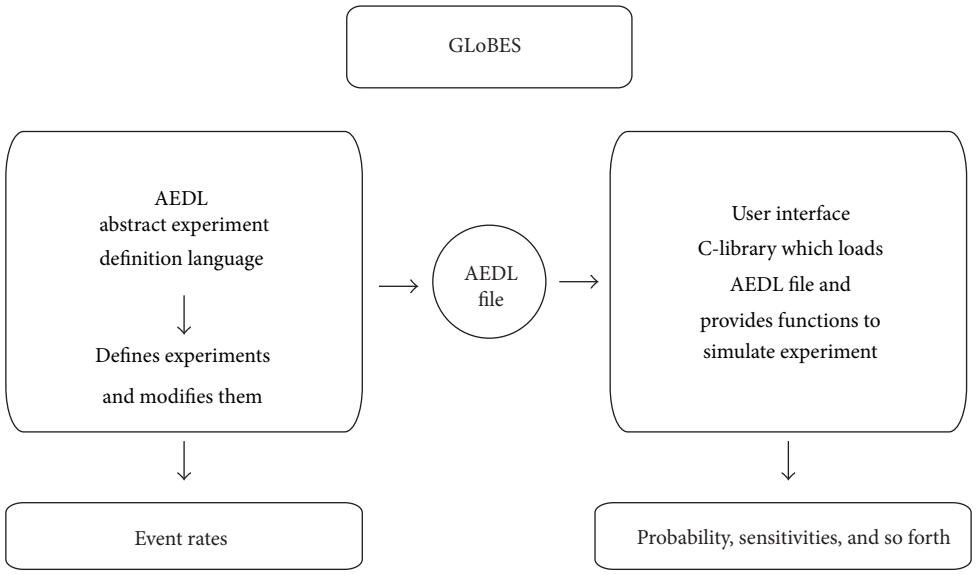

Figure 1: Schematics of GLoBES package, which mainly consists of two parts: AEDL and user interface C-library.

experiment with the baseline of ~50 km could be a natural extension of the current RENO θ_{13} experiment.

For this study, we used the general long baseline experiment simulator (GLoBES) [15]. Developed by Patrick Huber, Joachim Kopp, Manfred Lindner, Mark Rolinec, and Walter Winter, GLoBES is a computer-based simulator used for long baseline neutrino oscillation by setting a neutrino source, baseline, and detector. GLoBES is the only open source software and is based on the C-library language. As shown in Figure 1, GLoBES consists of two parts. Firstly, abstract experiment definition language (AEDL) provides the experimental setup for neutrino sources. Secondly, the C-library corresponds to the detector for processing to provide oscillation probabilities, rate vectors, and χ^2-values.

2. Results from RENO

2.1. Experimental Setup. The Reactor Experiment for Neutrino Oscillation (RENO) is a reactor-based neutrino oscillation experiment to measure the smallest neutrino mixing angle (θ_{13}) using electron antineutrinos emitted from the Hanbit (previously named Yonggwang) nuclear power plant in Korea. It is located on the west coast of the southern part of Korea, about 300 km from Seoul. The power plant consists of six pressurized water reactors producing a total thermal power of 16.4 GW_{th}. The six reactors, each with a maximum thermal output of 2.8 GW_{th} (reactors 3, 4, 5, and 6) or 2.9 GW_{th} (reactors 1 and 2), are aligned roughly equal distances and span ~1.3 km. The RENO uses two identical near and far detectors to reduce systematic uncertainties. The near and far detectors are placed approximately 290 m and 1.4 km away, respectively, from the center of the reactor array. The near detector (ND) is located under a 70 m high hill with an overburden of ~110 m.w.e. (meterwater equivalent) and the far detector (FD) is placed under a 260 m high mountain with an overburden of ~450 m.w.e. [10, 16].

2.2. Result on θ_{13} Measurement. Data-taking began at RENO in August, 2011. A clear disappearance of reactor antineutrinos is observed. At RENO, the value of $\sin^2 2\theta_{13}$ with two identical detectors has been successfully measured. The measured value using rate-only analysis is $\sin^2 2\theta_{13} = 0.100 \pm 0.010$ (stat.) $\pm$ 0.015 (sys.), corresponding to 6.3σ significance for 403 days data [10]. Therefore, the current size of the total error is ±0.018 [10]. Based on the next three years of projected data-taking, the statistical error will be ±0.006 and the systematic error will reach ±0.005. Therefore, RENO will reach $\sin^2 2\theta_{13}$ at an 8% precision level.

In current RENO environment, there are mainly three types of backgrounds which mimic IBD signals: accidental, fast neutron and the ^{9}Li/^{8}He backgrounds. The accidental backgrounds are caused by external gammas such as radioactivity from detector and environment. The estimated accidental background rate is 3.61 ± 0.05 (0.60 ± 0.03) events/day for the ND (FD) [10]. In addition, when atmospheric muons pass through rocks surrounding detector, fast neutrons are produced and the estimated fast neutron background rate is 3.14 ± 0.09 (0.68 ± 0.04) events/day for the ND (FD) [10]. Furthermore, when an energetic muon interacts with ^{12}C in liquid scintillator, unstable isotopes such as ^{9}Li and ^{8}He emitting (β, n) followers are produced and mimic IBD signals. Currently, the ^{9}Li/^{8}He background uncertainty is the largest contribution to the uncorrelated systematic error in the current results and its value is 13.73 ± 2.13 (3.61 ± 0.60) events/day for the ND (FD) [10]. By combining these three backgrounds, the total background rate is estimated as 20.48 ± 2.13 (4.89 ± 0.60) events/day for the ND (FD). After subtracting backgrounds, currently daily observed IBD rates are 737.69 ± 2.57 (70.13 ± 0.74) events/day in the ND (FD), respectively [10]. Therefore the level of signal/noise (S/N) ratio is ~37 (15) for the ND (FD). The ratio of observed to expected numbers (without oscillation) of antineutrinos in the FD is 0.929 ± 0.006 (stat.) ± 0.009 (syst.). A clear ~7% of

disappearance of the reactor antineutrinos in the FD is seen [10]. Further reductions of these backgrounds will continue at RENO by requiring a tighter muon veto cut. Furthermore, a spectral shape analysis will maximize the use of energy-dependent information in the data.

3. Physics Reach and Sensitivity of RENO-50

A relatively large value of θ_{13} allows us to explore mass hierarchy (MH) and neutrino CP violation effects (δ_{CP}) from the reactor, accelerator, atmospheric, and very long baseline neutrino experiments. The reactor experiment can determine the neutrino mass hierarchy. Identifying the neutrino mass hierarchy is possible by using a precision measurement of the electron antineutrino survival probability from a nuclear reactor. The survival probability $P(\bar{\nu}_e \to \bar{\nu}_e)$ of the $\bar{\nu}_e$ disappearance probability can be written as follows:

$$\begin{aligned} 1 - P(\bar{\nu}_e \longrightarrow \bar{\nu}_e) &= 4\sum_{j>k} |U_{ej}|^2 |U_{ek}|^2 \sin\left(\frac{\Delta m_{jk}^2 L}{4E}\right) \\ &= \sin^2(2\theta_{13}) \sin^2\left(\frac{\Delta m_{31}^2 L}{4E}\right) \\ &\quad + \cos^4\theta_{13} \sin^2(2\theta_{12}) \sin^2\left(\frac{\Delta m_{21}^2 L}{4E}\right) \\ &\quad + \sin^2\theta_{12} \sin^2(2\theta_{13}) \cos\left(\frac{\Delta m_{31}^2 L}{2E}\right) \sin^2\left(\frac{\Delta m_{21}^2 L}{4E}\right) \\ &\quad \pm \frac{1}{2} \sin^2\theta_{12} \sin^2(2\theta_{13}) \sin\left(\frac{\Delta m_{31}^2 L}{2E}\right) \sin^2\left(\frac{\Delta m_{21}^2 L}{2E}\right). \end{aligned} \tag{1}$$

Here, $\pm$ is the mass hierarchy difference. The oscillations are governed by two quadratic mass splittings: Δm_{21}^2 and Δm_{31}^2. Figure 2 shows the $\bar{\nu}_e$ disappearance probability as a function of L with the current best values of Δm^2 and $\sin^2 2\theta_{12}$ and $\sin^2 2\theta_{13}$ at the upper bound. At smaller L, only the θ_{13} contribution appears. As the distance increases, the θ_{12} contribution will appear. A large θ_{12} neutrino oscillation effect appears at ~50 km. In the KamLAND experiment, a 40% disappearance of $\bar{\nu}_e$ was observed at the baseline of 180 km [17]. Figure 3 shows the reactor neutrino spectrum at ~50 km for normal hierarchy (NH) and inverted hierarchy (IH). From the large deficit of $\sin^2 2\theta_{12}$, θ_{12} can be precisely measured.

In order to distinguish between normal and inverted mass hierarchy, an extremely good energy resolution of more than 3% is required, as shown in Figure 4. Energy resolution can be expressed as follows:

$$\frac{\sigma_E}{E} = \frac{a}{\sqrt{E}} + b. \tag{2}$$

Term a depends on energy resolution. For better energy resolution, we need to increase the number of photoelectrons,

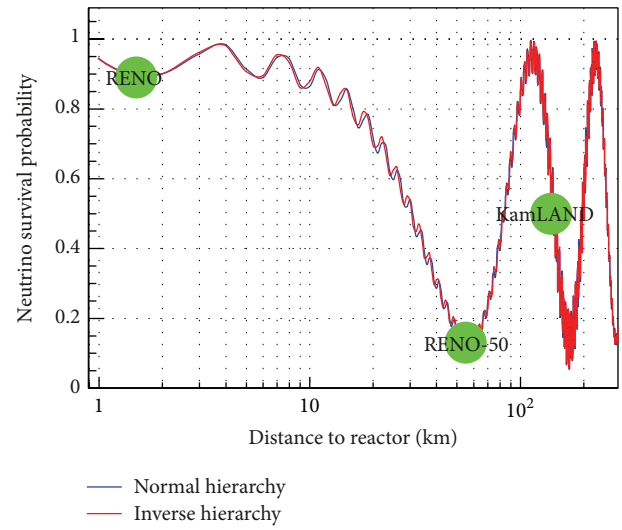

Figure 2: Survival probability of $\bar{\nu}_e$ as a function of distance (L). Normal hierarchy (NH) and inverted hierarchy (IH) drawn. RENO-50 is located at ~50 km from the reactor center. The KamLAND experiment is ~180 km away from the reactors.

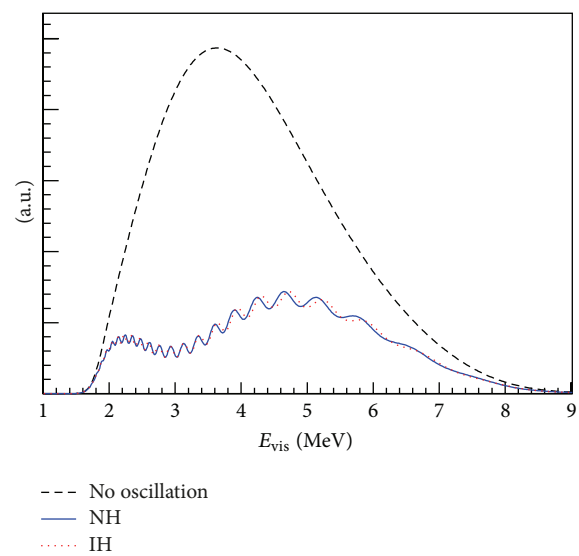

Figure 3: Reactor neutrino spectrum at 50 km for normal hierarchy (NH) and inverted hierarchy (IH). Due to oscillation, deficit of neutrinos will be observed.

N_{pe}. Term b is an energy independent term caused by random processes and is related to PMT noise, thermal noise and electronic noise, and so forth. Currently, the KamLAND energy resolution is at a ~6% level. In order to achieve 3% energy resolution, RENO-50 will use high transparency liquid scintillator (LS) which will be used at RENO-50 linear alkyl benzene (LAB, C_nH_{2n+1}–C_6H_5), where n = 10~13 is a base candidate solvent for LS [18–21]. Through the careful purification and production process of the base solvent, the attenuation length will be increased from 15 m to 25 m. Most dirty material used in the LS is PPO ($C_{15}H_{11}NO$, 2,5-diphenyloxazole), which is a fluor used to

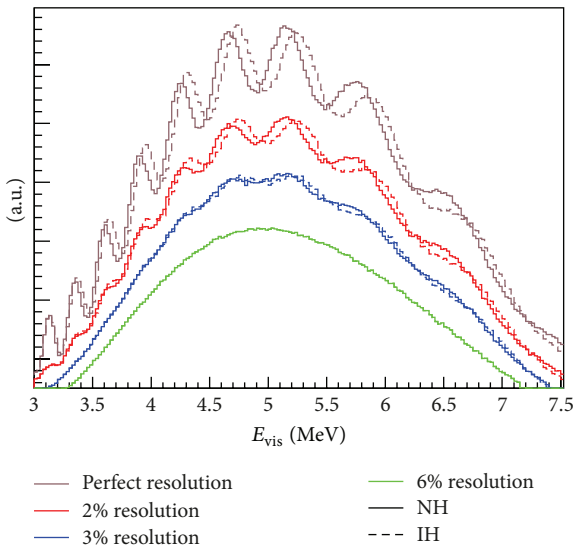

Figure 4: Survival probability with different energy resolutions. Solid line refers to NH and dashed line refers to IH. Energy resolution affects the sensitivity significantly.

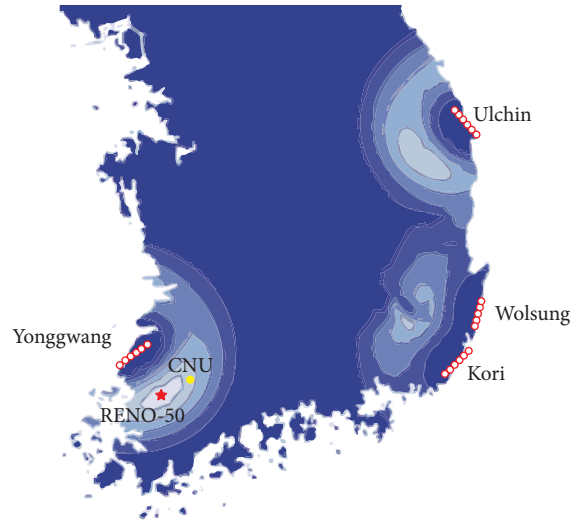

Figure 5: RENO-50 candidate site. The asterisk (∗) is a candidate site for RENO-50. The direction to RENO-50 strongly affects the sensitivity. Distribution of four reactors (Ulchin, Wolsung, Kori, and Yonggwang) is considered.

produce light emission. By using better quality PPO with no impurities, LS quality will be enhanced. Using 15,000 20-inch PMTs will provide large photocathode coverage from 34% to 67%; Hamamatsu 20-inch PMTs will be used, which have an enhanced quantum efficiency (QE) from 20% to 35%. By adding more PPO 5 g/L from 1.5 g/L, 1.5 times more light yield (LY) in the liquid scintillator can be obtained.

4. Experimental Site and Detector for RENO-50

Korea has 4 nuclear reactor power plant sites (Ulchin, Wolsung, Kori, and Yonggwang). RENO-50 is dedicated to the Yonggwang nuclear power plant. The contribution from other nuclear power plants can be negligible. In RENO-50, RENO will be used as a near detector, so that precise reactor neutrino fluxes can be measured. In the KamLAND case, this site is surrounded by 53 Japanese commercial nuclear power plants. Therefore, all of the nuclear reactors are served as a source. A careful survey of the candidate site for RENO-50 has been performed. Several conditions for the selection of the site are required. This should provide a sufficient overburden to reduce cosmic backgrounds. Furthermore, interference among reactor sites and reactor cores significantly affects the sensitivity. The direction of RENO-50 is decided to maximize this sensitivity. A RENO-50 candidate site is shown in Figure 5. An optimal candidate site is at the 450 meter high Mt. Geumseong located in the city of Naju. This corresponds to a ~900 m.w.e. overburden and it is located 47 km away from the Yonggwang nuclear power plant.

The RENO-50 detector will use 18,000 tons of ultralow-radioactive liquid scintillator (LS) as shown in Figure 6. The diameter of the RENO-50 detector is 30 m and the height is 30 m and is 18 times larger than the KamLAND detector. It consists of three layers: from the inner to the outer structure, it is target, mineral oil (MO) layer, and the water veto layer. A total of 15,000 20-inch high efficiency PMTs will be installed and this will provide 67% surface coverage. Based on these detector configurations, the number of neutrino events for a year as a function of the baseline is shown in Figure 7. Observed reactor neutrino rate is estimated as ~15 events/day. Table 1 shows a comparison between RENO-50 and KamLAND.

5. Physics with RENO-50

5.1. Mass Hierarchy. In principle, the mass hierarchy (MH) from precision measurements of $|\Delta m^2_{31}|$ and $|\Delta m^2_{32}|$ can be determined using $\Delta m^2_{31} = \Delta m^2_{32} + \Delta m^2_{21}$. For NH, $|\Delta m^2_{31}| = |\Delta m^2_{32}| + |\Delta m^2_{21}|$. For IH, $|\Delta m^2_{31}| = |\Delta m^2_{32}| - |\Delta m^2_{21}|$. Advantage of reactor neutrino experiments is to determine MH independently from the CP phase and matter effects. In addition, a relatively smaller size detector can be employed, unlike the next generation megaton detectors. However, in the RENO-50 case, the determination of MH is challenging, as it requires an extremely high energy resolution of more than 3%. By using an 18 kton detector, RENO-50 will acquire ~3σ significance with 3 years data-taking.

5.2. Precise Measurement of Mixing Parameter θ_{12} and Δm^2_{21}. In RENO-50, the near and far detectors of RENO could be used as near detectors and thus would reduce the relevant systematic uncertainties significantly. For baselines longer than 50 km, the reactor antineutrino oscillations due to Δm^2_{31} average out and the survival probability becomes

$$P = \cos^4\theta_{13}\left[1 - \sin^2(2\theta_{12})\sin^2\left(\frac{\Delta m^2_{21}L}{4E}\right)\right]. \quad (3)$$

Table 1: Comparison between RENO-50 and KamLAND.

Experiment	Oscillation reduction	Reactor flux	Detector size	Systematic error (flux)	Error on $\sin^2 2\theta_{12}$
KamLAND	40%	53	1 kton	3%	5.4%
RENO-50	77%	6 × 14.7	18 kton	~0.3%	0.4%

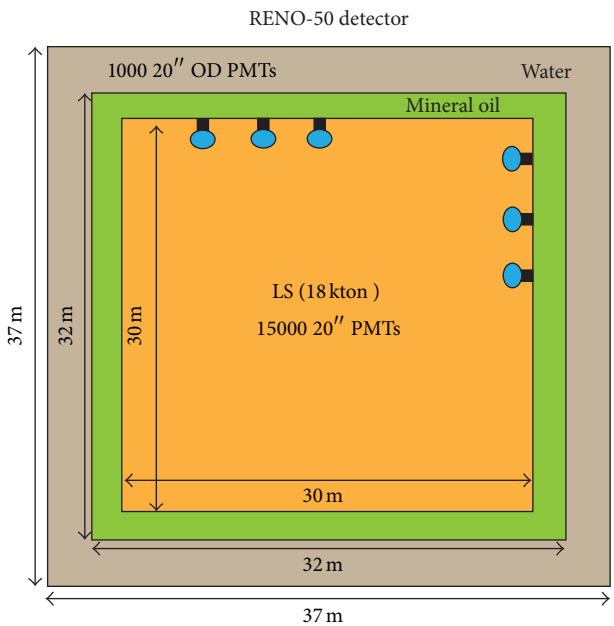

Figure 6: Conceptual design of RENO-50 detector. KamLAND detector is ~1 kton LS and RENO-50 18 kton LS. 15000 20-inch PMTs will be used. RENO-50 is 18 times larger than the KamLAND detector.

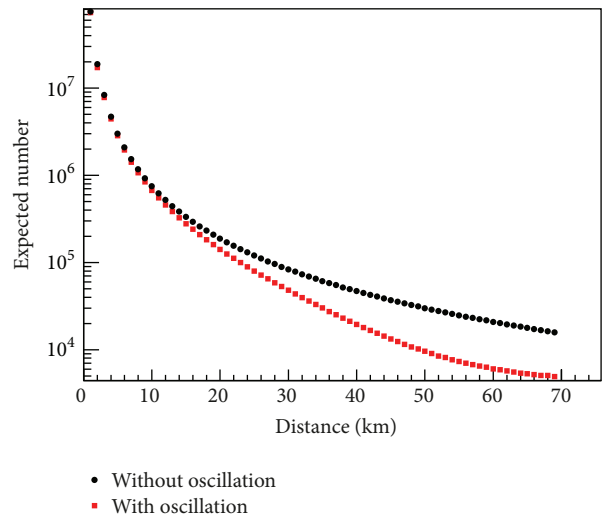

Figure 7: Number of neutrino event for a year with oscillation (rectangular) or without oscillation (circle) as a function of baseline from Yonggwang nuclear site.

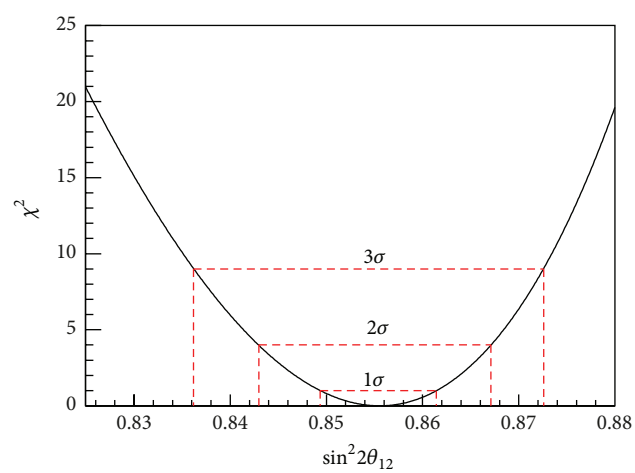

Figure 8: χ^2 distribution as a function of $\sin^2 2\theta_{12}$.

The oscillations due to θ_{12} and Δm^2_{21} were observed in the KamLAND experiment [3, 4]. Because the antineutrino survival probability becomes minimal for $\sin^2(\Delta m^2_{21} L/4E) \approx 1$, the optimal baseline for measuring θ_{12} is about 50~70 km. Namely, $P \approx 1 - \sin^2 2\theta_{12}$ is very sensitive to the value of θ_{12}. The RENO-50 detector is expected to improve the error of the θ_{12} value. The current value of $(\delta \sin^2\theta_{12})/(\sin^2\theta_{12})$ is at a ~5.4% level [3, 4]. RENO-50 will improve this value to ~1.0% (1σ) in 1 year. Furthermore, $(\delta\Delta m^2_{12})/(\Delta m^2_{12})$ will be improved from the current value of 2.6% to ~1.0% (1σ) in 2 years. Figure 8 shows the χ^2 distribution as a function of $\sin^2 2\theta_{12}$.

The sensitivity of the experiment to $\sin^2 2\theta_{12}$ is calculated using the pull approach through pseudoexperiment [16]. The χ^2 function is written as follows:

$$\chi^2 = \sum_i \frac{\left[N^i_{\text{obs}} - \left(1 + a + \xi^i + f_r\right) N^i_{\text{exp}} - (1 + b_d) B^i\right]^2}{N^i_{\text{exp}} + B^i + \left(\sigma^i_b B^i\right)^2} + \frac{a^2}{\sigma^2_a} + \sum_i \left(\frac{\xi^i}{\sigma_\xi}\right)^2 + \frac{f_r^2}{\sigma_f^2} + \frac{b_d^2}{\sigma_b^2}. \quad (4)$$

χ^2 consists of pull terms with observed neutrino events (N^i_{obs}), expected events (N^i_{exp}), background (B^i), and systematic uncertainties for neutrino energy bin i. Here, a is global normalization and 2.5% (σ_a) uncertainty is used. ξ^i, f_r, and b_d are pull parameters. For calculation, detection uncertainty 1.5% (σ_ξ), reactor uncertainty 3% (σ_f), and background uncertainty 5% (σ_b) are used.

5.3. Neutrino Burst from a Supernova. The RENO-50 detector filled with highly purified LS will be sensitive to a burst of neutrinos of all flavors from a Galactic supernova in the

energy range of a few to tens of MeV. The time scale of the burst is tens of seconds. We assume that the energy of 3.0×10^{53} erg is released during the burst. The background in the RENO-50 detector in a 10-second period is low enough for an observation of the neutrino signals from the supernova burst. The RENO-50 detector contains 1.35×10^{33} free protons, 0.81×10^{33} carbons, and 6.21×10^{33} electrons. The RENO-50 detector would observe ~4000 events from a supernova at 8 kpc [22, 23]. RENO-50 will serve as a long-term astronomical neutrino telescope over 10 years after RENO has recorded data for the θ_{13} measurement.

5.4. Solar Neutrinos. With an ultralow activity liquid scintillator such as the Borexino level, RENO-50 will search for the matter effect on neutrino oscillation [24]. Therefore, the center of the sun can be probed. Furthermore, the standard solar model would be examined and tested.

5.5. Geoneutrinos. Geoneutrinos are electron antineutrinos produced by β-decays of ^{238}U, ^{232}Th, and ^{40}K decay in the earth's crust and mantle. They provide the surface information on the content of radioactive elements for the entire planet. Their detection can provide information on the sources of the terrestrial heat flow on the present composition and on the origins of the earth. Therefore, the heat generation mechanism inside the earth can be investigated. KamLAND first measured geoneutrinos in 2005 and its value was 40.0 ± 10.5 (stat.) ± 11.5 (sys.) terrestrial neutrino units (TNU) [25]. In addition, the Borexino detectors are currently collecting geoneutrino data and have reported that the signal rate is 64 ± 25 (stat.) ± 2 (sys.) TNU, after correcting for detection efficiency and the background subtraction [26]. Furthermore, several proposed experiments (e.g., SNO+, Lena, Hanohano, and Earth) will measure geoneutrinos as their primary goals [27–29]. For geoneutrino detection, all experiments use the inverse beta decay (IBD, $\overline{\nu}_e + \mathrm{p} \rightarrow \mathrm{e}^+ + \mathrm{n}$) process. The threshold energy of IBD is 1.8 MeV. The measured shape of neutrino spectrum will be essential for determining the observation of geoneutrinos and their radioactive progenitors. The RENO-50 detector is large enough for the sensitive geoneutrino measurement and is able to observethem.

5.6. Reactor Neutrino Physics. Currently, RENO observes ~70 reactor neutrino events per day at the near detector and ~700 events at the far detector. The RENO and RENO-50 detectors will detect an order of 1 million neutrino events per year. They will measure the flux and energy distribution of the reactor neutrinos with a greater accuracy than previously. This information would then lead to a meaningful comparison of thermal power and reactor fuel loading between measurements and calculations. Such comparison will allow us to measure real-time and direct reactor thermal power with the RENO and RENO-50 detectors. In addition, a precise determination of the reactor neutrino spectrum might be useful for reducing the flux uncertainty [11–13]. Therefore, the reactor neutrinos could be used as an application for the direct monitoring of nuclear fuels and fuel evolution without the need to stop running the nuclear plant.

5.7. Other Physics Topics. Neutrino beams produced from J-PARC (Japan Proton Accelerator Research Complex) in Japan are airborne and appear on Korean peninsula, which is ~1000 km away from J-PARC. J-PARC beams with an off-axis angle (~3°) can reach the RENO-50 detector at the level of ~400 per year. Furthermore, RENO-50 will test nonstandard physics such as sterile neutrino physics. The discovery of sterile neutrinos would have a revolutionary impact on neutrino physics [30–34]. While recent neutrino oscillation results are understood in the framework of 3 active neutrino mixings, they do not completely exclude the admixture of sterile neutrinos [35, 36]. The liquid scintillator neutrino detector (LSND) collaboration implied that gave sterile neutrinos comes from the unconfirmed observation on $\nu_\mu \rightarrow \nu_s$ [37–39]. Mixing with sterile neutrinos based on the LSND signal predicts that the disappearance of the reactor neutrinos with $\Delta m^2 \sim \mathrm{eV}^2$ is very close to the current upper bound from the Bugey experiment [40]. Meanwhile, a scalar field of acceleron associated with the dark energy of the universe implies mass varying neutrinos. Possible couplings of acceleron to matter fields could introduce a very different feature of neutrino oscillation parameters. The mass varying neutrinos could also produce a possible effect in RENO-50. Combined data from the reactor and accelerator neutrino experiments with different path lengths in air and matter will give meaningful information on the mass-varying neutrinos.

6. Summary of RENO-50 and Outlook

A surprisingly large value of θ_{13} will strongly promote the next round of neutrino experiments to find the CP phase and determine the mass hierarchy. The main goals of RENO-50 are to measure the most accurate (1%) value of θ_{12} and to attempt to determine the neutrino mass hierarchy. RENO-50 is expected to detect neutrinos from nuclear reactors, the Sun, Supernova, the Earth, any possible stellar objects, and J-PARC neutrino beam. It could act as a neutrino telescope.

RENO-50 is a long-term operational and multipurpose detector. A candidate site has been found at the 450 meter high Mt. Geumseong, 47 km from the Hanbit nuclear power plant. RENO-50 requires an inclined tunnel to obtain a deeper location. It will use 18,000 tons of ultralow-radioactivity unloaded liquid scintillator and 15,000 20-inch high quantum efficiency PMTs with a 67% surface coverage. The current RENO detectors can serve as near detectors. The sensitivities are studied to determine the MH. Determining MH is very challenging, but not impossible with very good energy resolution of more than a 3% level. In addition, neutrino oscillation parameters, θ_{12} and Δm^2_{12}, will be precisely measured at less than a 0.5% level, which can constrain new physics. In summary, the RENO-50 reactor experiment with the medium baseline of ~50 km is expected to perform high-precision measurements of θ_{12}, Δm^2_{21}, and Δm^2_{31} and to determine the mass hierarchy. It will provide nuclear fuel monitoring with reactor neutrinos. Reactor experiments have played and will play an important role in both new discoveries and precision measurements in the neutrino sector. Therefore, a complete understanding of

neutrino oscillation will provide an opportunity to explore new physics.

Conflict of Interests

The authors declare that there is no conflict of interests regarding the publication of this paper.

Acknowledgments

This work was supported by the Korea Neutrino Research Center, which was established by the National Research Foundation of Korea (NRF) Grant funded by the Korea Government (MSIP) (no. 2009-0083526) and the Basic Science Research Program through the National Research Foundation of Korea (NRF) funded by the Ministry of Education (2010-0007850, 2012-0001177, and 2012M2B2A6030210).

References

[1] B. Pontecorvo, "Neutrino experiments and the problem of conservation of leptonic charge," *Journal of Experimental and Theoretical Physics*, vol. 53, pp. 1717–1725, 1967.

[2] Z. Maki, M. Nakagawa, and S. Sakata, "Remarks on the unified model of elementary particles," *Progress of Theoretical Physics*, vol. 28, no. 5, pp. 870–880, 1962.

[3] K. Eguchi, S. Enomoto, K. Furuno et al., "First results from KamLAND: evidence for reactor antineutrino disappearance," *Physical Review Letters*, vol. 90, no. 2, Article ID 021802, 6 pages, 2003.

[4] T. Araki, K. Eguchi, S. Enomoto et al., "Measurement of neutrino oscillation with KamLAND: evidence of spectral distortion," *Physical Review Letters*, vol. 94, no. 8, Article ID 081801, 5 pages, 2005.

[5] E. Aliu, S. Andringa, S. Aoki et al., "Evidence for muon neutrino oscillation in an accelerator-based experiment," *Physical Review Letters*, vol. 94, no. 8, Article ID 081802, 5 pages, 2005.

[6] M. H. Ahn, S. Aoki, H. Bhang et al., "Indications of neutrino oscillation in a 250 km long-baseline experiment," *Physical Review Letters*, vol. 90, no. 4, Article ID 041801, 5 pages, 2003.

[7] M. Apollonio, A. Baldini, C. Bemporad et al., "Search for neutrino oscillations on a long base-line at the chooz nuclear power station," *The European Physical Journal C*, vol. 27, no. 3, pp. 331–374, 2003.

[8] Y. Abe, C. Aberle, J. C. dos Anjos et al., "Reactor electron antineutrino disappearance in the Double Chooz experiment," *Physical Review D*, vol. 86, no. 5, Article ID 052008, 21 pages, 2012.

[9] F. P. An, J. Z. Bai, A. B. Balantekin et al., "Observation of electron-antineutrino disappearance at daya bay," *Physical Review Letters*, vol. 108, no. 17, Article ID 171803, 7 pages, 2012.

[10] J. K. Ahn, S. Chebotaryov, J. H. Choi et al., "Observation of reactor electron antineutrinos disappearance in the RENO experiment," *Physical Review Letters*, vol. 108, no. 19, Article ID 191802, 6 pages, 2012.

[11] T. A. Muller, D. Lhuillier et al., "Improved predictions of reactor antineutrino spectra," http://arxiv.org/abs/arXiv:1101.2663.

[12] A. A. Hahn, K. Schreckenbach, W. Gelletly, F. von Feilitzsch, G. Colvin, and B. Krusche, "Antineutrino spectra from ^{241}Pu and ^{239}Pu thermal neutron fission products," *Physics Letters B*, vol. 218, no. 3, pp. 365–368, 1989.

[13] G. Mention, M. Fechner, T. Lasserre et al., "Reactor antineutrino anomaly," *Physical Review D*, vol. 83, no. 7, Article ID 073006, 20 pages, 2011.

[14] K. Abe, T. Akin, N. Abgrall et al., "Recent results from the T2K experiment," *Nuclear Physics B*, vol. 246-247, pp. 23–28, 2014.

[15] http://www.mpi-hd.mpg.de/personalhomes/globes.

[16] J. Ahn, S. R. Baek, S. Choi et al., "RENO: an experiment for neutrino oscillation parameter θ_{13} using reactor neutrinos at Yonggwang," http://arxiv.org/abs/1003.1391.

[17] K. Eguchi, S. Enomoto, K. Furuno et al., "A High sensitivity search for anti-nu(e)'s from the sun and other sources at KamLAND," *Physical Review Letters*, vol. 92, Article ID 071301, 2004.

[18] J. S. Park, S. B. Kim, J. Lee, B. C. Kim, S. H. Kim, and K. K. Joo, "Feasibility study of a liquid scintillator using domestically produced Linear Alkyl Benzene (LAB)," *New Physics*, vol. 58, no. 1, pp. 62–67, 2009.

[19] I. S. Yeo and K. K. Joo, "Study on the optical properties of a linear alkyl benzene-based liquid scintillator in the RENO," *New Physics*, vol. 61, no. 8, pp. 739–743, 2011.

[20] J. S. Park, J. Lee, I.S. Yeo et al., "Production and optical properties of Gd-loaded liquid scintillator for the RENO neutrino detector," *Nuclear Instruments and Methods in Physics Research A*, vol. 707, pp. 45–53, 2013.

[21] B. K. Kim, S. H. So, S. H. Song, and K. K. Joo, "Investigation of the physical and optical properties of various base solvents for the liquid scintillator in a neutrino detector," *Journal of Korean Physical Society*, vol. 62, no. 1, pp. 26–33, 2013.

[22] K. Scholberg, "Supernova neutrino detection," http://arxiv.org/abs/astro-ph/0701081.

[23] L. Cadonati, F. P. Calaprice, and M. C. Chen, "Supernova neutrino detection in Borexino," *Astroparticle Physics*, vol. 16, no. 4, pp. 361–372, 2001.

[24] G. Alimonti, C. Arpesella, M. Balata et al., "Light propagation in a large volume liquid scintillator," *Nuclear Instruments and Methods in Physics Research A*, vol. 440, no. 2, pp. 360–371, 2000.

[25] T. Araki, S. Enomoto, K. Furuno et al., "Experimental investigation of geologically produced antineutrinos with KamLAND," *Nature*, vol. 436, pp. 499–503, 2005.

[26] G. Fiorentini, G. L. Fogli, E. Lisi, F. Mantovani, and A. M. Rotunno, "Mantle geoneutrinos in KamLAND and borexino," *Physical Review D*, vol. 86, no. 3, p. 033004, 2012.

[27] J. Hahn, R. L. Boger, J.K. Rowleyand et al., "The sudbury neutrino observatory," *Nuclear Instruments and Methods in Physics Research A*, vol. 449, no. 1-2, pp. 172–207, 2000.

[28] G. Fiorentini, M. Lissia, and F. Mantovani, "Geo-neutrinos and earth's interior," *Physics Reports*, vol. 453, no. 5-6, pp. 117–172, 2007.

[29] A. Mazumdar and M. M. Sheikh-Jabbari, "Noncommutativity in space and primordial magnetic field," *Physical Review Letters*, vol. 87, no. 1, Article ID 011301, 4 pages, 2001.

[30] D. O. Caldwell and R. N. Mohapatra, "Neutrino mass explanations of solar and atmospheric neutrino deficits and hot dark matter," *Physical Review D*, vol. 48, no. 7, pp. 3259–3263, 1993.

[31] J. T. Peltnoniemi, D. Tommasini, and J. W. F. Valle, "Reconciling dark matter and solar neutrinos," *Physics Letters B*, vol. 298, pp. 383–390, 1993.

[32] J. T. Peltnoniemi and J. W. F. Valle, "Reconciling dark matter, solar and atmospheric neutrinos," *Nuclear Physics B*, vol. 406, no. 1-2, pp. 409–422, 1993.

[33] K. Benakli and A. Y. Smirnov, "Neutrino-modulino mixing," *Physical Review Letters*, vol. 79, no. 22, pp. 4314–4317, 1997.

[34] B. Kayser, "Neutrino mass: where do we stand, and where are we going?" http://arxiv.org/abs/hep-ph/9810513.

[35] G. Mention, M. Fechner, M. Cribier et al., "The reactor antineutrino anomaly," http://arxiv.org/abs/arXiv:1101.2755.

[36] T. A. Muller, D. Lhuillier, M. Fallot et al., "Improved predictions of reactor antineutrino spectra," http://arxiv.org/abs/arXiv:1101.2663.

[37] C. Athanassopoulos, L. B. Auerbach, R. L. Burman et al., "Evidence for $\overline{\nu_e} \rightarrow \overline{\nu_e}$ oscillations from the LSND experiment at the los alamos meson physics facility," *Physical Review Letters*, vol. 77, no. 15, pp. 3082–3085, 1996.

[38] A. Aguilar, L. B. Auerbach, and R. L. Burman, "Evidence for neutrino oscillations from the observation of $\overline{\nu}_e$ appearance in a $\overline{\nu}_\mu$ beam," *Physical Review D*, vol. 64, no. 11, Article ID 112007, 22 pages, 2001.

[39] C. Athanassopoulos, L. B. Auerbach, and R. L. Burman, "Results on $\nu_\mu \rightarrow \nu_e$ neutrino oscillations from the LSND experiment," *Physical Review Letters*, vol. 81, p. 1774, 1998.

[40] M. Maltoni, T. Schwetz, M. A. Tórtola, and J. W. F. Valle, "Ruling out four-neutrino oscillation interpretations of the LSND anomaly?" *Nuclear Physics B*, vol. 643, no. 1–3, pp. 321–328, 2002.